University of Tehran

Print ISSN: 2322-2093

Online ISSN: 2423-6691

Volume 56, Number 2, December 2023

Civil Engineering Infrastructures Journal

CEIJ

Available online at
http://ceij.ut.ac.ir/

Civil Engineering Infrastructures Journal (CEIJ)

Volume 56, Number 2, December 2023

Civil Engineering Infrastructures Journal (CEIJ)
Semiannual Publication

Published by:

University of Tehran
College of Engineering

Indexed by:

Web of Science (ESCI)

Scopus

Civil Engineering Infrastructures Journal (CEIJ)
College of Engineering
University of Tehran
P.O. Box: 11155-4563
Tehran, Iran.
Tel/ Fax: +98-21-88956097
Email: ceij@ut.ac.ir
Web Site: www.ceij.ir

Editorial Board

Advisory Board

Civil Engineering Infrastructures Journal 2023, 56(2): 221-233
DOI: 10.22059/CEIJ.2023.341456.1828

RESEARCH PAPER

Rehabilitation Prospects of Concrete Pavements with Self-Compacting Concrete Containing Wollastonite Micro-Fiber

Jindal, A.[1*], G.D. Ransinchung, R.N.[2], Kumar, P.[2], Kumar, V.[3] and Rana, D.[3]

[1] Assistant Professor, Department of Civil Engineering, School of Engineering and Technology, Central University of Haryana, India.
[2] Professor, Department of Civil Engineering Indian Institute of Technology, Roorkee, India.
[3] Assistant Professor, Department of Civil Engineering, School of Engineering and Technology, Central University of Haryana, India.

Received: 11 Apr. 2022; Revised: 22 Sep 2022; Accepted: 22 Oct. 2022

ABSTRACT: Full depth repair remains to be the favored pavement restoration method amongst the common rehabilitation and repair activities carried out for concrete pavements. This paper explores the prospects of utilizing behavioral benefits of Self-Compacting Concrete (SCC) with the inclusion of Wollastonite micro-fiber, for repair and rehabilitation of concrete pavements. Wollastonite was included in the study by replacing fine aggregates in concrete mix in proportions 10%, 20%, 30%, 40% and 50%. The mixes were investigated for their behavioral properties including flow ability, resistance to segregation, filling ability and mechanical properties i.e. compressive strength, flexural strength, water absorption and hardened density. The rehabilitation prospect of concrete pavements with SCC was studied by conducting a joint repair study on pavement prototypes specially designed and tested for the purpose. It was found that the concrete mix with Wollastonite were more cohesive and workable which is attributed to its acicular structure and lustrous appearance. During the rehabilitation study, prototypes representing a jointed section of concrete pavement were repaired with SCC mixes. The prototypes repaired with SCC having Wollastonite micro-fiber at levels of 10%, 20% and 30% reported better flexural strength in comparison to those repaired with conventional concrete or with plane self-compacting concrete mix.

Keywords: Concrete Pavement, Rehabilitation, Self-Compacting Concrete, Wollastonite Micro-Fiber.

1. Introduction

Repair and rehabilitation of concrete pavements involves many pavement restoration techniques depending upon the desired repair effects. Pavement restoration techniques available for concrete roads include full depth repair, partial depth repair, diamond grinding, dowel bar retrofit, joint and crack resealing, slab stabilization, cross stitching, grooving, retrofitting edge drains and retrofitting concrete shoulder etc. (National Concrete Pavement Technology Center, 2014). Out of all pavement restoration methods full-depth repair is the most common technique implemented for

* Corresponding author E-mail: ajindal@cuh.ac.in

rigid pavements, as they provide better ride ability, structural integrity, and extend pavement service life (Federal Highway Administration, 2019).

The repair of concrete needs materials with different properties and techniques for application which also require material compatibility and structural efficiency while finalizing a material and requisite technique for implementation. Pavement repairs often need material in minor quantities which makes selection of proper material important considering service life of repaired pavements. Furthermore, the restoration and repair techniques also differ from techniques for new construction which is also a point of consideration while finalizing a material for repair.

While implementing patch repairs, generally the repair and maintenance is approached with the thought of general concrete paving thus leading to many factors overlooked which otherwise are important for patch repairs. Furthermore, the repair techniques and complexities involved for existing roads are different then the construction of new pavements thereby involving proper investigation of failure cause and thus recommending requisite repair methodology.

Self-compacting concrete with the benefit of its flowing property is preferred for applications finding heavy / congested reinforcements thus omitting the need for any external compaction (Center for Portland Cement Concrete Pavement Technology, 2005). Repairing concrete pavements with conventional concrete requires proper compaction, which would cause stress generations in adjoining previous parts thus compromising with its service life. However, SCC on the other hand once laid does not require any aided compaction or vibration, which makes it more advantageous in context of repairs for rigid pavements. Furthermore, the added advantage of a levelled surface reduces the need for surface finishing thereby saving time and energy for the same.

2. Review of Literature

The history of concrete pavements goes back to 1890's with the construction of first PCC pavement in Ohio (Rao et al., 2013). In 1909, Wayne County, Michigan, constructed a rural pavement upon testing of materials such as brick, stones, blocks of wood, and concrete. The inclusion of dowel bars started around 1917 in Virginia, which led to various slab configurations considering sections, joints and reinforcements (Thomas, 1998).

With the passage of time, lot of work has been done in this field and has widened the area with regular additions from new discoveries. As the research progressed, different researchers explored different techniques and materials for construction and maintenance of concrete pavements. Gibbons (1999) discussed different materials for construction of pavements such as asphalt, concrete, brick, stone, tile, wood, earth materials and synthetics. Concrete Pavement Maintenance/Repair report, discussed the repair and rehabilitation of concrete pavements by distress classification and highlighted different techniques used for maintenance of concrete pavements (Cement Concrete and Aggregates Australia, 2009). Mailvaganam (2001) outlined the issues and trends in the sphere of concrete repair and rehabilitation and gave a compelling description of the latest developments which could shape the future along with its potential for further innovation. Kumar and Kaushik (2003) highlighted the development of concrete as a building material with focus on infrastructure development and discussions on recent research scenario concerning utilization of concrete in different forms in the country. Dhir et al. (2019) highlighted the environmental impact and specifications associated with use of waste materials such as recycled aggregates etc. and their effects on concrete and concrete pavements. Sharifi et al. (2019) discussed different design practices and materials for concrete

pavement in addition to conditions leading to inadequate or reduced pavement performance.

With advent of time, self-compacting concrete came into existence to achieve durability amongst structures with heavy reinforcement and where external compaction is not feasible. Hajime Okamura and Masahiro Ouchi (1998) shared that the first prototype of self-compacting concrete was prepared with the objective of achieving durability amongst concrete structures. Over the period of time, advancement in research has led to SCC applications in various structures by major construction houses (Okamura and Ouchi, 1998). Collepardi (2003) highlighted that the application of SCC came into effect around 1980's in Europe, parts of Asia and United States. Some other pioneering application include discussion of Akshi Kaikyo bridge by Tanaka et. al. (2003) in Japan (The European Project Group, 2005).

European Project Group (2005) defined self-compacting concrete as "concrete that has ability to flow under its own weight thereby completely filling the formwork in the presence of dense reinforcement, without compromising with homogeneity and requirement of external compaction". Gesoglu et al. (2009) defined SCC as a concrete which is characterized by its self-flowing property owing to higher cement content and higher levels of superplasticizers. Despite the self-flowing behavior of SCC, the cost factor involved with SCC motivates researchers to include different types of mineral admixtures or additives to reduce the cost of SCC.

Literature could be found on use of different materials depicting pozzolanic behavior (likes of fly ash and silica fume) in SCC leading to improvement in concrete properties. Few studies include study of lower strength grade concrete (20 MPa to 30 MPa) with fly ash as replacement of cement (by volume) at 70% to 85% and higher strength grade concrete for replacement levels of 30% to 50% of cement by fly ash by Dinakar et al. (2008). Gutha (2010) discussed incorporation of fly ash as replacement of fine aggregate upto 15% resulting in compressive strength of SCC mix. Sharma et al. (2018) studied the effects of including Wollastonite, fly ash and micro silica to produce an economical SCC. They reported that SCC with 20% Wollastonite and 5%-7.5% micro silica showed higher flexural strength and lesser shrinkage. Uysal and Yilmaz (2011) studied the inclusions of rock powder such as limestone, basalt and marble as a partial replacement of binder in SCC. They reported an increase in elastic modulus and compressive strength of SCC with mineral admixtures improved with reduction in cost. Sharma (2019) investigated the properties of SCC prepared with addition of different pozzolans and recycled concrete aggregates and recommended a part replacement of binder up to 30% by Wollastonite micro-fibre, fly ash and microsilica for production of high strength self-compacting concrete. Hemlatha and Ramujee (2021) studied the influence of TiO_2 on self-compacting concrete with flyash, GGBS and wollastonite. Khayat and Roussel (1999) studied the inclusion of steel fibres in SCC to produce fibre reinforced concrete. They reported an increased flow ability and filling capacity with the inclusion of fibres in SCC.

Gru¨newald and Walraven (2001) studied the effects of including steel fibres in SCC by investigating the material behavior of fresh concrete along with the impact of content of aggregates, their types and amount of steel fibres on the flowing capacity of SCC. Bui et al. (2003) suggested reduced ratio of aggregates (coarse to fine) in order to achieve better cohesiveness of mix by surrounding coarse aggregates with a mortar layer. Furthermore, they also concluded that for increased fibre volume, higher volume of paste and lower content of coarse aggregate has to be maintained in the mix. Johnston (2001) also concluded that in order to ease the pumping of concrete, the content of coarse aggregates must be reduced by 10%. Bertil (2001) carried out

practical and analytical studies of behavioral properties of concrete and concluded that the elastic modulus parameters, creep and shrinkage behavior of self-compacting concrete was not found to have significant difference from that of conventional concrete. Gnanaraj et al. (2020) discussed the effects of different mineral and chemical admixtures in self-compacting concrete and their impact on mechanical behavior of SCC. Gholamzadeh-Chitgar and Berenjian (2021) proposed a neural network-based model to forecast the property parameters of SCC with low test error using data from literature.

Wollastonite is a mineral which occurs naturally and is majorly used in ceramic, porcelean and paint industries. For past few years Wollastonite has been a material of interest for researcher's owing to its chemical composition and its ability to enhance the behavior of cement matrix and concrete. Ransinchung et al. (2009) studied the feasibility of using Wollastonite micro-fibre and micro silica for part replacement of binder in concrete. They highlighted that incorporating 15% Wollastonite upto 15% and micro silica up to 7.5% leads to improvement in pore behavior of concrete. Jindal et al. (2020) discussed that incorporating Wollastonite micro-fibre as a part replacement of cement in by 30% leads to improvement in flowability, cohesiveness and higher strength values. Öz and Güne (2021) studied the effects of Wollastonite alongside calcite and quartz on high performance mortars. Kalla et al. (2015) highlighted the feasibility of substituting 10%-15% cement by Wollastonite to improve the concrete's strength and durability along with reduction in porosity and more dense concrete. Investigations have been made on self-compacting concrete using Wollastonite and other materials such as Kumar et al. (2017) incorporated ultrafine stealite powder; use of recycled concrete aggregates in self-compacting concrete by Santos et al. (2019). Similar discussions on benefits of incorporating Wollastonite in concrete were observed from Abdel et al. (2017), Sharma et al. (2018), Huang et al. (2019), Zareei et al. (2019), Abdolrasool and Mousavi (2020), Kuldasheva et al. (2020), Vishnu et al. (2021), Nair et al. (2021), Dutkiewicz et al. (2022), Bong et al. (2022), Gouse et al. (2022) and many more.

3. Objective of The Study

Incorporation of self-compacting concrete for general / structural applications have been into practice for past few decades. Various mineral and chemical admixtures have been included in SCC in different proportions for enhancement or behavior improvement. However, very scanty work has been done with the application of SCC for rehabilitation of concrete pavements. Moreover, only a few handful of studies could be found pertaining to repair and rehabilitation of concrete pavements with SCC incorporating Wollastonite micro-fiber.

This study thus investigates the potential of SCC for repairing and rehabilitating concrete pavements. The SCC mixes used for repair purposes were also admixed with Wollastonite micro-fiber, to estimate the likelihood of part replacing fine aggregates by Wollastonite micro-fibre.

4. Experimental Programme

Pavement prototypes repaired and rehabilitated using self-compacting concrete having Wollastonite micro-fiber were tested for investigating the efficacy of the mix for rehabilitation prospects. In previous part of study, it was established that partial inclusion of Wollastonite micro-fiber by replacing fine aggregates improves the cohesiveness and flowability with recorded increase in flexural strength when compared with referral mix (Jindal et al, 2020). The study reports the effects and change in behavior of self-compacting concrete upon the inclusion of Wollastonite micro-fiber as part replacement to sand at 5

levels namely 10%, 20%, 30%, 40% and 50%.

The design mix was prepared in accordance with IRC: 44 (2017) for pavement quality concrete, however iterative process using slump flow of mix was adopted to work out the proportions for SCC. Finally, mix with flow diameter greater than 600 mm were considered to be suitable. Referral mix without any Wollastonite is designated as mix S0, while mix incorporating Wollastonite micro-fiber at levels of 10%, 20%, 30%, 40% and 50% are designated as S1, S2, S3, S4, and S5 respectively. The composition of different mix in study are summarized in Table 1.

The rehabilitation study for pavement prototypes was carried out by repairing the prototypes at their joints using different mixes of self-compacting concrete incorporating Wollastonite micro-fiber at different levels as discussed above. In order to investigate the efficacy of rehabilitating concrete pavement using self-compacting concrete, a total of 16 pavement prototypes (2 prototypes for 1 set) were prepared and studied for failure loads under flexure in order to ascertain joint efficacy with the use of SCC. One set of prototype was repaired with conventional M40 mix i.e. RC, one set of prototype were prepared of SCC mix alone and designated as SS0, one set of prototypes each were repaired with SCC mixes S1, S2, S3, S4 and S5 designated as RS1, RS2, RS3, RS4 and RS5 respectively. These prototypes were then investigated for their flexural behavior at age 7 and 14 days.

5. Results and Discussions

5.1. Study on SCC Mixes

5.1.1. Fresh and Hardened State Investigations

SCC unlike conventional concrete requires much detailed investigation in fresh and hardened states in order to assess its efficacy. In the light of same, SCC mixes used in study were studied for fresh state properties such as horizontal flowability by slump flow test, filling ability by v-funnel test, segregation by probe ring test. The hardened state behavior of mix was studied by testing specimens under compressive and flexural conditions.

Table 1. Mixture compositions

Mix No.	Mix name	Water Kg/m^3	Cement kg/m^3	Fine materials Kg/m^3		Coarse aggregate kg/m^3		SP Kg/m^3
				Sand	Wollastonite	10 mm	6.3 mm	
S0	100 S	255	425	888.5	0	444.25	444.25	12.75
S1	90 S	255	425	799.65	88.85	444.25	444.25	12.75
S2	80 S	255	425	710.8	177.7	444.25	444.25	12.75
S3	70 S	255	425	621.95	266.65	444.25	444.25	12.75
S4	60 S	255	425	533.1	355.4	444.25	444.25	12.75
S5	50 S	255	425	444.25	444.25	444.25	444.25	12.75

Table 2. Test results for fresh SCC mix

Mix No.	Slump flow value (mm)	V-funnel reading (sec)	Probe test reading (mm)
S0	672	9	7
S1	663	9	8
S2	651	10	8
S3	637	11	8
S4	625	11	9
S5	610	12	9

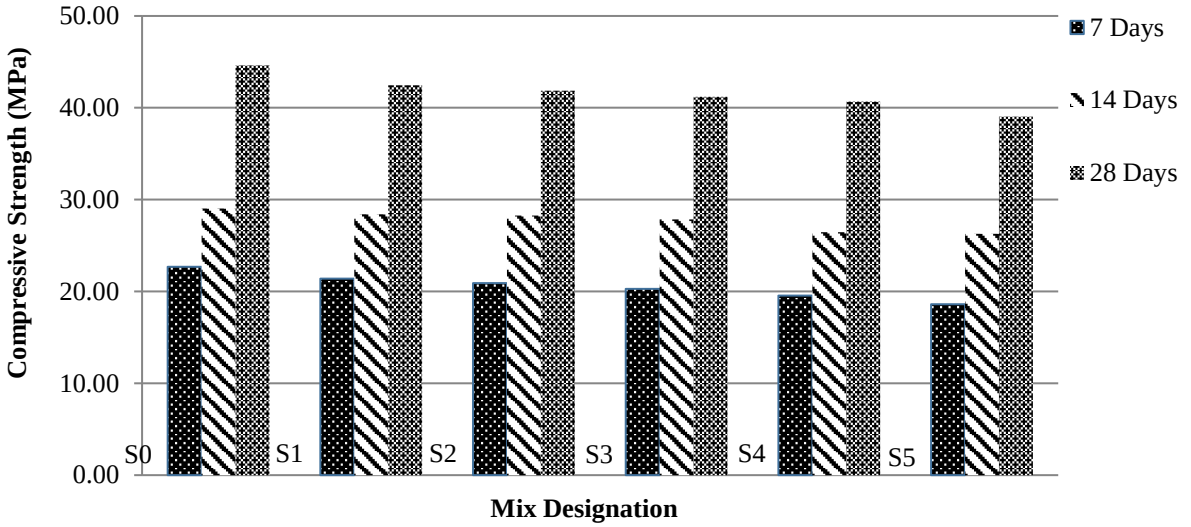

Fig. 1. Compressive Strength trend for SCC mixes

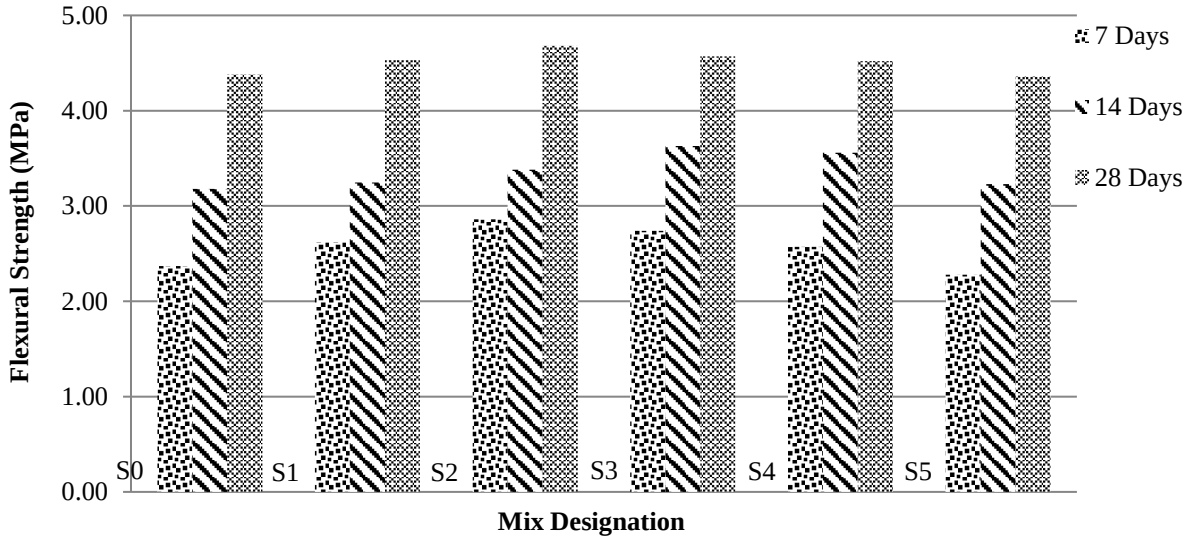

Fig. 2. Flexural Strength trend for SCC mixes

Table 2 discusses the fresh properties of SCC mix under study while Figures 1 and 2 illustrate the strength parameters obtained for the SCC mixes after testing. Results discussed for SCC mixes in earlier part of study (Jindal et al, 2020) concluded that Wollastonite micro-fiber when incorporated in self-compacting concrete results in more cohesive and flowable mix. Furthermore, the study of Jindal et al. (2020) concluded that SCC mix with Wollastonite micro-fiber recorded comparable compressive strength and better flexural strength values, thus indicating the acceptability of admixing Wollastonite micro-fiber in SCC mix.

5.1.2. SEM and XRD Investigations

SEM and XRD investigations were performed on hardened cement pastes of SCC mix under study to assess the impact of admixing Wollastonite as a micro-fibre at microscopic levels. The investigation of SEM images discussed in earlier part of study (Jindal et al., 2020) concluded that the SCC mixes upon incorporation of Wollastonite micro-fiber reported more cohesive rich and dense mix due to increase in fine content of the matrix.

The powdered specimens of cement mortar matrix as a representative of different mixes under study were analyzed using XRD technique to determine the crystalline phases developing in the

concrete mixes. The results obtained from phase analysis illustrates the peaks for respective compounds identified for mix under study shown in Figures 3 to 8. During the phase analysis the labeled peaks show that a particular peak may represent diffraction patterns of one or more phases in consideration. Thus, intensities of all probable compounds were matched to find out the presence of a given compound in the mix under study.

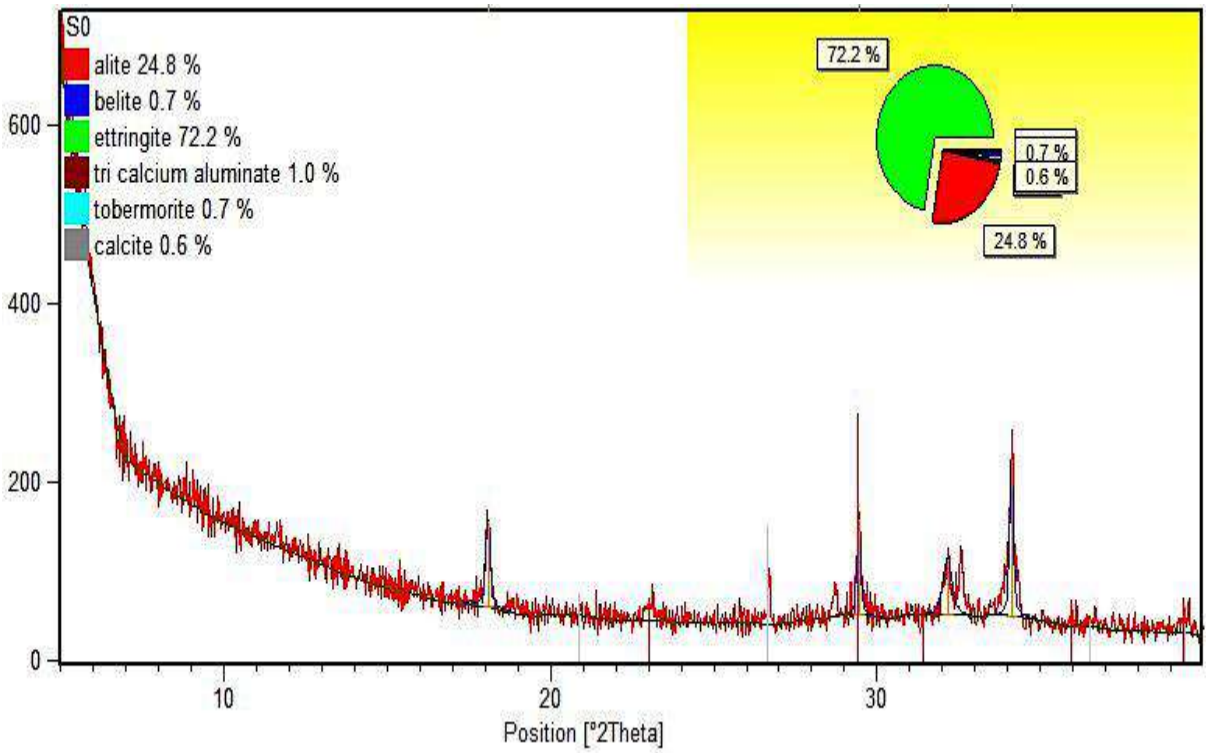

Fig. 3. XRD pattern for S0

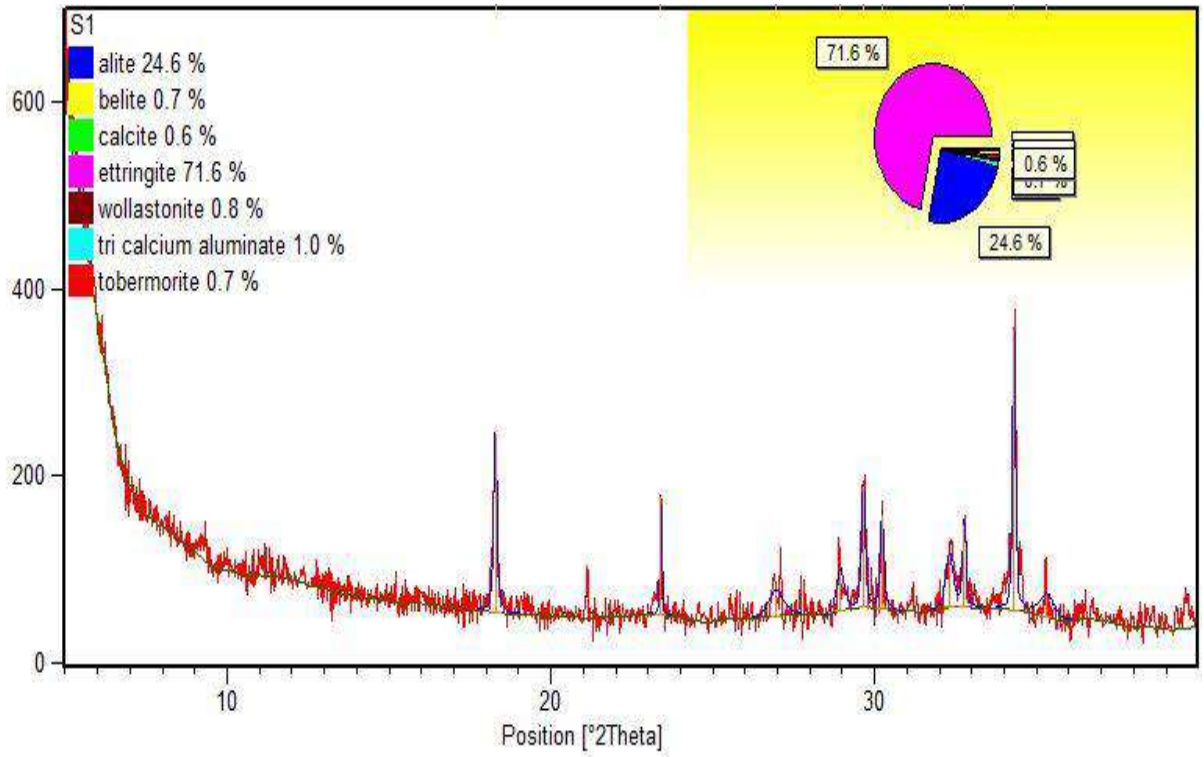

Fig. 4. XRD pattern for S1

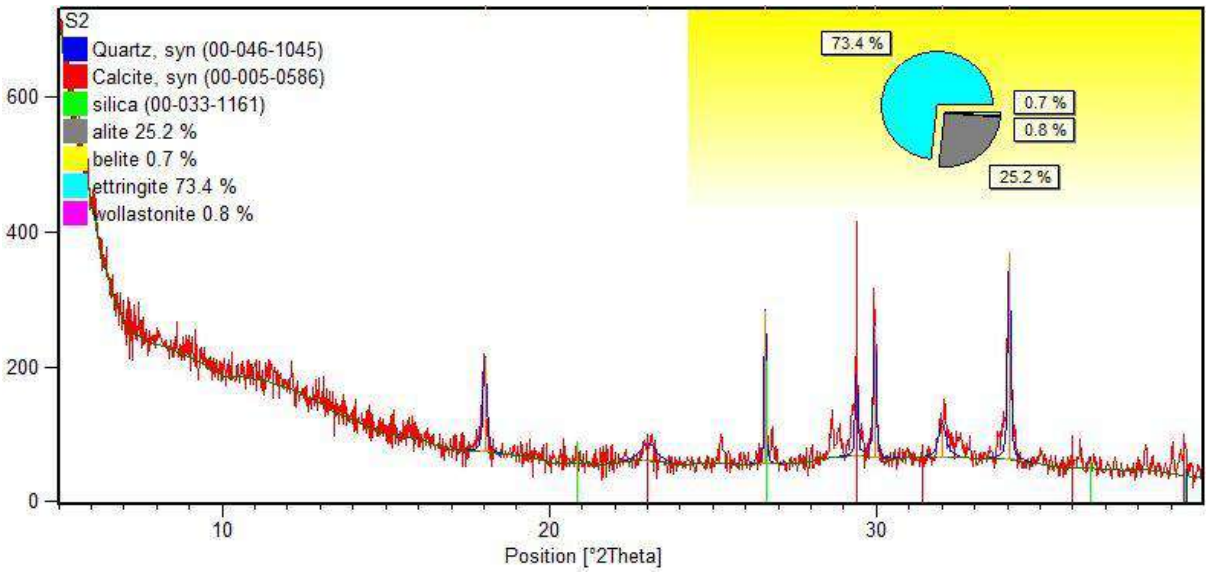

Fig. 5. XRD pattern for S2

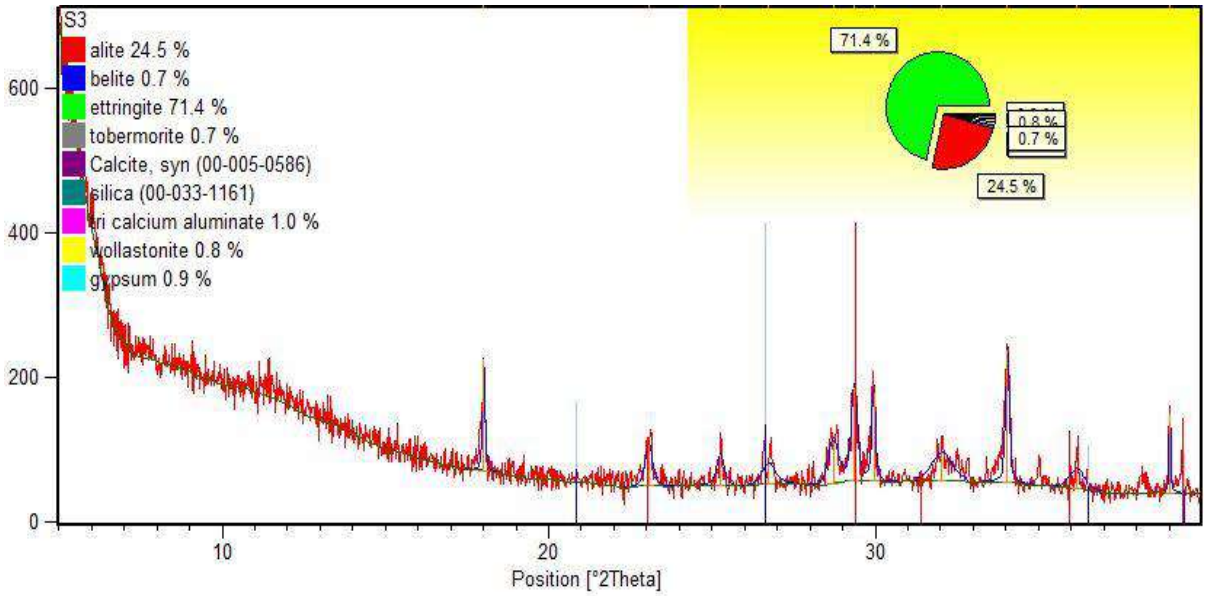

Fig. 6. XRD pattern for S3

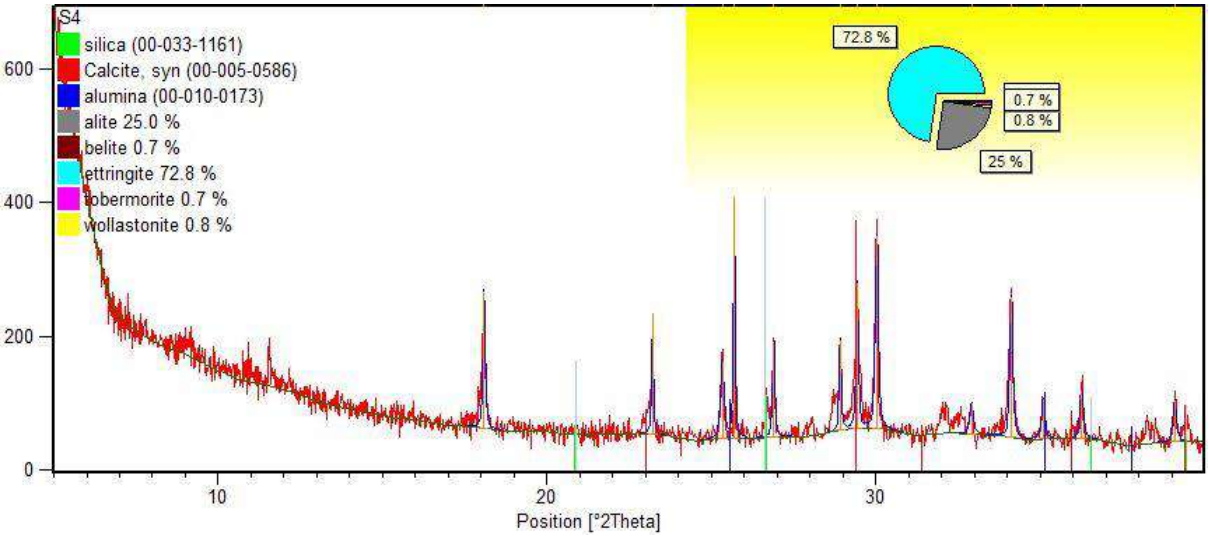

Fig. 7. XRD pattern for S4

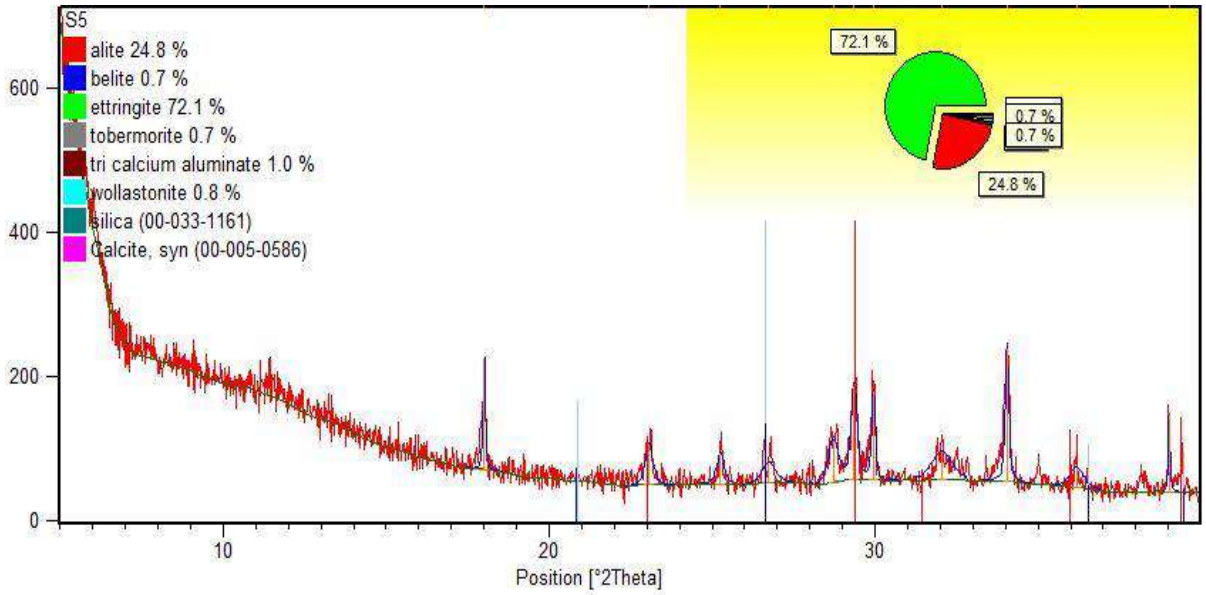

Fig. 8. XRD pattern for S5

It was found that presence of ettringites and tri-calcium aluminates was more pronounced for specimens representing S0 mix (i.e. without Wollastonite micro-fiber). Wollastonite, a fine particulate micro-fiber prominently consisting of calcium and silica when incorporated in concrete contributed to more hydration products which is also visible as peaks of Wollastonite and tobermorite in mixes with Wollastonite micro-fiber. This increase in hydration products is also reflected in better compressive and flexural strength of mix with Wollastonite micro-fiber.

5.2. Pavement Rehabilitation Study

The pavement rehabilitation study was carried out on prototypes of special sized specimens (700×300×200 mm^3) casted with conventional M40 grade pavement quality concrete to represent the concrete slabs being casted in concrete pavements. Special moulds (shown in Figure 9) were prepared to cast the required sized prototypes. In order to create an effect of transverse joint of the pavements in the prototypes, a partition up to mid depth was made in the prototypes. These partitions in the moulds were provided with the groove to be used for placement of dowel bars.

The specimens to be repaired were coated with Multi-Surface Bonding Primer (MPB bonding agent) to achieve proper bonding amongst existing and fresh concrete. A total of 16 specimens were prepared for 8 sets of prototypes. One set of prototype was repaired with conventional M40 mix i.e. RC, one set of prototype were prepared of SCC mix alone and designated as SS0, one set of prototypes each for repairing with SCC mixes S1, S2, S3, S4 and S5 defined as RS1, RS2, RS3, RS4 and RS5 respectively. These specimens were investigated for their flexural behavior at age 7 and 14 days. Figure 9 shows the schematic representation of rehabilitation and testing of pavement prototypes in the study.

The flexural strength parameters recorded for different prototypes till failure at 7 days and 14 days of moist curing are summarized in Table 3. Figure 10 illustrates strength pattern depicted by tested prototypes. It could be interpreted from the pattern that flexural strength improved when the prototypes were repaired with SCC. During the study of prototypes repaired with different concrete mixes it was observed that the flexural strength of prototypes repaired with Wollastonite micro-fibre replacing fine aggregates at levels 10%, 20% and 30% were more in comparison to those of repaired with conventional concrete or with referral self-compacting concrete mix.

Fig. 9. Schematic representation of rehabilitation and testing of pavement prototypes

Table 3. Strength parameters for repaired pavement prototypes

Repaired prototypes	Prototype designation	Load at 7 days (tonnes)		7 days Strength (Mpa)	Load at 14 days (tonnes)		14 days Strength (Mpa)
		1st crack	Failure load		1st crack	Failure load	
Conventional C1	RC	10	13	4.25	14.2	14.4	4.70
SCC Slab S0	SS0	8.1	10	3.27	7.9	10.3	3.36
Repaired with S0	RS0	12	13.5	4.41	14	15.2	4.97
Repaired with S1	RS1	11.4	13.9	4.54	14.6	16.4	5.36
Repaired with S2	RS2	10.8	14.23	4.65	14.1	15.1	4.93
Repaired with S3	RS3	9.8	14.14	4.62	15.4	17.3	5.65
Repaired with S4	RS4	9.3	13.86	4.53	15.2	16.1	5.26
Repaired with S5	RS5	9	12.84	4.19	12.7	14.3	4.67

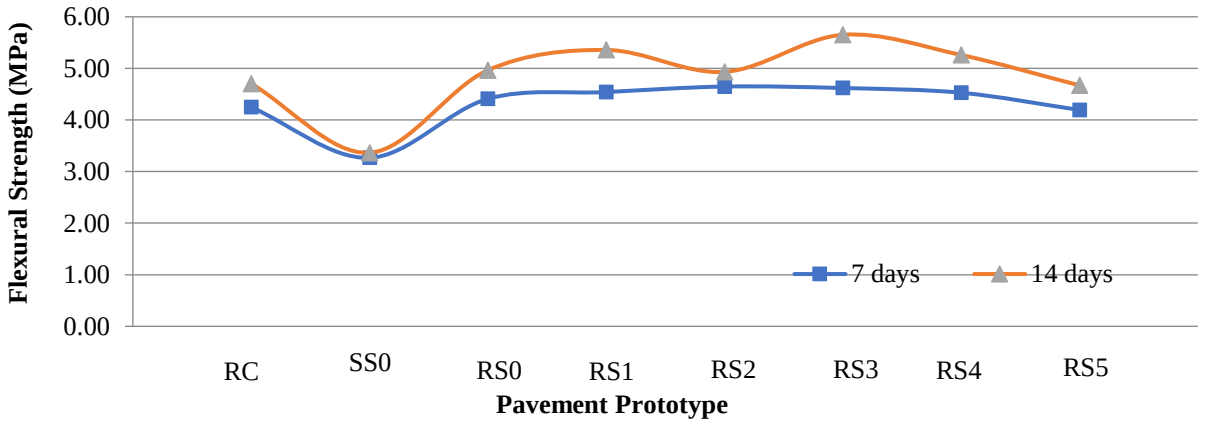

Fig. 10. Flexural strength of repaired prototypes

6. Conclusions

The conclusions made from study are as follows:

a) The mix incorporating Wollastonite micro-fiber depicted improved compressive and flexural strength parameters which is attributed to its fine

particulate behavior that led to densification of matrix visible in XRD results thereby resulting in better strength.

b) The results obtained from investigations of fresh SCC mix showed comparable parameters for flow related properties such as slump flow rate, V-funnel and segregation behavior by probe test thereby indicating the suitability of admixing Wollastonite micro-fiber for preparation of SCC.

c) The flexural strength of prototypes repaired with Wollastonite micro-fibre replacing fine aggregates at levels 10%, 20% and 30% were more in comparison to those of repaired with conventional concrete or with referral self-compacting concrete mix.

d) Thus, it could be concluded that SCC incorporating Wollastonite micro-fibre up to 30% could be suitably used for repair/rehabilitation of concrete pavements.

7. Recommendations

From the present laboratory investigations, it is concluded that inclusion of Wollastonite micro-fibre on a partial basis for replacement of fine aggregates leads to improvement in flexural strength of SCC. Also, up to 30% replacement levels provides added advantage of better flowability and cohesiveness of the mix. Also, better finishing of the specimens was observed for SCC with Wollastonite micro-fibre. Hence, Wollastonite in fibrous form could be considered as a beneficial material for inclusion in SCC to be used for repair and rehabilitation of PQC slabs.

7. Abbreviations

SCC: Self-Compacting Concrete, OPC: Ordinary Portland Cement, PCC: Plain Cement Concrete, SEM: Scanning Electron Microscopy, IRC: Indian Road Congress, IS: Indian Standards, MPB: Multi-Surface Bonding Primer, ITZ: Interfacial Transition Zone, XRD: X-Ray Diffraction.

8. References

Abdel W.M., Abdel L.I., Kohail M. and Almasry A. (2017). "The use of Wollastonite to enhance the mechanical properties of mortar mixes", *Construction and Building Materials*, 152, 304-309, https://doi.org/10.1016/j.conbuildmat.2017.07.005.

Abdolrasool A. and Mousavi S.Y. (2020). "Effects of Wollastonite powder on the fresh properties of self-compacted concrete", *Concrete Research*, 13(1), 53-65, https://doi.org/10.22124/jcr.2020.13137.1362.

Bertil P. (2001). "A comparison between mechanical properties of self-compacting concrete and the corresponding properties of normal concrete", *Cement and Concrete Research*, 31(2), 193-198, https://doi.org/10.1016/S0008-8846(00)00497-X.

Bong, S.H., Nematollahi B., Xia M., Ghaffar S.H., Pan J. and Dai J.G. (2022). "Properties of additively manufactured geopolymer incorporating mineral Wollastonite microfibers", *Construction and Building Materials*, 331, 127282, https://doi.org/10.1016/j.conbuildmat.2022.127282.

Bui V.K., Geiker M.R., and Shah, S.P. (2003). "Rheology fiber-reinforced cementitious material", *International Workshop High Performance Fiber Reinforced Cement Composites (RELIM PRO 30)*, A.E. Naaman and H.W. Reinhardt (eds.), 221-232, https://www.rilem.net/publication/publication/35?id_papier=798.

Cement Concrete and Aggregates Australia. (2009). "Concrete pavement maintenance/ repair", Australia, Report, https://www.ccaa.com.au/common/Uploaded%20files/CCAA/Publications/Reports/PavementRepair.pdf.

Center for Portland Cement Concrete Pavement Technology. (2005). "Self-consolidating concrete-applications for slip-form paving: Phase I (feasibility study)", Iowa State University, U.S., Report, https://intrans.iastate.edu/app/uploads/2018/03/scc_pave.pdf.

Collepardi, M. (2003). "Self-compacting concrete: What is new?", *Seventh CANMET/ACI International Symposium on Superplasticizers and Other Chemical Admixtures in Concrete*, Malhotra, V.M., (ed.), 1-16, Berlin, Germany.

Dhir, R.K., Brito, J.de., Silva, R.V. and Lye, C.Q. (2019). *Sustainable construction materials recycled aggregates*, Woodhead Publishing Series in Civil and Structural Engineering, pp.

495-583, https://doi.org/10.1016/C2015-0-00466-X.

Dinakar P., Babu K.G. and Santhanam M. (2008). "Durability properties of high volume fly ash self-compacting concretes", *Cement and Concrete Composites*, 30(10), 880-886, https://doi.org/10.1016/j.cemconcomp.2008.06.011.

Dutkiewicz, M., Yücel, H.E. and Yıldızhan, F. (2022). "Evaluation of the performance of different types of fibrous concretes produced by using Wollastonite", *Materials*, 15(19), 6904, https://doi.org/10.3390/ma15196904.

Federal Highway Administration. (2019). "Strategies for concrete pavement preservation", Interim Report, FHWA-HIF-18-025, Washington D.C., https://www.fhwa.dot.gov/pavement/pubs/hif18025.pdf.

Gesoglu, M., Guneyisi, E. and Ozbay, E. (2009). "Properties of self-compacting concretes made with binary, ternary, and quaternary cementitious blends of fly ash, blast furnace slag, and silicafume", *Construction and Building Materials*, 23(5), 1847-1854. https://doi.org/10.1016/j.conbuildmat.2008.09.015.

Gholamzadeh Chitgar, A. and Berenjian, J. (2021). "Performance evaluation of RBF networks with various variables to forecast the properties of SCCs", *Civil Engineering Infrastructures Journal*, 54(1), 59-73, https://doi.org/10.22059/ceij.2020.288257.1611.

Gibbons, J. (1999). "Pavement and surface materials", Technical Paper 8, Nonpoint Education for Municipal Officials, University of Connecticut, 1-7.

Gnanaraj S.C., Chokkalingam, R.B. and Thankam, G.L. (2020). "Effects of admixtures on the self-compacting concrete state of the art report", *IOP Conference Series: Materials Science and Engineering*, Vol. 1006, *Sustainable Construction Technologies and Advancements in Civil Engineering (ScTACE-2020)*, 9-10 October, Bhimavaram, India, https://doi.org/10.1088/1757-899X/1006/1/012038.

Gnanaraj, S., Christopher, S. and Chokkalingam, R.B. (2020). "Influence of ultra-fine steatite powder on the fresh and hardened properties of self-compacting concrete", *IOP Conference Series: Materials Science and Engineering*, 998(1), 012040, https://doi.org/10.1155/2021/6627450.

Gouse Mohiuddin, M.D., Malagavelli, V. and Kumar Balguri, P. (2022). "Influence of Wollastonite-GGBS on properties of ternary blended self-compacting concrete", *Materials Today Proceedings*, 62(6), 3027-3032. https://doi.org/10.1016/j.matpr.2022.03.073.

Gru¨newald S. and Walraven, J.C. (2001). "Parameter-study on the influence of steel fibers and coarse aggregate content on the fresh properties of self-consolidating concrete", *Cement and Concrete Research*, 31(12), 1793-1798, https://doi.org/10.1016/S0008-8846(01)00555-5.

Gutha, S. (2010). "Comparative study of properties of different types of binder mixes modified with silica fume", Thesis, Department of Civil Engineering, National Institute of Technology, Rourkela, http://ethesis.nitrkl.ac.in/1858/.

Hemalatha, P. and Ramujee, K. (2021). "Influence of nano material (TiO_2) on self-compacting geo polymer concrete containing flyash, GGBS and Wollastonite", *Materials Today Proceedings*, 43(2), 2438-2442. https://doi.org/10.1016/j.matpr.2021.02.279.

Huang, H., Guo, R., Wang, T., Hu, X., Garcia, S., Fang, M., Luo, Z. and Maroto-Valer, M.M. (2019). "Carbonation curing for Wollastonite-Portland cementitious materials: CO_2 sequestration potential and feasibility assessment", *Journal of Cleaner Production*, 211(20), 830-841, https://doi.org/10.1016/j.jclepro.2018.11.215.

IRC 44. (2017). "Guidelines for cement concrete mix design for pavements", *Indian Road Congress*, New Delhi, India.

Jindal, A., Ransinchung, G.D. R.N. and Kumar, P. (2020). "Behavioral study of self-compacting concrete with Wollastonite microfiber as part replacement of sand for Pavement Quality Concrete (PQC)", *International Journal of Transportation Science and Technology*, 9(2), 170-181, https://doi.org/10.1016/j.ijtst.2019.06.002.

Johnston, C.D. (2001). *Fiber-reinforced cements and concretes*, Gordon and Breach Science Publishers, Amsterdam, https://doi.org/10.1201/9781482298154.

Kalla, P., Rana, A., Chad, Y.B., Misra, A. and Csetenyi, L. (2015). "Durability studies on concrete containing Wollastonite", *Journal of Cleaner Production*, 87(15), 726-734. https://doi.org/10.1016/j.jclepro.2014.10.038.

Khayat, K.H. and Roussel, Y. (1999). "Testing and performance of fiber-reinforced, self-consolidating concrete", In: Skarendahl, A. and Petersson O. (eds.), *Proceedings of the First International RILEM Symposium on Self-Compacting Concrete*, Stockholm, Sweden, 13-14 September, 509-521, https://www.rilem.net/publication/publication/12?id_papier=1316.

Kuldasheva, A., Saidmuratov, B. and Kuldashev, H. (2020). "The use of Wollastonite fiber to enhance the mechanical properties of cement compositions", *International Journal of Progressive Science and Technology*, 22, 37-45,

http://dx.doi.org/10.52155/ijpsat.v22.2.2175.

Kumar, P., Sudalaimani, K. and Shanmugasundaram, M. (2017). "An investigation on self-compacting concrete using ultrafine natural steatite powder as replacement to cement", *Advances in Materials Science and Engineering*, Hindawi, Vol. 2017, Article ID 8949041, https://doi.org/10.1155/2017/8949041.

Kumar, P. and Kaushik, S.K. (2003). "Some trends in the use of concrete: Indian scenario", *The Indian Concrete Journal*, 77(12), 1503-1508.

Mailvaganam, N.P. (2001). "Concrete repair and rehabilitation: issues and trends", *The Indian Concrete Journal*, 75(12), 759-764.

Nair, N.A. and Sairam, V. (2021). "Research initiatives on the influence of Wollastonite in cement-based construction material, A review", *Journal of Cleaner Production*, 283, 124665, https://doi.org/10.1016/j.jclepro.2020.124665.

National Concrete Pavement Technology Center. (2014). *Concrete pavement preservation guide*, Second Edition, Iowa State University Research Park, U.S., https://intrans.iastate.edu/app/uploads/2022/08/concrete_pvmt_preservation_guide_3rd_edition_web.pdf.

Okamura, H. and Ouchi, M. (1998). "Self-compacting high performance concrete", *Progress in Structural Engineering and Materials*, 1(4), 378-383, https://doi.org/10.1002/pse.2260010406.

Öz, H.Ö. and Güne, S.M. (2021). "The effects of synthetic Wollastonite developed with calcite and quartz on high performance mortars", *Structural Concrete*, 22, E257-E272, https://doi.org/10.1002/suco.201900520.

Ransinchung, R.N. G.D., Kumar, B. and Kumar, V. (2009). "Assessment of water absorption and chloride ion penetration of pavement quality concrete admixed with Wollastonite and microsilica", *Construction and Building Materials*, Elsevier, 23(2), 1168-1177, https://doi.org/10.1016/j.conbuildmat.2008.06.011.

Rao, S., Darter, M., Tompkins, D., Vancura, M., Khazanovich, L., Signore, J., Coleri, E., Wu, R., Harvey, J. and Vandenbossche, J., (2013). "Composite pavement systems: Volume B, PCC/PCC composite pavements", SHRP2 Final Report, Transportation Research Board, Washington D.C., https://onlinepubs.trb.org/onlinepubs/shrp2/shrp2_pb_r21_2014-05.pdf.

Santos, S., Da Silva, P.R. and Brito, J.de. (2019). "Self-compacting concrete with recycled aggregates, A literature review", *Journal of Building Engineering*, 22, 349-371, https://doi.org/10.1016/j.jobe.2019.01.001.

Sharifi, N.P., Chen, S., You, Z., Van Dam, T. and Gilbertson, C. (2019). "A review on the best practices in concrete pavement design and materials in wet-freeze climates similar to Michigan", *Journal of Traffic and Transportation Engineering* (English Edition), 6(3), 245-255, https://doi.org/10.1016/j.jtte.2018.12.003.

Sharma, S.K. (2019). "Properties of SCC containing pozzolans, Wollastonite micro fiber, and recycled aggregates", *Heliyon*, 5(8), e02081, https://doi.org/10.1016/j.heliyon.2019.e02081.

Sharma, S.K., Ransinchung, G.D. and Kumar, P. (2018). "Investigating the use of Wollastonite micro fiber in yielding SCC", *Advances in Concrete Construction*, 6(2), 123-143, https://doi.org/10.12989/acc.2018.6.2.123.

Tanaka, K., Sato, K., Watanabe, S., Arima, I. and Suenaga, K. (1993). "Development and utilization of high performance concrete for the construction of the Akashi Kaikyo Bridge", In SP-140: *High Performance Concrete in Severe Environments*, Zia, P. (ed.), Detroit, MI: American Concrete Institute, 147-161, https://doi.org/10.14359/3905.

The European Project Group. (2005). "The European guidelines for self-compacting concrete", SCC European Project Group, https://www.theconcreteinitiative.eu/images/ECP_Documents/EuropeanGuidelinesSelfCompactingConcrete.pdf.

Thomas, J.P. (1998). "Pavements: Past, present and future", *Concrete International*, 20(5), 47-52, http://worldcat.org/oclc/4163061.

Uysal, M. and Yilmaz, K. (2011). "Effect of mineral admixtures on properties of self-compacting concrete", *Cement and Concrete Composites*, 33(7), 771-776, https://doi.org/10.1016/j.cemconcomp.2011.04.005.

Vishnu, N., Kolli, R. and Ravella, D.P. (2021). "Studies on self-compacting geopolymer concrete containing flyash, GGBS, Wollastonite and graphene oxide", *Materials Today Proceedings*, 43(2), 2422-2427, https://doi.org/10.1016/j.matpr.2021.02.142.

Zareei, S.A., Ameri, F., Shoaei, P. and Bahrami, N. (2019). "Recycled ceramic waste high strength concrete containing Wollastonite particles and micro-silica: A comprehensive experimental study", *Construction and Building Materials*, 201, 11-32, https://doi.org/10.1016/j.conbuildmat.2018.12.161.

Civil Engineering Infrastructures Journal 2023, 56(2): 235-255
DOI: 10.22059/CEIJ.2023.342419.1837

RESEARCH PAPER

A Simplified Continuum Damage Model for Nonlinear Seismic Analysis of Concrete Arch Dams Using Different Damping Algorithms

Hashempour, S.A.R.[1], Akbari, R.[1*] and Lotfi, V.[2]

[1] M.Sc., Department of Civil and Environmental Engineering, Amirkabir University of Technology (Tehran Polytechnic), Tehran, Iran.
[2] Professor, Department of Civil and Environmental Engineering, Amirkabir University of Technology (Tehran Polytechnic), Tehran, Iran.

Received: 02 May 2022; Revised: 14 Sep 2022; Accepted: 22 Oct. 2022

ABSTRACT: In this research, a nonlinear model is presented to explore the seismic response of concrete arch dams. This model is much more simplified and efficient in comparison with plastic-damage models. It can represent softening, hardening and stiffness degradation of concrete due to load reversal. Additionally, it is able to predict the final and residual strength of the structure in softening with good accuracy. Employing different scale factors to monitor the failure of the dam, this model is used to analyze the nonlinear response of Morrow Point arch dam. The dam-reservoir interaction is considered with modified Westergaard's approach, and the dam body is modeled with second order 20-node isoparametric elements. Moreover, two different damping algorithms are included to evaluate their impact on nonlinear analysis. It is concluded that the employed model can predict realistic crack patterns through the dam body, and it can be a good replacement for other time consuming and complicated models. In addition, it is shown that the damping algorithm plays a significant role in the nonlinear dynamic analysis of concrete arch dams.

Keywords: Concrete Arch Dams, Damage Mechanics, Different Damping Algorithms, Finite Element, Nonlinear Model.

1. Introduction

Most of the concrete dams have been built based on simple and inadequate seismic design assumptions in the past. Therefore, the seismic safety of these essential infrastructures needed for water supply and flood control is upon question. Moreover, the endangered population in downstream of dams is expanding continuously. Therefore, the failure of dams would lead to drastic socioeconomic damages. The increasing concern of the seismic safety of such critical structures has created a high demand for nonlinear models capable of reassessing existing dams.

In this regard, there are two primary nonlinear models, continuum and discrete (Jenabidehkordi, 2019; Mauludin and Oucif, 2020). In discrete models, the split between element edges is adopted, which has two major disadvantages (Cabral et al., 2019; Nguyen et al., 2019; Sinaie et al., 2018). First, connectivity should change as

* Corresponding author E-mail: r.akbari96@aut.ac.ir

crack propagates, which conflicts with the intrinsic trend of Finite Element Analysis (FEA). Second, the crack line is predetermined, and it has a fixed direction during the analysis (Qin et al., 2021; Rots and Blaauwendraad, 1989). Continuum models overcome these two significant shortcomings. They are classified into smeared crack and damage models (Ghrib and Tinawi, 1995; Park et al., 2021; Voyiadjis et al., 2021). Although researchers have employed both nonlinear approaches for the dynamic analysis of concrete arch dams (Alegre et al., 2022; Alegre and Oliveira, 2020; Ardakanian et al., 2006; Mirzabozorg et al., 2007, 2004; Mirzabozorg and Ghaemian, 2005; Xu et al., 2017), the damage model has become more prevalent recently. The basis of the continuum damage model is using an internal variable called the damage variable to showcase the average material degradation on macro-mechanics scale (Farahani, 2005; Voyiadjis and Kattan, 2017). It should be mentioned that often plasticity theories are coupled with damage mechanics in order to consider irreversible strain that evolves during loading. In this regard, there have been researches incorporating plastic models for nonlinear analysis (Daneshyar and Ghaemian, 2019; Komasi and Beiranvand, 2021; Omidi and Lotfi, 2017a; Park et al., 2021).

There have been some researches for nonlinear analysis of concrete dams using damage-based models. Ghrib and Tinawi (1995) proposed a damage model functioning on the basic properties of fracture energy and concrete strength for exploring the nonlinear response of concrete gravity dams. Cervera et al. (1195) utilized an isotropic damage model which could consider tension and compression damage, and stiffness. A rate-dependent isotropic damage model capable of considering stiffness degradation and stiffness recovery and strain-rate sensitivity was presented by Cervera et al. (1996). Valliappan et al. (1996) investigated the seismic response of concrete gravity dams using the concept of Continuum Damage Mechanics (CDM). The damage criterion utilized in their research was a second order tensor model based on elastic-brittle characterization. The results indicated that there is a considerable difference between the seismic response of a damaged and undamaged concrete. Lee and Fenves (1998) proposed a new nonlinear model based on plastic-damage concept and investigated the seismic behavior of Koyna gravity dam. This model could consider the effect of strain softening, elastic stiffness degradation, large cracks formation and the stiffness recovery after closure of cracks. Valliappan et al. (1999) developed a finite element program based on HHT and used the nonlinear concept of CDM to present the seismic damage response of arch dams. The methodology employed was proved to be computationally efficient and consistent in its treatment of both growth and propagation of damage. In another research, Omidi and Lotfi (2017a) used a plastic-damage model in combination with the discrete crack (DC) model for 3-D cases to study the seismic damage response of concrete arch dams. The core of their material constitutive law relied on the presented model by Lee and Fenves (1998). It was proved that using the combination of DC and PD models yields a more consistent and reliable response compared to employing DC or PD approaches alone. Daneshyar and Ghaemian (2019) used a rate-dependent anisotropic PD model for dynamic analysis of concrete arch dams. In addition to material inelasticity, the nonlinearity of joints was also considered.

In a previous study by Akbari and Lotfi (2022), a simplified isotropic damage model was utilized for seismic assessment of a concrete gravity dam. In addition to its simple formulation and easy programming, it could successfully determine acceptable crack patterns in comparison to previous studies. This model was implemented in studying the nonlinear behavior of the Koyna dam utilizing three different damping algorithms. The results indicated

that the chosen damping could significantly influence the nonlinear results. Herein, the model is utilized to analyze the nonlinear behavior of concrete arch dams. This model has two internal damage variables for tensile and compressive state, separately. It also includes stiffness recovery due to load reversal as moving from tension to compression regime. The central part of the model employs Lubliner et al. (1989) stress functions to define tensile and compressive uniaxial behavior. The strain equivalence assumption is the basis of the model. The criteria for damage evolution are relatively simple and efficient which is based on two threshold effective principal stresses. This model is validated by uniaxial tension, compression, and full cyclic tension-compression tests in the initial stages. Thereafter, nonlinear response of the Koyna gravity dam is evaluated in 3-D modeling, and finally the developed program is employed for the seismic damage evaluation of Morrow Point arch dam using two different damping algorithms.

The remaining part of this paper is structured as follows. In Section 2, the fundamental equations of damage constitutive law are discussed. In Section 3, the dynamic equations of model are presented. In Section 4, three elementary clarification tests and applications of the model in 3-D analysis of Koyna dam are shown to verify the implementation of the presented model accuracy. Finally, in Section 5, by utilizing the damage model, the seismic damage response of a typical arch dam by means of three different damping algorithms is discussed.

2. Damage Constitutive Law

The stress $\boldsymbol{\sigma}$, and the effective stress $\bar{\boldsymbol{\sigma}}$ may be defined as:

$$\boldsymbol{\sigma} = (1 - D)\bar{\boldsymbol{\sigma}} \quad (1)$$

$$\bar{\boldsymbol{\sigma}} = \boldsymbol{E_0}\boldsymbol{\varepsilon} \quad (2)$$

where D, $\boldsymbol{E_0}$ and $\boldsymbol{\varepsilon}$: are damage variable, undamaged elastic rigidity matrix and strain matrix, respectively. In the present model to detect the damage in tension and compression two internal variables D^+ and D^- are considered, respectively, as the behavior of concrete in tension and compression is quite different (Cervera et al., 2017). Therefore, the Eq. (1) is changed into the following equation (Cervera and Tesei, 2017):

$$\boldsymbol{\sigma} = (1 - D^+)\bar{\boldsymbol{\sigma}}^+ + (1 - D^-)\bar{\boldsymbol{\sigma}}^- \quad (3)$$

In the presented equations the tension and compression are illustrated with (+) and (-), respectively. Damage variable D can be in the range of 0 to 1 (i.e., 0 for no damage and 1 for full damage). The D^+ and D^- are defined as follows for the present isotropic damage model:

$$D^+ = 1 - \frac{f^+_{max}}{\bar{f}^+_{max}} \quad (4)$$

$$D^- = 1 - \frac{f^-_{max}}{\bar{f}^-_{max}} \quad (5)$$

where $\bar{f}^+_{max}$and $\bar{f}^-_{max}$: are maximum tensile and compressive principal effective stresses reached up to that point in time, respectively. Moreover, f^+_{max} and f^-_{max}: are corresponding nominal uniaxial tensile and compressive stresses.

The uniaxial stress functions of Lubliner et al. (1989) are the basis of the model, which are demonstrated as follows:

$$f^+ = f_0^+\left[(1 + A^+)e^{-B^+(\varepsilon^+ - \varepsilon_0^+)} - A^+ e^{-2B^+(\varepsilon^+ - \varepsilon_0^+)}\right] \quad (6)$$

$$f^- = f_0^-\left[(1 + A^-)e^{-B^-(\varepsilon^- - \varepsilon_0^-)} - A^- e^{-2B^-(\varepsilon^- - \varepsilon_0^-)}\right] \quad (7)$$

The uni-axial stress curves of this model are illustrated in Figure 1. In the above equation, $f_0^{\pm}$: is the elastic strength of concrete, $\varepsilon^{\pm}$: is the strain and $\varepsilon_0^{\pm}$: is the maximum linear elastic strain.

The A^+ parameter can be calculated by taking the derivative of Eq. (6) at the onset of nonlinearity (i.e., $\varepsilon^+ = \varepsilon_0^+$), and setting

that equal to zero (i.e., $\frac{df^+}{d\varepsilon^+}\Big|_{\varepsilon^+=\varepsilon_0^+} = 0$) which results in:

$$A^+ = 1 \tag{8}$$

The A^- parameter can be calculated by taking the derivative of Eq. (7) at the strain corresponding to maximum compressive stress of concrete and setting that equal to zero $\left(\frac{df^-}{d\varepsilon^-}\Big|_{\varepsilon^-=\varepsilon_{max}^-} = 0\right)$. Thereafter, set the maximum compressive stress equal to f_1^-. This would lead to the following relation by defining $\beta^- = \frac{f_1^-}{f_0^-}$:

$$A^- = (2\beta^- - 1) + 2\sqrt{\beta^-(\beta^- - 1)} \tag{9}$$

In order to calculate the parameter $B^\pm$, there is a need to use specific fracture energy per characteristic length ($g = \int_0^\infty \sigma d\varepsilon^*; \varepsilon^* = \varepsilon - \varepsilon_0$), knowing the fact that this energy is equal to the area of stress-strain curve. The $B^\pm$ parameter are defined as follow:

$$B^\pm = \frac{2 + A^\pm}{\varepsilon_0^\pm \left(\frac{2EG_f^\pm}{l^{*\pm}\left(f_0^\pm\right)^2} - 1\right)} \tag{10}$$

where $G_f^\pm$ and $l^{*\pm}$: are the fracture energy and the characteristic length, respectively. $l^{*\pm}$ is derived by calculating the cube root of the tributary volume at each integration point of finite element (Oliver, 1989).

The process of calculating stress based on the CDM and updating the damage variable is depicted in Figure 2.

3. Nonlinear Dynamic Formulation

In order to solve the dynamic equilibrium equation in the time domain, a step-by-step procedure is employed (Eq. (11)).

$$\boldsymbol{M\ddot{U}} + \boldsymbol{P}\left(\boldsymbol{U}, \dot{\boldsymbol{U}}\right) = \boldsymbol{R}^{st} - \boldsymbol{MJa}_g \tag{11}$$

where $\boldsymbol{M}$: is the mass matrix, including the mass of dam body and added mass; $\boldsymbol{U}$, $\dot{\boldsymbol{U}}$ and $\ddot{\boldsymbol{U}}$: are displacement, velocity and acceleration vectors, respectively; $\boldsymbol{P}$: is the restoring force vector; $\boldsymbol{R}^{st}$: is the applied static loads, including hydrostatic pressures and gravity effects; $\boldsymbol{J}$: is the influence matrix for $\boldsymbol{a}_g$. The restoring force vector containing internal and damping forces, is defined as:

$$\boldsymbol{P}^e = \boldsymbol{F}^e + \boldsymbol{C}^e\dot{\boldsymbol{U}}^e \tag{12}$$

where $\boldsymbol{F}^e$: is the internal force vector, and in an element domain Ω_e, can be calculated as follows:

$$\boldsymbol{F}^e = \int_{\Omega_e} \boldsymbol{B}^T\boldsymbol{\sigma}d\Omega \tag{13}$$

where $\boldsymbol{B}$: is the strain-displacement transformation matrix.

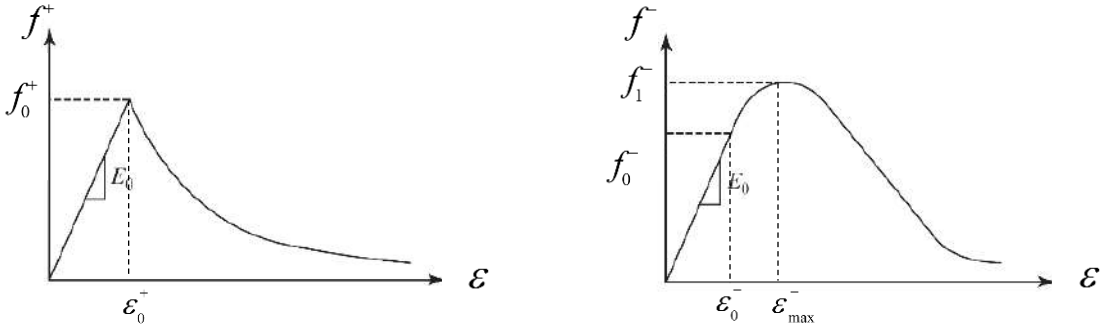

(a) Tension **(b) Compression**

Fig. 1. The uniaxial behavior of Lubliner model (Lubliner et al., 1989)

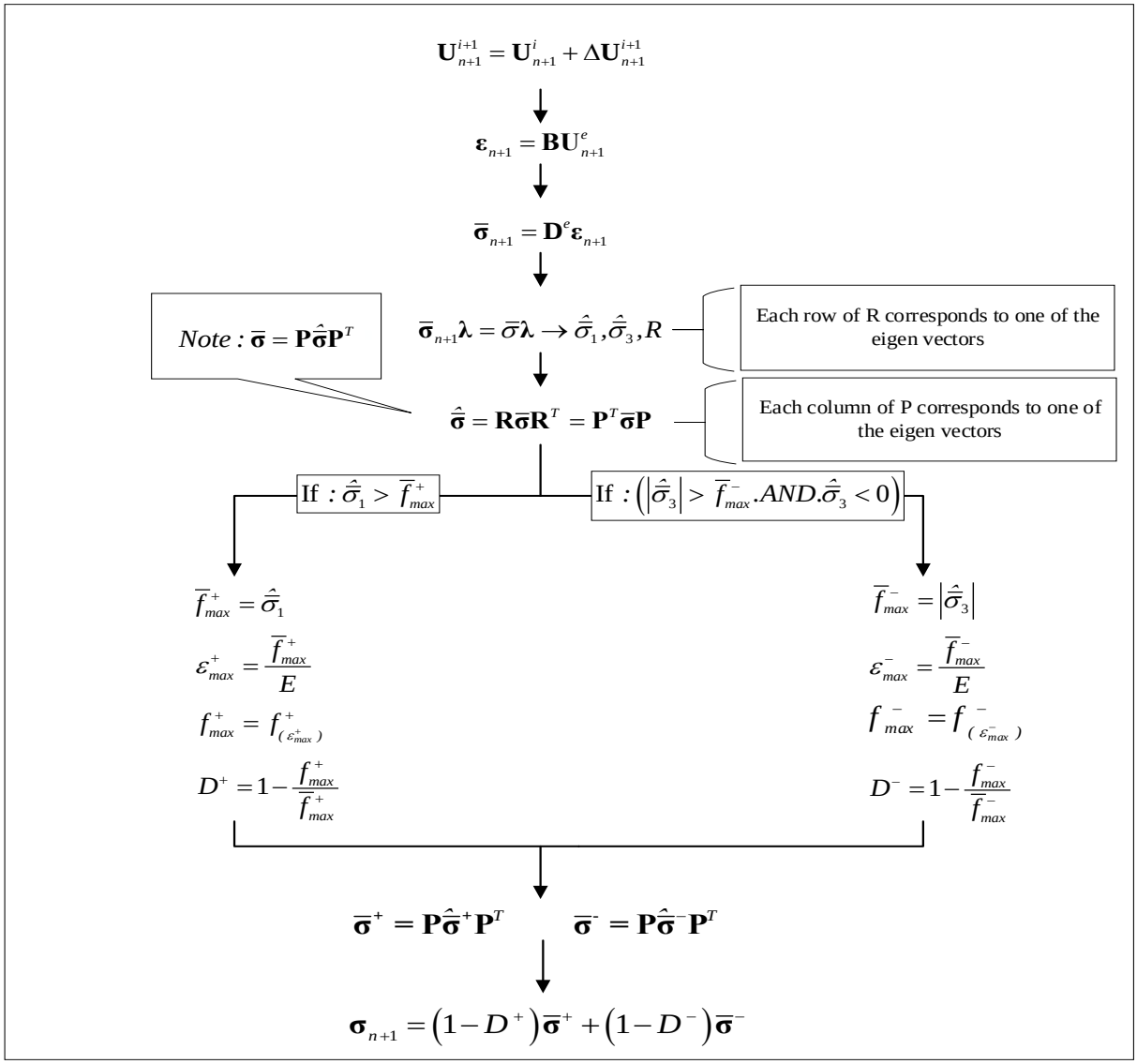

Fig. 2. The stress calculation layout with the presented model

Furthermore, $\boldsymbol{C}^{e}$: the Rayleigh damping matrix consists of damping associated with stiffness ($\boldsymbol{C}_K^e = \alpha_K \boldsymbol{K}^e$) and mass ($\boldsymbol{C}_M^e = \alpha_M \boldsymbol{M}^e$) is defined as follows (Rayleigh and Lindsay, 1945):

$$\boldsymbol{C}^{e} = \boldsymbol{C}_K^e + \boldsymbol{C}_M^e \tag{14}$$

3.1. Damping Algorithm

In this research, two different damping algorithms are utilized in dynamic equations, which are categorized based on the update time of the damping matrix in the procedure of dynamic equations and identified by JDAMP parameter. In the dynamic analysis, $\boldsymbol{C}^{e}$ is defined as:

$$\boldsymbol{C^e} = \alpha_k \int_V \boldsymbol{B}^T (1 - D) \boldsymbol{E}_0 \boldsymbol{B} dV \tag{15}$$

where total damage (D), following the definition proposed by Lee and Fenves (1998), is defined as:

$$D = 1 - (1 - sD^{+})(1 - D^{-}) \tag{16}$$

The s parameter varies from 0 to 1 demonstrates stiffness recovery during the unloading process from tensile to compressive state, and can be obtained as (Lee and Fenves, 1998; Omidi and Lotfi, 2017a):

$$s = \frac{\sum_{i=1}^{3} \langle \hat{\bar{\sigma}}_i \rangle}{\sum_{i=1}^{3} |\hat{\bar{\sigma}}_i|} \tag{17}$$

The notation $\langle . \rangle$: is the Macaulay bracket, which yields the enclosed entity and zero for positive and negative values, respectively. The $\widehat{\boldsymbol{\sigma}}$: is effective principal stress matrix.

Moreover, $\boldsymbol{E}_0$: is the elastic rigidity matrix. In the first case (JDAMP = 0), the damping matrix is fixed through the whole analysis and equals to the undamaged state damping. That means:

$$\boldsymbol{C}_{n+\varphi}^{i} = \boldsymbol{C}_0 \tag{18}$$

in which $\boldsymbol{C}_0$: is explained as:

$$\begin{aligned} \boldsymbol{C}^e &= \alpha_k \int_V \boldsymbol{B}^T (1 \\ &- D)\boldsymbol{E}_0 \boldsymbol{B} dV \xrightarrow{D=0 \text{ undamaged state}} \boldsymbol{C}_0^e \\ &= \alpha_k \int_V \boldsymbol{B}^T \boldsymbol{E}_0 \boldsymbol{B} dV \end{aligned} \tag{19}$$

Therefore, the dynamic equilibrium relation can be transformed to the following equation based on the HHT method as Eq. (20). The HHT time integration method is summarized in Appendix A, which for more details can be referred to Akbari and Lotfi (2022).

$$\begin{aligned} [a_0 \boldsymbol{M} + (1-\alpha) a_1 \boldsymbol{C}_0 + (1-\alpha)\boldsymbol{K}_0] \Delta \boldsymbol{U}_{n+1}^{i+1} \\ = \boldsymbol{R}_{n+\varphi} - \boldsymbol{F}_{n+\varphi}^{i} - \boldsymbol{C}_0 \dot{\boldsymbol{U}}_{n+\varphi}^{i} \\ - \boldsymbol{M} \ddot{\boldsymbol{U}}_{n+1}^{i} \end{aligned} \tag{20}$$

In the second case (JDAMP = 1), the damping matrix would be updated just at the first iteration of each step in the analysis.

$$\boldsymbol{C}_{n+\varphi}^{i} = \boldsymbol{C}_{n+1}^{0} = \boldsymbol{C}_n \tag{21}$$

Thus, the dynamic equilibrium relation can be written as Eq. (22).

$$\begin{aligned} [a_0 \boldsymbol{M} + (1-\alpha) a_1 \boldsymbol{C}_0 + (1-\alpha)\boldsymbol{K}_0] \Delta \boldsymbol{U}_{n+1}^{i+1} \\ = \boldsymbol{R}_{n+\varphi} - \boldsymbol{F}_{n+\varphi}^{i} - C_n \dot{\boldsymbol{U}}_{n+\varphi}^{i} \\ - \boldsymbol{M} \ddot{\boldsymbol{U}}_{n+1}^{i} \end{aligned} \tag{22}$$

4. Verification of the Presented Model

To examine the accuracy of proposed model and the developed finite element program, two kinds of tests are conducted. The first one is the primary uniaxial test to investigate the capability of program for considering softening and hardening and stiffness degradation. The second test is implementation of the 3-D program for analyzing the nonlinear behavior of Koyna gravity dam to investigate the crack patterns.

4.1. Primary Test of the Model

To verify the primary behavior and accuracy of the presented nonlinear model, an eight-node three dimensional isoparametric element whose 4 nodes are constrained in the perpendicular to its plane direction and the other 4 nodes are subjected to several cyclic loadings (i.e., specified controlled displacement). Moreover, two of the adjacent side-planes are also restrained in the perpendicular directions to prevent rigid body motions in those directions. The model mechanical properties are depicted in Table 1.

The results of three different uniaxial tests are demonstrated in Figure 3. It is vivid that the model can capture softening and hardening-softening of concrete in tension and compression, respectively. Moreover, it also takes into the account the stiffness degradation regarding unloading. Furthermore, in the tension-compression test, the capability of stiffness recovery is proved when the stress state changes from tension to compression. As a result, the proposed model can determine the behavior of concrete relatively well, considering the simplicity of the model.

Table 1. Mechanical properties of the model

E(GPa)	ρ ($^{kg}/_{m^3}$)	υ	f_0^+(MPa)	f_0^-(MPa)	f_1^-(MPa)	G_f^+($^{MN}/_{m}$)	G_f^-($^{MN}/_{m}$)
30	2.580D+3	0.18	1.8	11.70	18	0.18D-3	72D-3

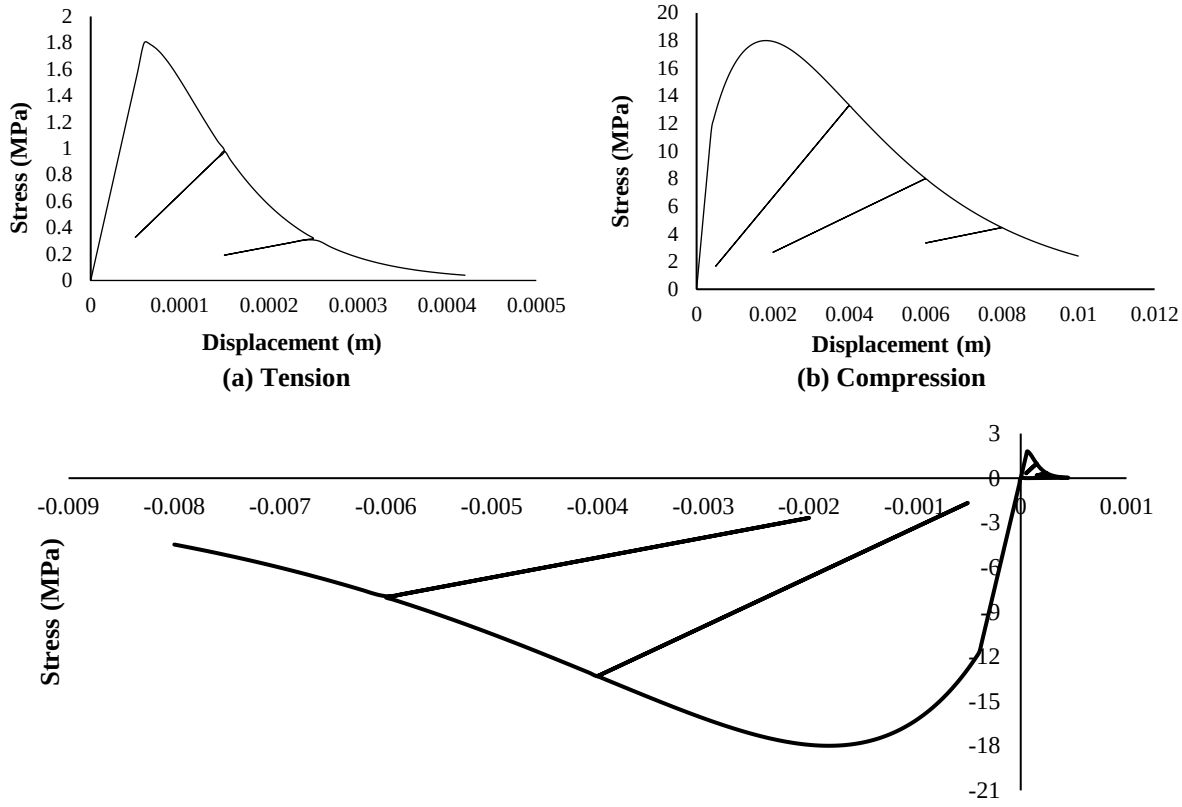

Fig. 3. Uniaxial tests on an 8-noded element

4.2. Application of the Model for Koyna Dam

Herein, the seismic response of Koyna dam with 3-dimensional 8-node elements is compared with results of the shake table test conducted in the Berkeley university laboratory (Hall, 1988). The concrete properties are: $E_0 = 30GPa$, $\rho = 2630\frac{kg}{m^3}$, $\nu = 0.2$, $f_0^+ = 2.9MPa$, $f_1^- = 24.10MPa$, $G_f^+ = 0.0002\frac{MN}{m}$ and $G_f^- = 0.02\frac{MN}{m}$. Moreover, the rigid foundation assumption and modified Westergaard method for dam-water interaction are considered (Omidi and Lotfi, 2017b). As it can be observed, the location of crack pattern in numerical results agrees with the experiment data and the accuracy of the results obtained by the personal program is quite acceptable.

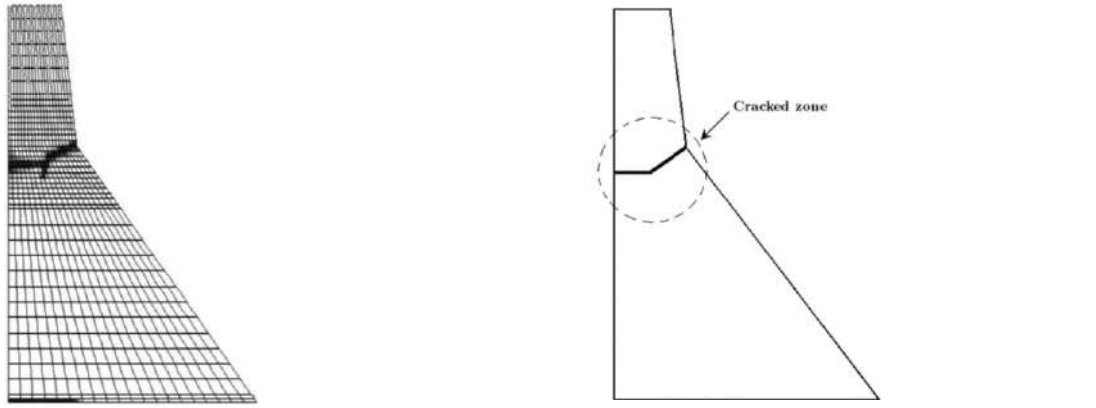

(a) Results of the presented model

(b) Experimental crack pattern at the scale of 1:150 simulation (Hall, 1988)

Fig. 4. Crack pattern of Koyna dam

5. Seismic Damage Analysis of Morrow Point Arch Dam Utilizing the Damage Model

Herein, the stability and the nonlinear behavior of Morrow Point arch dam are studied by applying the damage model previously discussed. Morrow Point is a thin-arch, double-curvature arch dam located approximately 35 km east of Montrose on the Gunnison River in southwestern Colorado. The dam structure is 143 m high with a crest length of 221 m. The thickness of the crown cantilever ranges from 3.7 m at the top to 16 m at the bottom (Wikipedia Contributors, 2022).

5.1. Numerical Simulations, Mechanical Properties and Loading

The dam is discretized by 3870 second-order isoparametric finite elements as shown in Figure 5. The hydrodynamic pressures are considered based on modified Westergaard's approach and the foundation is assumed to be rigid. These assumptions are selected to minimize computational efforts. Of course, it is vivid that the rigidity of foundation has a drastic impact on the boundary stresses in a linear analysis leading to significant tensile stresses near the base. However, these high stresses are expected to be released in the nonlinear analysis. Moreover, this release of stresses can examine the nonlinear model accuracy. The mechanical properties of concrete are depicted in Table 2.

In all analyses, time step Δt = 0.005 sec is utilized, and the stiffness coefficient of Rayleigh damping (α_k) is considered as 0.006297. The static load comprises Gravity and Hydrostatic pressures (maximum water depth = 141.73 m), and the dynamic loading is the seismic excitations consisting of the stream and the vertical components of the Taft earthquake, as demonstrated in Figure 6. The cross-canyon excitation is omitted for a complete symmetric loading condition. This can be helpful as an extra tool for the verification of the analysis results.

5.2. Analysis Results

Three analysis types are considered: a linear analysis (LN), a nonlinear analysis with damage model using constant damping option (JDAMP = 0), and a nonlinear analysis with damage model using variable damping option (JDAMP = 1). It should be mentioned that time is divided into negative and positive part. Although negative time is not real, it is just considered for static analysis, including gravity and hydrostatic loads. In this part of analysis, the gravity loads are implemented in 20 increments and the hydrostatic loads in the next 20 increments at negative range of time. The dynamic analysis started with initial conditions induced by static analysis at time zero.

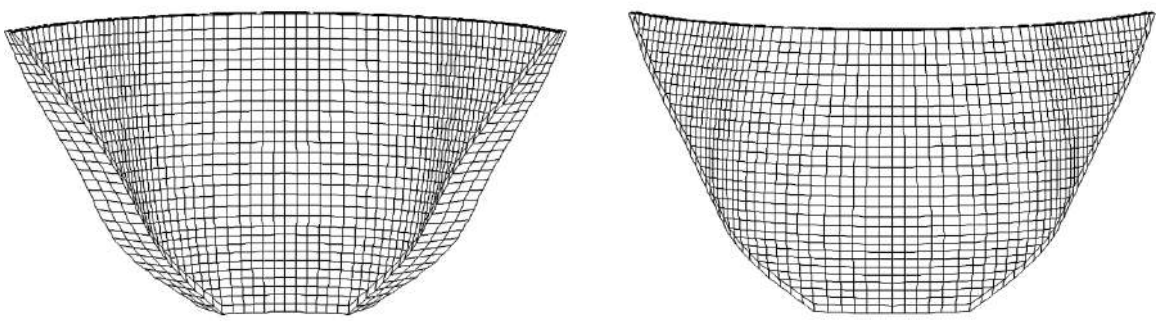

Fig. 5. Finite element mesh of Morrow Point arch dam

Table 2. Mechanical behavior of concrete

E (GPa)	ρ ($^{kg}/_{m^3}$)	υ	f_0^+(MPa)	f_0^-(MPa)	f_1^-(MPa)	$G_f^+(^{MN}/_m)$	$G_f^-(^{MN}/_m)$
27.5	2.528D+3	0.2	3.0	19.50	30.0	0.4D-3	55.0D-3

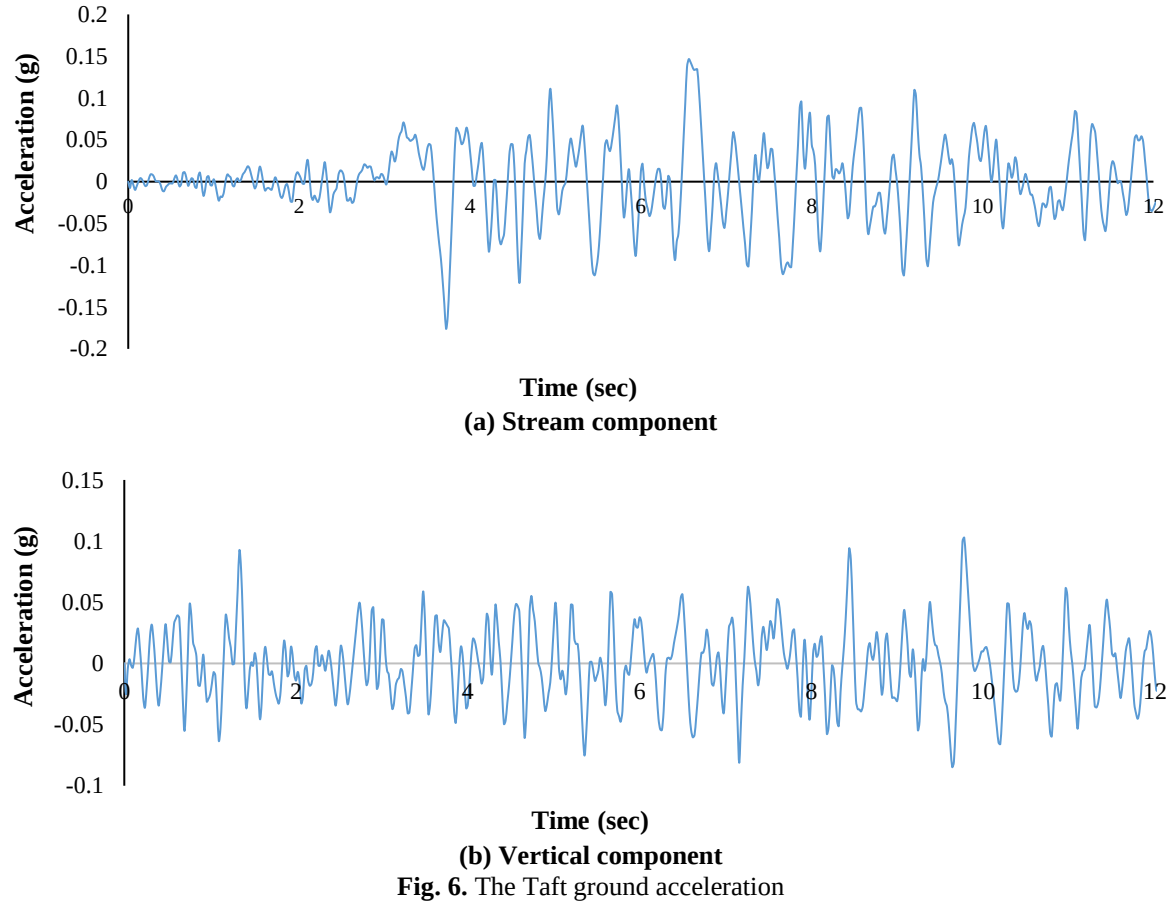

Fig. 6. The Taft ground acceleration

5.2.1. Linear Results

In this section, linear analysis results are presented. Two primary analyses are conducted for this case to examine the effect of the reservoir and various Scale Factors (SC) on the analysis results.

5.2.1.1. The Influence of Hydrodynamic Pressures

For the aim of saving computational time in this study, the exact modeling of the dam reservoir is ignored. However, an approximate method (i.e., Westergaard's approach) is used to include the effect of the hydrodynamic pressures. The time history of stream-component of dam crest displacement is depicted in Figure 7. As observed, by considering the effect of the hydrodynamic pressures, the dam crest displacement is raised significantly as expected.

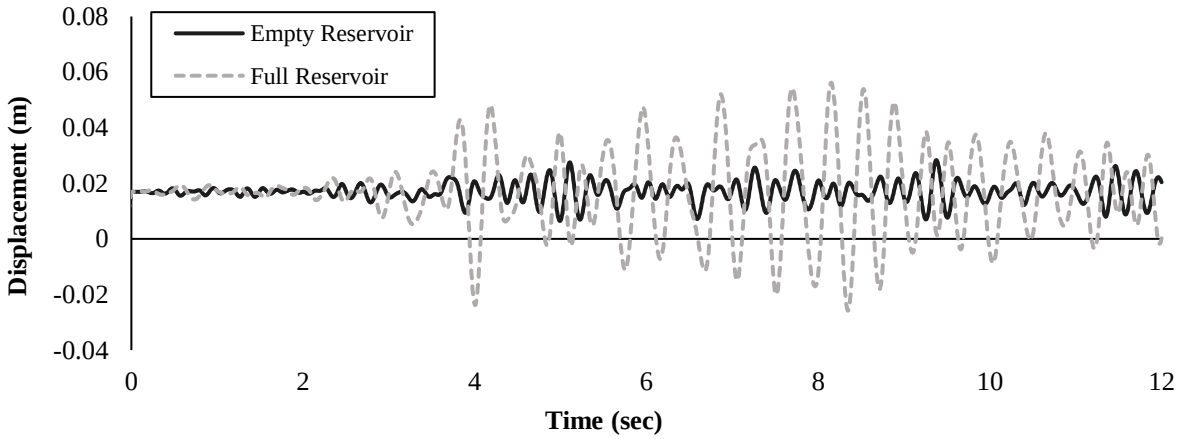

Fig. 7. The dam mid-crest displacement in the stream direction

5.2.1.2. The Effect of Different Scale Factors

To investigate the linear dynamic response of the dam under severe seismic loads, the Taft acceleration components are multiplied by a scale factor of 1.2, 1.3, and 1.4. These magnified records are applied to the dam in turn. As it can be observed, increasing the acceleration components leads to the increase in the displacement of the dam mid-crest as shown in Figure 8. Moreover, the maximum tensile principal stresses at abutments and the dam's mid-crest region are increased from 11.70 to 12.27 MPa (Figure 9). These stresses are much higher than concrete tensile strength. Therefore, these parts of the dam are presumably prone to cracks during severe earthquakes. Of course, one would actually capture much lower tensile stresses at these locations due to contraction joint or peripheral joint modeling that is neglected herein for simplification purposes. The maximum compressive principal stresses are increased from -10.61 to -11.11. Although the compressive stresses are increased, they do not surpass the concrete's compressive strength and are not a matter of concern.

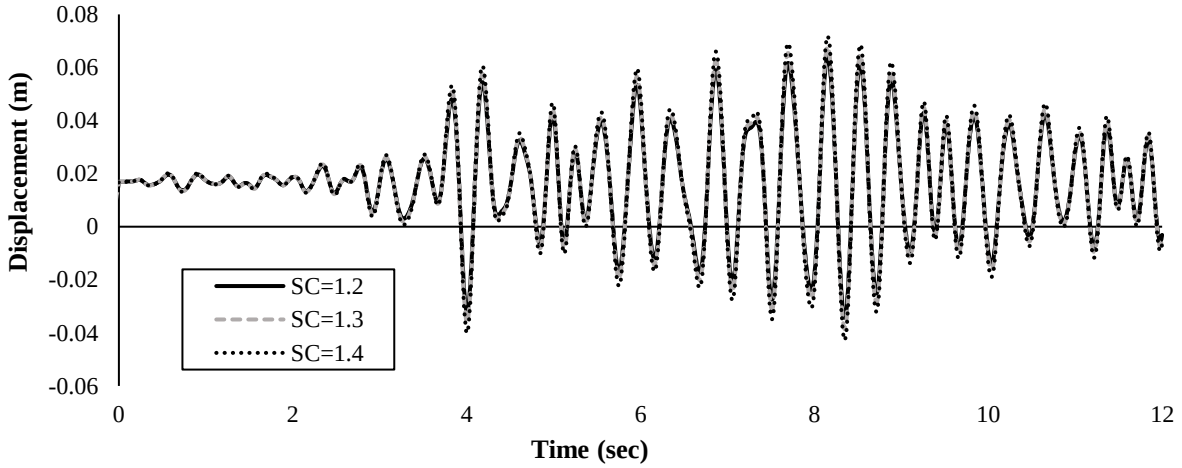

Fig. 8. The dam mid-crest displacement in the stream direction

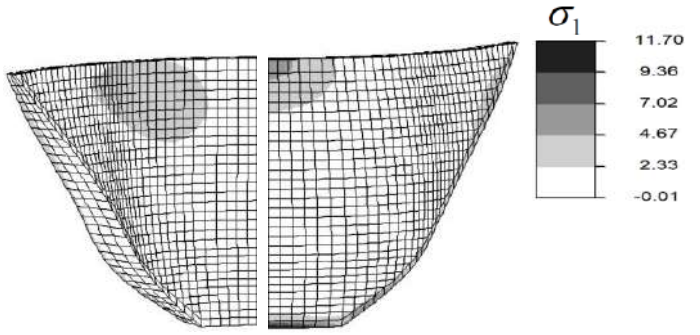

(a) Maximum tension SC = 1.2

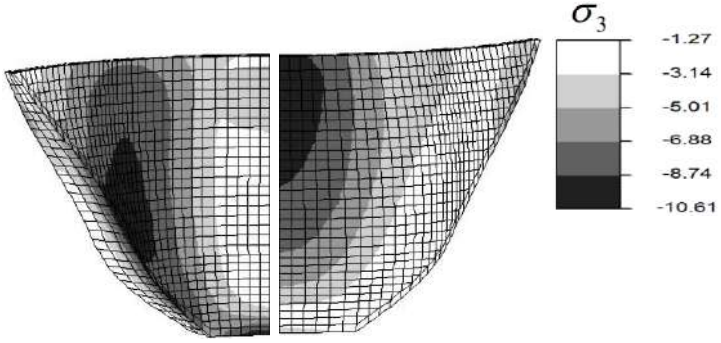

(b) Maximum compression SC = 1.2

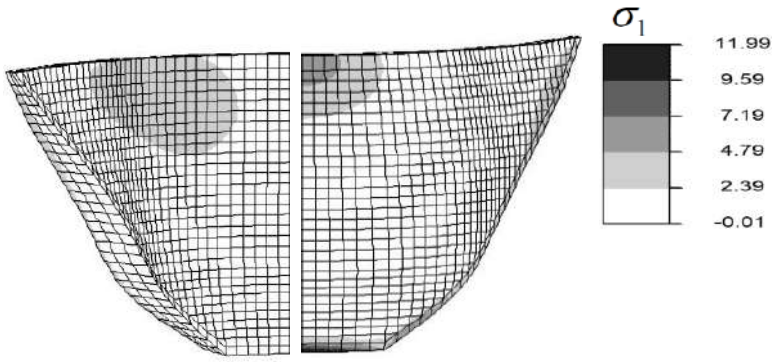

(c) Maximum tension SC = 1.3

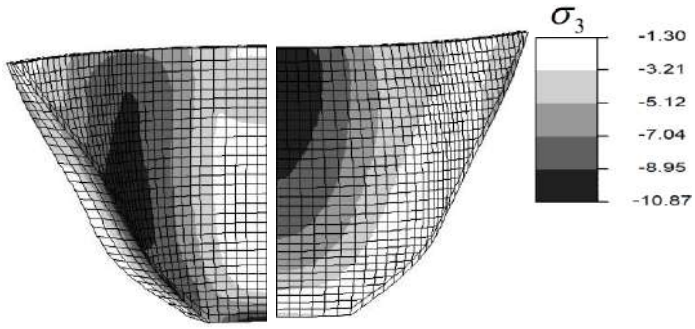

(d) Maximum compression SC = 1.3

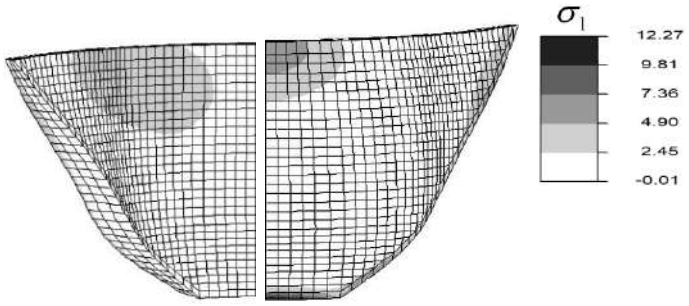

(e) Maximum tension SC = 1.4

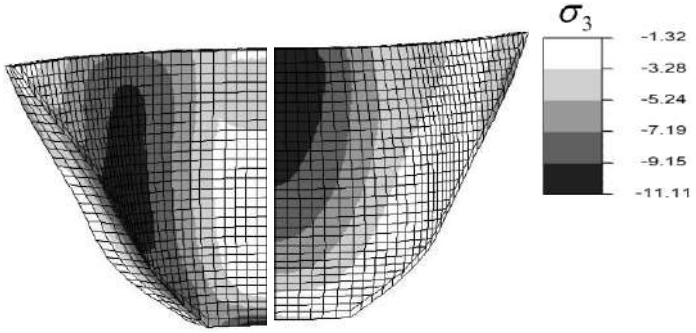

(f) Maximum compression SC = 1.4

Fig. 9. Envelope of principal stresses (MPa) for linear case

5.2.2. Nonlinear Results

In this section, two primary analyses are conducted with different damping algorithms: 1) Constant Damping (JDAMP = 0); and 2) Varying damping (JDAMP = 1). In each part, different Scale Factors (SC) of Taft acceleration are applied to the Morrow Point dam to investigate its nonlinear response due to extreme dynamic loading.

5.2.2.1. Constant Damping (JDAMP=0)

This case results are summarized in Table 3. Moreover, the envelopes of maximum tensile and compressive principal stresses throughout the analysis are

demonstrated in Figure 10. It is observed that tensile stresses are now bounded to the concrete tensile strength, illustrating one of the main capabilities of the present model. Moreover, high compressive principal stresses have occurred in the dam's mid-crest region (U/S face), dam's base and abutments (D/S face). However, they do not exceed the concrete compressive strength even for 1.4 scale factor. Therefore, no compressive damage is expected in these cases. It is also noticed that tensile and compressive stresses are distributed in a broader range as scale factor increases.

The tensile damage resulted for various parts of the dam body at the end of analysis is demonstrated in Figure 11. It is noticed that there are tensile damages in the base and abutments, as well as dam's mid-crest region on the U/S face. However, these are mainly occurring due to lack of peripheral and contraction joint modeling. Therefore, our concrete model has actually replaced joint modeling at those locations in an approximate manner. It is also noticed that there is tensile damage at dam's top portion on the D/S face which is growing in length as scale factor increases. However, it is noted that it has not yet formed a complete failure mechanism even for 1.4 scale factor.

Table 3. Maximum displacement of dam mid-crest and maximum stresses in dam body (JDAMP = 0)

Scale Factor	U_y^{Max} (mm)	U_z^{Max} (mm)	σ_1^{Max} (MPa)	σ_3^{Max} (MPa)
1.2	66.0	-4.32	3.0	-14.05
1.3	71.2	-4.33	3.0	-14.35
1.4	76.9	-4.6	3.0	-14.65

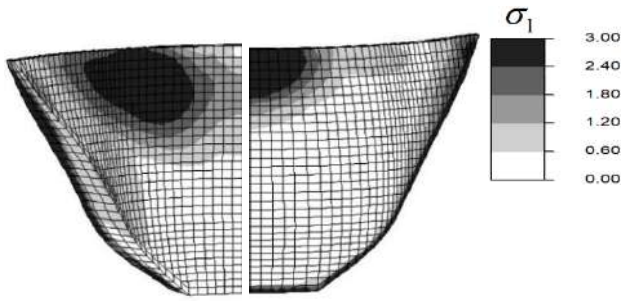

(a) Maximum tension SC = 1.2

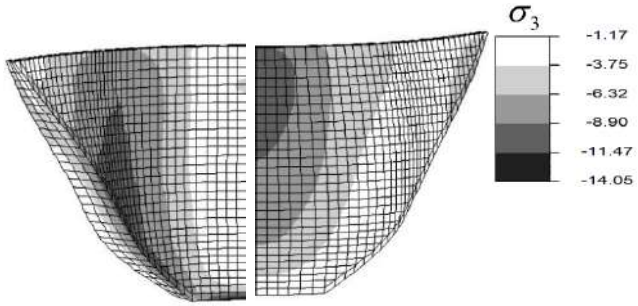

(b) Maximum compression SC = 1.2

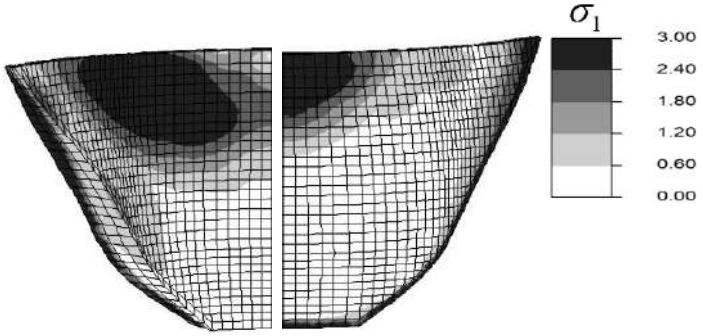

(c) Maximum tension SC = 1.3

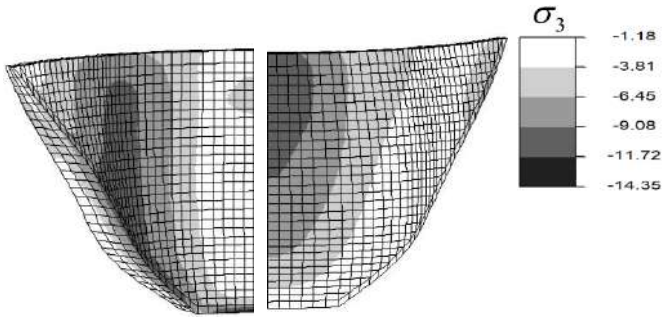

(d) Maximum compression SC = 1.3

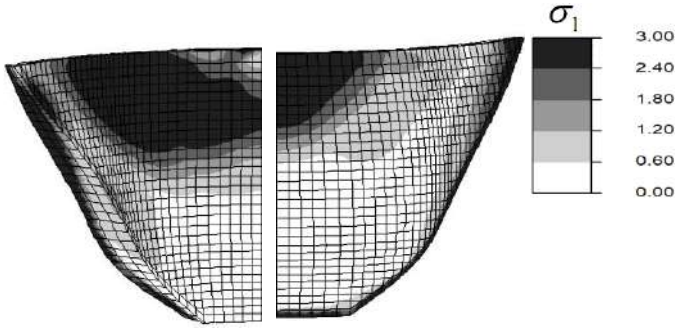

(e) Maximum tension SC = 1.4

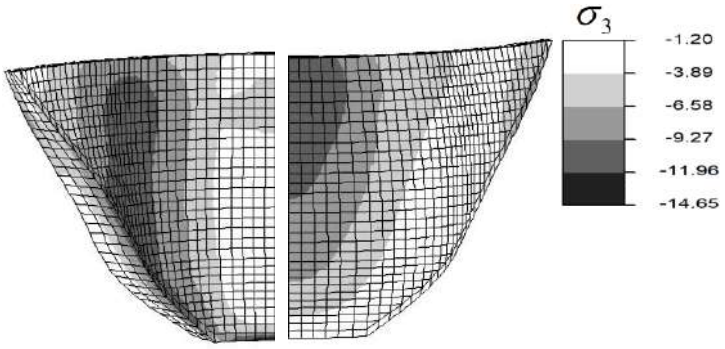

(f) Maximum compression SC = 1.4

Fig. 10. Envelope of maximum stresses nonlinear case JDAMP = 0

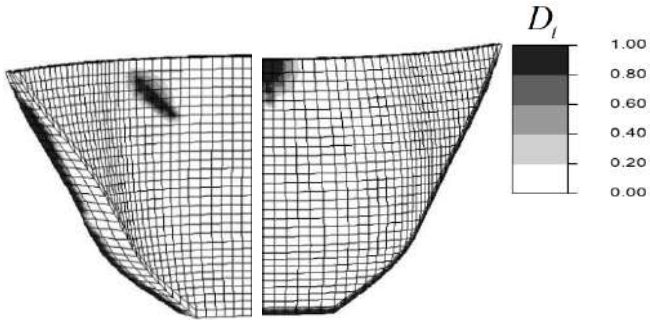

(a) SC = 1.2

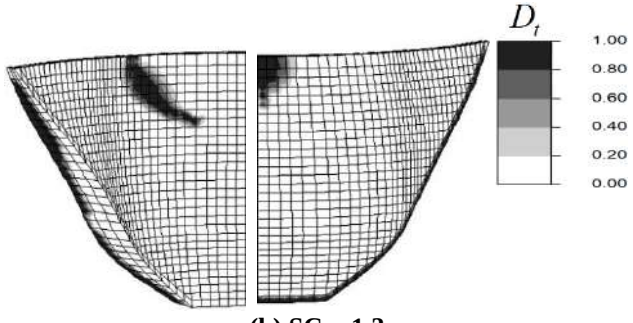

(b) SC = 1.3

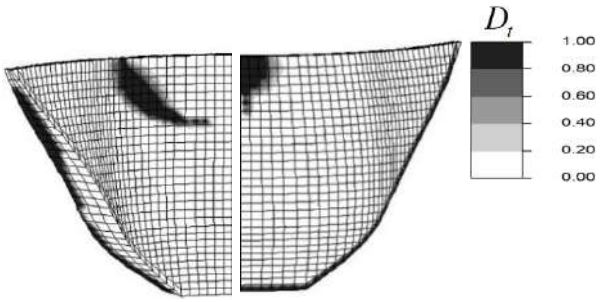

(c) SC = 1.4

Fig. 11. Distribution of damage at the end of analysis for the nonlinear case JDAMP = 0

5.2.2.2. Variable Damping (JDAMP = 1)

In this section, six models are investigated. Each model has a different scale factor. The scale factors vary from 1.2 to 1.55. These factors are increased gradually in a way that leads to the failure of the dam. The maximum dam mid-crest displacement in the stream and vertical direction are presented in Table 4. It is noticed that displacement at mid-crest increase for variable damping cases in comparison with their corresponding constant damping cases (Table 4 versus Table 3). Moreover, when the scale factor exceeds 1.4, displacement of the dam mid-crest has a considerable amount of increase which is the initial sign of failure. For 1.55 scale factor, the stream-component of displacement reaches a high value of 22 cm. Moreover, the displacement of the dam mid-crest in the stream direction in the range of 6 to 12 sec (where the notable changes have been happened) is shown in Figure 12.

The envelopes of maximum tensile and compressive principal stresses are also depicted in Figure 13. Moreover, tensile damage for these cases is presented in Figure 14. It is noticed that there is more extensive tensile damage for variable damping cases in comparison with corresponding constant damping cases. Moreover, the maximum compressive principal stresses have also increased. For instance, when we consider the 1.4 scale factor case of variable damping, it is noticed that tensile damage on the top portion form a complete loop on the D/S face while this is not the case for corresponding constant damping case. Furthermore, the maximum compressive principal stresses reach a high value of -20.99 MPa (in comparison with -14.65 MPa for corresponding constant damping case).

It is also noted that as scale factor reaches the value of 1.55, the tensile damage at the top portion extends along the dam thickness and similar loop begins to form starting at dam crest. This means that we are getting very close to a complete failure mechanism occurring at the top portion of the dam. Moreover, the maximum compressive principal stress reaches a high value of -29.96 MPa and its location is at dam mid-crest which is a sign of crushing in that vicinity.

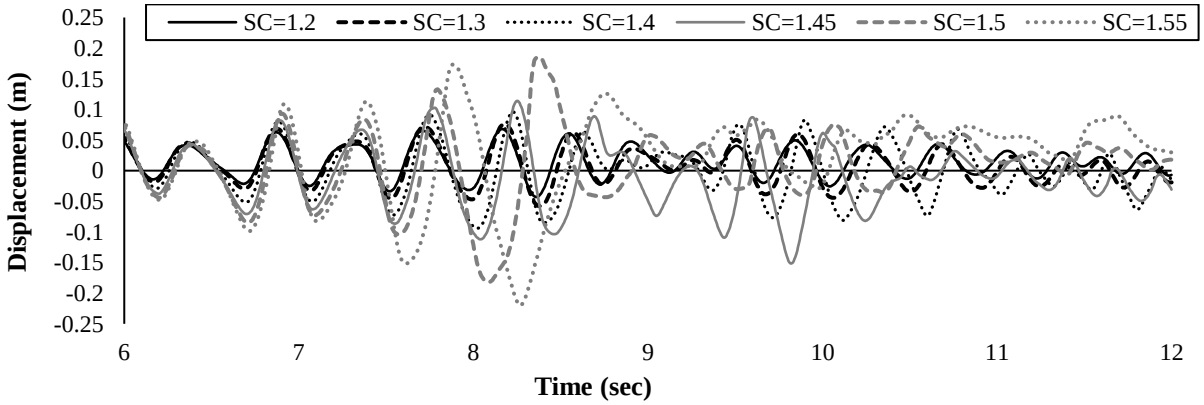

Fig. 12. The dam mid-crest displacement in the stream direction in the nonlinear case

Table 4. Maximum displacement of dam mid-crest and maximum stresses in dam body (JDAMP = 1)

Scale factor	U_y^{Max} (mm)	U_z^{Max} (mm)	σ_1^{Max} (MPa)	σ_3^{Max} (MPa)
1.2	67.9	-4.46	3.0	-14.50
1.3	76.4	-8.24	3.0	-14.77
1.4	96.4	-11.4	3.0	-20.99
1.45	-152	21.5	3.0	-26.42
1.5	186	38.0	3.0	-29.58
1.55	-220	70.9	3.0	-29.96

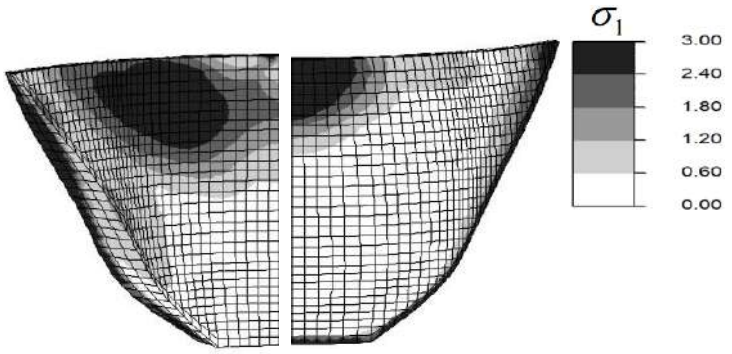

(a) Maximum tension SC = 1.2

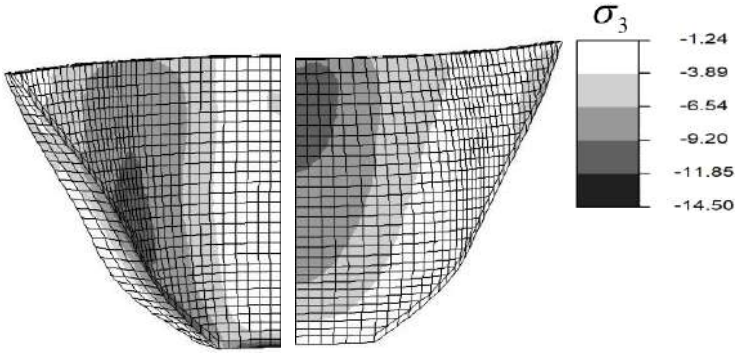

(b) Maximum compression SC = 1.2

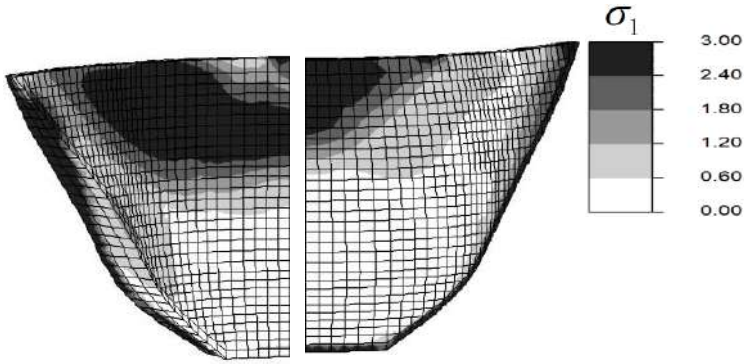

(c) Maximum tension SC = 1.3

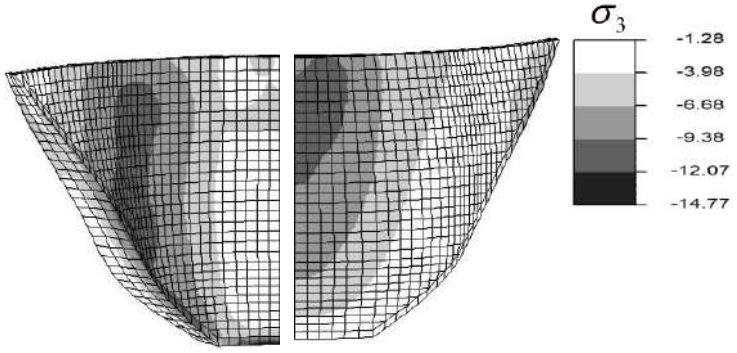

(d) Maximum compression SC = 1.3

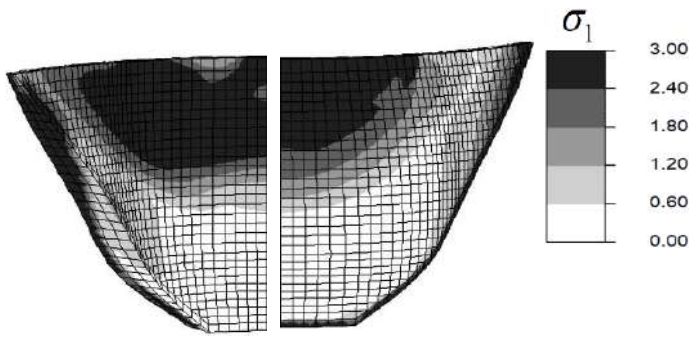

(e) Maximum tension SC = 1.4

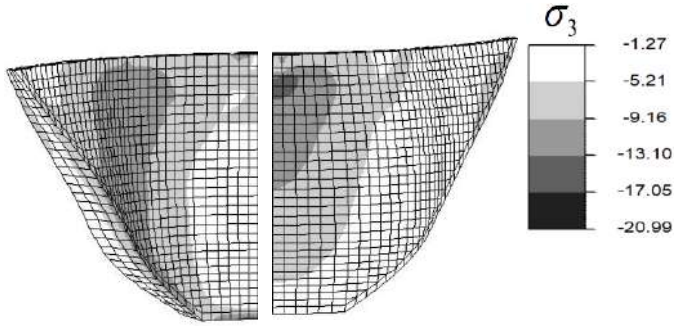

(f) Maximum compression SC = 1.4

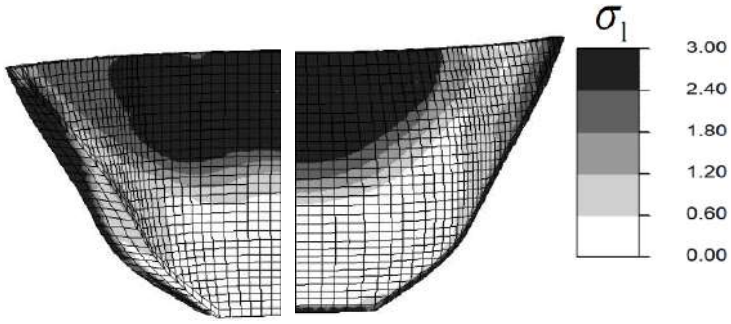

(g) Maximum tension SC = 1.45

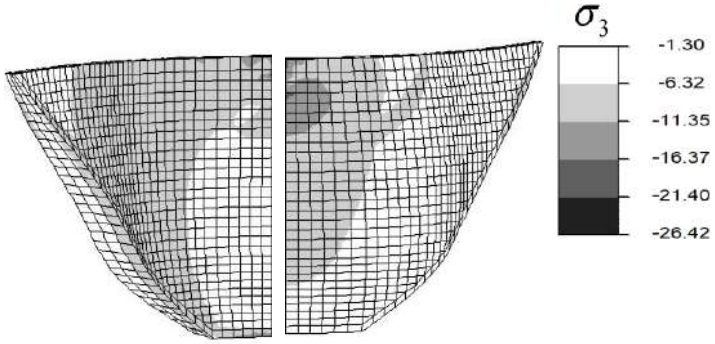

(h) Maximum compression SC = 1.45

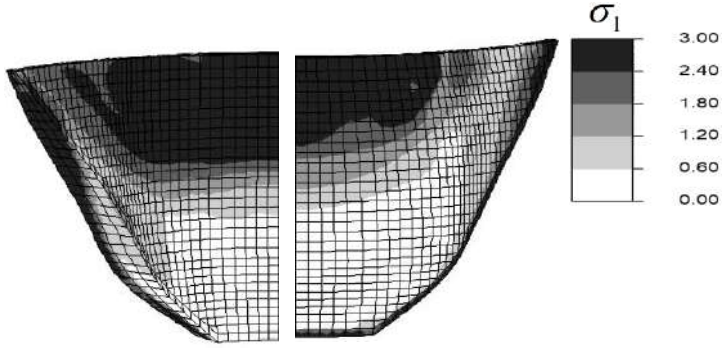

(i) Maximum tension SC = 1.5

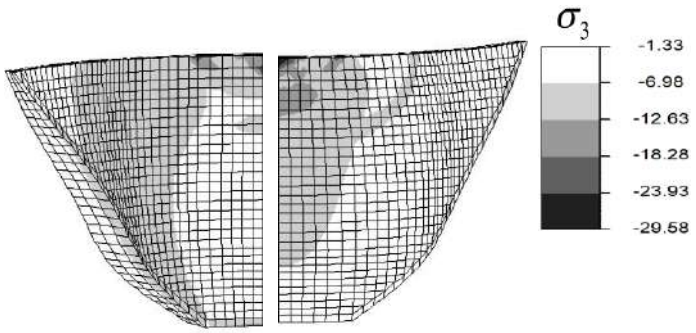

(j) Maximum compression SC = 1.5

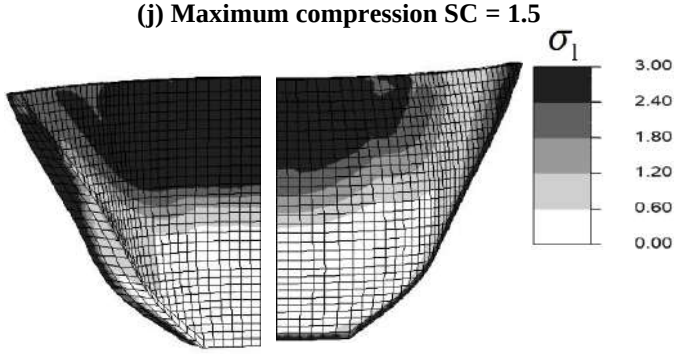

(k) Maximum tension SC = 1.55

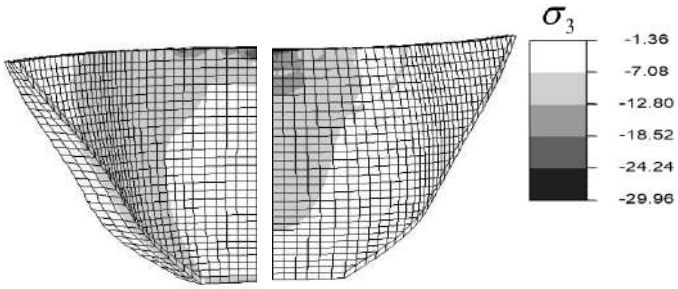

(l) Maximum compression SC = 1.55

Fig. 13. Envelope of maximum stresses in nonlinear case JDAMP = 1

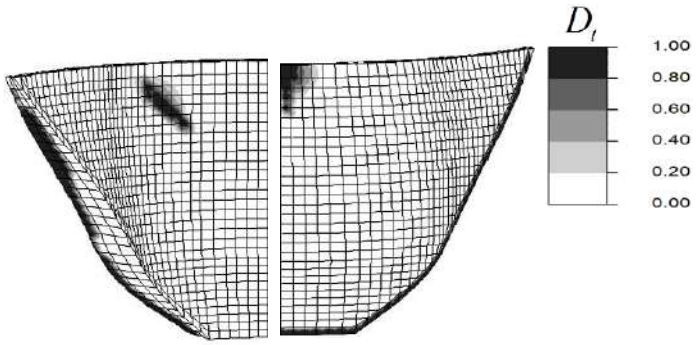

(a) SC = 1.2

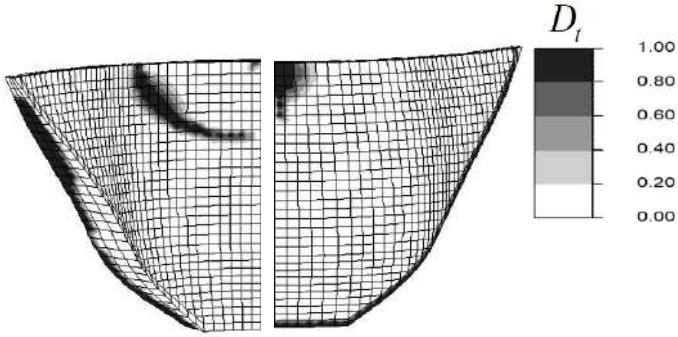

(b) SC = 1.3

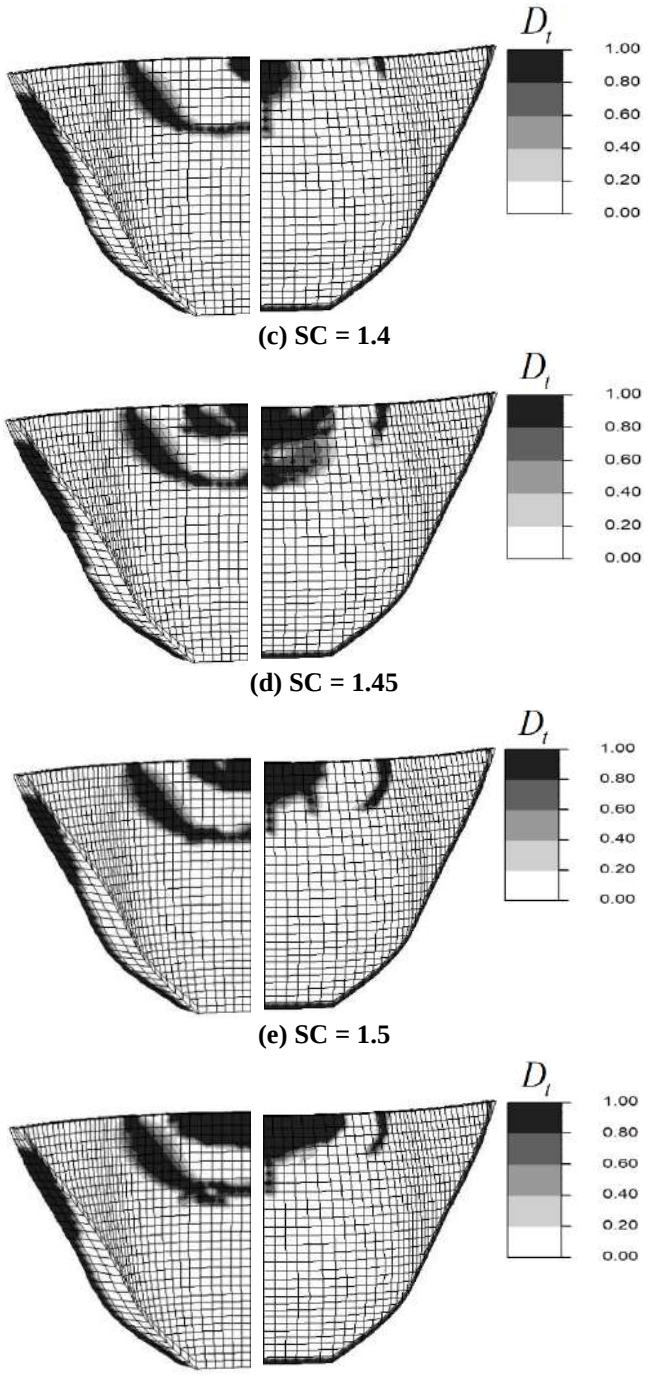

(c) SC = 1.4

(d) SC = 1.45

(e) SC = 1.5

(f) SC = 1.55

Fig. 14. Distribution of damage at the end of analysis for the nonlinear case JDAMP = 1

6. Summary and Conclusions

A special finite element program based on the proposed damage model was developed to evaluate the seismic damage response of concrete arch dams. An idealized symmetric model of 143 m high Morrow Point dam located in Colorado was subjected to Taft earthquake components. The components of the earthquake were multiplied by different scale factors to investigate the failure of the dam. Three cases were analyzed; 1) Linear case; 2) Nonlinear case with constant damping; 3) Nonlinear case with variable damping. The principal outcomes are summarized as follows:

- The proposed nonlinear model can predict the ultimate strength of the structure and the process of forming cracks in the arch dam.
- Considering the effect of the reservoir

has a significant impact on the analysis results

- Morrow Point arch dam can stand high compressive stresses; however, its tensile strength cannot bear the induced stresses, so tensile damage is inevitable, and cracks will be formed.
- The displacements and stresses are increased in the case of variable damping more than in constant damping case with the same alpha factors which is due to the update of damping matrix leading to softening of structure.
- In the case of constant damping, the main location of tensile damages is in the base and abutments, as well as dam's mid-crest region on the U/S face, and dam's top portion on the D/S face in which by increasing the scale factor, they tend to grow in length and form an unstable part on the crest of the dam.
- In the case of variable damping, the main location of tensile cracks is the same as the constant damping case. However, it seems that cracks are extended more in this case, and they form a complete loop on the D/S face of the top portion.
- The analyses indicate an early sign of failure in the structure based on the adopted methodology when significant displacements are enforced on the dam due to severe seismic loadings.
- This model can practically restrain the maximum tensile stresses to the tensile strength of concrete, and predicts a realistic distribution and stress levels in the dam body.
- The nonlinear case results with variable damping demonstrate that the arch dam can experience considerable damage in the time of a strong earthquake and when the scale factor reaches 1.55, there is the probability of failure.
- Overall, the model is proved to predict crack propagation consistent with failure in concrete arch dams. Moreover, this model is undoubtedly a step toward reducing the computational time while having an acceptable level of accuracy in dam engineering practice.

7. Appendix A

Table A.1: The HHT time integration method

0	$\boldsymbol{i = 0}$, $\boldsymbol{\dot{U}^{0}_{n+1} = -a_4\dot{U}_n - a_5\ddot{U}_n}$, $\boldsymbol{\ddot{U}^{0}_{n+1} = -a_2\dot{U}_n - a_3\ddot{U}_n}$ and $\boldsymbol{U^{0}_{n+1} = U_n}$
1	$R_{n+1} = R^{st} - MJa^{g}_{n+1}$
2	$U^{i}_{n+\varphi} = \alpha U_n + (1-\alpha)U^{i}_{n+1}$
3	$\varepsilon_{n+\varphi} = B(U^{e})^{i}_{n+\varphi}$, then obtain $\sigma_{n+\varphi}$and $D_{n+\varphi}$
4	$\Psi^{i}_{n+1} = M\ddot{U}^{i}_{n+1} + C\dot{U}^{i}_{n+\varphi} + F^{i}_{n+\varphi} - R_{n+\varphi}$
5	IF $\left\|\Psi^{i}_{n+1}\right\| \le Tol_G$ Then Exit
6	Solve $\left(\frac{\partial\Psi}{\partial U}\right)_{n+1} \Delta U^{i+1}_{n+1} = -\Psi^{i}$
7	$U^{i+1}_{n+1} = U^{i}_{n+1} + \Delta U^{i+1}_{n+1}$
8	$\dot{U}^{i+1}_{n+1} = \dot{U}^{i}_{n+1} + a_1\Delta U^{i+1}_{n+1}$
9	$U^{i+1}_{n+1} = \ddot{U}^{i}_{n+1} + a_0\Delta U^{i+1}_{n+1}$
10	i=i+1 and GOTO Step 2.

6. References

Akbari, R. and Lotfi, V. (2022). "Nonlinear dynamic analysis of concrete gravity dams utilizing a simplified continuum damage model and different damping algorithms", *Asian Journal of Civil Engineering*, 24(2), 453-468, https://doi.org/10.1007/s42107-022-00511-2.

Alegre, A. and Oliveira, S. (2020). "Non-linear seismic analysis of arch dams considering joint movements and a concrete damage model", *Dam World 2020*, Lisbon, Portugal.

Alegre, A., Oliveira, S., Mendes, P., Proença, J., Carvalho, E. and Matsinhe, B. (2022). "Numerical models for seismicanalysis of arch dams", *Congreso de Métodos Numéricos En Ingeniería*, 1-20.

Ardakanian, R., Ghaemian, M. and Mirzabozorg, H. (2006). "Nonlinear behavior of mass concrete in 3-D problems using damage mechanics approach", *European Earthquake Engineering*, 20(2), 65-89.

Cabral, N.R., Invaldi, M.A., D'Ambra, R.B. and Iturrioz, I. (2019). "An alternative bilinear peridynamic model to simulate the damage process in quasi-brittle materials", *Engineering Fracture Mechanics*, 216(1), 106494, DOI:10.1016/j.engfracmech.2019.106494.

Cervera, M., Oliver, J. and Faria, R. (1995). "Seismic evaluation of concrete dams via continuum damage models" *Earthquake Engineering & Structural Dynamics*, 24(9), 1225-1245, https://doi.org/10.1002/eqe.4290240905.

Cervera, M., Oliver, J. and Manzoli, O., (1996). "A rate-dependent isotropic damage model for the seismic analysis of concrete dams", *Earthquake Engineering & Structural Dynamics*, 25(9), 987–1010, 25, 987-1010,

https://doi.org/10.1002/(SICI)1096-9845(199609)25:9<987::AID-EQE599>3.0.CO;2-X.

Cervera, M. and Tesei, C. (2017). "An energy-equivalent d+/d− damage model with enhanced microcrack closure-reopening capabilities for cohesive-frictional materials", *Materials*, 10(4), 433. https://doi.org/10.3390/ma10040433.

Cervera, M., Tesei, C. and Ventura, G. (2017). "Cracking of quasi-brittle structures under monotonic and cyclic loadings: A d+/d− damage model with stiffness recovery in shear", *International Journal of Solids and Structures*, 135(1), 148-171, https://doi.org/10.1016/j.ijsolstr.2017.11.017.

Daneshyar, A. and Ghaemian, M. (2019). "Seismic analysis of arch dams using anisotropic damage-plastic model for concrete with coupled adhesive-frictional joints response", *Soil Dynamics and Earthquake Engineering* 125(1), 105735, https://doi.org/10.1016/J.SOILDYN.2019.105735.

Farahani, A.V. (2005). *Advances in fatigue, fracture and damage assessment of materials,* Vol. 6, WIT Press.

Ghrib, F. and Tinawi, R., (1995. "Nonlinear behavior of concrete dams using damage mechanics", *Journal of Engineering Mechanics*, 121(4), 513-527, https://doi.org/10.1061/(ASCE)0733-9399(1995)121:4(513).

Hall, J.F. (1988). "The dynamic and earthquake behaviour of concrete dams: review of experimental behaviour and observational evidence", *Soil Dynamics and Earthquake Engineering* 7(2), 58-121, issue?? https://doi.org/10.1016/S0267-7261(88)80001-0.

Jenabidehkordi, A. (2019). "Computational methods for fracture in rock: A review and recent advances", *Frontiers of Structural and Civil Engineering*, 13(2), 273-287.

Komasi, M. and Beiranvand, B. (2021). "Seepage and stability analysis of the Eyvashan Earth Dam under drawdown conditions", *Civil Engineering Infrastructures Journal*, 54(2), 205-223, https://doi.org/10.22059/ceij.2020.293429.1634.

Lee, J. and Fenves, G.L. (1998). "A plastic-damage concrete model for earthquake analysis of dams", *Earthquake Engineering & Structural Dynamics*, 27(9), 937-956, https://doi.org/10.1002/(SICI)1096-9845(199809)27:9<937::AID-EQE764>3.0.CO;2-5.

Lubliner, J., Oliver, J., Oller, S. and Oñate, E., (1989). "A plastic-damage model for concrete", *International Journal of Solids and Structures*, 25(3), 299-326, https://doi.org/10.1016/0020-7683(89)90050-4.

Mauludin, L.M. and Oucif, C. (2020). "Computational modeling of fracture in concrete: A review", *Frontiers of Structural and Civil Engineering*, 14(3), 586-598, https://doi.org/10.1007/s11709-020-0573-z.

Mirzabozorg, H. and Ghaemian, M. (2005). "Non-linear behavior of mass concrete in three-dimensional problems using a smeared crack approach", *Earthq Eng Struct Dyn*, 34(3), 247-269, https://doi.org/10.1002/eqe.423.

Mirzabozorg, H., Ghaemian, M. and Kianoush, M.R. (2004). "Damage mechanics approach in seismic analysis of concrete gravity dams including dam-reservoir interaction", *European Earthquake Engineering*, 18(3), 17-24.

Mirzabozorg, H., Khaloo, A.R., Ghaemian, M. and Jalalzadeh, B. (2007). "Non-uniform cracking in smeared crack approach for seismic analysis of concrete dams in 3D space", *International Journal of Earthquake Engineering and Engineering Seismology* (EEE), 2(1), 48-57.

Nguyen, N.H.T., Bui, H.H., Kodikara, J., Arooran, S. and Darve, F. (2019). "A discrete element modelling approach for fatigue damage growth in cemented materials", *International Journal of Plasticity*, 112(1), 68-88, https://doi.org/https://doi.org/10.1016/j.ijplas.2018.08.007.

Oliver, J., (1989). "A consistent characteristic length for smeared cracking models", *International Journal for Numerical Methods in Engineering*, 28(2), 461-474, https://doi.org/10.1002/nme.1620280214.

Oliver, J., Cervera, M., Oller, S. and Lubliner, J. (1990). "Isotropic damage models and smeared crack analysis of concrete", *Proceedings of SCI-C Computer Aided Analysis and Design of Concrete Structures*, Pineridge Press, pp. 945-957.

Omidi, O. and Lotfi, V. (2017a). "Seismic plastic–damage analysis of mass concrete blocks in arch dams including contraction and peripheral joints", *Soil Dynamics and Earthquake Engineering*, 95(1), 118-137, https://doi.org/10.1016/j.soildyn.2017.01.026.

Omidi, O. and Lotfi, V. (2017b). "A symmetric implementation of pressure-based fluid-structure interaction for nonlinear dynamic analysis of arch dams", *Journal of Fluids and Structures*, 69(1), 34-55, https://doi.org/https://doi.org/10.1016/j.jfluidstructs.2016.12.003.

Park, T., Ahmed, B. and Voyiadjis, G.Z., (2021). "A review of continuum damage and plasticity in concrete, Part I: Theoretical framework", *International Journal of Damage Mechanics*, 31(6), 901-954, https://doi.org/10.1177/10567895211068174.

Qin, X., Guo, J., Gu, C., Chen, X. and Xu, B., (2021). "A discrete-continuum coupled numerical

method for fracturing behavior in concrete dams considering material heterogeneity", *Construction and Building Materials*, 305(1), 124741, https://doi.org/https://doi.org/10.1016/j.conbuildmat.2021.124741.

Rayleigh, J.W.S. and Lindsay, R.B., (1945). The theory of sound, Dover Publications.

Rots, J.G., Blaauwendraad, J., (1989). "Crack models for concrete, discrete or smeared? Fixed, multi-directional or rotating?", HERON, 34(1), 1-56.

Sinaie, S., Ngo, T.D. and Nguyen, V.P., (2018). "A discrete element model of concrete for cyclic loading", *Computers & Structures*, 196(1), 173-185, https://doi.org/https://doi.org/10.1016/j.compstruc.2017.11.014.

Valliappan, S., Yazdchi, M. and Khalili, N. (1999). "Seismic analysis of arch dams, A continuum damage mechanics approach", *International Journal for Numerical Methods in Engineering*, 45(11), 1695-1724, https://doi.org/10.1002/(SICI)1097-0207(19990820)45:11%3C1695::AID-NME651%3E3.0.CO;2-2.

Valliappan, S., Yazdchi, M. and Khalili, N., (1996). "Earthquake analysis of gravity dams based on damage mechanics concept", *International journal for numerical and analytical methods in geomechanics*, 20(10), 725-751, https://doi.org/10.1002/(SICI)1096-9853(199610)20:10%3C725::AID-NAG843%3E3.0.CO;2-X.

Voyiadjis, G.Z., Ahmed, B. and Park, T. (2021). "A review of continuum damage and plasticity in concrete, Part II: Numerical framework", *International Journal of Damage Mechanics*, 31(5), 762-794, https://doi.org/10.1177/10567895211063227.

Voyiadjis, G.Z. and Kattan, P.I. (2017). "A theory of damage and self-regenerating materials", *Acta Mechanica*, 228(12), 4249-4268, https://doi.org/10.1007/s00707-017-1928-y.

Wikipedia Contributors. (2022). Morrow Point Dam, (accessed 2.18.2022), https://en.wikipedia.org/w/index.php?title=Morrow_Point_Dam&oldid=1071488832.

Xu, L., Jing, S., Liu, J. and Huang, Y. (2017). "Cracking behavior of a concrete arch dam with weak upper abutment", *Mathematical Problems in Engineering*, 2017, 6541975, https://doi.org/10.1155/2017/6541975.

Civil Engineering Infrastructures Journal 2023, 56(2): 257-276
DOI: 10.22059/CEIJ.2022.342561.1840

RESEARCH PAPER

Performance Improved Multi-Objective Optimization in Applying Low-Impact Development Strategies to Control Urban Runoff

Naghibzadeh, H.[1], Saadat, M.[2*], Basirat, S.[2] and Iranpour Mobarakeh, M.[3]

[1] Ph.D. Candidate, Department of Civil Engineering, Najafabad Branch, Islamic Azad University, Najafabad, Iran.
[2] Assistant Professor, Department of Civil Engineering, Najafabad Branch, Islamic Azad University, Najafabad, Iran.
[3] Assistant Professor, Department of Civil Engineering, Lenjan Branch, Islamic Azad University, Isfahan, Iran.

Received: 08 May 2022; Revised: 01 Jul. 2022; Accepted: 17 Jul. 2022

ABSTRACT: Best Management Practices (BMPs) can play a vital role to control natural disasters like floods. In this paper, retention pond and vegetative swale are considered to restrain urban runoff. Storm water management modeling (SWMM) is used for runoff modeling. A piece of code is developed based on Non-dominated Sorting Genetic Algorithm (NSGA-II) in MATLAB to optimize the BMPs application. The aim is comparing the effect of roulette wheel, tournament and random selection operators to obtain the optimal location and area of BMPs. Minimizing the runoff volume and pollution in sub-catchments and the construction cost of the BMPs are three objective functions. Rafsanjan city located in southeast of Iran is selected as an appropriate case study. Estimating the best pressure of selection operator in roulette wheel and the best selection size in tournament operator and simultaneous quantitative and qualitative optimization using two BMPs are the innovations of this study. The results indicate that the pressure of the selection operator in roulette wheel which leads to the optimal answer is three and nine while the best size of selection in the tournament operator is nine. Optimum location, type, area and volume for each BMP are obtained after running the code.

Keywords: Best Management Practices, Roulette Wheel, Selection Operators, SWMM, Tournament.

1. Introduction

Recently, due to climate change, the amount of rainfall and its intensity has been affected. This phenomenon has caused a sharp increase in the quantitative characteristics of runoff in some areas which in turn reduces its quality. Quantitative and qualitative control of urban runoff in order to reduce human, environmental, health and financial losses is of interest to different communities. To reduce the risk of flooding, Best Management Practices (BMPs), known as Low-Impact Developments (LIDs), have been developed. These new flood

* Corresponding author E-mail: mohsen.saadat@pci.iaun.ac.ir

management methods are hydrological controllers that use two processes of storage and absorption at different scales to manage the quantity and quality of runoff. Some of these LIDs are retention pond, green roof, rain barrel, absorption well, vegetative swale, permeable pavement and infiltration trench. To achieve a suitable control program, it is necessary to identify the goals and use optimization methods. For this purpose, several algorithms called Multi-Objective Evolutionary Algorithms (MOEAs) have been developed in recent decades. Mathematical models (analytical, numerical and optimization) are employed in many fields including planning, engineering and water resources management. Particle Swarm Optimization algorithm (PSO) and Non-dominated Sorting Genetic Algorithm (NSGA-II) are two of them. These algorithms try to find the best values of the objective functions on the Pareto front while satisfying the existing constraints. In the structure of genetic algorithms, selection operators are used to determine the ability of a particular strand to participate in the reproduction process. These operators play an important role in selecting the most appropriate population in the algorithm. Thus, they are also called reproduction operators. Selection scheme is also an important issue in Genetic Algorithm (GA). A chromosome from the current generation would be selected to enter the next population (Kumar et al., 2016). Selection of operator pressure is important in the degree of convergence of GA. Therefore, determining the appropriate pressure of the selection operator or the appropriate size of the populations participating in the crossover operation can play an important role in the optimal performance of the selected algorithm and achieving better results.

Siriwardene and Perera (2006) selected appropriate operators in GA to optimize parameters of urban drainage model. The sensitivity of these operators was analyzed by repeated simulation through numerical experiments considering one GA operator at a time, by consolidation urban drainage modeling software and GA. In that study the tested GA operators were population size, number of generations, number of model parameter sets that should be considered from the previous generation to settle the optimum set, selection type, crossover and mutation rates. Results showed that models of urban drainage with a small number of parameters (two or less) could be optimized with any of the tested GA operator sets. Therefore, proper selection of operators in GA is essential to reach the optimum parameters in urban drainage models with large number of parameters (five or more). The performance of roulette wheel, elitism and tournament was compared as parents selection operators in Travelling Salesman problem (Chudasama et al., 2011). The results showed that elitism is the best compared to other methods. Sharma et al. (2014) delivered some selection strategies in GA for solving optimization problems and compared their performance. Roulette wheel, rank, tournament and elitism were four types of selection operators in the study. Best result achieved by applying roulette wheel and tournament selection with two points and one point crossover, respectively.

In a study two optimization algorithms, PSO and Global Gradient Algorithm (GGA) were used for hydraulic analysis of water distribution systems. The results showed that GGA and PSO perform better in convex and non-convex problems, respectively. However, by increasing the coefficient of the penalty function, the accuracy of the answers obtained from the two algorithms increased significantly (Moosavian and Jaefarzadeh, 2015).

Rathnayake (2015) improved the GA algorithm in such a way that it could control the storm migration. Optimal control of urban sewer networks was the main aim of the study. Solutions were acquired from the multi-objective optimization. Results showed the effective role of on-line storage tanks in controlling urban sewer flow. A method was presented by Martínez-Solano

et al. (2016) that limits the searching domain of solutions in GA in order to rehabilitate drainage networks. In this method, an iterative process was used which gradually reduced the search area that contains the optimal solution. The results showed the effectiveness of the procedure in reducing the search space for solutions to face the problem of matching the results of the algorithm with what happens. Modern Optimization Methods (MOMs) were used for planning, engineering and management of water resources (Tayfur, 2017) . The comparative analysis between seven types of GA-based algorithms showed that choosing the appropriate population size is necessary to verify the efficiency. It revealed the importance of selection operator. A study was conducted by Dastorani et al. (2018) in the Zayande Rood dam basin of Iran with the aim of predicting runoff volume caused by rainfall using data mining and machine learning methods. They concluded that Support Vector Machines (SVM), CART algorithm, model tree and artificial neural network methods have the highest accuracy in estimating runoff volume, respectively. A method was presented to improve Urban Drainage Systems (UDS) based on Model Predictive Control (MPC) (Abou Rjeily et al., 2018). Using EPA-SWMM and GA led to optimization of the time-scale schedules for actuators of UDS. The results indicated the high efficiency of the MPC method in improving the use of retention elements capacity in Lille university campus. Wang et al. (2018) compared MOEAs, MATLAB global optimization toolbox (MLOT), newly developed hybrid MOEA called GALAXY and NSGA-II in better adaptation to urban drainage system in China. GALAXY was the most powerful and the simplest tool among the three MOEAs because of its mechanism to significantly reduce parameterization issues. Non-dominated sorting genetic algorithm-III (NSGA-III) was used to calibrate storm water management model (SWMM) parameters (Swathi et al., 2019) . By comparing simulated and observed peak flow data, the efficiency of the calibration was evaluated. Results indicated that calibrated parameters related to a rainfall event are applicable for sequential runoff modeling. In a study, the reduction of Total Nitrogen (TN) and Total Phosphorus (TP) under the effect of two BMPs, namely, Fertilizer and Irrigation Reduction (FIR) and Vegetated Filter Strips (VFS) in the agricultural lands of Zrebar lake basin were investigated (Jamshidi et al., 2020). Soil and Water Assessment Tool (SWAT) was used for modeling and calibration of the basin. The results showed that the combination of these two BMPs reduced the concentration of TN and TP by up to 60 percent over eight years. A study was conducted to identify flow properties through grassed canal in Egypt during one year (Gad et al., 2020). Manning coefficient and specific energy were determined. The results were compared to those gathered from last studies in both grassed and ungrassed canals. Gene Expression Programming (GEP) and Statistical Package for the Social Sciences (SPSS) were used to derive formulas which relates Manning coefficient into specific energy of flow. Hai (2020) used the optimal design of permeable pavements, green roofs and tree boxes as LIDs to increase urban runoff quality. To reach the aim, NSGA-II was used to minimize the total relative cost of LIDs and maximize runoff quality. Rainfalls with a two year return period showed more effective results than the others in the Cau Bay river basin in Vietnam. Ochoa-Barragán et al. (2021) proposed a mathematical model that merge fair distribution schemes to design water allocation systems in the context of water scarcity in the city of Morelia in Mexico. The results provided optimal solutions for the equitable distribution of water supply resources in the scarcity scenario for the public consumptions. Alaneme et al. (2021) studied the fuzzy analytical hierarchical procedure to evaluate inefficiency of flexible pavement drainage system. The

research was done for a highway in Nigeria. It was proposed to redesign the flexible pavement of the highway, to evaluate the intensity of rainfall and to survey the topography along with the rehabilitation of the worn road using standard materials. In other research Huang et al. (2021) used GA to optimize LIDs distribution with concept of flood peak reduction. The reduction in LID performance was noticeable for return periods of more than ten years. The research results can afford general instruction for urban planning in order to design LIDs in urban areas. Xiong et al. (2021) optimized the service frequency and route network for shuttles by a solution that includes three components. The third component was GA procedure which consists of selection and mutation operators and multiple crossovers. This led to generate feasible solutions. Taban et al. (2021) used Multi-Variable Regression (MVR) and GA in order to select 3 out of 6 parameters that have the greatest influence on obtaining the Q-value in the Q-system (a technique used to determine the support system of a tunnel in rock). Subsequently, a fitness function was used to obtain optimal values in the GA.

Generally, in the previous studies, no steps have been taken to optimize the selection operator parameters in NSGA-II regarding the placement of BMPs in urban runoff control. This practice is performed for the first time in this study as the first innovation. In this paper, it is considered to reach the optimal location of BMPs, their types and area. Separate comparison of the different results of each scenario was the decision guide. The comparison of the results obtained from the use of different selection operators in the optimization algorithm illustrates the efficiency of each one. In the present study, two types of BMPs are used simultaneously in a multi-objective optimization to minimize runoff quantity and pollution. They should be assigned by a sub-catchment number that would be defined automatically. BMPs type selection is also done by the self-acting code to reach the optimal solution. The operator would be asked to determine the number of BMPs according to the organization budget at the beginning of running optimization program; also the range of land use percent for BMPs construction could be varied, both of which are other innovations of this study. Simultaneous qualitative and quantitative improvement of runoff, the type of BMPs, study region, the ability of user participation to determine the best solution compared to the real situation and proprietary optimization code using the NSGA-II algorithm which can be used for all other regions by defining the SWMM input file are the other distinctions compared to previous studies. Popular selection operators are roulette wheel, tournament, rank, stochastic universal sampling and Boltzmann (Katoch et al., 2021) as shown in Figure 1. Other operators used in GA are crossover, mutation and encoding.

Two selection operators have been used to compare with random selection of population in this research. First one is roulette wheel and the second is tournament. In the roulette wheel technique, all the chromosomes in the population are placed on a spinning wheel based on their fitness as shown in Figure 2. Genes that have a higher value based on the fitness function, play a larger role on this wheel and are used more frequently to produce offspring.

The tournament selection mechanism for selecting individuals is such that smaller populations are selected from the initial population. Genes selected from each population are used in the mating pool to produce the next generation (Shukla et al., 2015). The resulting offspring form the basis of the next generation as shown in Figure 3.

2. Methodology

The step-by-step procedure of the modeling and optimization is shown in Figure 4.

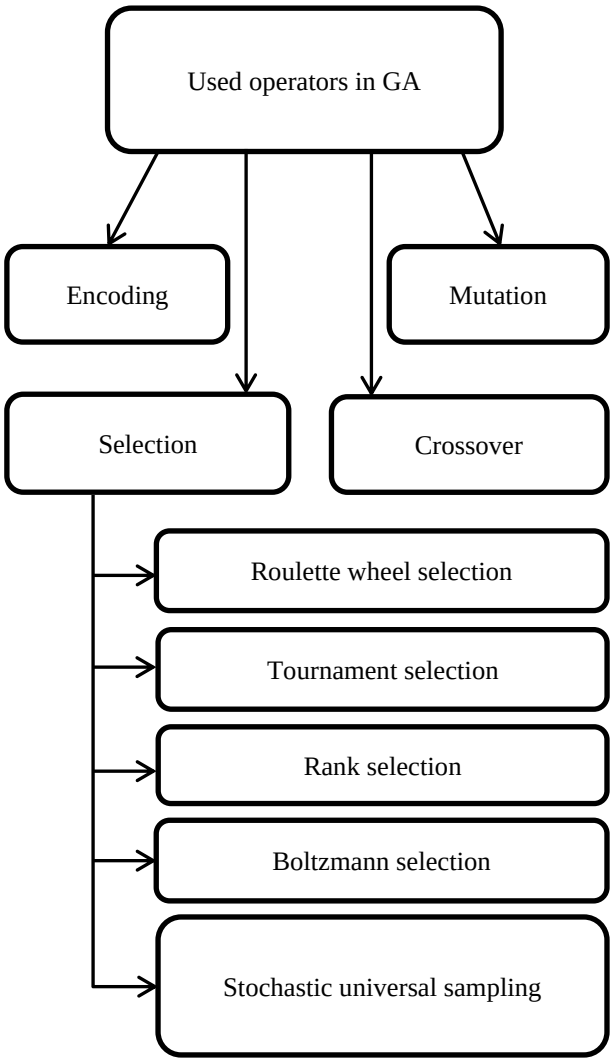

Fig. 1. Popular selection operators in Genetic Algorithm

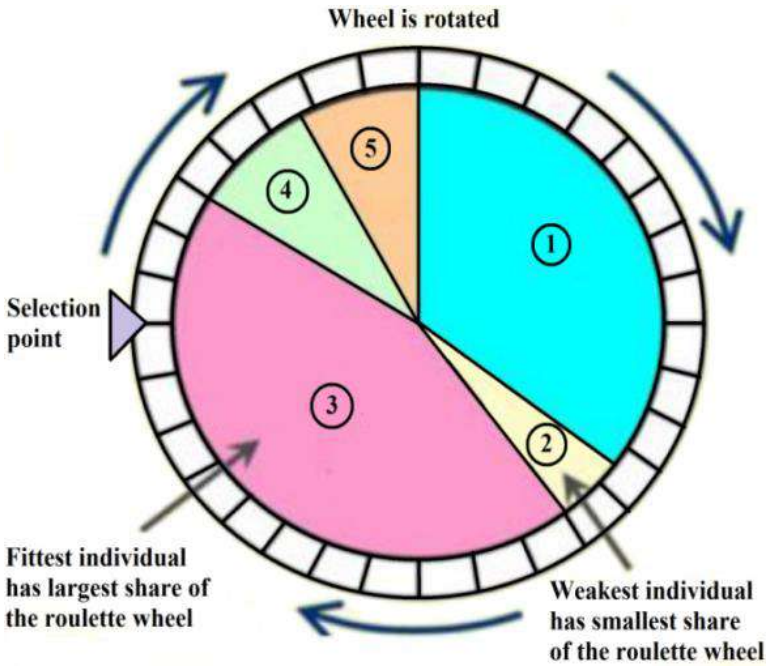

Fig. 2. Visual description of roulette wheel selection (Xavier et al., 2013)

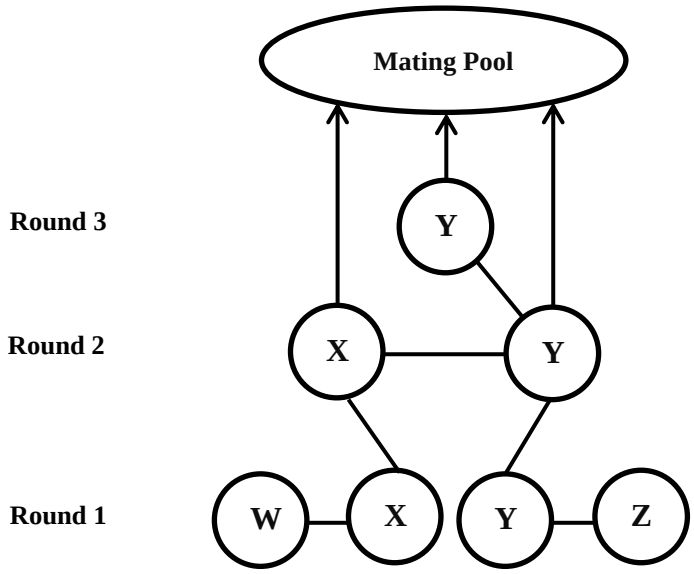

Fig. 3. Schematic concept of tournament selection (Höschel and Lakshminarayanan, 2019)

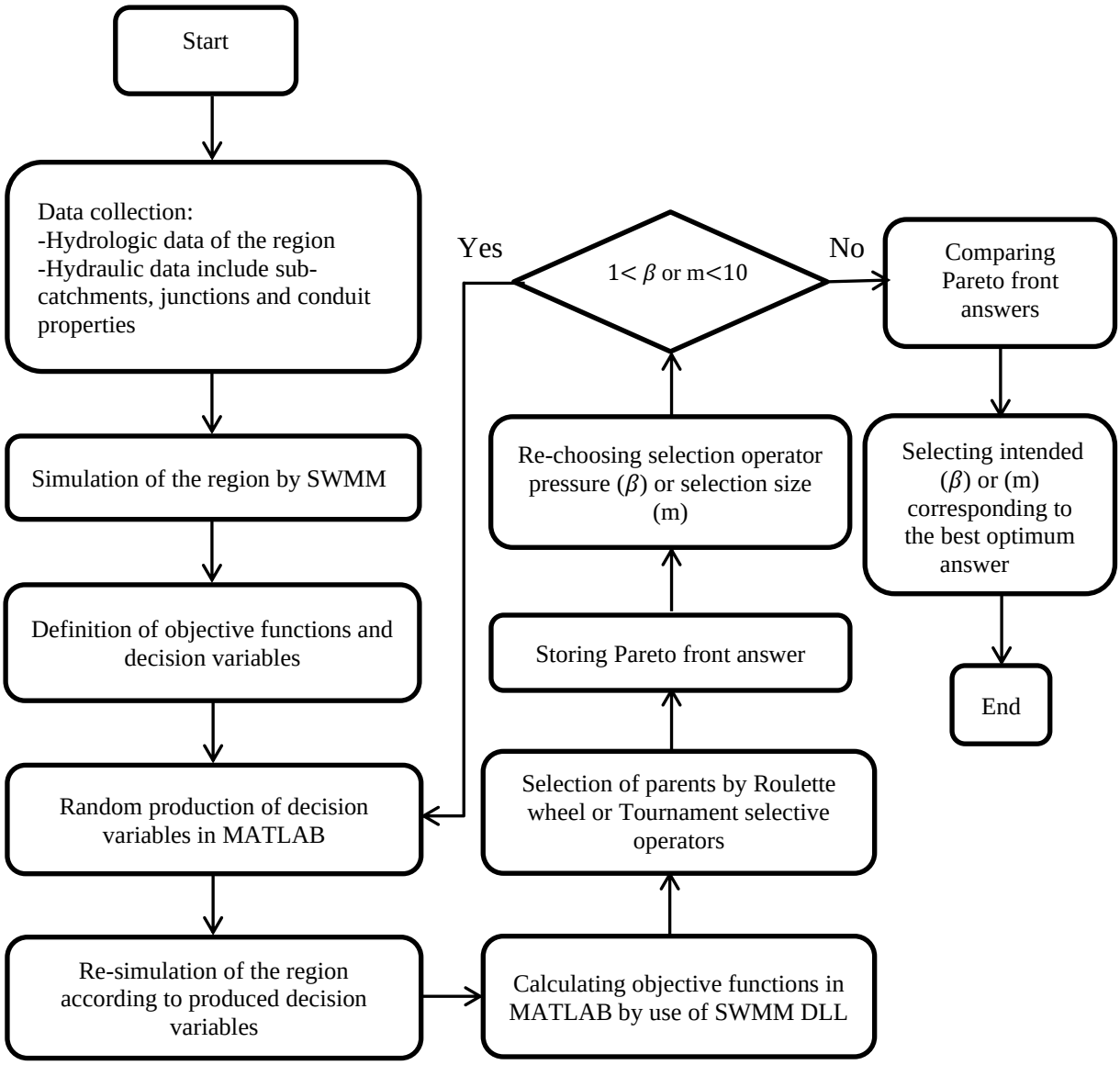

Fig. 4. Procedure of the modeling and optimization using selection operator pressure and selection size

2.1. Modeling in SWMM

In this study, first, the desired area is modeled using SWMM by employing two types of hydraulic and hydrological data. Hydraulic properties include physical characteristics of the area, such as topography, slope and permeability of each sub-catchment, land use and initial coefficients of build-up and wash-off. Other characteristics such as the area and outlet of each sub-catchment, the specifications and coordinates of conduits, outfalls and rain gage are defined as hydraulic data in the model. In addition to being divided into 127 sub-catchments, this region has 227 junctions and 19 outfalls. The total number of data entered into SWMM for modeling sub-catchments, junctions and conduits is 3940. Five types of land uses are considered which include residual (high, medium, low), commercial-industrial and green space. 635 input data have been used to define land uses and each sub-catchment includes five types of land uses. Finally, the percentage of each land use in each sub-catchment would be determined. The SWMM represents unsteady non-uniform flow by using differential equations of mass and momentum conservation known as the St. Venant equations. Volume conservation at each node, along with solving the St. Venant equations for each conduit simultaneously, provides information on temporal and spatial variation of discharge rates and water levels through the network. St. Venant flow equations would be solved by dynamic wave analysis and accurate theoretical answers would be obtained. Dynamic wave analysis account for backwater effects, flow reversal, channel storage, culvert flow and pressurized flow (Rossman , 2017). For unsteady free surface flow through a pipe or channel, the mass and momentum conservation are known as the St. Venant equations that can be expressed in terms of Eqs. (1) and (2).

$$\frac{\partial A}{\partial t}+\frac{\partial Q}{\partial x}=0 \quad (1)$$

$$\frac{\partial Q}{\partial t}+\frac{\partial (Q^2/A)}{\partial x}+gA\frac{\partial H}{\partial x}+gAS_f=0 \quad (2)$$

where x: is distance, t: is time, A and Q: are flow cross-sectional area and flow rate, respectively. H: is hydraulic head of water in the conduit (Z+Y). Z, Y and S_f: represent conduit invert elevation, conduit water depth and friction slope (head loss per unit length), respectively, and g: denotes acceleration of gravity.

The hydrological data of the region also include cumulative precipitation data with different return periods (Binesh et al., 2019). These data are obtained specifically for different regions of Iran by modifying the coefficients in the Bell method (Bell and Moore, 2000) (Figure 5). Precipitation data with a return period of two and five years is used in this paper. Selection of these two return periods is due to the fact that the recorded precipitation of the region is most similar to the precipitation height of the two and five years return period according to Figure 5. The calibrated runoff and Total Suspended Solid (TSS) related to the selected precipitation are compared with initial calculated results obtained by SWMM in Table 1.

As shown in Table 1, the greatest effect of SWMM parameters calibration is on rainfall results with a two-year return period and the initial and calibration results are very similar. Therefore, rainfall with a two-year return period was chosen to continue the study due to the high accuracy of its results.

2.2. Study Area

Rafsanjan is known as a city with a relatively high risk of floods in the northwest of Kerman province in southeast of Iran as shown in Figure 6. Rapid development without considering the requirements of sustainability has caused problems in the sanitary infrastructures and water supply in the region. Qualitative and quantitative management and improvement of runoff is very important alongside urban

development. The 2016 flood caused severe damage to the city residents and roads and disrupted traffic. The poor quality of the resulting runoff also affected the region's agriculture. Therefore, urban runoff control is becoming more important than before. In this research, the city of Rafsanjan has been considered as a suitable case according to the mentioned contents and the available topographic information. Two rivers named Shoor and Givdari pass through the city, which are the entrances of sub-catchments runoff in the region. The lowest elevation of the city is 1489 m while highest elevation is 1557 m above mean sea level. This region covers an area of 48.07 km^2 and is divided into 127 sub-catchments in SWMM according to Figure 7.

Table 1. Initial and calibrated parameters used in the simulations

Return period (year)	2		5	
Data type	Initial	Calibrated	Initial	Calibrated
Total runoff (m^3/s)	0.9	0.948	1.3	1.373
Total TSS (kg)	453.6	453.8	655.2	609.315

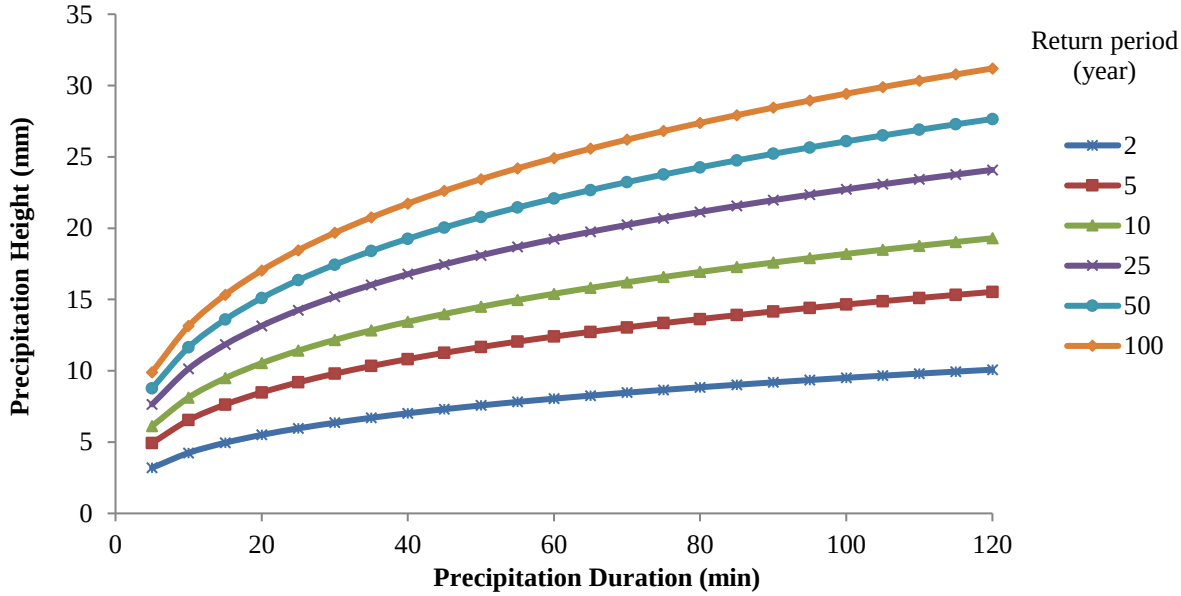

Fig. 5. Two-hour rainfall curves in different return periods for the study area (Binesh et al., 2019)

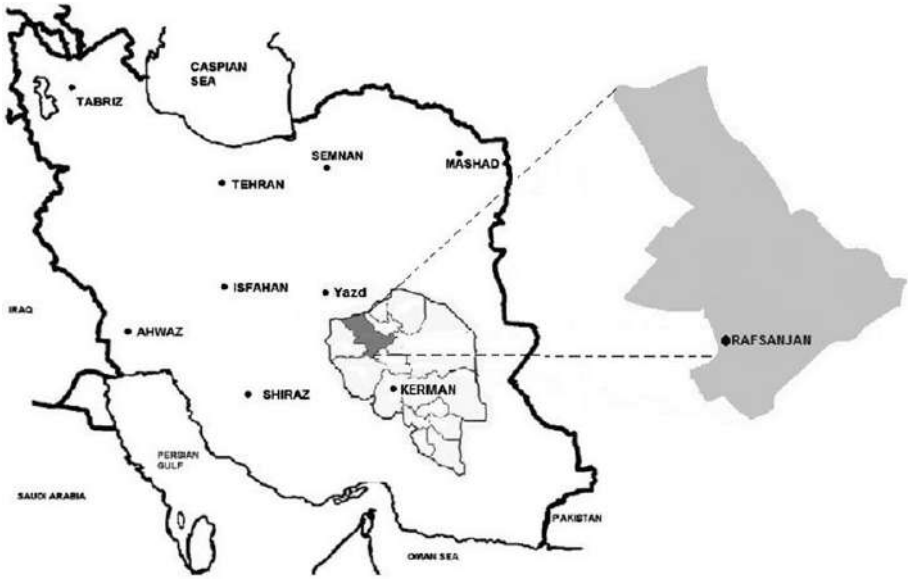

Fig. 6. Rafsanjan location in Iran, Kerman (Hakimi et al., 2021)

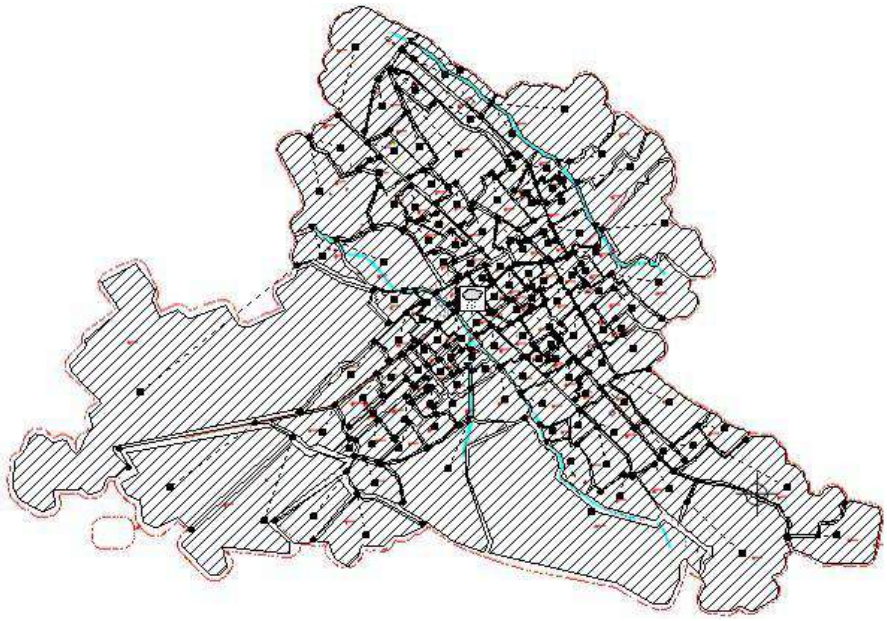

Fig. 7. Study area in SWMM including the plan of the region and separated sub-catchments

In this paper, locating the BMPs and determining the optimal area of each one has been done in order to achieve highest quality of urban runoff and the lowest flood volume for each sub-catchment. Two types of BMPs called retention ponds and vegetative swales indicated in Figures 8 and 9 have been recommended as the BMP for reducing Runoff Nonpoint Source (NPS) pollution (Li and Kuo, 2021). Minimizing the total cost of these BMPs is another goal that has to be met.

2.2.1. Retention Pond

Retention ponds are storm water control structures that help to retain the water and treat contaminated storm runoff. Retention ponds remove pollutants and should be surrounded by natural vegetation to improve sustainability and the overall view of the basin. Water is sent to the pool using a network of underground pipes and released through outlets to maintain the desired water level. The biggest advantage of using a retention pond is the simplicity of placement, improving water quality and creating new habitats.

Fig. 8. Implemented retention pond (Wanielista and Academy, 2007)

2.2.2. Vegetative Swale

Vegetated swales are shallow, broad channels designed to reduce runoff volume, improve infiltration and filter contaminants and sediments during runoff flow. Vegetated swales are an excellent ecological alternative to conventional curb and stream conveyance systems, while supplying pretreated and semi- distributed flows. Swales are often densely vegetated and include a variety of early-maturing, resistant and native plants with great potential of pollution reduction. The mechanism of a swale for reducing the pollutant contains vegetative sedimentary filtering and subsoil matrix filtering or infiltration into the underlying soils (Pennsylvania Department of Environmental Protection, Bureau of Watershed Management, 2006).

With a two-year return period precipitation, the original model is run. The build-up and wash-off coefficients are improved by comparing measured TSS amount with SWMM obtained results. The build-up and wash-off coefficients are confirmed by area modeling with the help of precipitation data with a return period of five years. The results are shown in Table 2.

In Table 2, C_1: is the maximum possible build-up (mass per unit of area or curb length). c_2: is rate constant of build-up function (1/day) in exponential function and c: represents the wash-off pollutant concentration in mass per liter in event mean concentration function. A similar method is performed to modify the Manning coefficient using simulated runoff values and observational data. The results are shown in Table 3. Finally, the model calibrated by obtained coefficients.

Table 2. Initial and modified build-up and wash-off coefficients after model calibration

Return period (years)		2		5		Average amount of calibration
Data type	**Land use**	**Initial**	**Calibrated**	**Initial**	**Calibrated**	
C_1 for Build-up exponential function (kg/m curb)	High dense residual	0.003	0.003	0.003	0.003	0.003
	Medium dense residual	0.003	0.002	0.003	0.003	0.0025
	Low dense residual	0.003	0.001	0.003	0.003	0.002
	Commercial and industrial	0.015	0.034	0.015	0.05	0.042
	Green space	0.08	0.08	0.08	0.08	0.08
c_2 For Build-up exponential function (1/day)	Residual, commercial and industrial	0.8	0.8	0.8	0.8	0.8
	Green space	0.1	0.1	0.1	0.1	0.1
c For wash-off event mean concentration function (kg/m curb)	High dense residual	200	180	200	250	210
	Medium dense residual	200	180	200	250	210
	Low dense residual	200	180	200	250	210
	Commercial and industrial	300	250	300	300	275
	Green space	65	65	65	100	83

Table 3. Initial and modified manning's coefficients after model calibration

Return period (years)		2		5		Average amount of calibration
Parameter	**Member**	**Initial**	**Calibrated**	**Initial**	**Calibrated**	
Manning's coefficient	conduits	0.025	0.025	0.025	0.035	0.03

Fig. 9. Implemented vegetative swale (Pennsylvania Department of Environmental Protection Bureau of Watershed Management, 2006)

2.3. Application of Optimization Algorithm

The NSGA-II optimization algorithm is used to optimize the three objective functions according to Eqs. (3) to (5).

$$Ob_1 = min(\sum_{i=1}^{127} R_i) \quad (3)$$

$$Ob_2 = min(\sum_{i=1}^{127}\sum_{j=1}^{2} Co_{ij}) \quad (4)$$

$$Ob_3 = min(\sum_{i=1}^{127} Po_i) \quad (5)$$

where R_i: is the runoff volume in ith sub-catchment. i and j: are the number of sub-catchments and BMP's type, respectively. Co_{ij}: represents construction and maintenance cost of the jth BMP in the ith sub-catchment and Po_i: denotes concentration of pollution in ith sub-catchment.

Based on the experimental studies of Bayou Land RC&D and Louisiana Public Health Institute (2010), the cost of manufacturing and maintenance of BMPs has been estimated employing Eqs. (6) to (10).

$$Co = RC_c + RC_m + VC_c + VC_m \quad (6)$$

$$VC_c = (0.25 - 0.5)A_i \quad (7)$$

$$VC_m = (0.25 - 0.5)(0.05 - 0.07)A_i \quad (8)$$

$$RC_c = 307.76V^{0.71} \quad (9)$$

$$RC_m = 307.76(0.03 - 0.06)V^{0.71} \quad (10)$$

Where VC_c and VC_m: are the construction or investment cost of vegetative swale and cost of maintenance for vegetative swale in USD, respectively. RC_C and RC_m: describe construction or investment cost of retention pond and cost of maintenance for retention pond in USD, respectively. V: is the retention pond volume in m^3 and A_i: is the vegetative swale area in m^2.

MATLAB is employed for coding and communication between DLL of SWMM and the code containing optimizer algorithm. Subsequently, the number of sub-catchments in which BMPs should be constructed, the type and the optimal area of each one, are derived in the form of results. In the next step, according to the selection operators that are used in the algorithm (roulette wheel, tournament and random), the results of using each operator in selecting the population of each generation are compared with each other. Finally, the best selection operator is determined according to the calculated quantitative and qualitative runoff values. Also, the best pressure of the selection operator in the roulette wheel and the best size of the tournament selection operator are selected, which leads to the optimal solutions.

2.4. Decision Variables

The first variable is a binary variable which its upper limit is the number of sub-catchments that is 127 in this study. It determines the chance of a sub-catchment being selected as a BMP construction site. The second variable considers whether a BMP is randomly selected within the sub-catchment. This variable is in form of 0 and 1. The third variable specifies the allowable range of BMP area for construction, which is considered to be between one and five percent. This value is selected according to the conditions and restrictions of the region and can be changed in the code. The corresponding code is developed with three types of selection operators that allow the user to select one of them at the beginning of the program execution. These operators are roulette wheel, tournament and random selection that are used in the algorithm. In roulette wheel, population members are ranked based on their fitness function. Population members with larger fitness functions have a better chance of being selected as parents in the crossover and mutation phases. The fitness function is described in Eq. (10) (Chetan and Nitesh, 2021).The flowchart on how to apply the roulette wheel selection operator code in MATLAB is shown in Figure 10.

$$P(y_i) = \frac{p(y_i)}{\sum_{i=1}^{N} p(y_i)} \quad (11)$$

where N: is the number of population in the selection pool. y_i: is the population i. p(y_i): is the value of objective function for population i and P(y_i): represents the fitness value for population i .

In Figure 10, parameter β: is the selection operator pressure. This parameter must be selected in such a way that the best answer is obtained according to the objective functions. N_{pop}: is the number of population which is selected. $pop(y)$: is the yth member of the population and cost(1) is the value of objective function for first member of the population. Last equation in Figure 10 is described in Eq. (11). The flowchart of the tournament selection operator code is shown in Figure 11.

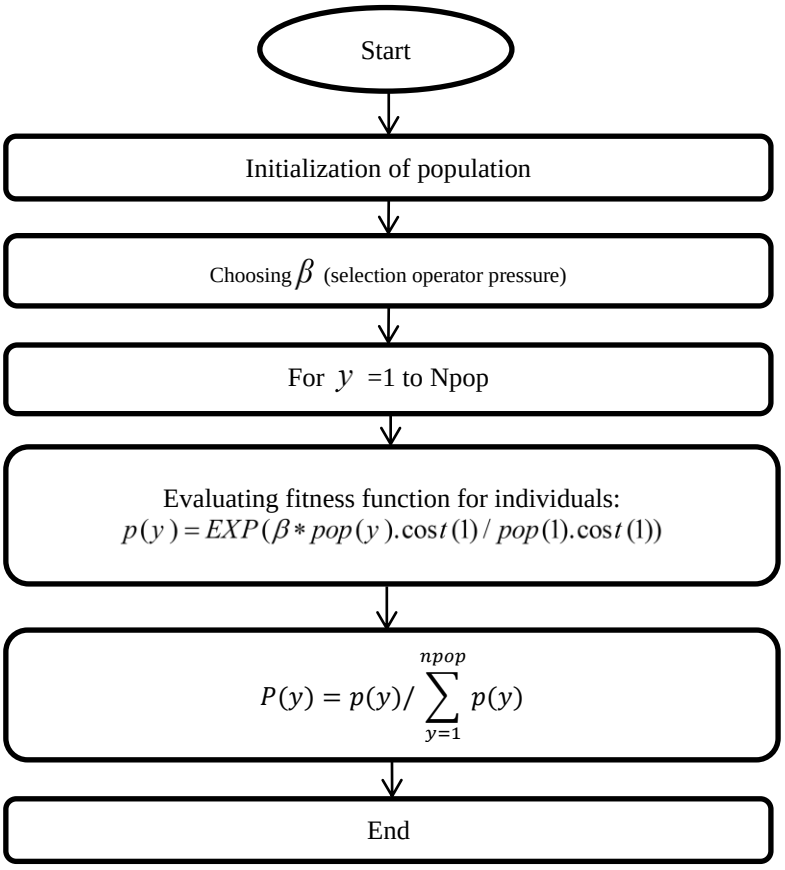

Fig. 10. Employing the roulette wheel selection operator

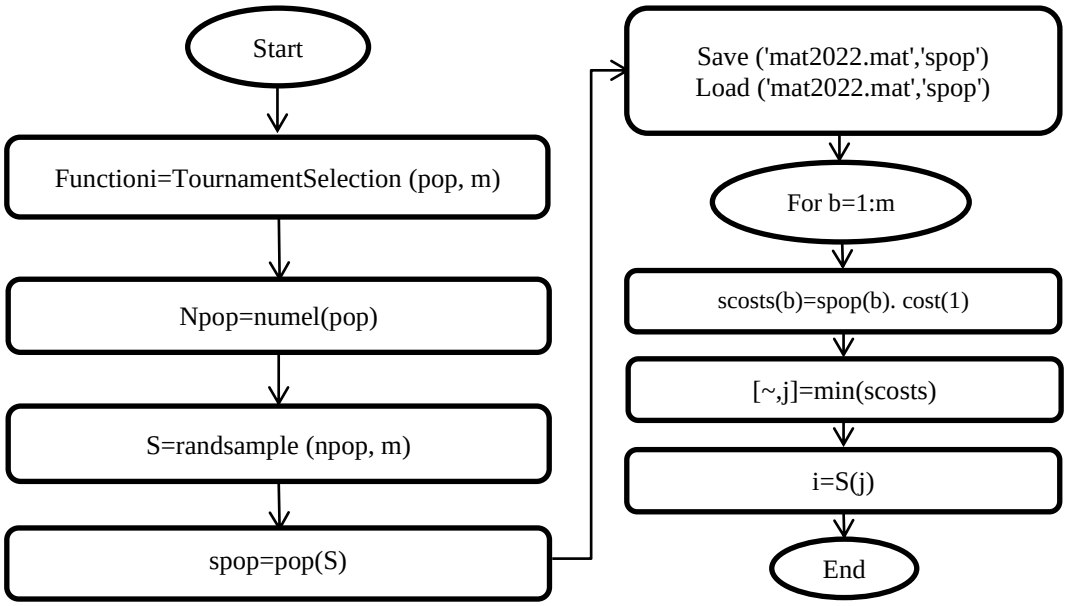

Fig. 11. Employing tournament selection operator

In Figure 11 for the tournament selection operator, m: is the tournament size. It should also be selected in such a way that the optimal solutions are determined according to the value of the objective functions. S: is a random selection of *m* from the selected population (npop). spop: is the population of the selected set S and 'mat2022.mat': represents the matrix related to the population S, which is first formed and then loaded to accommodate the members. In Figure 11, the optimal m produces the minimum value of 'scosts' and 'scosts(b)' is the product of each member of the matrix, 'spop(b)', multiplied by the value of the objective function for the first member of population (cost(1)). Finally, S(j): is the selected population of the tournament operator function. Ranking of answers is done by comparing the values of the objective functions in each iteration. The higher number of iterations and selected population leads to more accurate and convergent optimization results. In NSGA-II, the selection operator is used before using crossover and mutation operators (Deb et al., 2002). The selection operator is employed to determine the population of participants in the next steps, which are known as parents in the algorithm. The combination of simulation and optimization for the study area has been done using coding method in MATLAB and NSGA-II algorithm. The population size in the algorithm is 50 and the crossover percentage is 5. In order to obtain results to compare the performance of the selection operators, the maximum number of BMPs is considered as 6 and their maximum construction cost is considered 1.5 million USD in the code. Maximum area occupancy level of 5 percent for each sub-catchment is considered. In order to apply these restrictions, the optimization code works almost as a software and receives the mentioned information from the user as inputs at the beginning of the program execution. It is worth mentioning that this program has been prepared in such a way that it has the ability to call any type of INP file, which is the suffix of the urban runoff modeling file in SWMM and can be applied to any other areas. This is a significant innovation and advantage over other previous studies. Each of the input information (number of population, crossover percent, number of iteration, maximum number of LIDs that can be built, available budget and maximum percentage of allowable occupied area of each sub-catchment to construct BMPs) can be changed. This information can be adjusted depending on the urban architecture plan, municipal permissions, required accuracy and available budget. Subsequently, 'β' and 'm' are changed alternately, and the

results of the NSGA-II performance are compared with each other in the form of the objective function values, and the best 'β' and 'm' are selected.

3. Results and Discussions

The selection operator pressure in the roulette wheel and the selection size in the tournament operator are changed from 1 to 10, and the results have been obtained. Tables 4 and 5 show the results of the objective functions obtained by changing the parameter 'β' in the roulette wheel operator and 'm' in the tournament operator, respectively. In order to show the efficiency of using the selection operators compared to the random selection of the population participating in the crossover, the program has been executed once using the random selection operator. The results are shown in Table 6. For each selection operator pressure change (1 to 10), the values of the objective functions have been calculated using a three-objective genetic optimization algorithm. Runoff volume, pollutant amount and BMPs construction and maintenance costs are three objective function values, which are calculated in each program execution. This study is a pioneer in obtaining the best operator pressure selection and tournament size in multi-objective optimization of urban runoff. The numerical range obtained for the runoff volume is between 14781.8 and 14868.9 m^3 using the roulette wheel selection operator. This value varies between 14839.2 and 14873.4 if the tournament selection operator is used. The pollution range is also obtained between 2271.1 and 2291.05 kg for using the roulette wheel selection operator While, this value is between 2263.57 and 2290.9 kg for using the tournament selection operator. Finally, BMPs construction and maintenance costs for each selection are derived, which is varied from 133207 and 1630000 USD for roulette wheel and 162807 and 1008260 USD for tournament operator application. In the random selection operator, the optimal values of runoff volume, pollution and total BMPs costs are 14839.2 m^3, 2274.99 kg and 287702 USD, respectively.

Table 4. Optimization results employing of roulette wheel selection

Selection operator pressure (β)	Objective functions value		
	Runoff volume (m^3)	Pollutant (kg)	Cost (USD)
1	14867.1	2280.45	734200
2	14839.2	2274.99	287702
3	14868.9	2271.1	133207
4	14868.9	2279.73	1630000
5	14868.9	2290.66	1322425
6	14868.9	2281.28	1292460
7	14781.8	2284	1301470
8	14839.2	2274.99	287702
9	14868.9	2271.1	133207
10	14868.9	2291.05	269424

Table 5. Optimization results by use of tournament selection

Tournament size (m)	Objective functions value		
	Runoff volume (m^3)	Pollutant (kg)	Cost (dollar)
1	14868.9	2270.47	835972
2	14873.4	2276.79	530899
3	14868.9	2273.82	261919
4	14868.9	2283.22	353534
5	14839.2	2274.99	287702
6	14868.9	2271.71	652823
7	14868.9	2263.57	1008260
8	14868.9	2290.9	170596
9	14868.9	2280.66	162807
10	14868.9	2263.57	1008260

Table 6. Optimization results by use of random selection

Objective functions value		
Runoff volume (m^3)	**Pollutant (kg)**	**Cost (USD)**
14839.2	2274.99	287702

According to the results obtained from the tables, runoff values versus the values of parameters 'β' and 'm' for both selection operators are shown simultaneously in Figure 12. The minimum runoff value created in all sub-catchments is obtained for the roulette wheel selection operator in the amount of 'β' equal to seven hence the lowest amount of surface runoff in the tournament selection operator is obtained in the amount of 'm' equal to five.

A similar procedure is followed to represent the TSS pollution values of runoff in exchange for the quantities of 'β' and 'm'. The graph is indicated in Figure 13. Minimum value of TSS obtained from using the roulette wheel selection operator in 'β' equal to 3 and 9. For the tournament selection operator, this minimum is achieved at 'm' equal to 7 and 10.

Similarly, the minimum total costs of BMPs for each described parameters can be seen in Figures 14 and 15. Three and nine as selection operator pressures give the lowest construction and maintenance costs, while size nine in tournament selection presents the lowest costs.

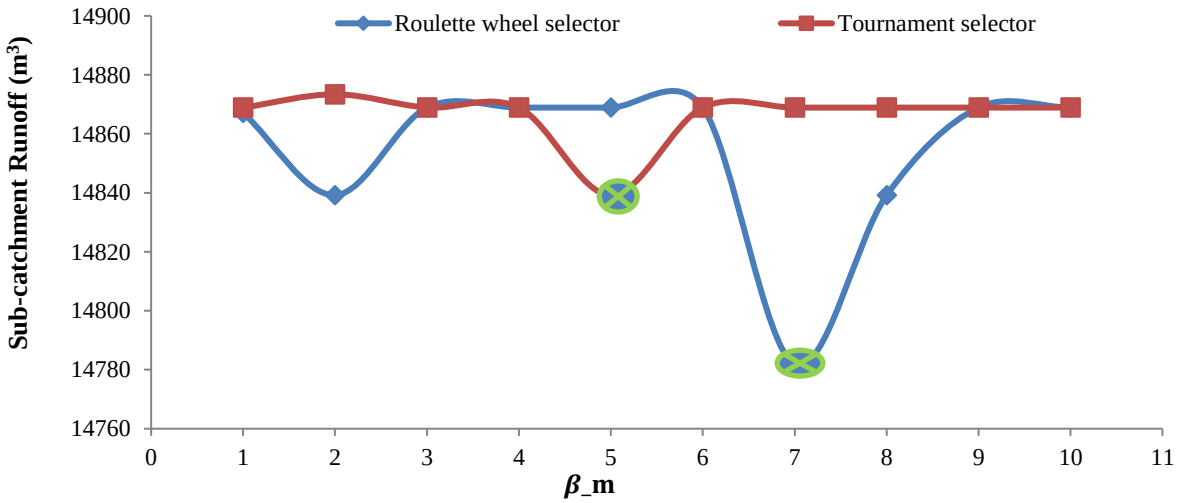

Fig. 12. Optimum runoff quantity derived by using different amounts of selection pressure and size in roulette wheel and tournament

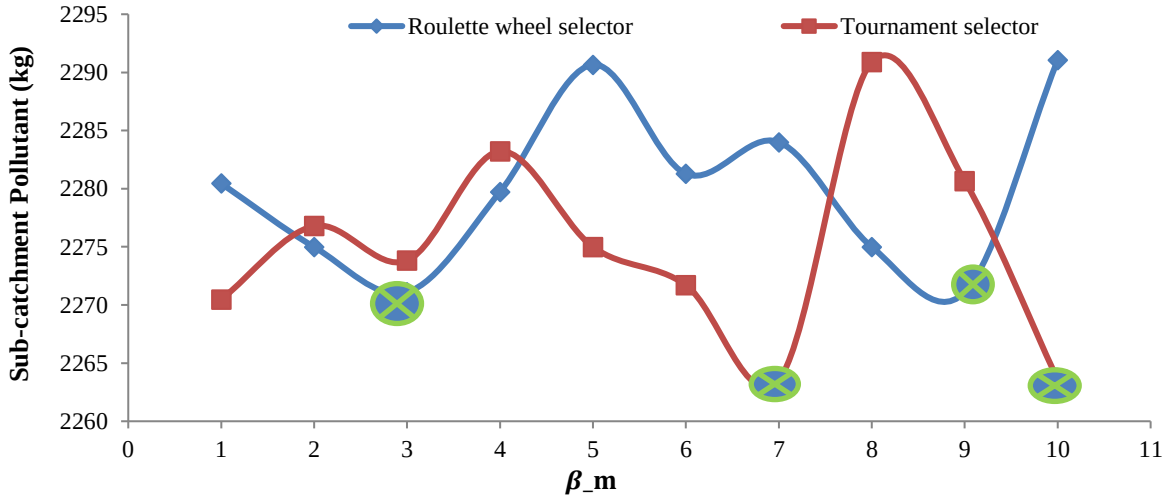

Fig. 13. Optimum pollution quantity derived by using different amounts of selection pressure and size in roulette wheel and tournament

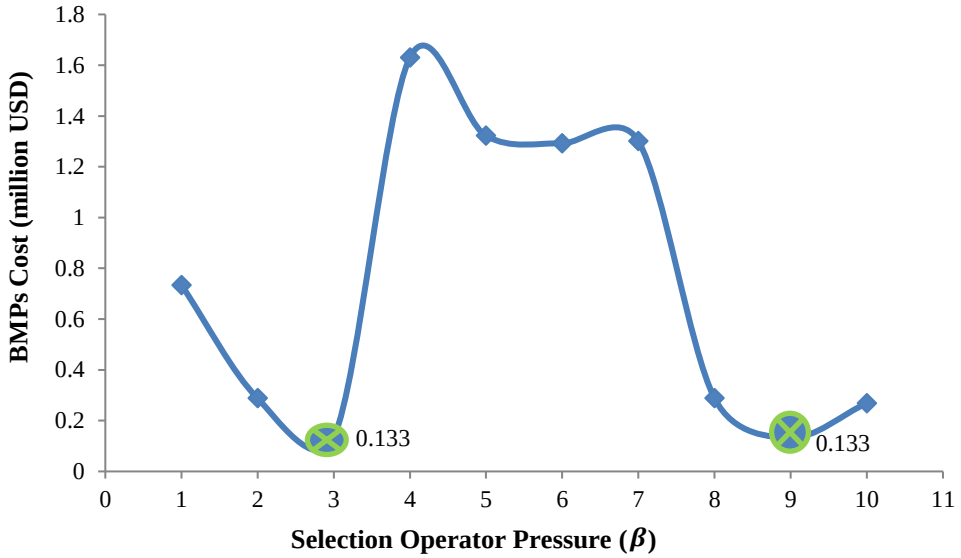

Fig. 14. Optimum cost of BMPs using different amounts of selection pressure in roulette wheel operator

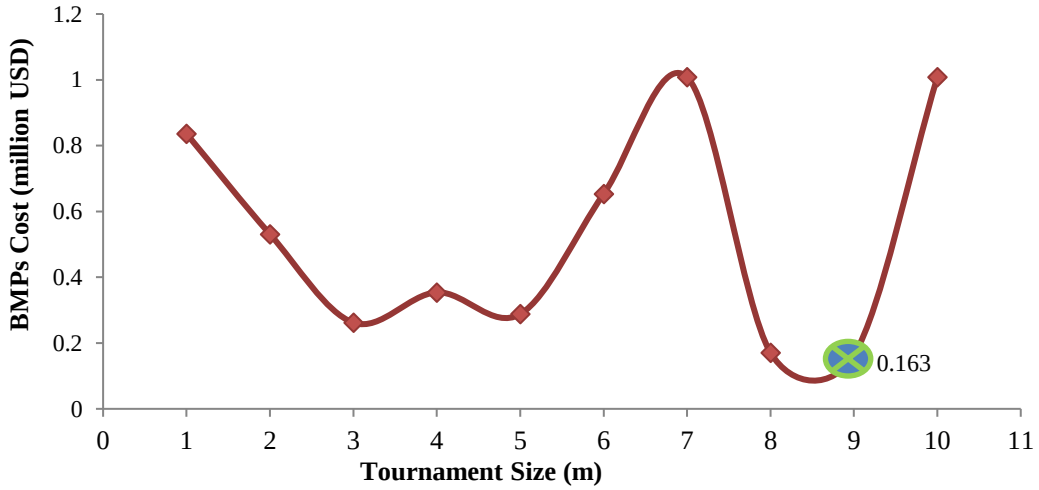

Fig. 15. Optimum cost of BMPs using different amounts of tournament size

According to the obtained results, it can be seen that the difference in the amount of runoff volume in the study area using the roulette wheel is 87.1 m^3 in the worst and best alternatives. This difference in runoff volume is 34.2 m^3 if the tournament selection operator is used. In a similar comparison, it can be seen that the difference between the maximum and minimum TSS pollution values using roulette wheel operator is approximately 20 kg, while this value is about 28 kg for the tournament operator. It is easy to see that these values are small and indicate that the selected options do not have much effect on the amount of runoff volume and pollution objective functions. But the difference in the values of the third objective function, which is the total cost of BMPs, is enormous. These values are 1496793 and 845453 USD, respectively, in case of using roulette wheel and tournament operators. Therefore, due to this large difference, the cost function can be the basis for making decision.

Due to the fact that the selection operator pressure with the value of three is the most effective choice in providing the optimal solution of the objective functions, multi-objective optimization in the study area is performed using this selection operator pressure (three). NSGA-II with roulette wheel operator is implemented in MATLAB to locate BMPs. Three sub-catchments are assumed to locate each type of BMPs as the maximum allowable

number and since two types of BMPs are used in this research, six sub-catchments are totally considered as the maximum number that can be used to place all two types of BMPs at the same time. The population size is selected as 50 and number of iteration is 100 that according to required accuracy they can be varied. Finally, the program is executed by defined characteristics.

The result that submit Pareto front is shown in Table 7 where the first eight populations have been ranked. The values of three objective functions are indicated in the first column in Table 7. The optimal area of BMPs (A_1 to A_6) and volume of each BMP located in the selected sub-catchment are also presented in columns two and three, respectively. It should be mentioned that in each row, first three optimum areas in bracket, are related to retention ponds and the other three values are related to vegetative swales. Subsequently, the number of optimum volumes in column three is equal to the number of retention ponds. The number, that each population is dominated, is known as dominated count. Besides, the ranking of selected BMPs construction locations in satisfying the objective functions is determined in rank column. When the solutions have the same rank the greater crowding distance represents better solution which is shown in last column.

The best selection of sub-catchments which derives optimum objective functions in each rank according to the Table 7 is shown in Table 8. In Table 8, the best selected sub-catchments number, for constructing each type of BMPs have been shown. These data correspond to the areas obtained in the second column of Table 7.

Table 7. Optimum results of objective functions by running the code in the studied region (Rafsanjan)

Objective functions value			**Optimum area for BMPs A_1 to $A_6(m^2)$**	**Optimum retention ponds volume (m^3)**	**Dominated count**	**Rank**	**Crowding distance**
Runoff (m^3)	**Pollutant (kg)**	**Cost (USD)**					
14869	2271	133207	[2090,1212,0,8453,7420,0]	[1463,848]	0	1	Inf
14794	2295	185361	[0,6521,0,0,19627,15436]	[4565]	0	1	9.5878×10^{-4}
14899	2309	161679	[0,0,5941,10726,0,0]	[4159]	0	1	5.4858×10^{-4}
14899	2313	188371	[7021,0,0,7198,16721,0]	[4915]	0	1	6.7807×10^{-5}
14899	2302	189706	[2521,0,3020,7169,0,8541]	[1765,2114]	0	1	8.2461×10^{-6}
14897	2313	199234	[0,4827,1524,0,6272,3668]	[3379,1067]	0	1	5.2536×10^{-6}
14897	2311	216266	[8125,0,0,21430,7940,10834]	[5688]	0	1	7.5736×10^{-7}
14899	2271	476545	[8050,12202,0,19751,16513, 6950]	[5635,8541]	0	1	0

Table 8. selected sub-catchments for optimum solutions

Sub-catchment number for locating BMPs					
Retention ponds			**Vegetative swales**		
88	124	-	11	62	-
-	123	-	-	127	86
-	-	112	66	-	-
88	-	-	11	62	-
103	-	92	96	-	86
-	20	12	-	41	19
113	-	-	119	41	127
61	56	-	108	56	9

The first row of results in Table 8 shows that two sub-catchments with numbers 88, 124 have been used for the construction of the retention ponds and sub-catchments 11, 62 have been used for the construction of the vegetative swales, respectively. These sub-catchments are the results of multi-objective optimization (NSGA-II), for locating BMPs. Comparing Tables 4 and 7, shows that the objective functions in the row corresponding to $\beta = 3$, in Table 4, is derived from the first row of Table 7, which is the best answer. This process is performed sequentially for each type of the selected operators ($'\beta'$,'m'), from 1 to 10 separately. The results are shown in Tables 4 and 5. The optimized areas of the selected BMPs are 2090, 1212, 8453 and 7420 m^2. The first two values belong to retention ponds and the other values relate to vegetative swales. The optimized volume of retention ponds are 1463 and 848 cubic meters. The wash-off, build-up and manning coefficients are calibrated but the physical characteristics of conduits like shape, max depth, length, roughness, inlet and outlet offset and invert elevation of the nodes are associated with some uncertainty in few parts of the city. Obviously the model is executed in SWMM by these input data. The other uncertainties incorporated in this study include curb length and sub-catchments specifications like permeability, slope and width.

4. Conclusions

The results of this paper indicated that the optimal choice of 'β'and 'm' in the roulette wheel and tournament selection operators had a significant effect on the construction costs of BMPs in the best selected alternatives. Therefore, construction cost can be used as a main decision criterion according to the values of the other two objective functions. However, it should be noted that in this study, due to show the ability of define limitations in the designed program, the budget and the maximum number of BMP types and the maximum occupancy of each sub-catchments were predefined and the population participating in the optimization algorithm process was determined. By increasing the values of each program inputs, the runoff volume and pollution could be reduced and the best sub-catchments for the construction of BMPs and their area could be obtained. Finally, according to the values of all three objective functions and the maximum effect of the selection operator pressure on each one, it can be concluded that the best 'β' in the roulette wheel operator is 3 or 9, which gives almost similar results. For the tournament operator, considering earlier given description, the best 'm' is 9. This study was conducted to design a program to be used in any desired region and any SWMM input file. The values of 'β' and 'm' are applicable for other similar studies in order to obtain optimal solutions. When optimal values of selection operator pressure and selection size are used, both roulette wheel and tournament selectors give better results than the random operator. The results of this study can be generalized to other similar studies that may be performed in the future.

5. References

Abou Rjeily, Y., Abbas, O., Sadek, M., Shahrour, I. and Hage Chehade, F. (2018). "Model predictive control for optimising the operation of urban drainage systems", *Journal of Hydrology*, 566, 558-565, https://doi.org/10.1016/j.jhydrol.2018.09.044.

Alaneme, G.U., Dimonyeka, M.U., Ezeokpube, G.C., Uzoma, I.I. and Udousoro, I.M. (2021). "Failure assessment of dysfunctional flexible pavement drainage facility using fuzzy analytical hierarchical process", *Innovative Infrastructure Solutions*, 6(2), 1-18, https://doi.org/10.1007/s41062-021-00487-z.

Bayou Land RC&D and Louisiana Public Health Institute. (2010). *Stormwater BMP guidance tool*, DEQ, Lousiana.

Bell, V.A. and Moore, R.J. (2000). "The sensitivity of catchment runoff models to rainfall data at different spatial scales", *Hydrology and Earth System Sciences*, 4(4), 653-667, https://doi.org/10.5194/hess-4-653-2000.

Binesh, N., Niksokhan, M.H., Sarang, A. and Rauch, W. (2019). "Improving resilience of urban

drainage system in adaptation to climate change (Case study: Northern Tehran, Iran)", *16th International Environmental Specialty Conference 2018, Held as Part of the Canadian Society for Civil Engineering Annual Conference 2018*, 16, 87-97.

Chetan, J.S. and Nitesh, M.S. (2021). "Genetic algorithm for test suite optimization: An experimental investigation of different selection methods", *Turkish Journal of Computer and Mathematics Education (TURCOMAT)*, 12(3), 3778-3787, https://doi.org/10.17762/turcomat.v12i3.1661.

Chudasama, C., Shah, S.M. and Panchal, M. (2011). "Comparison of parents selection methods of Genetic Algorithm for TSP", *International Conference on Computer Communication and Networks CSI- COMNET*, 1, 102-105.

Dastorani, M.T., Mahjoobi, J., Talebi, A. and Fakhar, F. (2018). "Application of machine learning approaches in rainfall-runoff modeling (Case study: Zayandeh Rood basin in Iran)", *Civil Engineering Infrastructures Journal*,1(2), 293-310, https://doi.org/10.7508/ceij.2018.02.004.

Deb, K., Pratap, A., Agarwal, S. and Meyarivan, T. (2002). "A fast and elitist multiobjective genetic algorithm: NSGA-II", *IEEE Transactions on Evolutionary Computation*, 6(2), 182-197, https://doi.org/10.1109/4235.996017.

Gad, M., sobeih, M.F., Rashwan, I.M.H. and Helal, E. (2020). "Hydraulic features of flow through grassed canal", *Innovative Infrastructure Solutions*, 5(2), 1-14, https://doi.org/10.1007/s41062-020-00308-9.

Hai, D.M. (2020). "Optimal planning of low-impact development for TSS Control in the upper area of the Cau Bay River basin, Vietnam", *Water (Switzerland)*, 12(2), 1-15, https://doi.org/10.3390/w12020533.

Hakimi, H., Ahmadi, J., Vakilian, A., Jamalizadeh, A., Kamyab, Z., Mehran, M., Malekzadeh, R., Poustchi, H., Eghtesad, S., Sardari, F., Soleimani, M., Khademalhosseini, M., Abolghasemi, M., Mohammadi, M., Sadeghi, T., Ayoobi, F., Abbasi, M., Mohamadi, M., Jalali, Z., Shamsizadeh, A. and Esmaeili-Nadimi, A. (2021). "The profile of Rafsanjan cohort study", *European Journal of Epidemiology*, 36(2), 243-252, https://doi.org/10.1007/s10654-020-00668-7.

Höschel, K. and Lakshminarayanan, V. (2019). "Genetic algorithms for lens design: A review", *Journal of Optics (India)*, 48(1), 134-144, https://doi.org/10.1007/s12596-018-0497-3.

Huang, S., Liu, P., Zhang, H. and DIng, Z. (2021). "Research on SWMM runoff control index decomposition based on constraint optimization method", *3rd International Symposium on Architecture Research Frontiers and Ecological Environment (ARFEE 2020)*, France, https://doi.org/10.1051/e3sconf/202123704008.

Jamshidi, S., Imani, S. and Delavar, M. (2020). "Impact assessment of Best Management Practices (BMPs) on the water footprint of agricultural productions", *International Journal of Environmental Research*, 14(6), 641-652, https://doi.org/10.1007/s41742-020-00285-y.

Katoch, S., Chauhan, S.S. and Kumar, V. (2021). "A review on genetic algorithm: Past, present, and future", *Multimedia Tools and Applications*, 80, 8091-8126, https://doi.org/10.1007/s11042-020-10139-6.

Kumar, A., Kumar, D. and Jarial, S. K. (2016). "A comparative analysis of selection schemes in the artificial bee colony algorithm" ,*Computacion y Sistemas*, 20(1), 55-66, https://doi.org/10.13053/cys-20-1-2228.

Li, R. and Kuo, Y.M. (2021). "Effects of shallow water table depth on vegetative filter strips retarding transport of nonpoint source pollution in controlled flume experiments", *International Journal of Environmental Research*, 15(1), 163-175, https://doi.org/10.1007/s41742-020-00305-x.

Martínez-Solano, F.J., Iglesias-Rey, P.L., Saldarriaga, J.G. and Vallejo, D. (2016). "Creation of an SWMM toolkit for its application in urban drainage networks optimization", *Water (Switzerland)*, 8(6), 1-16, https://doi.org/10.3390/w8060259.

Moosavian, N. and Jaefarzadeh, M.R. (2015). "Particle Swarm Optimization for hydraulic analysis of water distribution systems", *Civil Engineering Infrastructures Journal*, 48(1), 9-22, https://doi.org/10.7508/ceij.2015.01.002.

Ochoa-Barragán, R., Nápoles-Rivera, F. and Ponce-Ortega, J.M. (2021). "Optimal and fair distribution of water under water scarcity scenarios at a macroscopic level", *International Journal of Environmental Research*, 15(1), 57-77, https://doi.org/10.1007/s41742-020-00297-8.

Pennsylvania Department of Environmental Protection Bureau of Watershed Management. (2006). *PENNSYLVANIA stormwater BMP manual*, *Water*, Pennsylvania.

Rathnayake, U. (2015). "Migrating storms and optimal control of urban sewer networks", *Hydrology*, 2(4), 230-241, https://doi.org/10.3390/hydrology2040230.

Rossman, L. (2017). *Storm water management model reference manual, Volume II*: *Hydraulics*, Environmental Protection Agency, Cincinnati.

Sharma, P., Wadhwa, A. and Komal, K. (2014). "Analysis of selection schemes for solving an optimization problem in Genetic Algorithm", *International Journal of Computer Applications*, 93(11), 1-3, https://doi.org/10.5120/16256-5714.

Shukla, A., Pandey, H.M. and Mehrotra, D. (2015).

"Comparative review of selection techniques in genetic algorithm", *1st International Conference on Futuristic Trends in Computational Analysis and Knowledge Management (ABLAZE-2015)*, Noida, https://doi.org/10.1109/ABLAZE.2015.7154916

Siriwardene, N.R. and Perera, B.J.C. (2006). "Selection of genetic algorithm operators for urban drainage model parameter optimisation", *Mathematical and Computer Modelling*, 44(5-6), 415-429, https://doi.org/10.1016/j.mcm.2006.01.002.

Swathi, V., Srinivasa Raju, K., Murari R.R.V. and Sai Veena, S. (2019). "Automatic calibration of SWMM using NSGA-III and the effects of delineation scale on an urban catchment", *Journal of Hydroinformatics*, 21(5), 781-797, https://doi.org/10.2166/hydro.2019.033.

Taban, M.H., Hajiazizi, M. and Ghobadian, R. (2021). "Prediction of Q-value by multi-variable regression and novel Genetic Algorithm based on the most influential parameters", *Civil Engineering Infrastructures Journal*, 54(2), 267-280, https://doi.org/10.22059/CEIJ.2020.295339.1647.

Tayfur, G. (2017). "Modern optimization methods in water resources planning, engineering and management", *Water Resources Management*, 31(10), 3205-3233, https://doi.org/10.1007/s11269-017-1694-6.

Wang, Q., Zhou, Q., Lei, X. and Savić, D.A. (2018). "Comparison of multiobjective optimization methods applied to urban drainage adaptation problems", *Journal of Water Resources Planning and Management*, 144(11), 04018070, https://doi.org/10.1061/(ASCE)WR.1943-5452.0000996.

Wanielista, M. (2007). *Regional stormwater irrigation facilities*, Stormwater Management Academy University of Central Florida Orlando, Florida.

Xavier, C.R., Dos Santos, E.P., Da Fonseca Vieira, V. and Dos Santos, R.W. (2013). "Genetic algorithm for the history matching problem", *Procedia Computer Science*, 18, 946-955, https://doi.org/10.1016/j.procs.2013.05.260.

Xiong, J., Chen, B., He, Z., Guan, W. and Chen, Y. (2021). "Optimal design of community shuttles with an adaptive-operator-selection-based genetic algorithm", *Transportation Research Part C: Emerging Technologies*, 126, 1-37, https://doi.org/10.1016/j.trc.2021.103109.

Civil Engineering Infrastructures Journal 2023, 56(2): 277-299
DOI: 10.22059/CEIJ.2022.342784.1841

RESEARCH PAPER

Performance Evaluation of Terrazyme as Soil Stabilizer

Aswar, D.S.[1*], Bajad, M.N.[2] and Ambadkar, S.D.[3]

[1] Ph.D. Candidate, Sinhgad College of Engineering, Pune, India.
[2] Professor, Sinhgad College of Engineering, Pune, India.
[3] Associate Professor, G.H. Raisoni University, Amravati, India.

Received: 09 May 2022; Revised: 17 Sep. 2022; Accepted: 22 Oct. 2022

ABSTRACT: Literature published TerraZyme stabilization case studies are analyzed rationally for evaluating the performance of TerraZyme as a stabilizer. As a measure of the degree of stabilization, the percentage variation in soil index and engineering properties induced by enzyme treatment for various soil types are investigated. The literature shows inconsistent enzyme stabilization results. The causes of the inconsistency in test results and factors affecting the effectivity of enzyme stabilization are elaborated. The effect of soil characteristics on the efficacy of enzyme stabilization is analyzed. The results of enzyme treatment on soil properties such as Atterberg limits and indices, optimum moisture content, maximum dry density, unconfined compressive strength and California bearing ratio, for various soil groups with different enzyme doses and conditions of curing are also studied. An attempt has been made to quantify the attribute variation of treated soils, establishing, the underlying reasons, for the effectivity of enzyme stabilization and its performance within and among various soil groups. The effect of enzymatic treatment on each soil group is also classified. The research emphasizes the necessity of an elaborate organized study on the enzyme and soil characterization, to have a better knowhow of the effectiveness of enzymatic stabilization.

Keywords: Degree of Stabilization, Enzymes Stabilizers, Soil Classification, Soil Stabilization, Terrazyme.

1. Introduction

For improvement in engineering properties, the soil is stabilized either by chemical, or mechanical treatment or by other non-traditional methods such as Enzyme treatment (Mekonnen et al., 2020).

The enzyme treatment minimizes the mechanical compacting efforts and results in higher soil density, shear strength and lower permeability (Taha et al., 2013). Compared to other conventional stabilizers, the enzymes are cost-efficient, environmentally sustainable and convenient to use. Conventional soil stabilizers like lime and cement lead to environmental pollution, with carbon emissions. Enzymes are also, energy-efficient as they can reduce the compacting efforts required for mechanical stabilization. As a biological system catalyst, enzymes check the reaction rate and lower the activation energy essential for the new product formation thus facilitating the conversion state (Scholen, 1995). The enzymes are more efficient compared to inorganic catalysts. They

* Corresponding author E-mail: aswar.scoe@gmail.com

expedite the reaction rate up to 106 to 1012 times. Enzymatic reactions are sensitive to temperature and act better at moderate temperatures (35^{o} C). The enzyme reactivity is adversely affected by high temperatures. Enzymes are also pH-sensitive and efficient at a pH around the value of 7 (Ryan and Norris, 2014).

TerraZyme is an electrochemical product with fermented vegetable extract, mainly consisting of nonionic surfactants and carbohydrates. It is reactive with soils with clay contents. As per the recommendations by Saini and Vaishnava (2015) the soil for effective TerraZyme stabilization should have a liquid limit of less than 30%, particle size passing 75 micron greater than 15%, clay content greater than 6%, pH between 4.5 to 9.5 and soil temperature greater than 15 °C,

The soil sample analysis summary (Nature Plus Inc., 2021) for the TerraZyme application consists of an enquiry into, the work type and soil test data. The soil data consists of results of sieve analysis, Atterberg limits (liquid limit WL, plastic limit PL), Plasticity Index (PI), compaction characteristics (Standard Proctor test), unsoaked California Bearing Ratio (CBR) value and soil pH. These are the assessment parameter for checking the soil suitability, enzyme dose requirements and effectivity of the proposed enzyme stabilization (Myint and Swe, 2014; Shaka and Shaka, 2016).

2. Literature Review

According to Tingle et al. (2007), stabilizing the performance of enzymes is soil-specific. Enzymes are suitable for the treatment of water affine, clayey soils with high plasticity and with organic content. According to Woll et al. (2008) in several field applications, the enzyme performance was adversely affected due to the deficiency of clay/fine content. The initial reaction of the enzyme with the organic matter in the soil forms a gel which after crystallization forms a bond with soil particles. Loss of moisture by evaporation is essential for the crystallization of gels.

Organic matter and clay content are crucial for the enzymatic reaction, bond formation and consequent stabilization. For an effective enzymatic reaction, the soil must have the necessary clay contents. According to Bergmann (2000), at least 2% clay/fine is essential for enzymatic stabilization, and 10% to 15% clay content to ensure good stabilization. Enzyme products are effective for soils having 18% to 30% clay fines, a plasticity index between 2% to 10%, and a liquid limit of up to 30% (North Dakota DOT, 2014). According to Kestler (2009), the soil should have a plasticity index greater than 8% and a minimum clay content of 10%. Effective stabilization is obtained for soils with, plasticity indexes between 8 and 35% and clay content between 12 and 24% (even up to 30% for a few enzymes). The degree of stabilization is high at a water content 2-3% lesser than the Optimum Moisture Content (O.M.C.).

Literature also mentioned of treated SC, SM-GM and SP-Soils with 0-2% clay content also recorded some improvements in soil properties. However, as observed by Shankar et al. (2009) enzymatic stabilization is inefficient for soils having high cohesionless content.

Bio-Enzyme stabilization with suitable doses improves the index and engineering properties of soils and reduces the compressibility of soil. The improvement in the properties may be due to the reaction of bio-enzyme with soil minerals and other chemically active constituents. Hence the stabilizing effect of bio-enzyme on soil should be tested in the laboratory before the field application (Guthrie et al., 2015).

Bio-enzyme stabilized soils show a considerable improvement in shear strength. Shukla et al. (2003) observed that bio-enzyme stabilization of different soils with variable clay content has witnessed little to high improvement in physical properties due to their variable degree of reactivity with bio-enzymes. For silty to

sandy soils, there was an appreciable improvement in CBR and UCS values. A study on the effect of the enzyme on lateritic soil using UCS, CBR, compaction and permeability showed medium improvement in the physical properties of lateritic soil. Whereas it was ineffective in improving the consistency limits. Lateritic soil (Wl and PI greater than 25% and 6%, respectively) with higher enzyme dosage (200 ml / 2 m^3 of soil) results in a 300% increase in CBR, a 450% increase in UCS and a 42% decrease in permeability for four weeks of curing. The enzyme is also ineffective for cohesionless soil. Venkatasubramanian and Dhinakaran (2011), tested three soils with Wl = 28%, 30%, 46% and PI 6%, 5% and 6%, respectively, stabilized with different enzyme dosages. The increase in UCS was 152 to 200% and CBR was 157 to 673%, respectively, after 4 weeks of curing. According to Isaac et al. (2003) the lateritic soil and clayey soil for a curing period of 8 weeks TerraZyme, has increased the CBR in the range of 136 to 1800 times the untreated soil value. Whereas the CBR increase was less significant about 700 percent silty soils and clayey-sandy soil

Rauch et al. (1993) analyzed the effects of ionic, enzyme, and polymer stabilizers on two high-plasticity natural clays and three clays with one of the predominant clay minerals either kaolinite, illite, or sodium montmorillonite. Overall, there was no marked improvement in Atterberg limits, density, shear strength and swell potential of soils, still, there were individual cases of improvement. It was also concluded that higher doses may produce improvements in soil properties. Tingle and Santoni (2003) observed that enzymes treated in two soils of low and high plasticity have shown no improvement in saturated and unsaturated UCS tests of the strength of either soil. UCS tests on residual soil with three enzymes by Khan and Taha (2015); however, did not observe any improvement. A CL was treated with three enzymes but no betterment was observed. Similar variable results were obtained with other proprietary bio-enzyme such as Permazyme, EarthZyme etc. According to Milburn and Parsons (2004), compaction test (water content at 1% less than the optimum) on the bio-enzyme Permazyme 11-X treated ML and SM soils (fines 88% and 30%, LL 30% and 20% and PI 7% and 3%, respectively) at manufacturer's recommended dosage, the dry density increases by only 4% and 1%, respectively or stiffness, wet-dry and leaching tests no improvement was recorded for 28 days of curing. However, freeze-thaw indicates a very small improvement. Stabilization was done by Brandon et al. (2010) using bio-enzyme (Permazyme) on six single sources and three blended soils. There was a decrease in PI for soil-1 and soil-2 and an increase of 44% for soil-6. There is no definite trend of improvement in the properties of treated soils. However, there is an increase of 6 to 64% in cohesion due to the agglomeration of the soil particles. Mgangira (2009) observed little or no improvement in PermaZyme 11-X and EarthZyme treated two native soils and three reference clays (illite, kaolinite and montmorillonite).

The laboratory test results are also affected by the duration and conditions of sample curing studied the effect of air-dry curing (drying) and desiccator curing on the properties of Terrazyme stabilized black cotton soil and red earth for various curing periods. Unsoaked CBR, UCS strength of both Terrazyme treated black cotton soil and red earth showed tremendous improvement with drying than laboratory desiccator curing. Free Swell Index for black cotton soil showed better improvement with drying. The air-dry curing (or drying) condition proved more efficient in treating both soils than the desiccator curing condition. However, Atterberg limits for both black cotton soil and red earth did not exhibit any difference in either drying or desiccator curing (Daigavane and Ansari, 2021; Vastrad et al., 2020; Sen and Singh, 2015).

The studies show varying improvements in soil properties from very small to

significant degrees which necessitate laboratory testing before actual field application. Mostly the details of enzyme composition are provided by the manufacturers. Since the enzymes are often reformulated; their product-specific testing must be conducted to check their suitability. On contrary, the enzyme stabilizers have no specific laboratory tests available to assess their on-site performance. Due to the unfamiliarity of the enzyme manufacturers with the design process, the significant benefits of the non-standard enzyme stabilizers have remained unexplored (Scholen, 1992).

All the literature-suggested parameters are included in the study to check the efficacy of TerraZyme stabilization for various soil groups. The research on TerraZyme stabilized soils has witnessed, dissimilar experimental and field performance. Hence, the research attempted to generalize the stabilizing effects or performance of the TerraZyme on different soils and checks soil suitability for stabilization (Indian Standards: 1498, 1970).

3. Methodology

The enzyme stabilizes act but, they can be effective under certain conducive circumstances only. It is therefore essential that the correct stabilizer and soil type for stabilization are chosen. The variation in a characteristic of soils needs systematic study to determine the enzyme's stabilization performance. At present, soil stabilization by enzymes is predominately based on empirical guidance from past experiences and is not much subjected to technical evolutions. The study on enzyme stabilization concluded that these products work but, they can be applied successfully only in certain conditions. It is therefore imperative that the correct stabilizer and material for stabilization.

The literature indicates that the random variable results of enzyme stabilization also it is uncertain how and under which conditions the enzymes work better. The published results from literature about both untreated and TerraZyme-stabilized soils are checked to evaluate the effectivity of TerraZyme treatment. The objectives of the study are:

- To check the characteristics of soils that effects enzyme-based soil stabilization.
- To investigate the changes in soil index and engineering properties induced by enzyme stabilization.
- Analysis of enzyme-treated soil data from the literature to study performance evaluation of enzyme performance with various soil types.
- To investigate enzyme dose requirements to stabilize the various soil types.

The improvement in index and engineering properties of enzyme-stabilized soil can be an evaluation parameter for checking the degree of stabilization achieved. The improvement in soil properties is examined to resolve the effect of enzyme doses, curing conditions, and the type of soil. The laboratory results of Atterberg limits and indices, compaction characteristics, CBR, and UCS have been analyzed based on variations in soil type, enzyme doses and curing duration. The percentage difference in these results either positive (% increase) or negative (% decrease) is analyzed.

An attempt has been made to quantify the attribute variation of treated soils, establish, the underlying reasons, and correlations and to categorized the treated soil behaviour as per the individual soil groups. The literature on enzyme stabilization data consists of lots of parametric variations concerning enzyme types, doses, curing duration and type. The study attempts to maintain the uniformity of these parameters to the extent possible. However, considering the large quantity of data, only the minimum and maximum parametric value of the parameter for soil, enzyme doses and duration of curing are analyzed and presented. The lower value indicates the minimum percentage variation

in the property over the untreated sample, whereas, a higher value indicates the maximum percentage variation in the property after stabilization.

Considering the variation in literature results, the aspects of factors affecting the results of laboratory enzyme stabilization such as the enzyme application rates, sample preparation, sample curing conditions, test procedure etc. are also investigated and discussed (Muguda and Nagaraj, 2019).

The bio-enzyme stabilization is certainly economical and more sustainable stabilization technique. Several case studies discussed the economic benefits of TerraZyme stabilization for the construction of low-cost rural roads, road base course and subgrade stabilization. The contents of the research paper emphasize mainly the evaluation of the enzyme's stabilization performance. Hence the economical aspect of enzyme stabilization is not elaborated on.

3.1. Characterization of Soils

The soil type greatly influences the effectiveness of enzyme stabilization. Hence for the basis of comparison, various soils are classified as per IS Classification System (ISCS) as shown in Figure 1.

For better characterization of soils, an attempt was made to assess the degree of expansion and severity for fine-grained soils based on Atterberg's limits, free swell index and the presence of clay and mineralogical contents based on literature studies. However, conclusive remarks could not be made due to the non-availability of uniform soil data. For some of the soils, these comparison parameters cannot be applied as values are not falling within the defined ranges. The reason may be the empirical nature of the test and the lack of standard procedures.

The percentage of clay/fines and the mineral contents influence the stabilization mechanism. The soils are also classified based on plasticity and free swell index to check their principal clay minerals as shown in Appendix. This has been used as a simple parameter to the degree of suitability of clayey soil for an enzyme treatment.

3.2. Laboratory Tests

Improvements in the properties of bio-enzyme stabilized soil may be due to the chemical reaction of soil constituents with bio-enzymes. One of the parameters to check the degree of chemical reaction of the enzyme with soil is to check changes in the microscopic characteristics of stabilized soils.

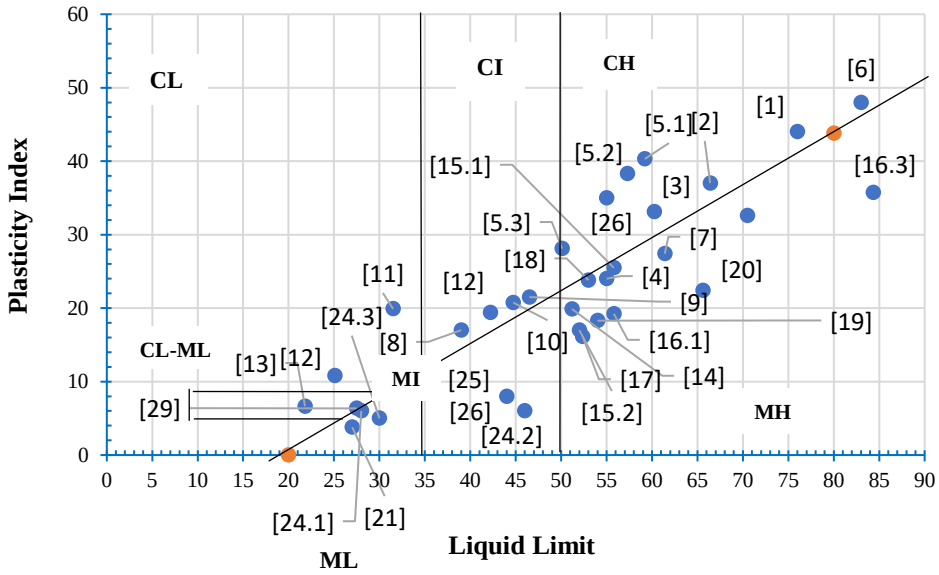

Fig. 1. Soil Classification for the soils included in the study

The changes in the microstructure of untreated and enzyme-treated soils with curing can be compared with advanced methods. (Indian Standard: 2720 (Parts 5,7,10,16), 1985). There are several methods suggested for checking the microstructural changes such as BET surface area analysis, Environmental Scanning Electron Microscopy (ESEM), X-Ray Diffraction (XRD) and X-Ray Fluorescence (XRF), Field Emission Scanning Electron Microscopy (FESEM), Scanning Electron Microscopy (SEM) (Zhang et al., 2013), etc. However, these micro-level observations seem to be too inconclusive to confirm the changes induced by enzymatic reactions with the curing. These changes are again variable with soil mineralogical contents.

Usually, the improvement in the index and engineering properties of stabilized soil is considered an evaluation parameter to check the degree of stabilization achieved. The consistency tests, proctor test, UCS, soaked/unsoaked CBR tests, Free Swell Index (FSI) test, swell pressure test, consolidation test, and permeability test may be carried out for evaluating the performance of stabilized soils. For the study, the result discussion is limited to the consistency test and the basic strength tests. These are the standard tests performed as per the procedure, material and equipment specifications defined by Indian Standards (IS). The section indicates the references and objectives of these tests.

- Index properties of the soil as per IS: 2720 (Part 5) (1985). The index properties such as liquid limit, and plastic limit are related to various properties of soil such as cohesion, and capillarity and also form the basis for soil classification and its specification as fill material.
- Compaction test as per IS: 2720 (Part 7) (1985). This test is used for determining the amount of water needed, for field compaction and as a measure of the degree of denseness that can be obtained at optimum moisture content. The water density relation obtained from the test can be used for better control of these tests of the field compaction.
- Unconfined Compressive Strength (UCS) test as per IS 2720 (Part 10) (1985). UCS test is used for the determination of compressive and shearing strength of clayey soils not to be subjected to lateral pressure in an undrained condition.
- California Bearing Ratio (CBR) test as per IS: 2720 (Part 16) (1985). The CBR value is an index measuring the soil strength based on the condition of the material during the testing. It can be correlated with important parameters like the modulus of subgrade reaction, modulus of resilience and plasticity index.

3.3. Analysis of Stabilization Results for Various Soil Groups

There are several mixed examples from literature where this laboratory testing shows highly beneficial or no substantial improvement in the properties of enzyme-stabilized soils. These results are analyzed for enzyme stabilization.

3.4. Analysis for CH-Soil

In general, the CH-soil are clay of high plasticity, with Montmorillonite as the dominant clay mineral and with high expansivity and swelling potential.

3.4.1. Analysis of Consistency Limits for CH-Soil

Table 1 shows the maximum % variation in Atterberg limits for CH-soils. For CH-soil 1 maximum percentage reduction in liquid limit is 14.47% for an enzyme dose of 200 ml / 2 m^3 of soil at the end of the 4^{th} week. CH-soil 1 shows a continuous decrease in plastic limit with an increase in enzyme doses and period of curing. For CH-soil 1 there is a maximum reduction in PL of 28.13% at an enzyme dose of 200 ml / 2 m^3 of soil at the end of the 4^{th} week. (CH-soil 1- WL(%) = 76, WP (%) = 32, PI (%) = 44, Ws(%) = 8, IS(%) = 68 clay content is 21.61%, Active, highly plastic, specific gravity G = 2.62)

Table 1. Maximum % variation in Atterberg limits for CH-soils

Soil		CH-soil 1		CH-soil 4		CH-soil 5	CH-soil 6		CH-soil 7	CH-soil 8
Doses 200 (ml/m^3)		2		1.5	1	6.6	13.2	6.6	6.6	1.5
% Variation (+ve increase, -ve decrease)	LL	-14.47, (4 weeks)		-	-	-	-	-	-	-7.78, (2 weeks)
	PL	-28.13, (4 weeks)		-	-	-	-	-	-	-8.16, (2 weeks)
	PI	11.36, (1 week)	-4.55, (4 weeks)	-24, (8 weeks)	-0.29, (0 weeks)	-20.60, (4 weeks)	-5.22, (4 weeks)	9.66, (4 weeks)	-30.6, (4 weeks)	-6.8, (1 week)
	Ws	12.5, (0 weeks)	50, (4 weeks)	-	-	-	-	-	-	-

CH-soil 1 shows an increase in shrinkage limit (Ws) value up to 50% for enzyme doses of 200 ml / 2.5 m^3 and 2 m^3 of soil. In general shrinkage limit (Ws) shows an increase with curing and moderate doses of enzyme treatment.

CH-soil 4 (W_L(%) = 55, WP(%) = 31, PI(%) = 24 clay content is 66.78%, clay of high plasticity, specific gravity G = 2.45) shows a reduction in PI values which further continue up to 24% at the end of 8th week of curing. CH-soil 7 (W_L(%) = 50.1, WP(%) = 22, PI(%) = 28.1, the clay content is 12.3%, sandy fat clay of high plasticity, active, specific gravity G = 2.73, FSI = 150) shows a maximum reduction of 30.60% in value of PI at the end of the 4th week for enzyme doses of 200 ml / 6.6 m^3 of soil. The CH-soil 4 and CH-soil 7 have comparable consistency limit values, however, the CH-soil 7 have shown a higher reduction in PI value over half the curing duration. The reason may be the higher specific gravity and lesser clay content for CH-soil 7.

All CH-soils show a reduction in plasticity index values with curing duration except however CH-soil 1 have shown a decrease in PI values after some initial increase. CH-soil 1 for all enzyme doses of 200 ml / 3 m^3, 2.5 m^3, 2 m^3 and 1.5 m^3 of soil shows an initial increase of liquid limit for the first week of curing. After that, there is a decrease in liquid limit values with further curing. CH-soil 6 however is the only soil that shows an increase in value of PI up to 9.6% at the end of the 4th week. This behaviour of CH-soil 6 is inconsistent compared to other CH-soils. The characterization of CH-soil 6 shows W_L(%) = 57.3, WP(%) = 19, PI(%) = 38.3, clay content is 20.2% FSI =163 specific gravity G = 2.71. There is nothing unusual that could explain this inconsistent behaviour.

The highlighted bold numbers in the tables show the maximum percentage variation in the parameter under consideration. Though the improvement in properties with an increase in curing duration, however, the degree of enzyme stabilization effect is variable and no conclusive correlation among maximum improvement achieved in consistency limits, optimum enzyme dose and duration of curing required can be established for the overall CH-soil group.

3.5. Unconfined Compression Strength (UCS) Results for Stabilized CH-Soil

Table 2 and Figure 2 show the percentage variation in UCS for CH-soils. For UCS CH-soil 1 air-dry cured specimen gives a consistent incremental increase in UCS values with duration. CH-soil 1 gives a maximum percentage increase in UCS of 942.86% for an enzyme dose of 200 ml / 1.5 m^3 of soil at the curing of 8 weeks. Whereas for the same soil CH-soil 1 desiccator-cured specimen gives the maximum increase of 244.90% for the same enzyme dose and curing duration. This example also highlights the effect of curing conditions on UCS values. The field curing conditions are closer to air dry curing. Also, conclude that air-dry curing is better than desiccator curing.

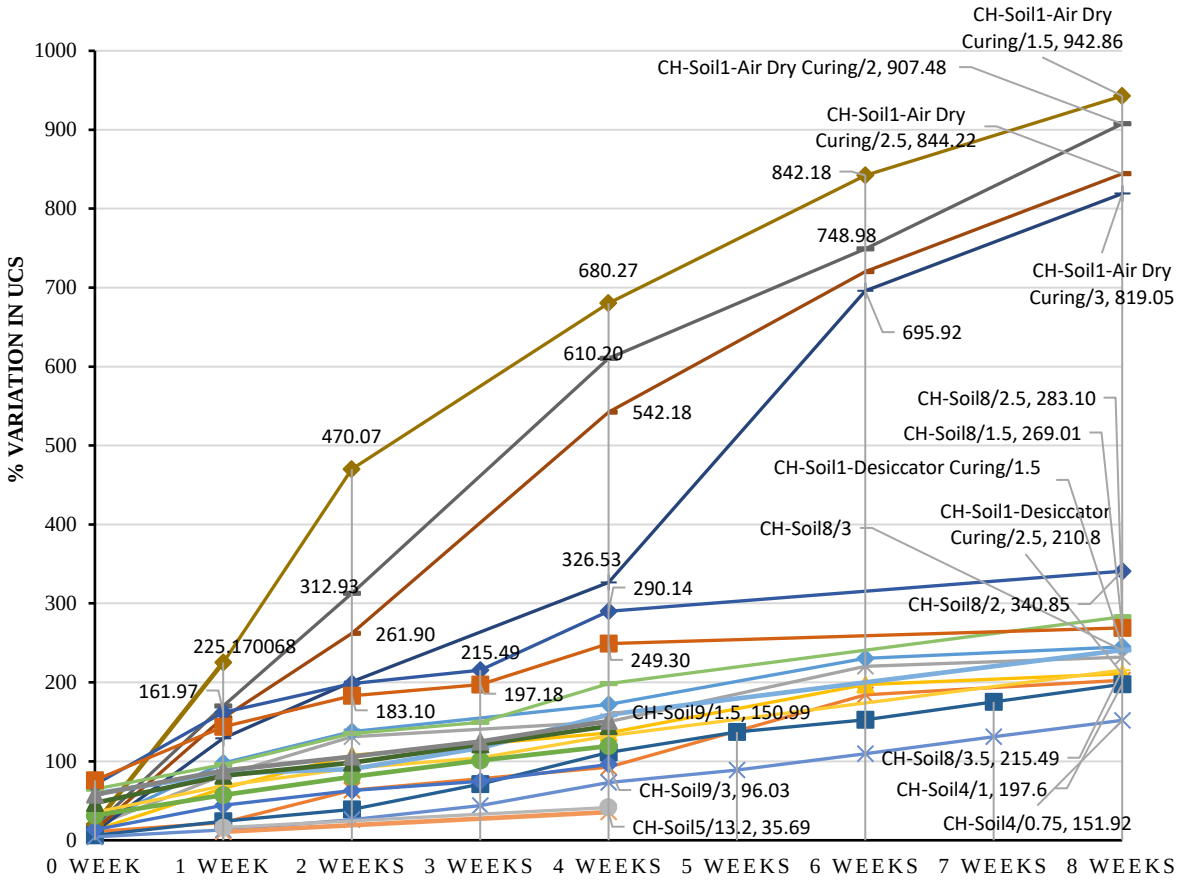

Fig. 2. Percentage variation in UCS for CH-soil

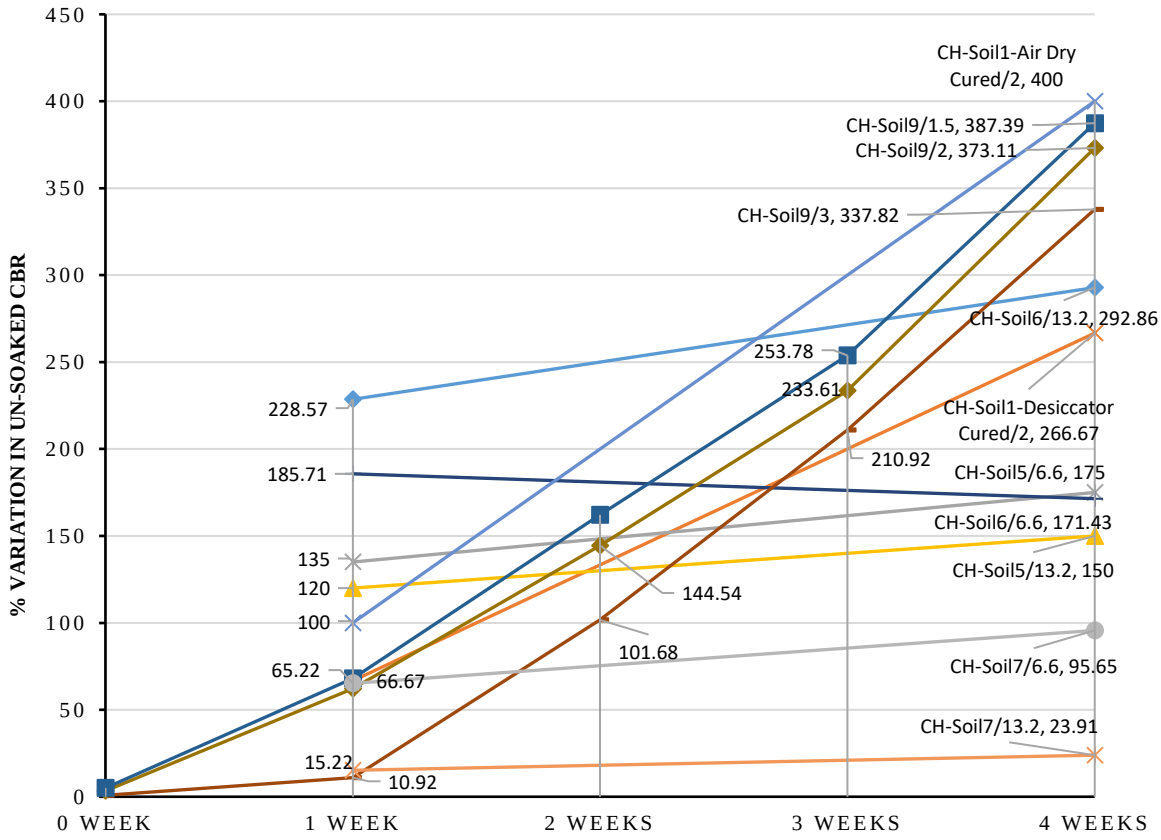

Fig. 3. Percentage variation in unsoaked CBR, CH-soil

UCS CH-soil1 gives a maximum percentage increase of 244.9% (Desiccator curing) and 942.9% (Air dry curing) for an enzyme dose of 200 ml /1.5 m^3 of soil for 8 weeks of curing.

The maximum percentage increase in UCS value for CH-soils with enzyme doses of 200 ml / 1 m^3, 1.5 m^3 and 2 m^3 shows uniform strength gain for a curing duration of 8 weeks. Whereas for CH-soil 5 (clay content 33%, FSI 170, Montmorrillonitic) the percentage maximum increase in UCS value is 41.49% with 200 ml / 6.6 m^3 enzyme dose for 4 weeks curing. The same soil shows a lesser improvement of 10.75% with a decrease in enzyme doses (200 ml / 13.2 m^3) and curing duration (1 week)

Both CH-soil 4 (197.6%, 200 ml / 1 m^3, 8 weeks) and CH-soil 9 (150.99%, 200 ml / 1.5 m^3, 4 weeks) show comparable maximum percentage increase in UCS values may be due to the similar characteristic of CH-soil 4 (W_L(%) = 55, WP(%) = 31, PI(%) = 24 clay content is 66.78%, clay of high plasticity, specific gravity G = 2.45) and CH-soil 9 (W_L(%) = 61.4, WP(%) = 34, PI(%) = 27.4 clay content is 68.7%, clay of high plasticity, specific gravity G = 2.48, FSI = 72.8).

CH-soil 8, a BC soil (W_L(%) = 83, WP(%) = 35, PI(%) = 48, specific gravity G = 2.65, FSI = 78) has shown the maximum increase in UCS of 340.9% (200 ml / 2 m^3, 8 weeks) due to its highly plastic nature.

3.6. California Bearing Ratio (CBR) Test Results for Stabilized CH-Soil

Table 3 and Figure 3 show the % variation in CBR values-CH-soils.

CBR-CH-soil 1 air dry cured sample shows a CBR value increase of 400% as compared to 266.67% of increase for the desiccator cured sample with the same enzyme dose of 200 ml/2 m^3 of soil at the end of the 4th week.

Among all the CH-soils, CH-soil 5 has recorded the least increase in soaked CBR value at a lower enzyme dose of 200 ml /13.2 m^3 (CH-soil 5- WL(%) = 59.2, WP(%) = 18.9, PI(%) = 40.3, clay content 33%, G = 2.72, FSI = 170, Montmorrillonitic). Such similar low improvement in CBR is also observed for CH-soil 7 (15.22%-unsoaked and 33.33%-soaked CBR), at low enzyme dose. However, the soil CBR-CH-soil 6 shows an increase of 292.86% in CBR value at the lower dose of 200 ml / 13.2 m^3, when compared with the higher dose of 200 ml / 6.6 m^3 of the same soil at the end of the 4th week with unexpected reduction trend. However, the same CH-soil 6 with 200 ml / 6.6 m^3 of the soil gives a 400% increase in CBR value compared to an increase of 366.67% for a dose of 200 ml /13.2 m^3 of soil at the end of 1st week of curing. CH-soil 5 and CH-soil 7 have greater FSI of 150, and 170, respectively and high montmorillonite contained with high swelling and expansivity. These soil on stabilization shows a high decrease in plasticity index. The same soil shows only moderate gain in soaked CBR values (Un-soaked CBR 175%, 4 weeks, 95.65%, 4 weeks % and soaked CBR 60%, 1 week, 122.22%, 1 week, respectively). CH-soil 6 having 20.2% clay content show better performance for both unsoaked (292.86%, 4 weeks) and soaked CBR (400, 1 week). CH-soil 1 having less percentage clay size fraction (21.61%) show a higher gain in UCS (942.86%) as compared to CH-soil 8 (UCS 340.85%) with a 30% clay size fraction.

Table 2. Maximum% variation in UCS values - CH-soils

Soil	**CH-soil 1**				**CH-soil 4**	**CH-soil 5**		**CH-soil 8**		**CH-soil 9**	
Doses	Curing type										
200	Desiccator		Air dry		1	13.2	6.6	3.5	2	3	1.5
(ml/m^3)	3	1.5	3	1.5							
% variation in UCS	10.88, (0 weeks)	244.9, (8 weeks)	10.88, (0 weeks)	942.9, (8 weeks)	197.6, (8 weeks)	10.75, (1 week)	41.49, (4 weeks)	35.21, (0 weeks)	340.9, (8 weeks)	13.31, (0 week)	150.99, (4 weeks)

Table 3. Maximum % variation in CBR values - CH-Soils

Soil	Doses 200 (ml/m^3)	% Variation (+ve increase, -ve decrease) Un-Soaked CBR	Soaked CBR
CH-soil 1	2 (Desiccator curing)	66.67, (1 week) 266.67, (4 weeks)	-
	2 (Air Dry curing)	100, (1 week) 400, (4 weeks)	-
CH-soil 2	3.5	59.92, (0 weeks)	-
	0.25	207.72, (0-week)	-
CH-soil 3	0.25	480, (3 weeks)	-
CH-soil 4	1	-	71.64, (0 weeks)
	0.75	-	71.64, (0 weeks) 329.85, (8 weeks)
CH-soil 5	13.2	120, (1 week)	20, (0 weeks) 20, (1 week)
	6.6	175, (4 weeks)	60, (1 week)
CH-soil 6	13.2	292.86, (4 weeks)	300, (0 weeks)
	6.6	171.43, (4 weeks)	300, (0 weeks) 400, (1 week)
CH-soil 7	13.2	15.22, (1 week)	33.33, (0 weeks)
	6.6	95.65, (4 weeks)	122.22, (1 week)
CH-soil 9	3	0.84, (0 weeks)	-
	1.5	387.39, (4 weeks)	-

3.6.1. Analysis of CI-Soil

CI-soils are clays of intermediate plasticity with normal activity.

3.6.2. Consistency Limits for Stabilized CI-Soil

Table 4 shows the % variation in Atterberg limits in CI-soils. CI-soil 1 shows a maximum reduction of 10.26% in LL with a dose of 200 ml / 2.5 m^3 for 4 weeks of curing after an initial increase of 12.82% in LL values in the first week. CI-soil 1 and CI-soil 2 both show a reduction in PL values up to 13.64% and 50% with an increase in dose and duration. The maximum percentage reduction in PL values for CI-soil 2 is 50% for or both doses of 200 ml / 0.8 m^3 and 0.6 m^3 of soil.

The soil CI-soil 2 shows a similar reduction trend in PI values with an increase in curing duration. The maximum reduction for CI-soil 2 is 44.19% for an enzyme dose of 200 ml / 0.6 m^3 of soil. However, PI values for CI-soil 1 decrease to 5.8 % at the end of the 4th week with an initial increase of 41.18% in the first week. However, the shrinkage limit for CI-soil 1 shows a continuous decrease with a maximum reduction of 22.22% for an enzyme dose of 200 bml / 2.5 bm^3 of soil at the end of 4 weeks of curing.

3.7. Compaction Characteristics for Stabilized CI-Soil

As shown in Table 5 CI-soil 2 shows a maximum increase of 68.71% in MDD value. All CI soils show better improvements in MDD values for higher enzyme doses.

Table 4. Maximum% variation in Atterberg limits - CI-Soils

Soil		CI-soil 1	CI-soil 2			CI-soil 3	CL-soil 2	
Doses 200 (ml/m^3)		**2.5**	**1.7**	**0.8**	**0.6**	**1.5**	**13.2**	**6.6**
% Variation (+ve increase, -ve decrease)	LL	12.82, (1 week) -10.26 (4 weeks)	-15.91, (0 weeks)	NS	-68.82, (3 weeks)	NS	NS	NS
	PL	-13.64 (4 weeks)	46.4, (0 weeks)	-50, (3 weeks)	-50, (3 weeks)	NS	NS	NS
	PI	41.18, (1 week) -5.88, (4 weeks)	58.14, (0 weeks)	-44.19, (3 weeks)	-44.19, (3 weeks)	NS	-42.59, (1 week) -58.33, (4 weeks)	-47.22, (1 week) -59.26, (4 weeks)
	Ws	-22.22, (4 weeks)	NS	NS	NS	25.38, (0 weeks)	NS	NS

Table 5. Maximum % variation in OMC & MDD in CI-soils

CI-soil	Doses 200 (ml/m^3)	% (+ve increase, -ve decrease) OMC		MDD	Remark
CI-Soil 2	1.7	-0.38, (0 weeks)	-0.38, (1 week)	21.84, (0 weeks)	Standard proctor test
	0.6	-18.08, (6 weeks)		68.71, (6 weeks)	
CI-Soil 3	Untreated	-17.78, (0 weeks)		9.26, (0 weeks)	Modified proctor test
	2	-23.70, (0 weeks)		13.30, (0 weeks)	

3.8. Unconfined Compression Strength (UCS) for Stabilized CI, CL and CL-ML Soils

Table 6 shows % variation in UCS in CI, CL and CL-ML soils. For UCS-CI-soil 1 there is a continuous incremental increase in UCS values and the maximum value reaches around 827.78% for 200 ml / 2.5 m^3 of the soil over the duration of 8 weeks.

Whereas for the same CI-soil 1 with desiccator curing the percentage increase in UCS value is 158.94% for an enzyme dose of 200 ml / 2.5 m^3 of soil over the duration of 8 weeks. CI-soil 1 shows a 357.14% increase in un-soaked CBR content with doses of 200 ml / 2.5 m^3 at the end of curing duration of 4 weeks (Table 7)

CI-soil 2 having the highest clay content (53%) among the CI group shows the maximum decrease in LL, PL and PI and an increase in MDD values. CI-soil1 having the lowest clay content (18.24%) among the CI group shows the maximum increase in UCS values.

3.9. Analysis of CL-Soil

CL-soils are clays of moderate plasticity maybe with normal activity.

3.9.1. Consistency Limits for Stabilized CL-Soil

CL-soil shows a consistent reduction in liquid limit values with a maximum reduction of 68.82% and at the end of the 3rd week with an enzyme dose of 200 ml / 0.6 m^3 of soil.

3.10. Unconfined Compression Strength (UCS) Results for CL-Soil

For UCS-CL-soil 2 with a dose of 200 ml / 13.2 m^3 there is an increase of up to 56% in UCS value for the duration of 4 weeks. However, for the same soil with an enzyme dose of 200 ml / 6.6 m^3 the increase in UCS value is up to 68% for the same duration of 4 weeks.

3.11. California Bearing Ratio (CBR) Test Results for Stabilized CL and CL-ML Soils

When compared among CL and CL-ML soils, CL soil having less clay content shows a greater percentage improvement in both Un-soaked and soaked CBR values (Table 8).

3.12. Analysis of CL-ML Soil

CL-ML soils are silty clays slightly plastic and may be normal or inactive based on their clay content. Unconfined Compression Strength (UCS) results for stabilized CL-ML soil, show that for CL-ML soil with the higher enzyme dose of 200 ml / 0.5 m^3 increase in UCS is up to 375% over a duration of 4 weeks. This increase in the UCS value for CL-ML soil (PI = 6.64%) is comparatively more than CI (Avg. PI = 19.76%) and CL (Avg. PI = 15.35) soils may be due to its low plasticity index.

Table 6. Maximum % variation in UCS in CI, CL and CL-ML soils

Soils	CI-soil 1				CL-soil 2		CL-ML
Soil / Doses 200 (ml/m^3)	Desiccator curing 4	2.5	Air dry curing 4	2.5	13.2	6.6	0.5
% UCS (+ve increase, -ve decrease)	7.73, (0 weeks)	158.94, (8 weeks)	7.73, (0 weeks)	827.78, (8 weeks)	11.33, (1 week)	68, (4 weeks)	375, (4 weeks)

Table 7. Maximum % variation in CBR values for CI-Soils

Soil	Doses 200 (ml/m^3)	(+ve increase, -ve decrease)	
		Un-soaked (%)	Soaked CBR (%)
CI-soil 1	3	214.29, (4 weeks)	NS
	2.5	357.14, (4 weeks)	NS

Table 8. Maximum % variation in CBR in CL-Soils and CL-ML Soils

Soil	Doses 200 (ml/m^3)	(+ve increase, -ve decrease)	
		Un-soaked (%)	Soaked CBR (%)
CL-Soil 2	13.2	63.64, (1 week)	266.67, (4 weeks)
	6.6	218.18, (4 weeks)	333.33, (4 weeks)
CL-ML	Untreated	56.88, (4 weeks)	NS
	0.5	185.32, (4 weeks)	NS

3.13. Analysis of MH-Soil

MH-soils are silts of high plasticity and their activity may be variable based on their clay content.

3.13.1. Consistency Limits for Stabilized MH-Soil

Table 9 shows the % variation in Atterberg limits in MH-soils. Both MH-soil 2 and MH-soil 3 shows a linear decrease in liquid limit values. The maximum reduction of 24.73% and 46.15% for enzyme dozes of 200 ml / 2 m^3 of soil for MH-soil 2 and MH-soil 3, respectively at the end of 2 weeks of curing. Plastic limit values for MH-soil 2 and MH-soil 3 also show a reduction in values with curing duration. The maximum reduction was 47.23% and 60% for MH-soil 2 and MH-soil 3, respectively for the same enzyme dose of 200 ml / 2 m^3 of soil at the end of 2 weeks of curing. Plasticity index values however show inconsistent variation with enzyme doses and duration. For MH-soil 2 variation behaviour in the plasticity index is inconclusive.

For MH-soils, consistency indices show an inconsistent decrease in values with enzyme doses and duration however the trend is inconclusive. MH-soil 3 (Clay content = 39.43%, G = 2.36 FSI = 48) shows a maximum decrease in LL and PL = 46.15% and 60%, respectively. MH-soil 2 (clay content = 40%, G = 2.26, FSI = 55) shows the maximum decrease in IP (21.51%) MH-soil 10 (clay content = 53.8%, G = 2.72, FSI = 93) shows the maximum increase in IP (30.36%).

3.14. Compaction Characteristics for Stabilized MH-Soil

Table 10 shows a very slight increase in MMD for MH-soil even at the high dose of enzyme contents

3.15. Analysis of Unconfined Compression Strength (UCS) Results for Stabilized MH-Soils

Table 11 shows the % variation in UCS in MH-soils. UCS-MH-soil 1 shows the inconsistent variation of UCS with time and doses with a final rise of nearly 38% and 14% with doses of 200 ml / 2.5 m^3 and 2 m^3, respectively. UCS shows an overall decreasing trend of values with a total decrease of nearly 43% for the dose of 200 ml / 3 m^3 of soil. UCS-MH-soil 2 (Clay content = 40%, G = 2.26, FSI = 55) shows the maximum increase in IP (30.36%) shows a continuous rising UCS raising trend, for all the enzyme doses. Though for all the doses with one-week curing the % increase in UCS is similar. There is a maximum increase of 135% for an enzyme dose of 200 ml / 2 m^3 of soil at the end of the fourth week. For UCS-MH-soil 3 there is a rise in UCS for all enzyme doses. However, the dose of 200 ml / 2 m^3 of the soil gives the highest increase of nearly 71% this dose also shows a high initial gain of strength of nearly 42% at the end of the first week. For UCS-MH-soil 7 there is an overall trend of consistent linear increase in percentage UCS values with a nearly 74% increase in UCS for a dose of 200 ml / 0.5 m^3 of soil over the duration of 4 weeks. Similar is a rising trend of UCS values for MH-soil 9. For UCS-MH-soil 10 there is an

increase of nearly 77% for a dose of 200 ml / 6.6 m^3 at the end of the 4th week.

3.16. California Bearing Ratio (CBR) Test Results for Stabilized MH-Soils

Figures 4 and 5 and Table 1[2] show % variation in CBR for MH-soils. CBR MH-soil 2 gave a maximum % increase in soaked CBR value of 423.08% for 4 weeks of curing with a dose of 200 ml / 2 m^3 of soil. MH-soil 2 (Clay content = 40%, G = 2.26, FSI = 55) shows the maximum increase in CBR. (Prakash and Sridharan, 2004)

Table 9. Maximum % variation in Atterberg limits for MH-soils

Soil		MH-soil 2			MH-soil 3		MH-soil 8			MH-soil 10
doses 200 (ml/m^3)		2.5	2	1.5	2	1.5	Untreated	0.4	0.1	6.6
% Variation (+ve increase, -ve decrease)	LL	-	-24.73, (2 weeks)		-46.15, (2 weeks)	-	-	-	--	-
	PL	-	-47.23, (2 weeks)		-60, (2 weeks)	NS	0.18, (0 weeks)		-18.42, (0 weeks)	NS
	PI	-21.51, (2 weeks)	-	13.8, (1 week)	-17.65, (2 weeks)	29.41, (0 weeks)	-2.82, (0 weeks)	-8.98, (0 weeks)	-	30.36, (1 week) -16.52, (4 weeks)

Table 10. Maximum % variation in OMC & MDD for MH-soil and ML-soil

Soil	Doses 200 (ml/m^3)	% OMC (+ve increase, -ve decrease)		% MDD (+ve increase, -ve decrease)	
MH-soil 8	Untreated	-2.22, (0 weeks)	NS	-0.02, (0 weeks)	NS
	0.4	-4.89, (0 weeks)	NS	1.28, (0 weeks)	NS
	0.3	-11.11, (0 weeks)	NS	5.83, (0 weeks)	NS
	0.1	-6.67, (0 weeks)	NS	2.58, (0 weeks)	NS
ML-Soil	3	-41.18, (1 week)	-41.18, (2 weeks)	0.00, (1 week)	0.56, (2 weeks)
	2.5	-17.65, (1 week)	-11.76, (2 weeks)	2.12, (1 week)	4.47, (2 weeks)
	2	-41.18, (1 week)	-17.65, (2 weeks)	1.84, (1 week)	5.03, (2 weeks)
	1.5	-23.53, (1 week)	-17.65, (2 weeks)	1.12, (1 week)	2.79, (2 weeks)

Table 11. Maximum % variation in UCS in MH-soils

Doses Soil	MH-soil 1		MH-soil 2		MH-soil 3		MH-soil 7		MH-soil 9		MH-soil 10	
200 (ml/m^3)	3	2.5	2	1.5	2.5	2	1.5	0.5	3	1.5	13.2	6.6
% UCS kPa (+ve increase, -ve decrease)	-42.7, (4 weeks)	109.60, (1 week)	135, (3 weeks)	51.6, (1 Week) 109.8 (3 weeks)	12.9, (1 week)	70.9, (3 weeks)	5.13, (0 weeks)	73.3, (4 weeks)	10, (0 weeks)	77.5, (4 weeks)	2.62, (1 week)	76.5, (4 weeks)

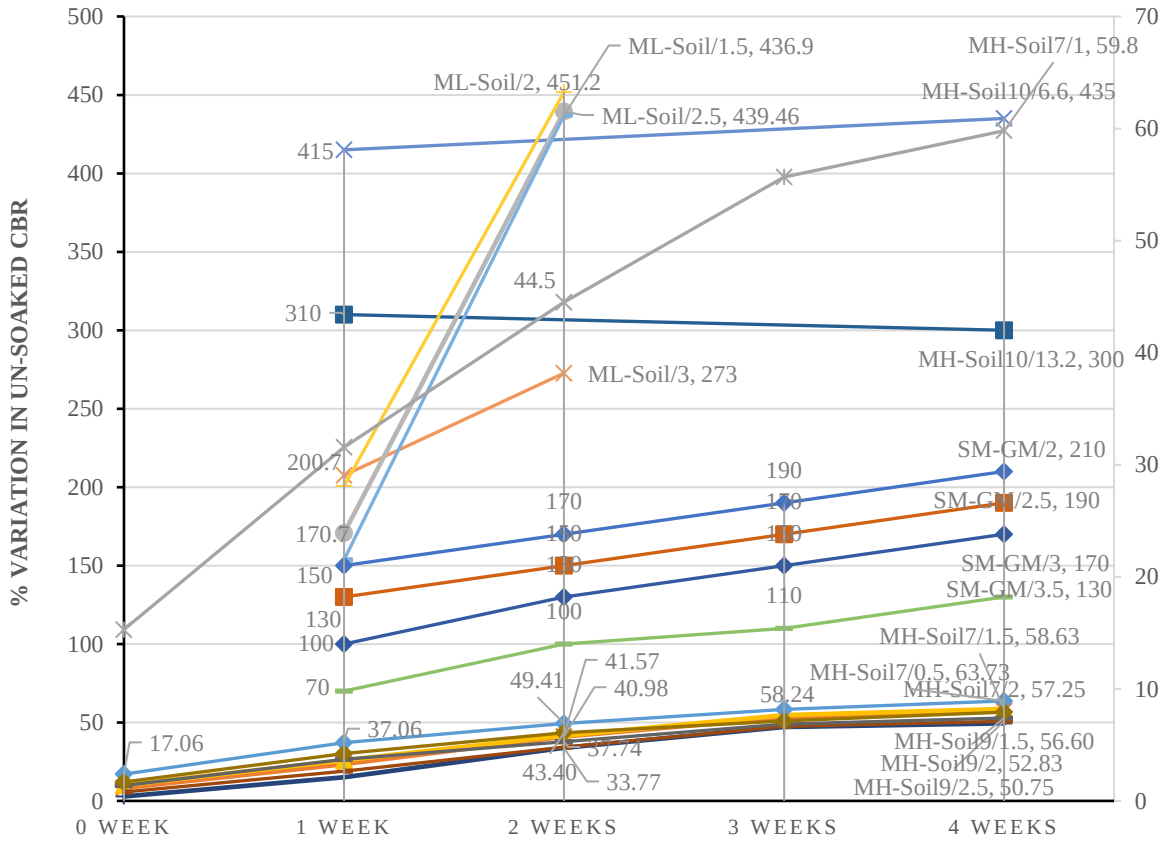

Fig. 4. % variation in unsoaked CBR-MH soils

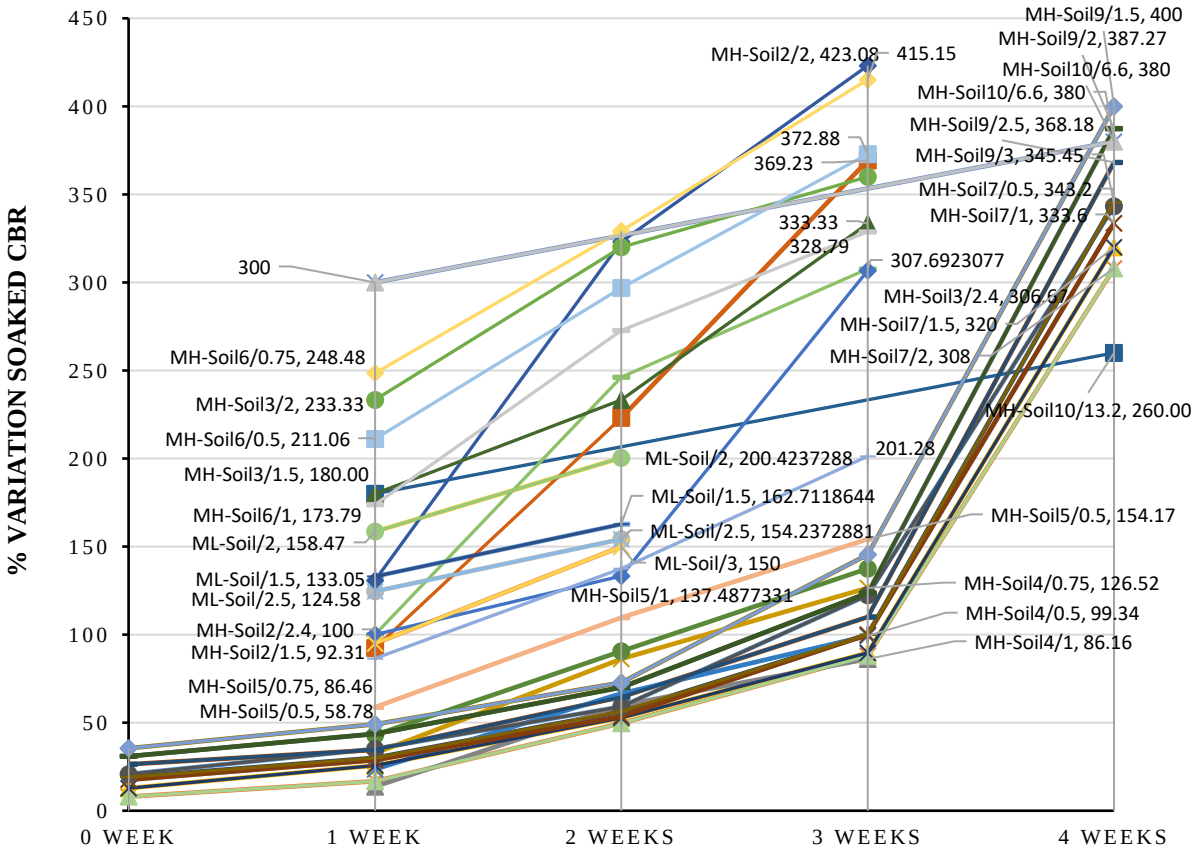

Fig. 5. % Variation in soaked CBR-MH soils

CBR MH-soil 6 (Clay content = 92%, G = 2.78, FSI = 90.5) shows a similar high increase of 415.15% for an enzyme dose of 200 ml / 0.75 m^3 of soil. CBR MH-soil 3 gives the maximum percentage increase omf 360% for a dose of 200 ml / 2 $m^3$of soil for 4 weeks of curing. CBR MH-soil 4 showed a continuous increase in soaked CBR up to 126.52% for an enzyme dose of 200 ml / 0.75 m^3 of soil for 4 weeks of curing.

CBR MH-soil 7 shows an incremental increase in unsoaked CBR with an increase in doses and period of curing with a dose of 200 ml / 0.5 m^3 of soil giving the highest increase of 63.73% at the end of the 4th week. MH-soil 9 shows a similar increase of 56.60% in unsoaked CBR for the same dose and duration of curing. However, both MH-soil 7 and MH-soil 9 give the minimum increases in the CBR values as compared to other soils. CBR MH-soil 7 and CBR MH-soil 9 show a similar consistent increase in the percentage soaked CBR with the maximum value of 343.20% and 400% for a dose of 200 ml / 0.5 m^3 of soil and 1.5 m^3 of soil respectively for 4 weeks curing. The %variation of soaked CBR for MH-soil 7 and MH-soil 9 showed similar trends with a maximum percentage increase of 343.20% and 400%, respectively at the 4th week of curing. Both MH-soil 7 (W_L(%) = 52.35, WP(%) = 36.20, PI(%) = 16.15 clay size 20.4, G = 2.61 silt of high plasticity, moderately plasticity with normal activity) and MH-soil 9 (W_L(%) = 54, WP(%) = 35.71, PI(%) = 18.29, G = 2.63% Clay size 20.2, the silt of high plasticity, high plasticity with normal activity) have similar properties showing similar improvement on enzyme stabilization

CBR MH-soil 10 (W_L(%) = 65.6, WP(%) = 43.2, PI(%) = 22.4, clay content = 53.8%, G = 2.72, elastic silt of high plasticity FSI = 93). Table 12 shows a very high percentage increase in unsoaked CBR values of 300% and 435% for enzyme dose of 200 ml / 6.6 m^3 of soil at the end of the first and 4th week, respectively. The high improvement in unsoaked CBR value for MH-soil 10 may be due to the well-graded nature of soil with higher clay and silt content.

3.17. Analysis of ML-Soil

ML-soils are silts of low plasticity, slightly plastic in nature and may be inactive.

Table 12. Maximum% variation in CBR in MH-soils

MH-soils	Doses 200 (ml/m^3)	(+ve increase, -ve decrease) Un-soaked CBR (%)	Soaked CBR (%)
MH-soil 2	2	NS	423.08, (3 weeks)
	1.5	NS	92.31, (1 week)
MH-soil 3	2.4	NS	100, (1 week)
	2	NS	360, (3 weeks)
MH-soil 4	1	NS	13.67, (1 week)
	0.75	NS	126.52, (3 weeks)
MH-soil 5	1	NS	42.98, (1 week)
	0.75	NS	201.28, (3 weeks)
MH-soil 6	1	NS	173.79, (1 week)
	0.75	NS	415.15, (3 weeks)
MH-soil 7	Untreated	6.86, (0-week)	NS
	2	NS	8.00, (0 weeks)
MH-soil 9	0.5	63.73, (4 weeks)	343.20, (4 weeks)
	3	2.83, (0 weeks)	19.09, (0 weeks)
	1.5	56.60, (4 weeks)	400, (4 weeks)
MH-soil 10	13.2	300, (4 weeks)	180, (1 week)
	6.6	435, (4 weeks)	380, (4 weeks)
ML-soil	3	NS	94.92, (1 week)
	2	451.79, (2 weeks)	200.42, (0 weeks)
	1.5	153.57, (1 week)	NS
SM-GM	3.5	70, (1 week)	NS
	2	210, (4 weeks)	NS

3.17.1. Consistency limits for ML-Soil and SM-GM Soils

Table 13 shows the maximum decrease of 27.78% in LL, the PI value increases initially and then decreases by 7.65% for an enzyme dose of 200 ml / 2 m^3.

The SM-GM soil shows better stabilizing results with the maximum decrease in PI values of 63.3% 200 ml / 2 m^3 at the end of the 4^{th} day. The improvement may be due to the well-graded nature and lesser 2% clay content.

3.18. CBR for ML-Soil

ML-Soil recorded a 451.79% increase in un-socked CBR value for a dose of 200 ml / 2 m^3 of soil. At the end of the 2^{nd} week. ML-Soil registers a maximum percentage increase of 200.42% for 200 ml / 2 m^3 of soil in soaked CBR for 2 weeks of curing.

3.19. CBR for ML-Soil

SM-GM are poorly graded silty sands or poorly graded sand with silt and gravel.

3.19.1. Unconfined Compression Strength (UCS) Results for Stabilized SM-GM and SP-Soils

Table 14 shows the % variation in UCS in SM-GM and SP-soils. UCS-SM-GM soil shows a maximum gain of nearly 450% of UCS with an enzyme dose of 200 ml / 2 m^3 of soil. All the doses show a consistent rising trend of UCS values.

3.20. California Bearing Ratio (CBR) Test Results for Stabilized SM-GM Soil

CBR SM-GM soil shows a linear percentage increase in values of CBR with a maximum percentage increase of 210.00% for a dose of 200 ml / 2 m^3 of soil at the end of the 4^{th} week. The sieve analysis indicates a lesser percentage of clay, and silt and the presence of sandy and gravelly content, SM-GM soil resister higher CBR values maybe because of the inherent strength of sand and gravel matrix bonded with enzyme-treated silt content.

3.21. Analysis of SP-Soil

SP-soils are poorly graded sands with little or no fines.

3.21.1. Unconfined Compression Strength (UCS) Results for Stabilized SP-Soil

UCS-SP-soil 1 shows a consistent increase in UCS values with the duration and doses, the highest rise of nearly 426.34% for intermediate enzyme dose of 200 ml /2.5 m^3 of soil at the end of the 4^{th} week. The same UCS-SP-soil 1 at dry of OMC however gives much higher overall consistent values. The maximum increase in UCS is nearly 475% for a dose of 200 ml / 2 m^3 of soil (Table 14). Also, enzyme treatment provides better stabilization at the moisture content of 2% to 3% lesser than the optimum (OMC). The same UCS-SP-soil 1 on the wet side of optimum gives the highest increase of nearly 339% for an enzyme dose of 200 ml / 2 m^3 of soil the maximum percentage increase in UCS values for SP-soil 1 is obtained at the dry of optimum. However, UCS-SP-soil 2 shows a maximum percentage increase of 111.45% for a dose of 200 ml / 2 m^3 of soil at the end of the first week. SP-soil 1 shows high UCS values as compared to SP-soil 2 despite both having similar clay content of 1% and 2.45%, respectively

SC-soils are clayey sands (sand-clay mixtures) with plasticity and may be normal to inactive based on their clay content. SP-SC soils are poorly graded sands with clay with slight plasticity. SM-soils are silty sands (sand-silt mixtures) with slight plasticity, generally inactive. The results for enzyme stabilization of these soils could be concluded due to insufficient data.

4. Factors Affecting Results

Laboratory tests for mapping improvements in index and engineering properties of stabilized soil are recommended before field applications. However, the results describing the efficacy of enzymes for soil stabilization vary greatly among available literature.

Table 13. Maximum % variation in Atterberg limits in ML-Soils and SM-GM soils

Soil		ML-soil				SM-GM			
Doses 200 (ml/m^3)		3	2.5	2	1.5	3.5	3	2.5	2
% Variation (+ve increase, -ve decrease)	LL	NS	NS	-27.78, (2 days)	-3.70, (1 day)	-14.29, (1 day)	-14.29, (1 day)	NS	-21.14, (4 days)
	PL	-33.22, (2 days)	-24.6, (1 day)	NS	NS	NS	NS	-4, (4 days)	-4, (4 days)
	PI	NS	71.50 (1 day)	-7.65 (2 days)	NS	-50 (1 day)	-50 (1 day)	NS	-63.3, (4 days)

Table 14. Maximum % variation in UCS for SM-GM and SP-Soils

Soil doses 200 (ml/m^3)	SM-GM		OMC		SP-soil 1 Dry of OMC		Wet of OMC		SP-soil 2	
	3.5	2	3	2	3	2	3	2	3	2
%UCS (+ve increase, -ve decrease)	44.37, (1 week)	450.7, (4 weeks)	101.88, (0 weeks)	440.8, (4 weeks)	216.64, (0 weeks)	475.85, (2 weeks)	63.60, (0 weeks)	339.37, (2 weeks)	-42.97, (4 weeks)	111.45, (1 week)

Though the analysis of laboratory test results is generalized for various soil groups, the study indicates the inconsistency of results even within and obviously across the soil groups without any conclusive reasons. This variation of the results also necessitates considering the factors that may affect test results. Hence the possible reasons affecting the effectivity of enzyme stabilization and laboratory test results are also elaborated. The factors influencing the laboratory results are enzyme application rates, sample preparation, sample curing conditions test procedure etc.

- Enzyme application rates: The literature test results show the variation in properties of treated soil with enzyme doses within and across the soil groups. The method of enzyme application and calculation of enzyme doses are also variable in research studies. Most of the studies have preferred enzyme doses calculation based on the bulk unit weight of soil whereas few have preferred dose calculation based on dry unit weight. Though the difference is small, still it can affect the results.
- Sample preparation and tests: During specimen preparation, initial moisture content, enzyme doses, method of enzyme application, method of curing controlled conditions during curing, temperature control, etc. will have a pronounced effect on test results. Hence needs to be monitored with utmost care. However, only a few authors have categorically mentioned these standards.
- Curing condition: The curing may be; air-dry at normal room temperature or in a sealed container under controlled conditions for preserving moisture content during the curing time. However, most of the studies discussed, have not specified details about the curing conditions. The improper curing conditions may have led to variations in test results. The controlled untreated samples also need to be tested for any thixotropic or ageing/curing strength gain specifically during UCS and CBR tests. Part of this significant improvement could be due to moisture loss as the moisture content variation during the sample preparation and testing stages was not categorically checked for many studies.
- Other factors: The enzymes are pH-sensitive too and work well around pH value 7 suggested that soil suitable for bio-enzyme stabilization should have some organic content. However, the laboratory studies have not specified organic contents and pH for the untreated soil. These parameters may have led to inconsistent, variable results among and within the soil groups. It is also a better idea to check and standardize the enzyme constituents to assured their consistent performance

which was also lacking in many of the studies. According to Aswar et al. (2022) along with the parameters of soil such as clay content, activity number (A), free swell index and mineralogical and organic content, the characterization of enzyme constituents' properties also need to be analyzed to understand the degree of the enzymatic reaction and the final stabilization.

5. Results

- All CH-soils show a reduction in PI and an increase in shrinkage limit with curing duration. CI-soils also show a reduction in PI values.
- The most prominent variation (negative sign indicates decrease) in consistency limits of untreated and treated soils (LL = -68.82%, PL = -50%, PI = -59.26%, Ws = +25.38%) was observed for CI-soils (average % clay content 32.25%). Also, among clayey and silty soils, the CI-soils have shown the maximum increase in dry density (+68.71%) and maximum decrease in OMC (-23.70%).
- There is substantial variation in optimal doses and curing period to obtain the maximum average % MMD for various soils (CH-Soils: 200 ml / 1.5 m^3 curing duration 0 weeks, CI-soils: 200 ml / 0.6 m^3 curing duration 6 weeks). CH-soils need higher doses to obtain the maximum average % MDD. The most marked variation in MDD and OMC was witnessed by the CI-soils, which show the best improvement in MDD value (+68.71%).
- The improved performance of CI soil may be because of lower the average clay/fine content among the clayey soils (Average % clay content CH = 36.82%, Cl = 32.25%, CL = 39.40%, CL-ML = 59.00%, MH = 54.95%) and thus lesser PI (average PI values CH = 35.59%, Cl = 19.76%, CL = 15.35%, CL-ML = 6.64%, MH = 23.13 %) of CI soils. Also, the comparatively well-graded nature may have resulted in improved compaction characteristics.
- TerraZyme stabilized CI, CL-ML, and CH and witnessed maximum betterment in UCS with curing periods. These clayey soil groups with significant clay/fine content, however, need a more curing period to achieve the maximum UCS. (CH = +942.9%, 8 weeks, CI = +827.78%, 8 weeks, CL-ML +375%, 4 weeks). However, as clay contents go on decreasing the time (curing duration) to reach maximum UCS also reduces.
- The contribution to UCS improvement may be contributed to enzymatic reaction with clay/fines or other factors such as thixotropic properties and/or reduction in water content with curing or the combination of all these factors which could not be confirmed. The causes are inconclusive as sample moisture content during testing or the effect of thixotropic properties is not mentioned. The UCS results for SP-soils are found least affected by clay content showing similar improvement in UCS values (+475.85%) with enzyme doses (200 ml / 2 m^3) and curing durations (2 weeks).
- For UCS and CBR, the performance of CH-soil for air dry curing (UCS = +942.9%, CBR unsoaked = +480%, soaked = +400%) is found better than desiccator curing (UCS = +244.9, CBR = NS). Similarly, improved performance for UCS values is observed for CI-soil with air dry curing (UCS = +827.78%) compared to desiccator curing (UCS = +158.94%).
- For the efficacy of enzymatic reaction, some initial moisture content should be available during the stabilization process however, the underperformance of desiccator-cured samples compared to air-dried specimens cannot be justified only by curing conditions. Further study on the effect of curing conditions on enzymatic reaction is required.
- The clay and silt-enriched soils have witnessed significant betterment in unsoaked and soaked CBR. However,

when compared among CL (Average % clay content = 39.40%) and CL-ML (59%) soils, CL soil having less clay content shows a greater percentage improvement in both Un-soaked CBR values (CL = +218.18, 4 weeks, CL-ML = 185.32, 4 weeks) and soaked CBR (CL = 333.33, 4 weeks, CL-ML = NS) values.

- For CH soils, higher clay content (Average % clay content = 36.82%) shows better performance for both unsoaked and soaked CBR however, for UCS performance the higher clay size fraction affects adversely. A similar reduction in UCS values with higher clay content was also found for CI-soils (Average % clay content = 32.25%).
- For CH-soils (Activity number A = 1.4) more enzyme doses (CH-soil 3 200 ml / 0.25 m^3) are needed for the maximum CBR value (+480%). The MH-soils (A = 0.49) attained the maximum value (423.08%) at a slightly lower dose (200 ml / 2 m^3). The ML and SM-GM soils with lower average clay/fine content (ML 15.65%, SM-GM 2%) attend the highest average CBR at moderate enzyme dose (un-socked CBR ML-soil +451.79% for 200 ml / 2 m^3, SM-GM +210.00% for 200 ml / 2 m^3 of soil). Normally curing period reaches the maximum average percentage, and CBR decreases with clay/fine contents (CH = +480%, 3 weeks, MH = 423.08%, 3 weeks, ML = 451.79, 2 weeks).
- In general, for MH-soils, the enzyme stabilization effect on consistency indices is inconclusive as the result shows an inconsistent variation in values with enzyme doses and duration. The ML-soils with the average PI (3.79%) and least average clay/fine content (15.65%) compared to other soil groups records higher betterment in optimum moisture content at a lower enzyme dose of 200 ml / 3 m^3.
- ML-soil with low clay/fine content and plasticity index witnessed higher improvement in optimum moisture content (-41.18%, 1 week) at a lesser enzyme dose (200 ml / 3 m^3). Thus clay/fine content and PI are prominent factors controlling the optimum dose. Similar results were recorded for MH-soils (A = 0.49) reaching maximum average % CBR (+423.08%) at a relatively lesser dose (200 ml / 2 m^3).
- Normally curing period of 4 weeks for CL-ML soils and Cl soils, 3 weeks for MH soils, and 2 weeks for ML soils is needed to attain the maximum average%, CBR. Thus, indicating the need for a lower curing period with a decrease in clay/fine contents. The soaked CBR requires a greater curing period of 3 weeks to 8 weeks to attain maximum CBR value. The higher duration may be due to the leaching of the enzyme during soaked CBR.

6. Conclusion

The CI-soils are found comparatively more suitable TerraZyme stabilization. In general, the improvement in soil properties depends on average clay content, particle size gradation, type and duration of curing. However, these parameters affect the individual test results for various soils differently as witnessed in the result discussion. There is substantial variation in optimum enzyme dose and curing period requirements for different soils based on the parameters being analyzed. The maximum individual parametric improvements for various soil types are at different enzyme doses. Hence optimal enzyme dose cannot be fixed. However, in general, optimized enzyme doses for various soil types are CH-soils 200 ml / 1.5-2 m^3, CI-soils and CL-soils 200 ml / 6.6 m^3, CL-ML soils 200 ml / 0.5 m^3, MH-soils 200 ml / 2-2.5 m^3, ML-soils, SP-soils and SM-GM soils 200 ml / 2 m^3. Similar variation is observed in the curing duration required to attain the maximum parametric variation hence it is necessary to ensure enough curing duration before use.

The enzyme stabilizer evaluation studies

have yielded unalike performances witnessing inconsistent improvement in properties even among the soils belonging to the same group. One of the causes for such an unforeseen result may be due to deviation from the standard test procedures. The limited specimens tested, under the non-uniform procedure and test conditions can also contribute to such unexpected results.

There are not any parametric ranges of improvements in index and engineering properties of stabilized soils specified and standardized for various engineering applications.

There is a need for specific laboratory tests for the assessment of the field performance of enzyme stabilizers. The enzyme stabilizers without significant improvement under controlled laboratory conditions are less likely to attain desired performance in less favourable field conditions. Hence both laboratory and field tests are recommended before large-scale application. The research emphasizes the necessity of an elaborate organized study on the enzyme and soil characterization, their suitability, and optimization of doses, curing type and duration to have a better knowhow of the effectiveness of enzymatic stabilization.

6. Declarations

6.1. Funding

The authors declare that no funds, grants, or other support were received during the preparation of this manuscript.

6.2. Conflict of Interest

The authors declared that they have no conflicts of interest in this work. We declare that we do not have any commercial or associative interest that represents a conflict of interest in connection with the work submitted.

6.3. Availability of Data and Material

Not applicable

6.4. Code Availability

Not applicable

6.5. Author Contributions

The corresponding author claims the major contribution of the paper including formulation, analysis and editing. The co-author provides guidance to verify the analysis result and manuscript editing.

6.6. Compliance with Ethical Standards

This article is a completely original work of its authors. It has not been published before and will not be sent to other publications until the journal's editorial board decides not to accept it for publication.

7. References

Agarwal, P. and Kaur, S. (2014). "Effect of bio-enzyme stabilization on unconfined compressive strength of expansive soil", *International Journal of Research in Engineering and Technology* (*IJRET*), 3(5), 30-33.

Aswar, D.S. Bajad, M.N. and Ambadkar, S.D. (2022). "Performance of TerraZyme for soil stabilization of various soil groups", *International Journal of Engineering Trends and Technology*, 70(4), 258-271, http://doi.org/10.14445/22315381/IJETT-V70I4P222.

Bergmann, R. (2000). *Soil stabilizers on universally accessible trails*, USDA Forest Service, San Dimas Technology and Development Center.

Brandon, F., Ding, C., Gary, H. and Charles, R. (2010). "Permazyme testing Volume I: Final testing summary report", California State University.

Chakrapani, K. (2016). "An experimental study on black cotton soil stabilization by using Terazyme", Ph.D. Thesis, Department of Civil Engineering, National Institute of Technology Rourkela.

Daigavane, P.B. and Ansari, A. (2021). "Stabilization of black cotton soil using Terrazyme", *New Arch-International Journal of Contemporary Architecture*, 8(2), 316-321.

Dhanesh, I.S. and Mohandas, T.V. (2016). "Effect of bio-enzyme on geotechnical properties of Thonnakkal clay", *International Journal of Engineering Trends and Technology*, 36(9), 474-476, http://doi.org/10.14445/22315381/IJETT-V36P286.

Farooq, T. and Sukhdeep, S. (2020). "Stabilization of black cotton soil by using bio-enzymes for pavement construction", *International Journal*

of Scientific Development & Research, 5(7), 687-693, http://dx.doi.org/10.13140/rg.2.2.19819.36649.

Guthrie, W.S., Simmons, D.O. and Eggett, D.L. (2015). "Enzyme stabilization of low-volume gravel roads", *Transportation Research Record*, 2511(1), 112-120, http://dx.doi.org/10.3141/2511-13.

Isaac, K.P., Biju, P.B. and Veeraragavan, A. (2003). "Soil stabilization using bio-enzyme for rural roads", *Integrated Development of Rural an Arterial Road Networks for Socio-Economic Development*, Delhi.

Indian Standards (IS): 1498. (1970). *Classification and identification of soils for general engineering purposes*, Bureau of Indian Standards (BIS).

Indian Standard (IS): 2720 (Parts 5,7,10,16). (1985). *Method of test for soils*, Bureau of Indian Standards (BIS).

Jenith P. and Parthiban M.C. (2017). "An experimental study of bio-enzyme on black cotton soil as a highway material", *International Journal of Engineering Research*, 5(13), 4.

Kestler, M.A. (2009). "Stabilization selection guide for aggregate-and native-surfaced low-volume roads", US Department of Agriculture, Forest Service, National Technology & Development Program.

Khan, T.A. and Taha, M.R. (2015). "Effect of three bioenzymes on compaction, consistency limits, and strength characteristics of a sedimentary residual soil", *Advances in Materials Science and Engineering*, Hindawi, 2015(Article ID 798965), https://doi.org/10.1155/2015/79896

Kumar, A. and Kumar Khan, A. (2018). "Stabilization of expansive soil using bio-enzyme", *Indian Geotechnical Conference (IGC-2018)*, Indian Institute of Science Bengaluru, pp. 13-15.

Lacuoture, A. and Gonzalez, H. (1995). "Usage of organic enzymes for the stabilization of natural base soils and sub-bases in Bagota", Pontificia Universidad Jevariana, Faculty of Engineering.

Marasteanu, M.O., Hozalski, R.M., Clyne, T.R. and Velasquez, R. (2005). "Preliminary laboratory investigation of enzyme solutions as a soil stabilizer", Report No. MN/RC-2005-25, University of Minnesota, Department of Civil Engineering, Minneapolis, MN.

Mekonnen, E., Kebede, A., Tafesse, T. and Tafesse, M. (2020). "Application of microbial bioenzymes in soil stabilization", *International Journal of Microbiology*, Hindawi, 2020(Article ID 1725482), https://doi.org/10.1155/2020/1725482.

Mgangira, M.B. (2009). "Evaluation of the effects of enzyme-based liquid chemical stabilizers on subgrade soils", *28th Annual Southern African Transport Conference (SATC)*, 6-9 July, Pretoria, South Africa.

Milburn, J.P. and Parsons, R.L. (2004). "Performance of soil stabilization agents (No. K-TRAN: KU-01-8)", Department of Transportation, Kansas.

Muguda, S. and Nagaraj, H.B. (2019). "Effect of enzymes on plasticity and strength characteristics of an earthen construction material", *International Journal of Geo-Engineering*, 10(2), 1-14, https://doi.org/10.1186/s40703-019-0098-2.

Myint, N.N.N. and Swe, T.M. (2014). "Investigation into soil stabilization with Enzyme".

Nandini, D., Amate, V. and Kumar, M.P. (2015). "Compaction and strength characteristics of terra-zyme stabilized red soil", *International Journal of Research Publications in Engineering, Technology and Management*, 1(1), 1-3.

Nandini, D.N., Reddy, Y.R. and Gowda, T. (2019). "An experimental study on strength characteristics of enzymatic hypo sludge stabilized soil", *SAMRIDDHI: A Journal of Physical Sciences, Engineering and Technology*, 11(SUP), 240-243.

Nandini, D.N, Gowda, T. and Reddy, Y.R. (2020a). "An experimental study on strength enhancement of locally available soil using Terrazyme", *International Journal of Future Generation Communication and Networking (IJFGCN)*, 13(3), 2902-2911.

Nandini, D.N. and Reddy, Y.R. (2020b). "Effect of bio enzymatic treatment on the strength characteristics of different soil samples", *International Journal of Advanced Science and Technology*, 29(6), 5200-5209.

Nature Plus, Inc. (2021). "How terrazyme works?", https://www.nature-plus.com/terrazyme-how-it-works, Retrieved on Dec 15, 2021.

North Dakota DOT Materials and Research Division, Experimental Study ND. (2014-01), "Evaluation of permazyme 11x™ soil stabilization work plan", SS-4-053(015) 030, https://www.dot.nd.gov/divisions/materials/research_project/ND201401workplan.pdf.

Patel, U., Singh, S. and Chaudhari, S. (2018). "Effect of bio enzymeterrazyme on compaction, consistency limits and strength characteristics of expansive soil", *International Research Journal of Engineering and Technology*, 5(3), 1602-1605.

Prakash, K. and Sridharan, A. (2004). "Free swell ratio and clay mineralogy of fine-grained soils", *Geotechnical Testing Journal*, 27(2), 220-225.

Ramesh, H.N. and Sagar, S.R. (2015). "Effect of drying on the strength properties of terrazyme treated expansive and non-expansive soils", *50th Indian Geotechnical Conference*, Pune, India.

Rauch, A.F., Katz, L.E. and Liljestrand, H.M.

(1993). "An analysis of the mechanisms and efficacy of three liquid chemical soil stabilizers: Volume 1", Report No. 1993-1, FHWA/TX-03/1993-1 (Volume 1), Center for Transportation Research, The University of Texas at Austin, Austin, TX.

Ryan, L. and Norris, R. (2014). *Cambridge international as and a level chemistry course book with CD-ROM*, Cambridge University Press.

Saini, V. and Vaishnava, P. (2015). "Soil stabilization by using terrazyme", *International Journal of Advances in Engineering & Technology*, 8(4), 566.

Scholen, D.E. (1992). "Nonstandard stabilizers", Report FHWA-FLP-92-011, Washington, DC: Federal Highway Administration (FHWA), US Department of Transportation, July.

Scholen, D.E. (1995). "Stabilizer mechanisms in nonstandard stabilizers", *Transportation Research Board Conference Proceedings* (No. 6).

Sen, J. and Singh, J.P. (2015). "Stabilization of black cotton soil using bio-enzyme for a highway material", *International Journal of Innovative Research in Science, Engineering and Technology*, 4(12), 12453-12459.

Shah, K. and Shah, M. (2016). "Soil stabilization using terrazyme", *International Journal of Advance Engineering and Research Development*, 3(12), 359-365.

Shaka, P.M. and Shaka, S.M. (2016). "Laboratory investigation on Black cotton soils and Red soil stabilized using Enzyme", *International Research Journal of Engineering and Technology*, 3(6), 325-330.

Shankar, A.U., Rai, H.K. and Mithanthaya, R. (2009). "Bio-enzyme stabilized lateritic soil as a highway material", *Journal of the Indian Roads Congress*, 70(2), 143-151.

Shukla, M., Bose, S. and Sikdar, P.K. (2003). "Bio-enzyme for stabilization of soil in road construction a cost-effective approach", Presented at *the IRC Seminar: Integrated Development of Rural and Arterial Road Networks for Socio-Economic Development*, New Delhi, 5-6 December.

Sodhi, P.S. and Ocean, Y.K. (2018). "Stabilization of soil using alkaline bio-enzyme (Alkazyme)", *International Research Journal of Engineering and Technology*, 5(8), 1681-1685.

Sweta, D. and Maheswar, M. (2017). "An investigation on behaviour of bio enzyme stabilized expansive soil", *International Journal of Recent Scientific* Research, 8(8), 19029-19034, http://dx.doi.org/10.24327/ijrsr.2017.0808.0615.

Taha, M.R., Khan, T.A., Jawad, I.T., Firoozi, A.A. and Firoozi, A.A. (2013). "Recent experimental studies in soil stabilization with bio-enzymes", *Electronic Journal of Geotechnical Engineering*, 18, 3881-3894.

Thomas, A., Tripathi, K. and Yadu, L.K. (2018). "A laboratory investigation of soil stabilization using enzyme and alkali-activated ground granulated blast-furnace slag", *Arabian Journal for Science and Engineering*, 43(10), 5193-5202.

Tingle, J.S. and Santoni, R.L. (2003). "Stabilization of clay soils with nontraditional additives", *Transportation Research Record*, 1819(1), 72-84.

Tingle, J.S., Newman, J.K., Larson, S.L., Weiss, C.A. and Rushing, J.F. (2007). "Stabilization mechanisms of nontraditional additives", *Transportation Research Record*, 1989(1), 59-67.

Vastrad, M., Karthik, M., Dhanavandi, V. and Shilpa, M.S. (2020). "Stabilization of black cotton soil by using GGBS, lime and nano-silica", *International Journal of Research in Engineering, Science and Management*, 3(9), 1-7.

Venkatasubramanian, C. and Dhinakaran, G. (2011). "Effect of bio-enzymatic soil stabilisation on unconfined compressive strength and California Bearing Ratio", *JEAS-Journal of Engineering & Applied Sciences*, 6(5), 295-298.

Vinay Kumar, K.S., Harikeerthan, M.K., Jayatheertha, H.S. and Girish, P. (2020). "Effect of bio enzyme on index & engineering properties of expansive soil", *International Research Journal of Engineering and Technology* (IRJET), 7(9), 2974-2977.

Woll, J.H., Surdahl, R.W., Everett, R. and Andresen, R. (2008). *Road stabilizer product performance: seedskadee national wildlife refuge* (No. FHWA-CFL/TD-08-005), Central Federal Lands Highway Division, FHWA, U.S. Department of Transportation, Lakewood, Colo.

Zhang, X., Zhang, X.P., Peng, H.T., Xia, Q. and Wang, J. (2013). "Relation of microstructure and unconfined compression strength of soil stabilized with TerraZyme," *Advanced Materials Research*, Vol. 664, pp. 760-763, Trans Tech Publications Ltd.

6. Appendix

Details and characterization of the soil types used in the study.

No.	References	IS Soil Classification		Clay size (%)	Soil Description	Soil Plasticity	Activity	FSI (%)	Soil nature based on FSI (North Dakota DOT, 2014)
1	Ramesh and Sagar (2015)	CH	CH-Soil1	21.6	Clay of high plasticity	Highly Plastic	Active	NS	-
2	Sweta and Maheswar (2017)		CH-Soil2	42	Clay of high plasticity	Highly Plastic	Normal	100	Montmorilloniti, Swelling, Very high expansivity
3	Patel Usha et al. (2018)		CH-Soil3	30	Clay of high plasticity	Highly Plastic	Normal	80	
4	Vinay Kumar et al. (2020)		CH-Soil4	66.8	Clay of high plasticity	Highly Plastic	Inactive	NS	-
5.1	Myint et al. (2014)		CH-Soil5	33	Lean clay	Highly Plastic	Normal	170	Montmorilloniti, Swelling, Very high expansivity
5.2			CH-Soil6	20.2	Fat clay with gravel	Highly Plastic	Active	163	
5.3			CH-Soil7	12.3	Sandy fat clay	Highly Plastic	Active	150	
6	Marasteanu et al. (2005)		CH-Soil8	30	Clay of high plasticity	Highly Plastic	Active	78	Montmorilloniti, Swelling, Very high expansivity
7	Joydeep et al. (2015)		CH-Soil9	68.7	Clay of high plasticity	Highly Plastic	Active	72.8	Montmorilloniti, Swelling, Very high expansivity
8	Ramesh and Sagar (2015)	CI	CI-Soil1	18.2	Intermediate plasticity	Highly Plastic	Normal	NS	-
9	Dhanesh and Mohandas (2016)		CI-Soil2	53	Intermediate plasticity	Highly Plastic	Inactive	NS	-
10	Shah and Shah (2016)		CI-Soil3	25.5	Intermediate plasticity	Highly Plastic	Normal	88	Montmorilloniti, Swelling, Very high expansivity
11	Nandini et al. (2015)	CL	CL-Soil1	78	Clay of low plasticity	Highly Plastic	Inactive	NS	-
12	Myint et al. (2014)		CL-Soil2	7.1	Sandy lean clay	Moderately Plastic	Active	170	Montmorillonitic, Swelling, Very high expansivity
13	Sodhi and Ocean (2018)	CL-ML	CL-ML	59	Silty clay	Slightly Plastic	Inactive	NS	-
14	Nandini et al. (2019)	MH	MH-Soil1	53	Silt of high plasticity	Highly Plastic	Inactive	NS	-
15.1	Kumar and Kumar Khan (2018)		MH-Soil2	40	Silt of high plasticity	Highly Plastic	Inactive	55	-
15.2			MH-Soil3	39.4	Silt of high plasticity	Highly Plastic	Inactive	48	-
16.1	Priyanka et al. (2016)		MH-Soil4	78	Silt of high plasticity	Highly Plastic	Inactive	75	Montmorillonitic Swelling, Very high expansivity
16.2			MH-Soil5	84	Silt with high plasticity	Highly Plastic	Inactive	81.82	
16.3			MH-Soil6	92	Silt of high plasticity	Highly Plastic	Inactive	90.5	
17	Farooq and Sukhdeep (2020)		MH-Soil7	20.4	Silt of high plasticity	Moderately Plastic	Normal	NS	-
18	Daigavane and Ansari (2021)		MH-Soil8	68.7	Silt of high plasticity	Highly Plastic	Inactive	NS	-
19	Jenith and Parthiban (2017)		MH-Soil9	20.2	Silt of high plasticity	Highly Plastic	Normal	NS	-
20	Myint et al. (2014)		MH-Soil10	53.8	Elastic silt	Highly Plastic	Inactive	93	Montmorillonitic, Swelling, Very high expansivity
21	Venika et al. (2015)	ML	ML-Soil	15.7	Silt of low plasticity	Slightly Plastic	Inactive	NS	-
22	Muguda and Nagaraj (2019)	SC	SC-Soil1	21	Clayey sand	Highly Plastic	Normal	120	Montmorillonitic, Swelling, Very high expansivity
23	Priyanka et al. (2016)		SC-Soil2	00	Clayey sand	Slightly Plastic	Inactive	25	-
24.1	Venkatasubramanian and Dhinakaran (2011)	SP-SC	SP-SC	8	Poorly graded sand with clay	Slightly Plastic	Normal	NS	-
24.2		SM	SM-Soil1	20	Silty sand	Slightly Plastic	Inactive	NS	-
24.3			SM-Soil2	12.5	Silty sand	Slightly Plastic	Inactive	NS	-
25	Shankar et al. (2009)	SM-GM	SM-GM	2	Silty sand	Moderate Plastic	Active	NS	-
26.1	Nandini et al., (2020a)	SP	SP-Soil1	1	Poorly graded sand	Moderate Plastic	Active	NS	-
26.2	Nandini et al. (2020b)		SP-Soil2	2.45	Poorly graded sand	Highly Plastic	Active	NS	-

Civil Engineering Infrastructures Journal 2023, 56(2): 301-319
DOI: 10.22059/CEIJ.2022.343391.1843

RESEARCH PAPER

The Comparison of Tunnel Convergence from Numerical Analysis with Monitoring Data Based on Different Constitutive Models in Rock Medium

Chalajour, S.[1] and Hataf, N.[2*]

[1] Ph.D., Graduate Student, Department of Civil Engineering, Shiraz University, Shiraz, Iran.
[2] Professor, Department of Civil and Environmental Engineering, Shiraz University, Shiraz, Iran.

Received: 21 May 2022; Revised: 12 Sep. 2022; Accepted: 22 Oct. 2022

ABSTRACT: Tunnels are used for numerous purposes; therefore, proper evaluation and prediction of tunnel behavior, influenced by the surrounding environment's characteristics, is of great concern for civil engineers. In this regard, two water convey and railway tunnels in rock medium were modelled to investigate the influence of various constitutive models on tunnels' behaviors prediction. The tunnel convergence predicted by each constitutive model was compared with the reported monitoring data. Then, the most appropriate constitutive models for tunnel analysis in each rock category were proposed according to the strength of each category's rocks. The results indicated that the Mohr-Coulomb criteria for very weak rocks, the Generalized Hoek-Brown for weak rocks and the Generalized Hoek-Brown with the residual parameter criteria for modelling medium rocks, had more reliable predictions of tunnel convergence. Also, utilizing shear strength parameters correlated from rock mass specific parameters to analyze tunnels in weak and medium rocks was not satisfactory.

Keywords: 3D Finite-Element Simulation, Constitutive Model, Monitoring Data, Rock Tunnel.

1. Introduction

Tunnels are generally used as underground structures for various purposes, including transportation routes, access paths, water transition ducts, powerhouse caverns, underground constructions, etc. Therefore, a proper evaluation and prediction of their behavior, which is influenced mainly by the materials of the surrounding media, is of great concern. Tunnel support system which is required to provide stability and safety, is also affected by tunnel behavior prediction (Hajiazizi et al. 2021). Various criteria and constitutive models have been proposed to simulate the ground behavior. Numerous studies have been conducted investigating the influence of different constitutive models on tunnel analysis. Oettl et al. (1998), based on the two-dimensional finite element analysis of the Vienna metro tunnel, investigated the effect of four different constitutive models on predicting settlements and stresses in the tunneling environment as well as forces developed in the support system by considering the

* Corresponding author E-mail: nhataf@shirazu.ac.ir

tunnel's monitoring data. Möller and Vermeer (2008), Rukhaiyar and Samadhiya (2016), Hejazi et al. (2008) investigated the results of two-dimensional finite element analysis using three different constitutive models of a hypothetical tunnel. Alejano and Alonso (2005) inspected the effects of constitutive models, for three rock categories, on the ground surface settlements prediction induced by tunneling. Vakili et al. (2014) studied the impact of different constitutive models on mechanized tunneling, for shallow and deep tunnels, by three-dimensional finite element analysis. In a three-dimensional analysis of the TBM tunnel, Jallow et al. (2019) examined the effect of different constitutive models on soil, adjusting surface settlement values with monitoring results. They also analyzed the effect of different parameters on long-term ground surface settlements. Mousivand and Maleki (2018) investigated the results of constitutive models in two-dimensional analysis by convergence-confinement method for shallow circular tunnels. Fong et al. (2022) investigated the appropriate anisotropic soils constitutive model in tunnel analysis by data matching and numerical simulation. Chen and Lee (2020) surveyed the deformation of tunnels by three-dimensional FEM analysis in horseshoe-shaped tunnels in different geological conditions by considering two Mohr-Coulomb and Hoek-Brown constitutive models and indicated that the magnitude and distribution of tunnel deformations were close by these two models. Further researches for analyzing deformations, induced by tunneling and comparing with data monitoring, have also been reported in the literature (Aksoy and Uyar, 2017; Su et al., 2019; Xing et al., 2018; Zhao et al., 2017; Beyabanaki and Gall, (2017), Sharifzadeh et al. (2012), Jin et al. 2020; Sun et al., 2020; Li et al., 2020; Xue et al., 2021).

Although numerous research has been performed on the effects of constitutive models on tunnel's characteristics, most investigations were carried out in the soil medium, and there is a lack of studies on rock characteristics. Basically, to obtain stresses and strains, a constitutive model is required to be introduced, and the simulations of rock and soil behaviors by utilizing numerical methods depend on the applied constitutive models.

This paper examines the effects of constitutive models on predicting the deformation and convergence of tunnels in homogeneous rock mediums. Based on the RMR classification system, a series of 3D numerical simulations with seven different constitutive models for three rock categories (very weak, weak and medium) commonly used in tunnel analysis have been conducted. Utilized models were Linear Elastic (LE) and Von Mises (VM) as general models; Mohr-Coulomb (MC), Drucker-Prager (DP) and Strain Softening (SS) as classical soil models; Generalized Hoek-Brown (GHB) and GHB with Residual parameters (GHBR) as special rock models.

In the LE model, the stress is linearly correlated with the strain, represented as Hooke's Law:

$$\sigma = E\varepsilon \tag{1}$$

where E: is the Young's modulus of the material; σ and ε: are the stress and strain, respectively. As seen, the constants of this model are only the Young's modulus and the Poisson's ratio. This model does not define a failure criterion.

In the VM model, the yield occurs when the value of the deviatoric stress reaches a critical value (Davis and Selvadurai, 2005). When this constitutive model is applied to a soil material, the effect of hydrostatic pressure is not considered, and the yield surface is the same for both tension and compression (Davis and Selvadurai, 2005). The von Mises yield condition is written as:

$$q = k \tag{2}$$

where q: is the deviatoric stress and k: is the yield stress of the material.

Mohr-Coulomb model is an elastic-perfectly plastic model and is one of the simplest and most widely models employed in geotechnical analyses. This is due to the few numbers of required model parameters and easy determination of them, despite the good model results. This model uses five parameters to express soil behavior. These include modulus of elasticity, *E*, and Poisson ratio, υ (both from Hooke's law), angle of internal friction, ϕ, and cohesion, *c*, (where both express the failure criterion), and the dilation angle, ψ, which is used to determine the plastic volume change due to shear stress (Ng et al., 2015). Mohr-Coulomb failure criterion is written as:

$$\tau = c + \sigma tan\phi \quad (3)$$

where τ and σ: represent the shearing and normal stress on the physical plane through which material failure occurs, respectively.

Drucker-Prager model is a modified von Mises model, introducing a dependence on the mean stress *p*:

$$q - \xi p = k \quad (4)$$

Constant parameters ξ and *k* could be selected such that the model agrees with the Coulomb surface. Similar to the Mohr-Coulomb failure criterion, this model is an elastic-perfectly plastic model, and its parameters are not complex. Unlike the MC model with the hexagonal yield surface on the deviatoric stress plane, the DP model has a circular yield surface (Davis and Selvadurai, 2005).

The SS model consists of a linear part until it reaches the peak shear strength value. After that, the failure occurs, and the shear strength is reduced to the residual shear strength. This model consists of three nonlinear parameters to define strain softening. These include peak cohesion, *Cp*, residual cohesion, *Cr*, and softening rate, *R* (MIDAS Information Technology Co., 2018).

The GHB failure criterion is used to estimate the strength and deformations of jointed rock masses. In this model, three characteristics of rock mass should be considered: uniaxial compressive strength of intact rock, σ_{ci}, Hoek-Brown constant values (i.e., m_i, m_b and *s*) and Geological Strength Index, GSI, for rock mass (Yasitli, 2016). The modified Hoek-Brown equation is defined by:

$$\sigma_1 = \sigma_3 + \sigma_{ci}\left(m_b\frac{\sigma_3}{\sigma_{ci}} + s\right)^a \quad (5)$$

$$m_b = m_i \exp\left(\frac{GSI - 100}{28}\right) \quad (6)$$

where σ_1 and σ_3: are maximum and minimum principal stresses, respectively. The Hoek-Brown parameters can be related to MC constitutive model parameters. More details can be found in Hoek et al. (2002), Eberhardt (2012), Chen and Lee (2019), Hoek and Brown (2019), He et al. (2022).

The GHBR constitutive model is obtained by substituting the GSI_{Peak} to $GSI_{Residual}$ in the Hoek-Brown model. This model behaves similar to the SS model and based on plastic softening behavior of rock, calculates smaller values for residual than the peak values. With respect to GSI, rock masses with GSI > 75 have brittle behavior, with 25 < GSI < 75 have softening behavior, and with GSI < 25 exhibit complete plastic behavior (MIDAS Information Technology Co., 2018). More information regarding determining the residual parameters based on Hoek-Brown criteria can be found in the investigations of He et al. (2020).

2. Geology, Location and Monitoring of Babolak Water Convey and Isfahan-Shiraz Railway Tunnels

2.1. Babolak Water Convey Tunnel

A cofferdam was constructed at a 700 m distance upstream of Temer Village (Alborz Province, Iran) on Babolak river to provide the required water for the Alborz storage dam. The cofferdam transmits Babolak river water to Babol river at Alborz main dam upstream by a diversion tunnel. Six boreholes were drilled in marl and

marlstone to investigate the properties of the rock as a part of the site investigation of the tunnel. Also, the overburden of the tunnel at three stations of 0 + 550, 0 + 603 and 0 + 638 m was 70, 85 and 89 m, respectively. Three other boreholes at stations 0 + 717, 0 + 732 and 0 + 848 m are located in sandstone with overburden depths equal to 105, 107 and 120 m, respectively. The excavation of the tunnel was performed by a road header machine (Asadollahpour et al., 2014) with an average excavation rate of 1 m/day. The tunnel's support system was shotcrete, wire mesh, a steel frame with 1 m spacing and rock bolts (Asadollahpour, 2011). Due to the sensitivity of the rock mass, after initial drilling, a 5 cm initial layer of shotcrete was applied in order to prevent the effects of moisture and weathering. Then, the steel frames and wire mesh grid were installed, and the second layer of shotcrete was applied with the progress of the tunnel face. Figure 1 shows the cross-section of the Babolak water convey tunnel. The joints and materials were characterized along the tunnel rout and the results are presented in Tables 1-3.

Table 4 presents the calculated parameters on station 0 + 603 km of Babolak tunnel route, which consists of marl according to RMR classification.

At station 0 + 603, five convergence pins, according to Figure 2 were installed. One was located at the tunnel crown, which is labelled as C, and four were on the wall, labelled as RC, LC, RL and R1L1 in Figure 2.

Figure 3 shows the monitored convergence data at this station for 290 days after the tunnel construction.

Table 1. Rock density ($\frac{gr}{cm3}$) of the Babolak tunnel (Asadollahpour. E, 2011)

Specimen type	Condition	Number of experiments	STD	AVE	MAX	MIN
Marl	Dry	5	0.17	1.90	2.14	1.73
	Wet	5	0.12	2.17	2.34	2.08
Sandstone	Dry	7	0.16	2.23	2.43	2.00
	Wet	7	0.10	2.38	2.52	2.24

Table 2. Rock uniaxial compressive strength (σ_{ci}) of Babolak tunnel (Asadollahpour, 2011)

Test condition	Rock mass type	Compressive strength (MPa)	Elasticity module (GPa)
Dry	Marl	7.5-15	0.5-7.29
Dry	Sandstone	-	-

Table 3. Discontinuity conditions and characteristics of the route of Babolak tunnel (Asadollahpour, 2011)

	Dip (Deg.)	Dip direction (Deg.)
Bedding	29	129
Discontinuity 1	26	116
Discontinuity 2	46	160
Discontinuity 3	51	300
Discontinuities endurance		1-3 m
Opening		1-5 mm (shallow parts) 0.1-1 mm (Deep parts)
Fillings		5 mm
Roughness		Smooth
Weathering		Little to average
Water condition in discontinuities		Damp

Table 4. Rock parameters of Babolak tunnel

	RMR89	Adjustment of joints orientation	Groundwater table condition	Discontinuity condition	Joints spacing (m)	σ_{ci} (MPa)	RQD
Condition/Value	-	Favorable or very favorable	Wet	According to Table 3	1-3	7.5-15	35
Grade	45-57	0 or -2	10	17-12	20-15	2	8

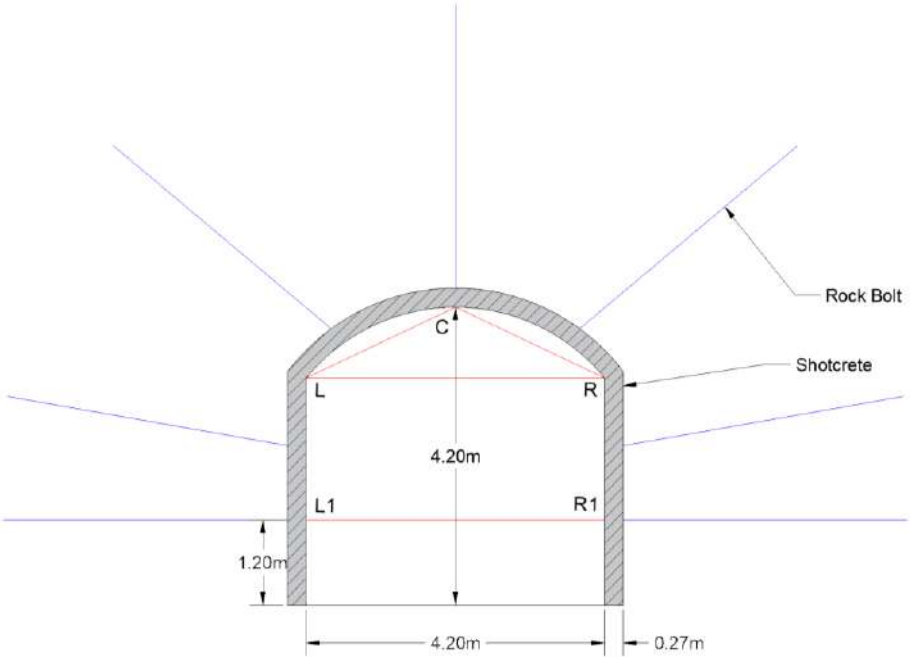

Fig. 1. The cross section of Babolak Tunnel (Dadashi et al., 2012)

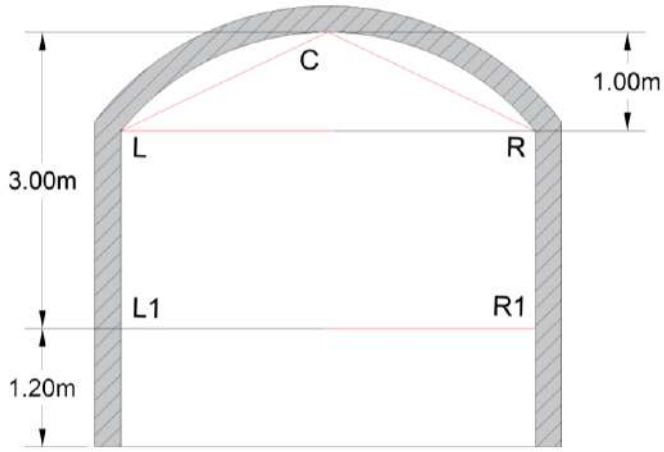

Fig. 2. The position of the monitoring instruments of Babolak tunnel (Asadollahpour, 2011)

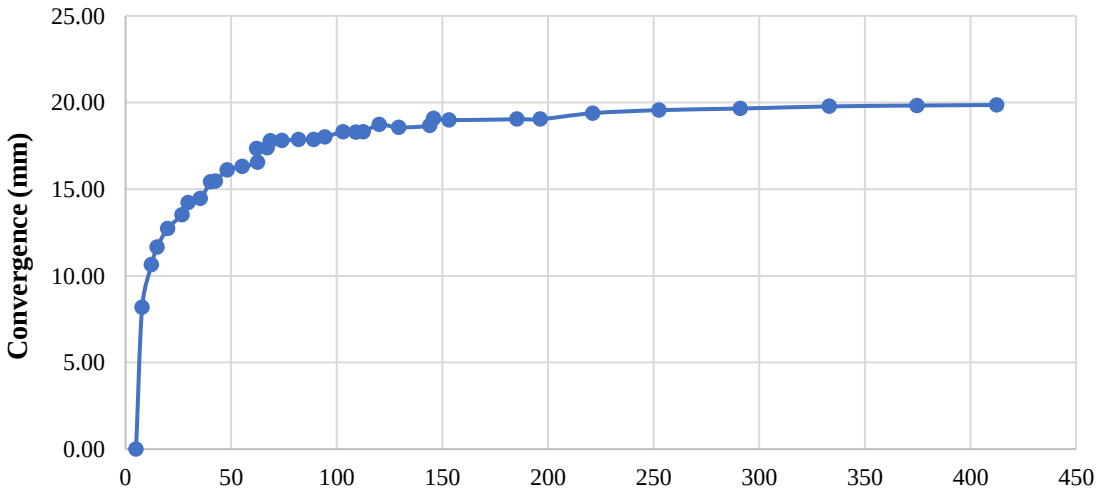

(a)

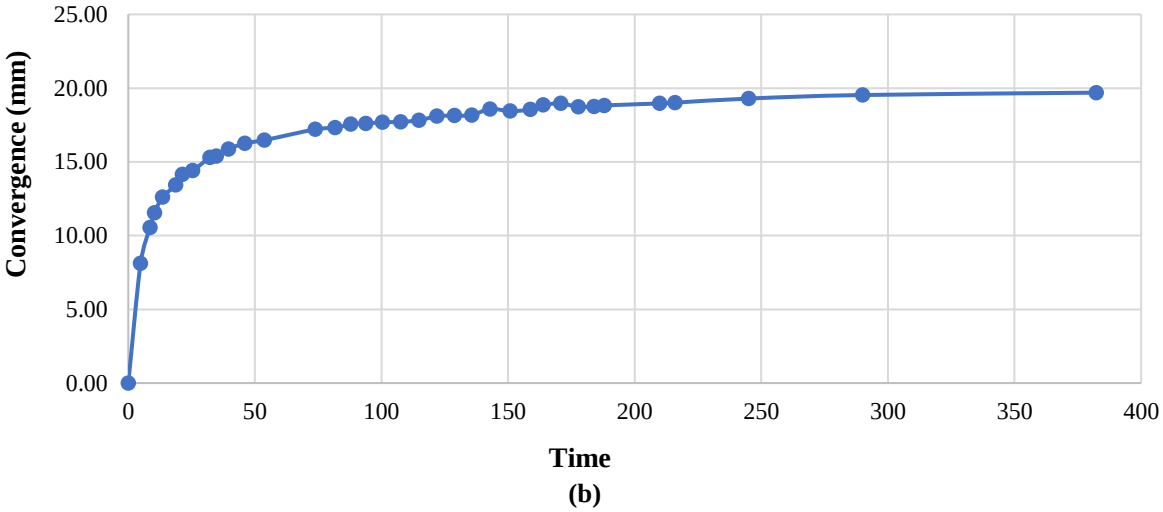

(b)

Fig. 3. Convergence data for R1L1 direction: a) According to the distance from the tunnel face; and b) Time at station 0 + 603 (Asadollahpour, 2011)

As shown in Figure 2, the convergence measurements are in the directions of RC, LC, RL, R1L1. The comparison of numerical results has been performed with R1L1 direction results only since due to the presence of the road header, and relatively low convergence in the directions of RC, LC, RL, inaccurate recordings of monitoring data was done. Consequently, the initial measurements of monitoring data were performed at far distances from the tunnel face except for the R1L1 direction, where the first measurements were done at a distance of approximately 3 to 5 m far from the tunnel face (Asadollahpour, 2011).

2.2. Isfahan-Shiraz Railway Tunnel

The Isfahan-Shiraz railway tunnel is located in Fars province (south of Iran). This tunnel is in the Shemshak formation, which is geologically related to the Jurassic age and includes shale coal and sandstone seams with a horseshoe-shaped cross-section. The tunnel has a length of approximately 820 m and 5.75 m height and 8.2 m in width. Figure 4 illustrates the cross-section of the Isfahan-Shiraz railway tunnel. As shown in this figure, the temporary support system of the tunnel consists of two layers of wire mesh, 25 cm thick shotcrete and the steel frame (Sarikhani Khorami, 2012). The B1-1 convergence station was situated at 269 + 047.5, which is located at a distance of about 717.5 m from the entrance of the tunnel. The tunnel overburden at this station is 29 m high, and the rocks are mostly shale and sandstone. Figure 5 shows the graphs of the tunnel convergence based on the distance from the tunnel axis (Sarikhani Khorami, 2012).

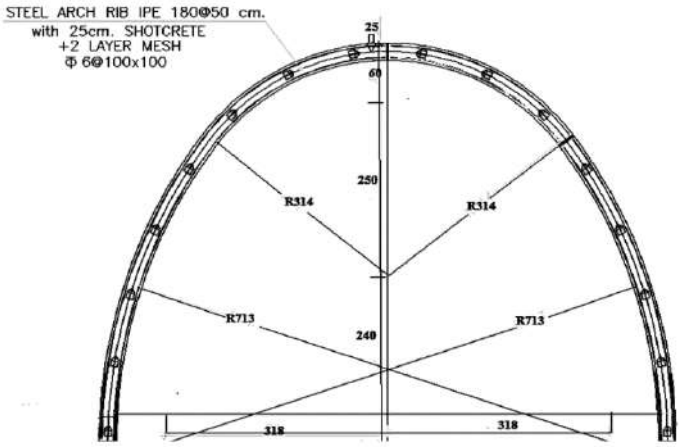

Fig. 4. The cross-section of the Isfahan-Shiraz railway tunnel (Sarikhani Khorami, 2012)

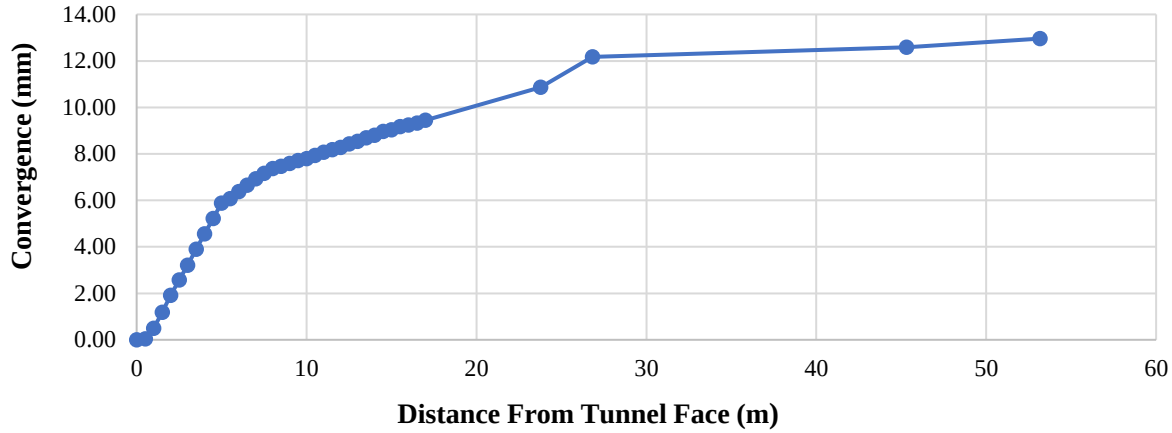

Fig. 5. The tunnel convergence, based on distance from the tunnel face (Sarikhani Khorami, 2012)

3. Determination of Rock Mass Parameters

The rock mass parameters were calculated utilizing RocData software (User's Guide of RocData, 2004) based on the Hoek-Brown failure criterion. The input parameters include compressive strength of intact rock, Geological Resistance Index (GSI), m_i for intact rock, disturbance factor (D), specific gravity of rock and the tunnel depth. Singh and Goel (1999) proposed a relation based on stress measurement in hydraulic fracture test in Himalaya weak rocks for overburden less than 400 m as follows:

$$\sigma_H = 1.5 + 1.2\,\sigma_v \quad (7)$$

$$\sigma_h = 1 + 0.5\,\sigma_v \quad (8)$$

$$\sigma_v = \gamma . z$$

where γ: is the unit weight of rock, Z: is the tunnel overburden. The σ_H, σ_h and σ_v: are maximum and minimum horizontal and vertical stresses, respectively. In this study, the mentioned method to determine the horizontal stress was considered.

3.1. Rock Mass Parameters of Babolak Water Convey Tunnel

To determine the rock mass parameters at station 0 + 603 km with an overburden of 88 m, the ratio of in situ horizontal stress coefficient (K) in Babolak water convey tunnel was calculated as 1.5 (Singh and Goel, 1999). According to the mentioned characteristics of the tunnel environment, the rock mass can be considered as weak to medium rock based on the geomechanics classification or the rock mass rating (RMR) (Bieniawski, 1993). In order to assess according to the RMR system, a site is divided into a number of geological structural units. Then each type of rock mass of the research site is represented by a separate geological structural unit. The six parameters are calculated for each structural unit, including uniaxial compressive strength of intact rock material, Rock Quality Designation (RQD), joint or discontinuity spacing, joint condition, groundwater condition, and joint orientation. Therefore, the RMR classification is determined based on an algebraic sum of ratings for all the parameters mentioned (Goel and Singh, 2011). For this study, the required rock mass information was obtained according to the site investigation and can be found in Tables 1-4. Various research has been conducted to calculate other parameters based on RMR classification.

Moreover, the unit weight and Poisson's ratio were estimated to be 19 kN/m^3 and 0.35, respectively, for the weak rock and 20 kN/m^3 and 0.3 for the medium rock. Also, the ground disturbance factor (D) was considered as zero for all simulations to reduce influenced factors and consistency for all rock conditions. The disturbance factor greater than zero can influence the behavior of each rock strength category variously. The rest of the calculated values are presented in Tables 5 and 6.

Table 5. The calculated parameters of the Babolak water convey tunnel

Rock type	Sample	σ_{ci}	RMR	GSI	Mi	Em	σ_{cm}	φ	C	ψ	GSI residual	C residual
Unit	-	MPa	-	-	-	MPa	kPa	Deg.	kPa	Deg.	-	kPa
Weak	Marl, Sandy Marl	15	45	40	9	2170	1980	26.71	459	1.9	23.4	327
Medium	Marl, Sandy Marl	15	57	52	9	4350	2600	30.21	560	4.07	25.91	348

Table 6. The Hoek and Brown parameters obtained from RocData for Babolak water convey tunnel

Parameter	a	s	m_b
For weak category	0.511	0.0013	1.056
For medium category	0.505	0.0048	1.621

In Table 5, σ_{ci}: is the uniaxial compressive strength of the intact rock, RMR: is rock mass rating, GSI: is the geological strength index of the rock mass, Mi: is the value of the Hoek-Brown constant, Em: is elastic modulus of the rock mass, σ_{cm}: is the compressive strength of rock mass, φ: is fraction angle, C: is cohesion value, ψ: is rock mass dilation angle, GSI and $C_{residual}$: are the residual geological strength index and cohesion of the rock mass, respectively.

3.2. Rock Mass Parameters for Isfahan-Shiraz Railway Tunnel

Table 7 indicates the rock mass parameters of the tunnel environment in addition to the shear strength parameters calculated based on the ground characteristics. According to the characteristics of the tunnel, the site rock mass is located at very weak rock category based on the RMR classification, which could almost be classed as engineering soils (Hoek and Brown, 1997). The behavior of these types of rock mass differs considerably from the tightly interlocked hard rock mass (Hoek et al., 1992). Also, the in-situ horizontal stress in the Isfahan-Shiraz railway tunnel with 29 m overburden was obtained 2.48. In this table, γ: is rock mass unit weight, κ: is the ratio of horizontal over vertical stress at tunnel depth, and ν: is Poisson's ratio.

Table 8 summarizes the parameters selected for each constitutive model according to the previous discussion based on the input required parameters in the software. It should be noted that the selected values are based on the median of rock properties categories according to the RMR classification.

4. Numerical Simulation

In this study, the numerical analyses were performed by the commercially available software MIDAS GTS NX 2018; a simulation program developed to evaluate geotechnical aspects and the interaction of soils and structures based on the Finite Element Method (FEM). Moreover, to simulate the longitudinal dimension of the tunnel, Panet equation (Sulem et al., 1987) was used. According to this equation, 98% of the total tunnel displacements occur at a distance of up to 2 times the tunnel diameter from its face. The creep and time-dependent behavior of rocks showed no significant impact at this distance (Asadollahpour et al., 2014).

Table 7. The Ground parameters for the Isfahan-Shiraz railway tunnel

Rock type	Sample	σ_{ci}	RMR	GSI	Mi	E_m	σ_{cm}	φ	C	ψ	γ	κ	ν
Unit	-	MPa	-	-	-	MPa	kPa	Deg.	kPa	Deg.	kN/m^3	-	-
Very weak	Shale	8.2	17	12	7	321	391	16.15	112	0	24	2.48	0.25

Table 8. Input parameters for each constitutive model for numerical simulations

Rock type	Constitutive model	Em (MPa)	γ (kN/m^3)	ν	σ_{cm} (kPa)	Φ (Deg.)	C (kPa)	Ψ (Deg.)	C residual (kPa)	a	s	m_b	GSI	GSI residual
Very weak	EL	321	24	0.25	-	-	-	-	-	-	-	-	-	-
	VM	321	24	0.25	391	-	-	-	-	-	-	-	-	-
	DP	321	24	0.25	-	16.15	112	0	-	-	-	-	-	-
	MC	321	24	0.25	-	16.15	112	0	-	-	-	-	-	-
Weak	EL	2170	19	0.35	-	-	-	-	-	-	-	-	-	-
	VM	2170	19	0.35	1980	-	-	-	-	-	-	-	-	-
	DP	2170	19	0.35	-	26.71	459	1.9	-	-	-	-	-	-
	MC	2170	19	0.35	-	26.71	459	1.9	-	-	-	-	-	-
	SS	2170	19	0.35	-	26.71	459	1.9	327	-	-	-	-	-
	GHB	2170	19	0.35	-	-	-	-	-	0.511	0.0013	1.056	40	-
	GHBR	2170	19	0.35	-	-	-	-	-	0.511	0.0013	1.056	40	23.4
Medium	EL	4350	20	0.3	-	-	-	-	-	-	-	-	-	-
	VM	4350	20	0.3	2600	-	-	-	-	-	-	-	-	-
	DP	4350	20	0.3	-	30.21	560	4.07	-	-	-	-	-	-
	MC	4350	20	0.3	-	30.21	560	4.07	-	-	-	-	-	-
	SS	4350	20	0.3	-	30.21	560	4.07	348	-	-	-	-	-
	GHB	4350	20	0.3	-	-	-	-	-	0.505	0.0048	1.621	52	
	GHBR	4350	20	0.3	-	-	-	-	-	0.505	0.0048	1.621	52	25.91

4.1. Numerical Simulation of Babolak Water Convey Tunnel

Dimensions of the FEM model for this tunnel are 46.5 × 114 × 36 m and the numerical modeling results are extracted within 5 m of the tunnel face, corresponding to field measurements. The dimensions of the Finite Element (FE) models are considered to be greater than five times the tunnel diameter on each side (Vitali et al., 2018) and 12 times greater than the tunnel diameter in the longitudinal direction. The tunnel face is located at a distance of 6 times the diameter of the tunnel's beginning. According to the 4.2 m span of the Babolak water convey tunnel, the results are considered 13 m in the longitudinal direction of numerical modeling compared with monitoring data. Table 9 shows the properties and types of the tunnel support system in the numerical modeling. The equivalent thickness of the shotcrete and steel frame was considered 26.6 cm in numerical simulation, and 25 mm diameter rebars of AIII steel were utilized for rock bolts. Figure 6 shows the FE model of the tunnel in the software.

Table 9. Properties of Babolak water convey tunnel support system in numerical modeling

Parameter	Rock bolt	Shotcrete and Latice
Material	Steel	Concrete
Model type	Elastic	Elastic
Mesh type	1D-Embedded truss	2D-shell
Elastic modulus(kPa)	2.1×10^8	2.2×10^7
Thickness	2.5	26.6
Poisson's ratio	0.3	0.25
Density (kN/m^3)	78	24

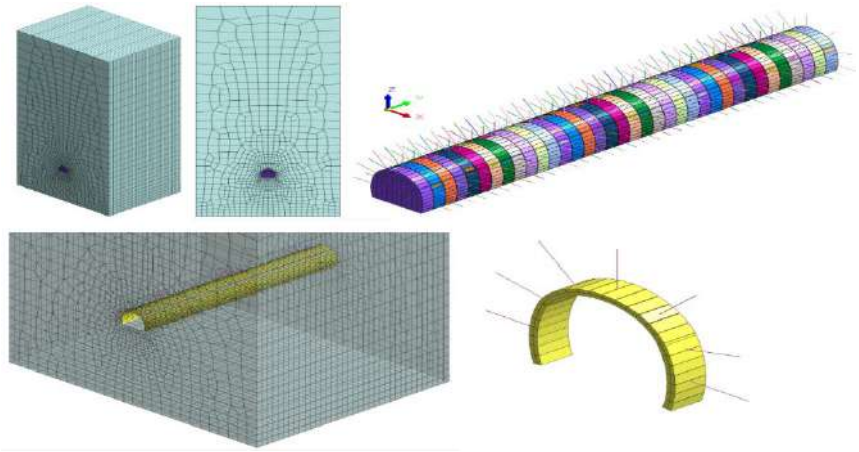

Fig. 6. Babolak tunnel cross-section and support system FE models

4.2. Numerical Simulation of Isfahan-Shiraz Railway Tunnel

Seventeen meters of the Isfahan-Shiraz railway tunnel with 8.2 m span was considered for numerical modeling. The simulation steps were whole cross-section drilling and applying shotcrete simultaneously. The average distance between the tunnel face and the installation of the support system is approximately 0.5 m, and the temporary tunnel support system was modeled as the equivalent of shotcrete thickness. Figure 7 shows the FE model of the tunnel. Shotcrete material properties are also mentioned in Table 8. The boundary conditions of the models were applied by closing the degrees of freedom in the vertical direction and vertical and horizontal directions at the side and bottom of the model, respectively.

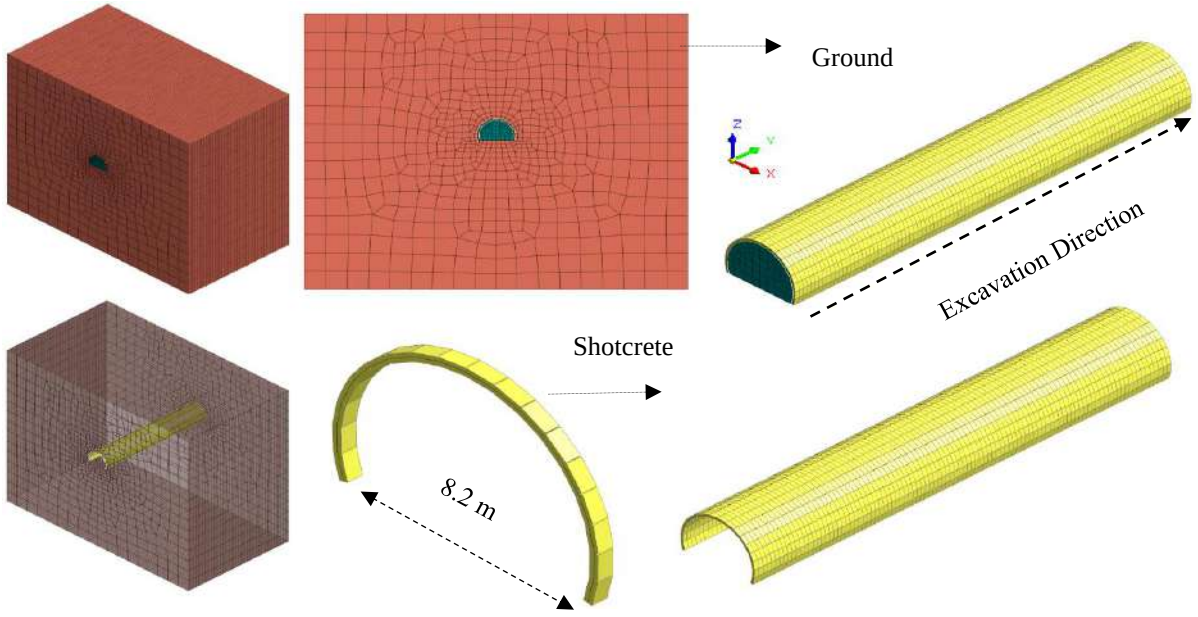

Fig. 7. Isfahan-Shiraz railway tunnel cross section and support system models in software

The numerical modeling procedure for both tunnels was conducted in seven steps:

1- Define the model geometry;
2- Define the material constitutive model and support system material parameters;
3- Excavation and support system in the geometry of the model;
4- Define boundary conditions and mesh generation;
5- Define analysis sequence in the mesh of the model (Stage construction sequence: Apply the in-situ condition, Ground excavation, Application and activation of the tunnel support systems);
6- Perform analysis;
7- Compare the obtained results with monitoring data.

5. Results and Discussions

The results of the numerical analysis of the Isfahan-Shiraz tunnel as well as the Babolak water convey tunnel were compared with the monitoring data of each tunnel.

5.1. Very Weak Rocks (Isfahan-Shiraz Railway Tunnel)

In this rock category, rock-specific constitutive models (GHB and GHBR) and SS were not able to converge equilibrium equations, and only simulation with four constitutive models of LE, VM, DP, and MC indicated the results. It is believed that the very weak rocks behave as a geomaterial; therefore, the rock-specific models are not able to analyze the geomaterial properties. Investigations have revealed that the relationship between RMR and m and s is no longer linear in these very low ranges; therefore, the rock mass specific model of Hoek-Brown cannot be suitable for this rock category (Hoek et al., 2000).

Input parameters for each model are mentioned in Table 7 and were consistent during the analysis in order to obtain the predicted convergence value for each constitutive behavior model. For instance, elastic modulus and Poisons ratio were considered 321 Mpa and 0.25, respectively, for this rock category. The shear strength parameters, including cohesion value and friction angle, also were considered 112 kPa and 16.12 degrees. These shear strength parameters were the same for MC and DP models. Moreover, the uniaxial shear strength parameter for the rock mass was derived at 391 kPa based on very weak rock strength properties.

The predicted values of the tunnel convergence under the four mentioned constitutive models and monitoring data are presented in Figure 8. The results of the numerical simulation considered for approximately 16 m in order to reduce the influence of the time-dependent behavior of rock mass in numerical simulation. It can be observed that MC constitutive model can predict the results in good agreement with the monitoring data of the tunnel. The VM model showed higher values of convergence, and both LE and DP models showed lower than the monitoring data.

5.2. Weak Rocks (Babolak Water Convey Tunnel)

Similarly, for all numerical simulations in weak rocks, the input parameters of the selected models were considered constant. The elastic modulus and Poisson's ratio were 2170 Mpa and 0.35, respectively. Also, the shear strength parameters for MC and DP were 459 kPa and 26.51 degrees. Other required parameters as input values for behavior models can be found in Tables 5 and 6.

In this rock category, the equations of all seven constitutive models were converged in numerical modeling. As shown in Figure 9 the GHB model is in good agreement with the monitoring results, but SS and the GHBR models showed the tunnel convergence value greater difference than the monitoring data. In this category, the general (LE and VM) and soil (MC and DP) constitutive models provided approximately similar results, which are less than the values predicted by rock mass constitutive models. The figures from these models are coincident in Figure 9. It can be

justified as the rock mass specific constitutive models consider the rock mass strength properties with parameters such as disturbance factor, uniaxial compressive strength, rock classification coefficient and geological strength index; therefore, these models have more realistic results compared with general and soil mechanics models for rock mass analysis.

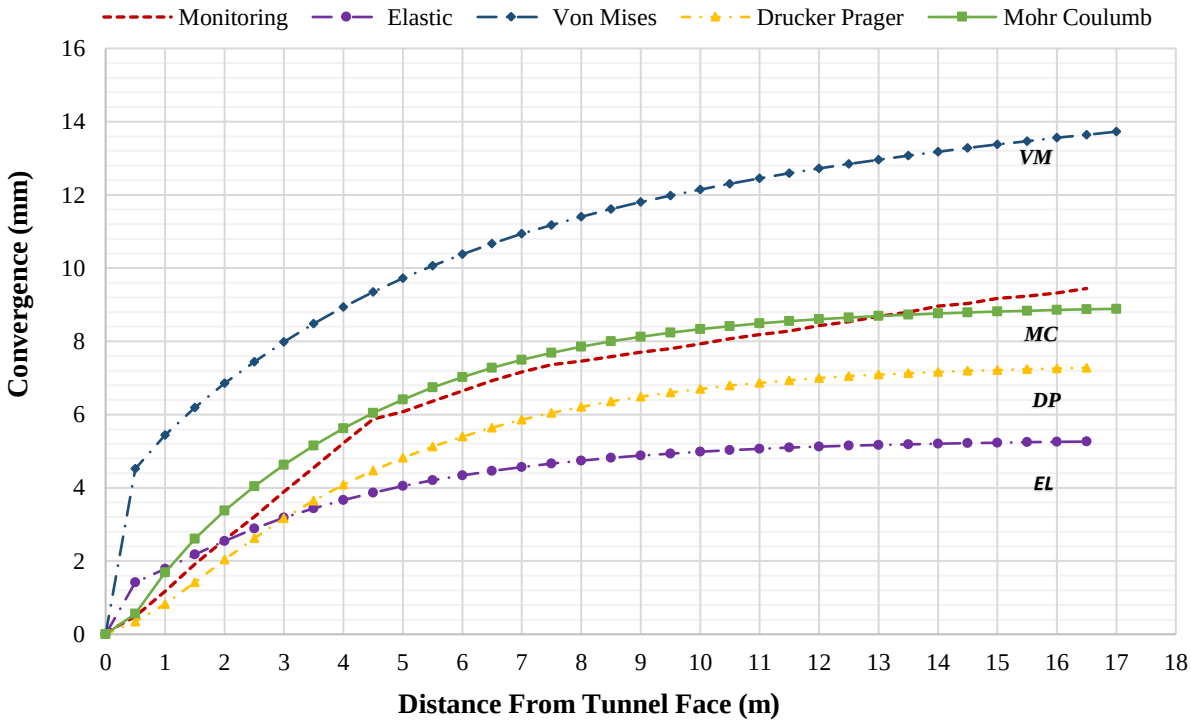

Fig. 8. The comparison of Isfahan-Shiraz railway tunnel modeling results with monitoring data in very weak rock

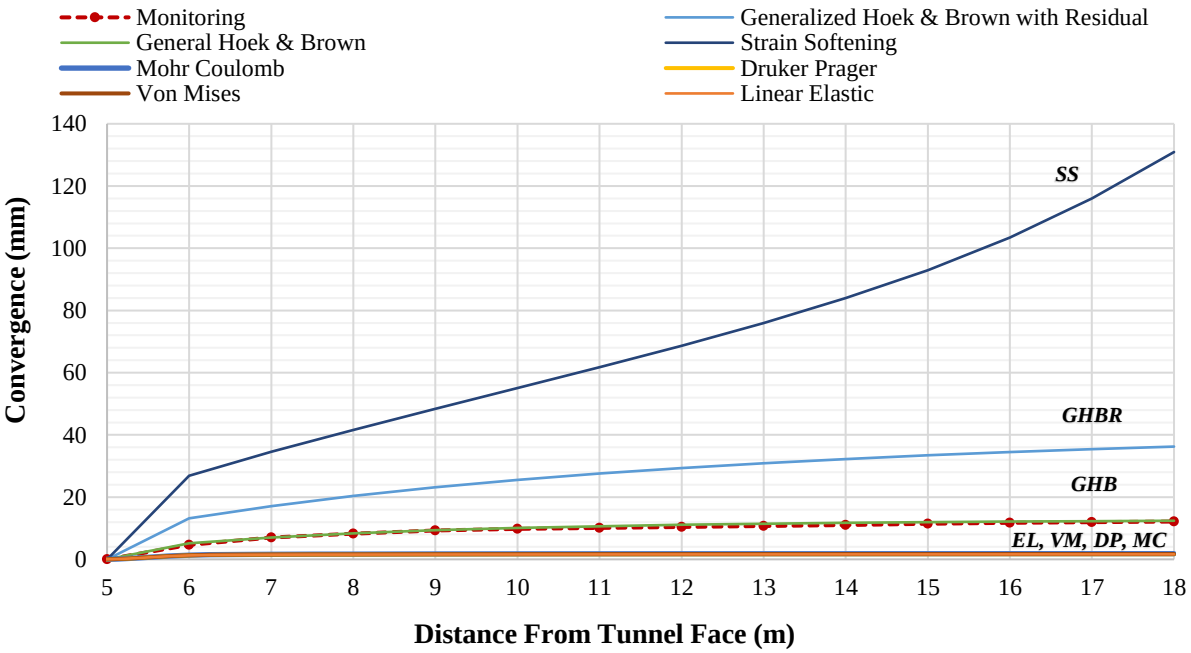

Fig. 9. The Comparison of Babolak Water convey tunnel numerical modeling results with monitoring in weak rock category

5.3. Medium Rocks (Babolak Water Convey Tunnel)

Input parameters for medium rocks were mentioned in Tables 5 and 6. In this category of rocks, the equations of all seven constitutive models were converged in numerical modeling. According to Figure 10, the results of the GHBR were most compatible with the monitoring data, and the LE, VM, DP, as well as MC, showed the same results and were lower than the monitoring data. Therefore, the predicted values are coincident in Figure 10. In this category, the GHB indicated the tunnel convergence of nearly one-quarter, and SS showed almost twice the monitoring data. The other general and soil mechanics models showed the same results and by far less than the monitoring data. However, the GHBR predicted the results in good agreement with the monitoring data.

5.4. Comparison of Numerical Analysis Results of Tunnel Crown Settlement Profile

Figure 11 presents the values of crown settlements along with the longitudinal axis of the mentioned tunnels, obtained from numerical analysis using different constitutive models for the three rock categories of very weak, weak and medium. According to Figure 11 in very weak rock categories (Isfahan-Shiraz railway tunnel), the VM constitutive model predicted the vertical crown settlements at the front of the tunnel face 14.35 mm and more than that of other models. The values of 12.15, 7.58, and 2.44 mm were also obtained for the vertical crown settlements at the tunnel face for MC, DP, and LE constitutive models, respectively. Moreover, the difference between the two models of MC and DP is considerable, and the MC constitutive model showed higher values than the DP model. The least value was predicted by LE. In the numerical simulation in this rock category, the constitutive models of GHB, GHBR and SS were not converged.

According to Figures 12 and 13, in the weak and medium rock categories (Babolak water convey tunnel), three constitutive models of VM, DP, and MC showed approximately the same values for the vertical settlements of the tunnel crown. Also, the LE model indicated the crown settlement slightly lower values than the models mentioned above. However, SS model in the weak and medium rock categories showed the crown settlement more than all other constitutive models. From the GHB and GHBR models, the crown settlement was higher than the other models. Table 10 summarizes the values of the crown settlement of the tunnel for two categories of weak and medium rocks.

5.5. Investigation of Rocdata and Back Analysis Shear Strength Parameters in Convergence Value

Calculation of shear strength parameters of rock mass in the absence of experimental lab test data was performed by back analysis and empirical equations for this study. As mentioned in Section 4, the shear strength parameters calculated by RocData were derived from the Hoek and Brown parameters. In this section, a comparison of the shear strength data obtained from the back analysis and RocData is performed. Table 11 indicates the difference between the results of back analysis and the obtained shear strength parameters from rock mass parameters. Furthermore, Figure 14 compares the numerical modeling results based on the shear strength parameters obtained from the two mentioned methods with Babolak water convey tunnel monitoring data.

Table 10. The amount of crown settlement in Babolak tunnel face (mm)

	Elastic	Von mises	Drucker prager	Mohr coulomb	Generalized Hoek and Brown	Generalized Hoek and Brown with residual
Weak rocks	0.68	0.72	0.7	0.74	2.78	5.41
Medium rocks	0.42	0.43	0.43	0.43	1.00	2.17

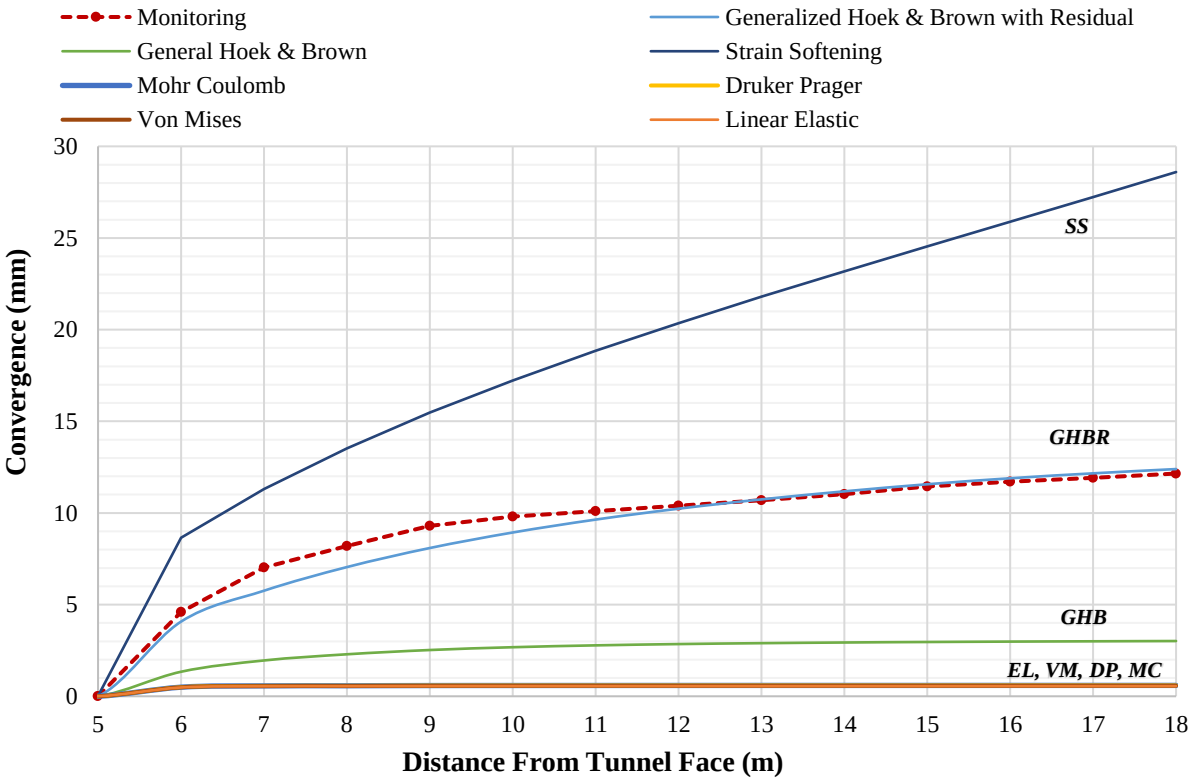

Fig. 10. The Comparison of Babolak water convey tunnel numerical modeling results with monitoring in medium rock category

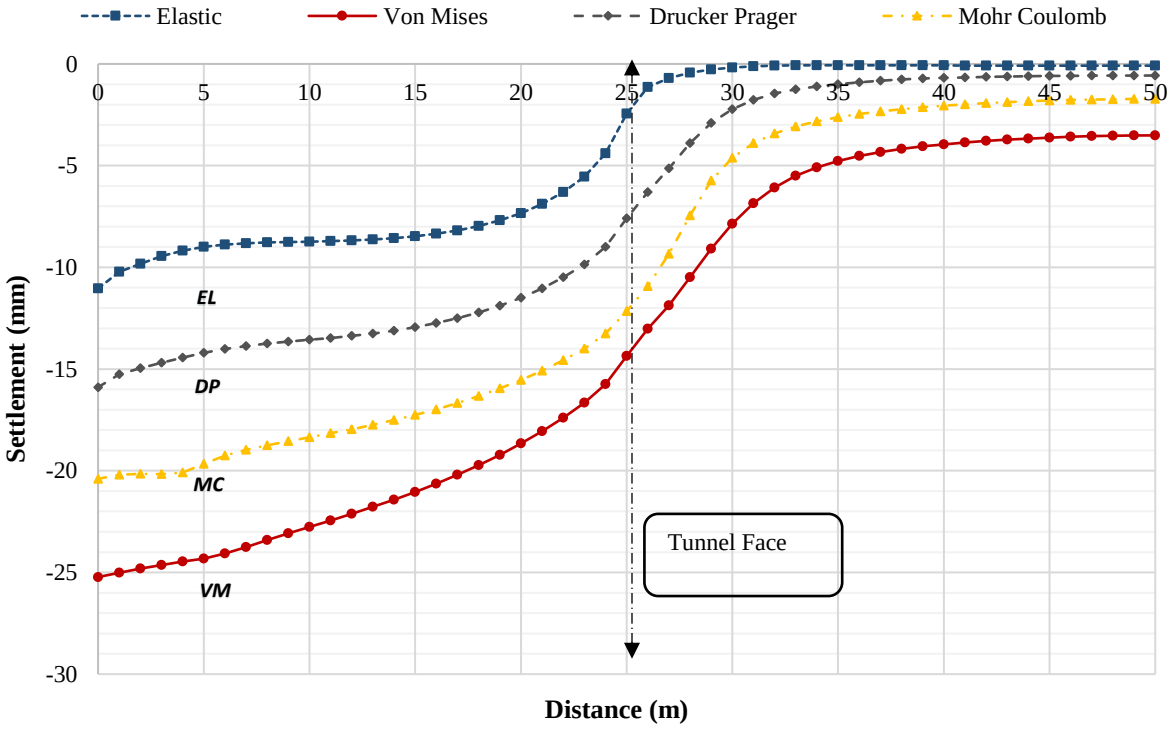

Fig. 11. The Comparison of Babolak water convey tunnel numerical modeling results with monitoring in medium rock category

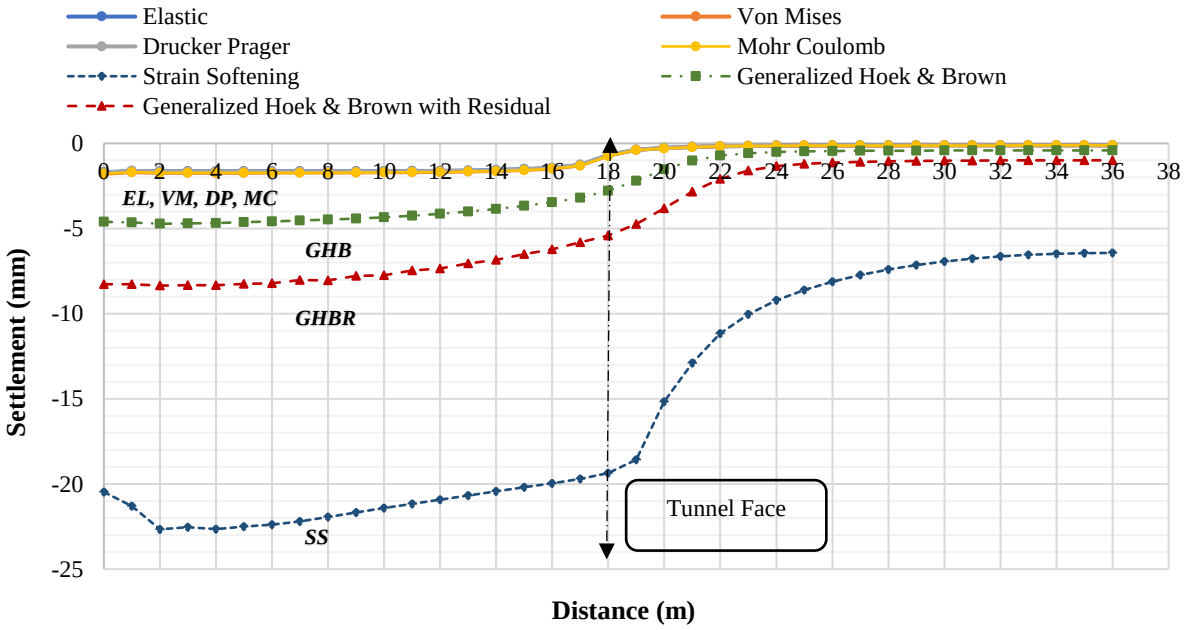

Fig. 12. Crown settlement values along the longitudinal axis of the tunnel obtained from numerical analysis of Babolak water convey tunnel in weak rock category

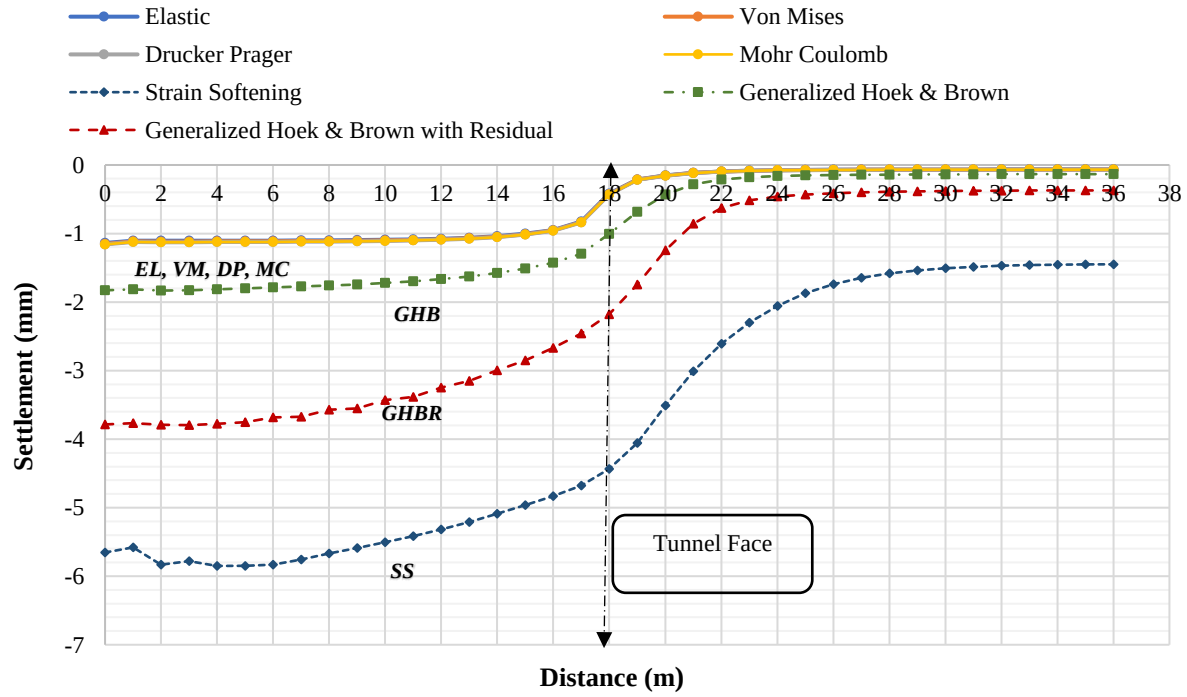

Fig. 13. Crown settlement values along the longitudinal axis of the tunnel obtained from numerical analysis of Babolak water convey tunnel in medium rock category

Table 11. Comparison of the results of shear strength parameters obtained from RocData software and back analysis for Babolak water convey tunnel

Parameter	Cohesion (kPa)	Friction angle (Deg.)	Elastic modules (MPa)
RocData	459	26.7	2170
Back analysis	90	27.0	2170

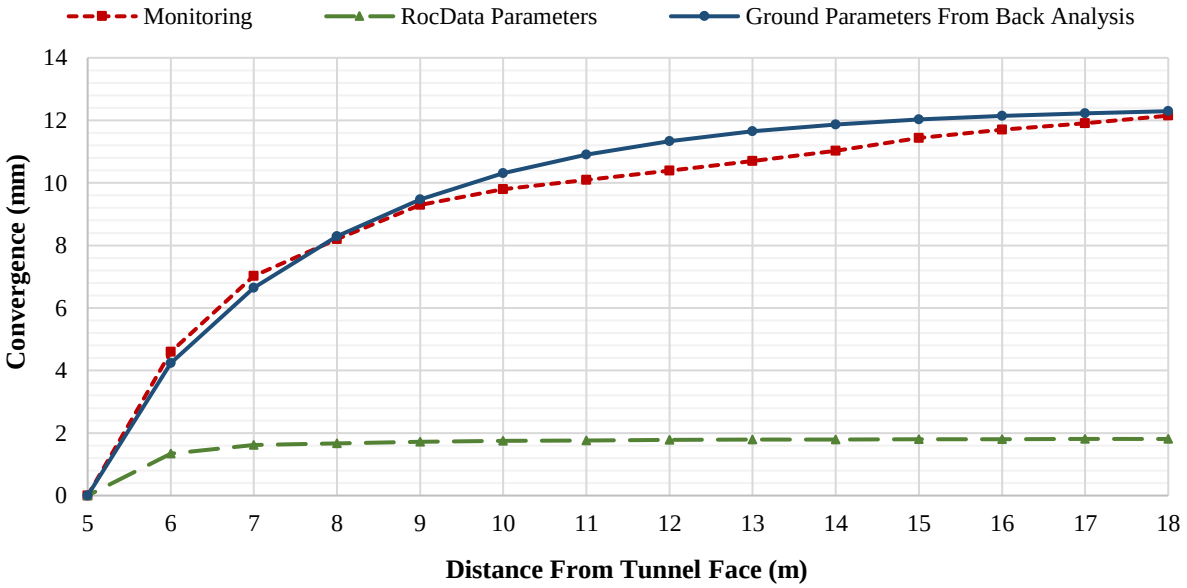

Fig. 14. Comparison of crown settlement values along the longitudinal axis of the tunnel with RocData and back analysis shear strength parameters of Babolak water convey tunnel in medium category of rocks

It can be understood from Table 10 that in the constant elastic modulus, the friction angle of the RocData was pretty close to the friction angle calculated from the back analysis method, However, the obtained cohesion value based on the correlation from the Hoek and Brown theory was approximately five times the cohesion calculated from the back analysis.

6. Conclusions

In this study, tunnel behaviors were examined under different constitutive models in three rock categories. Initially, calculating the rock mass parameters in the absence of sufficient experimental data and in-situ tests was discussed. Then, two case studies of Babolak water convey and Isfahan-Shiraz railway modeled in the finite element software in order to assess the influence of various constitutive models on the tunnels' face convergence and ground settlement. The obtained results from the numerical simulations were compared with the monitoring data to propose the most appropriate model for tunnel analysis in rocks. Then, a comparison was made between the correlation of the shear parameters from the empirical equations and the back analysis approach. According to the performed analyses, the following results are presented in predicting the behavior of rock tunnels for the assumed conditions in this study:

- Since constitutive models represent the material behavior, they can significantly influence the analysis results. Therefore, utilizing an appropriate constitutive model is the most stage in numerical modeling, and it should be implemented based on accurate data.
- The LE model does not have a failure criterion and utilizing this model should be with caution where there is a probability of failure of the elements.
- The MC model was in the good agreement range with the monitoring data in very weak rocks. However, the difference between the convergence of MC and DP was not significant for this rock category.
- The GHBR showed more convergence values than the monitoring data in the category of weak rocks. According to the recommended range of GSI index for the softening behavior of rocks, weak rocks are placed at the beginning of the

softening behavior interval; therefore, the results of this model cannot be reliable. However, GHB constitutive model results were almost in accordance with the monitoring data. Thus, the GHB model is suggested in this category of rocks.

- For the medium rocks, as this category is located at the recommended range of softening behavior of rocks, this behavior of the rock mass should be considered in the analysis. Also, the predictions of GHBR model from numerical analysis are almost compatible with monitoring data.
- Although soil shear strength parameters can be obtained by correlation from the rock mass parameters, the difference between the results of the correlated data and parameters from back analysis was considerable in weak and medium rocks.
- It is recommended to use rock-specific constitutive models to analyze the tunnels in rock medium since the rock mass conditions are taken into account in these models. However, in very weak rocks that behave similar to soils, shear strength tests may be used to determine the model parameters.

7. References

Aksoy, C.O. and Uyar, G.G. (2017). "Non-deformable support system in swelling and squeezing rocks", In: *Rock Mechanics and Engineering*, Volume 4 (pp. 179-203), CRC Press.

Alejano, L.R. and Alonso, E. (2005). "Considerations of the dilatancy angle in rocks and rock masses", *International Journal of Rock Mechanics and Mining Sciences*, 42(4), 481-507, https://doi.org/10.1016/j.ijrmms.2005.01.003.

Asadollahpour, E. (2011). "An investigation into the behaviour of a tunnel in a viscoplastic medium case study: Babolak water conveyance tunnel", M.Sc. Thesis, Shahid Bahonar University of Kerman, Kerman, Iean.

Asadollahpour, E., Rahmannejad, R., Asghari, A. and Abdollahipour, A. (2014). "Back analysis of closure parameters of Panet equation and Burger's model of Babolak water tunnel conveyance", *International Journal of Rock Mechanics and Mining Sciences*, 68, 159-166, https://doi.org/10.1016/j.ijrmms.2014.02.017.

Beyabanaki, A.R. and Gall, V. (2017). "3D numerical parametric study of the influence of open-pit mining sequence on existing tunnels", *International Journal of Mining Science and Technology*, 27(3), 459-466, https://doi.org/10.1016/j.ijmst.2017.03.018.

Bieniawski, Z.T. (1993). "Classification of rock masses for engineering: The RMR system and future trends", In: *Rock Testing and Site Characterization*, (pp. 553-573), Pergamon, https://doi.org/10.1016/B978-0-08-042066-0.50028-8.

Chen, S.-L. and Lee, S.-C. (2020). "An investigation on tunnel deformation behavior of expressway tunnels", *Geomechanics and Engineering*, 21(2), 215-226, https://doi.org/10.12989/gae.2020.21.2.215.

Chen, Y. and Lin, H. (2019). "Consistency analysis of Hoek–Brown and equivalent Mohr–Coulomb parameters in calculating slope safety factor", *Bulletin of Engineering Geology and the Environment*, 78(6), 4349-4361, https://doi.org/10.1007/s10064-018-1418-z.

Dadashi, E., Ahangari, K., Noorzad, A. and Arab, A. (2012). "Support system suggestion based on back-analysis results case study: Babolak water conveyance tunnel", *Arabian Journal of Geosciences*, 5(6), 1297-1306.

Davis, R.O. and Selvadurai, A.P.S. (2005). *Plasticity and geomechanics*, Cambridge University Press.

Eberhardt, E. (2012). "The hoek–brown failure criterion", In: *The ISRM Suggested Methods for Rock Characterization, Testing and Monitoring*: 2007-2014, (pp. 233-240), Springer, Cham.

Fang, Y., Cui, J., Wanatowski, D., Nikitas, N., Yuan, R. and He, Y. (2022). "Subsurface settlements of shield tunneling predicted by 2D and 3D constitutive models considering non-coaxiality and soil anisotropy: A case study", *Canadian Geotechnical Journal*, 59(3), 424-440, https://doi.org/10.1139/cgj-2020-062.

Goel, R.K. and Singh, B. (2011). *Engineering rock mass classification: Tunnelling, foundations and landslides*, Elsevier.

Hajiazizi, M., Taban, M.H. and Ghobadian, R. (2021). "Prediction of Q-value by multi-variable regression and novel Genetic Algorithm based on the most influential parameters", *Civil Engineering Infrastructures Journal*, 54(2), 267-280, https://doi.org/10.22059/CEIJ.2020.295339.1647.

He, M., Zhang, Z., Zhu, J. and Li, N. (2022). "Correlation between the constant mi of Hoek–Brown criterion and porosity of intact rock", *Rock Mechanics and Rock Engineering*, 55(2), 923-936.

He, M., Zhang, Z., Zheng, J., Chen, F. and Li, N. (2020). "A new perspective on the constant mi of the Hoek–Brown failure criterion and a new

model for determining the residual strength of rock", *Rock Mechanics and Rock Engineering*, 53(9), 3953-3967, https://doi.org/10.1007/s00603-020-02164-6.

Hejazi, Y., Dias, D. and Kastner, R. (2008). "Impact of constitutive models on the numerical analysis of underground constructions", *Acta Geotechnica*, 3(4), 251-258, https://doi.org/10.1007/s11440-008-0056-1.

Hoek, E., Carranza-Torres, C. and Corkum, B. (2002). "Hoek-Brown failure criterion-2002 edition", *Proceedings of NARMS-Tac*, 1(1), 267-273

Hoek, E. and Brown, E.T. (1997). "Practical estimates of rock mass strength", *International Journal of Rock Mechanics and Mining Sciences*, 34(8), 1165-1186, https://doi.org/10.1016/S1365-1609(97)80069-X.

Hoek, E. and Brown, E.T. (2019). The Hoek-Brown failure criterion and GSI-2018 edition", *Journal of Rock Mechanics and Geotechnical Engineering*, 11(3), 445-463, https://doi.org/10.1016/j.jrmge.2018.08.001.

Hoek, E., Kaiser, P.K. and Bawden, W.F. (2000). *Support of underground excavations in hard rock*, CRC Press.

Hoek, E., Wood, D. and Shah, S. (1992). Support of underground excavations in hard rock, A modified Hoek–Brown failure criterion for jointed rock masses", In: *Rock Characterization: ISRM Symposium, Eurock'92*, Chester, UK, 14-17 September, (pp. 209-214), Thomas Telford Publishing.

Jallow, A., Ou, C.Y. and Lim, A. (2019). "Three-dimensional numerical study of long-term settlement induced in shield tunneling", *Tunnelling and Underground Space Technology*, 88, 221-236, https://doi.org/10.1016/j.tust.2019.02.021.

Jin, Y.F., Zhu, B.Q., Yin, Z.Y. and Zhang, D.M. (2019). "Three-dimensional numerical analysis of the interaction of two crossing tunnels in soft clay", *Underground Space*, 4(4), 310-327, https://doi.org/10.1016/j.undsp.2019.04.002.

Li, C., Hou, S., Liu, Y., Qin, P., Jin, F. and Yang, Q. (2020). "Analysis on the crown convergence deformation of surrounding rock for double-shield TBM tunnel based on advance borehole monitoring and inversion analysis", *Tunnelling and Underground Space Technology*, 103, 103513, https://doi.org/10.1016/j.tust.2020.103513.

MIDAS Information Technology Co. (2018). Chapter 4: Mesh, In: *Midas GTS NX User Manual*, (pp. 145-146).

Möller, S.C. and Vermeer, P.A. (2008). "On numerical simulation of tunnel installation", *Tunnelling and Underground Space Technology*, 23(4), 461-475, https://doi.org/10.1016/j.tust.2007.08.004.

Mousivand, M. and Maleki, M. (2018). "Constitutive models anddetermining methods effects on application of convergence-confinement method in underground excavation", *Geotechnical and Geological Engineering*, 36(3), 1707-1722, https://doi.org/10.1007/s10706-017-0426-2.

Ng, C.W.W., Sun, H.S., Lei, G.H., Shi, J.W. and Mašín, D. (2015). "Ability of three different soil constitutive models to predict a tunnel's response to basement excavation", *Canadian Geotechnical Journal*, 52(11), 1685-1698, https://doi.org/10.1139/cgj-2014-0361.

Oettl, G., Stark, R.F. and Hofstetter, G. (1998). "A comparison of elastic-plastic soil models for 2D FE analyses of tunnelling", *Computers and Geotechnics*, 23(1-2), 19-38, https://doi.org/10.1016/S0266-352X(98)00015-9.

Rocdata Software Manual. (2004). *R.I.R. Version 3.0 User's Guide of RocData: Strength analysis of rock and soil masses using the generalized Hoek–Brown, Mohr–Coulomb, Barton–Bandis and power curve failure critera"*, Toronto, Ontario, Canada, (n.d.).

Rukhaiyar, S. and Samadhiya, N.K. (2016). "Analysis of tunnel considering Modified Mohr-Coulomb criteria", *Recent Advances in Rock Engineering (RARE 2016)*, Atlantis Press.

Sarikhani Khorami, M. (2012). "Analysis of geomechanical parameters and in situ stress of rock mass in Isfahan-Shiraz railway tunnel using back analysis based on displacement monitoring", M.Sc. Thesis, Isfahan University of Technology, Isfahan, Iran.

Sharifzadeh, M., Daraei, R. and Broojerdi, M.S. (2012). "Design of sequential excavation tunneling in weak rocks through findings obtained from displacements based back analysis", *Tunnelling and Underground Space Technology*, 28, 10-17, https://doi.org/10.1016/j.tust.2011.08.003.

Singh, B. and Goel, R.K. (1999). *Rock mass classification: A practical approach in civil engineering*, (Vol. 46), Elsevier.

Su, K., Zhang, Y.-J., Chang, Z.-H., Wu, H.-G., Wang, T. and Zhou, W. (2019). "Transverse extent of numerical model for deep buried tunnel excavation", *Tunnelling and Underground Space Technology*, 84, 373-380, https://doi.org/10.1016/j.tust.2018.11.034.

Sulem, J., Panet, M, and Guenot, A. (1987). "Closure analysis in deep tunnels", *International Journal of Rock Mechanics and Mining Sciences and Geomechanics Abstracts*, 24(3), 145-154, https://doi.org/10.1016/0148-9062(87)90522-5.

Sun, H., Liu, S., Zhong, R. and Du, L. (2020). "Cross-section deformation analysis and visualization of shield tunnel based on mobile

tunnel monitoring system", *Sensors*, 20(4), 1006, https://doi.org/10.3390/s20041006.

Vakili, K., Lavasan, A.A., Schanz, T. and Datcheva, M. (2014). "The influence of the soil constitutive model on the numerical assessment of mechanized tunneling", *Proceedings of the 8th European Conference on Numerical Methods in Geotechnical Engineering*, Delft, The Netherlands, 889-894.

Vitali, O.P.M., Celestino, T.B. and Bobet, A. (2018). "3D finite element modelling optimization for deep tunnels with material nonlinearity", *Underground Space*, 3(2), 125-139, https://doi.org/10.1016/j.undsp.2017.11.002.

Xing, Y., Kulatilake, P. and Sandbak, L.A. (2018). "Investigation of rock mass stability around the tunnels in an underground mine in USA using three-dimensional numerical modeling", *Rock Mechanics and Rock Engineering*, 51(2), 579-597, https://doi.org/10.1007/s00603-017-1336-6.

Xue, Y., Zhou, B., Li, S., Qiu, D., Zhang, K., and Gong, H. (2021). "Deformation rule and mechanical characteristic analysis of subsea tunnel crossing weathered trough", *Tunnelling and Underground Space Technology*, 114, 103989, https://doi.org/10.1016/j.tust.2021.103989.

Yasitli, N.E. (2016). "Comparison of input parameters regarding rock mass in analytical solution and numerical modelling", *Journal of African Earth Sciences*, 124, 497-504, https://doi.org/10.1016/j.jafrearsci.2016.08.010.

Zhao, C., Alimardani Lavasan, A., Barciaga, T., Kämper, C., Mark, P. and Schanz, T. (2017). "Prediction of tunnel lining forces and deformations using analytical and numerical solutions", *Tunnelling and Underground Space Technology*, 64, 164-176, https://doi.org/10.1016/j.tust.2017.01.015.

Civil Engineering Infrastructures Journal 2023, 56(2): 321-332
DOI: 10.22059/CEIJ.2023.343951.1847

RESEARCH PAPER

Behavioral Study of Raft Reinforced with Geogrid and Geocell Through Experiments and Neural Models

Kumar, V.[1*], Priyadarshee, A.[2], Chandra, S.[3], Jindal, A.[4] and Rana, D.[4]

[1] Assistant Professor, Department of Civil Engineering, SoET Block, Central University of Haryana, Mahendergarh, India.
[2] Assistant Professor, Department of Civil Engineering, MIT Muzaffarpur, Bihar, India.
[3] Ph.D. Candidate, Scientist, CSIR-NEERI, Delhi Zonal Centre, India.
[4] Assistant Professor, Department of Civil Engineering, School of Engineering and Technology, Central University of Haryana, India.

Received: 02 Jun. 2022; Revised: 29 No. 2022; Accepted: 16 Jan. 2023

ABSTRACT: The stability of a structure could be achieved either by adopting strong foundation or by improving the strength of the soil. This study is an attempt to investigate the behavior of a raft foundation (U-R_F) upon reinforcing with geogrid (R_F-R-G_r) and reinforcing with geocell (R_F-R-G_c). The results of the study showed that optimal depth for placement of geogrid was found to be 0.3B (B is width of raft) while optimal depth for geocell varied from 0.1B to 0.15B. It was also found that the Bearing Capacity Ratio (BCR) for R_F-R-G_r was typically six times higher than U-R_F, while for R_F-R-G_c it was eleven times higher than U-R_F. Further, the outcomes of experimental study were modeled using Artificial Neural Networks (ANN) to predict the settlements. It was found that ANN models predicted settlement with higher values of correlation coefficient (r) as 0.9996 for R_F-R-G_r and 0.9995 for R_F-R-G.

Keywords: ANN, BCR, Geocell, Geogrid, Raft.

1. Introduction

India is accelerating at a rapid rate on the infrastructural front with smart city based development implemented in different parts of the country. These developments in the geographically diverse country are challenged with existing topography and varied soil conditions. The challenges range from stability of substructure to durability of the superstructure. The focus on substructure is obvious of the fact that big and complex structures like skyscrapers, bridges, and industrial plants, etc. require stable and economical foundations.

A raft foundation (UR_F) is generally used when the area required under the isolated footing is much higher for the distribution of load with low bearing capacity of soil. However, under poor soil conditions the raft undergoes differential settlement in instances. In such cases, available ground improvement techniques like utilization of the admixture, stone column, soil reinforcement, etc., can be implemented (Jindal and G.D. Ransinchung, 2021, Priyadarshee et al., 2020; Verma et al., 2018; Kumar and Thyagaraj, 2020). Also,

* Corresponding author E-mail: vikaskumarnitk@gmail.com

to improve the behavior of the raft different geosynthetic materials are brought into applications with soil strata. The inclusions of geogrid and geocell as reinforcement has opened new avenues for the constructions of structures even in those areas too which have poorly graded sand beds. In this study, the behavior of raft reinforced with geogrid (R_F-R-G_r) and raft reinforced with geocell (R_F-R-G_c) were explored under loose sand and dense sand condition.

Reinforced Soil Foundation (RSF) has been an area of interest for various researchers in the past too. Binquet and Lee (1975) evaluated the bearing capacity of sand reinforced with metal strips and later many studies were conducted to evaluate footings rested on reinforced sandy soil. Priyadarshee et al. (2014) discussed that, different forms of reinforcement like planar, geocell etc., are available for improving the BCR of soil; however planar and geocells are the most popular alternatives practiced amongst engineers. In planar reinforcement technique geogrids, geotextiles etc., are placed in layers of soil which mobilizes the reinforcing action through interaction between soil and reinforcement. Different works carried out by researchers such as Adams and collin (1997), Sawaaf (2007), etc., describes the mechanism of planar reinforcement and the factors affecting the same.

Geocell is another important form of reinforcement wherein three-dimensional confinement provided by geosynthetic material resists the deformation during the shearing action which increases the load carrying capacity of soil. Different model tests on shallow foundations like strip footing, circular footing etc., and numerical analysis were carried out by different researchers such as Bathurst and Karpurapu (1993), Latha et al. (2008) and many more.

Most of the studies on model foundation supported by reinforced soil have been done on the isolated foundations. Under the isolated foundations like circular footing, square footing etc., reinforcements are extended beyond the footing. Because of this additional resistance mobilizes due to additional length of the reinforcement. Also, numerical analysis done by different researchers like Han et al. (2008), Latha et al. (2008) etc. on the foundation supported by reinforced soil, is mainly based on the mesh analysis to predict the performance of soil-foundation system (Han et al. 2008). Also statistical analysis is used for prediction by different researchers. Different studies using ANN have been done on problems like prediction of compressive strength for stabilized soil using ANN, evaluation of lateral spreading using ANN (Baziar et al., 2005), assessing geotechnical properties using neural model models (Yang et al., 2002). A hybrid PSO-ANN model for rock-socketed piles was developed by Armaghani et al. (2017) for predicting the ultimate bearing capacity. The intricate problems in geotechnical engineering have used AI models for comparatively better results than statistical models as discussed by Suman et al. (2016) and Doley et al. (2021, 2022).

However, performance of the planner reinforcement and geocell reinforcement is not yet properly investigated under the raft foundation. This study, thus investigates the performance of soil reinforced with planar and geocell reinforcement under raft footing. Also, a comparative study is done to understand the relative performance of these reinforcement under the raft footing. Under different experimental setups, series of test are performed on the reinforced soil-raft foundation systems. Also, to predict the load carrying capacity of the reinforced soil Artificial Neural Network (ANN) is applied in the present study.

2. Methodology and Test Set up

The methodology adopted for this study is illustrated in Figure 1. For studying the performance of U-R_F, R_F-R-G_r and R_F-R-G_c, model raft 300 mm × 300 mm × 25 mm was prepared, and property of sand were investigated. The photographic view of raft and testing tank are shown in Figures 2a and

2b.

As per the Unified Soil Classification System (USCS), (ASTM D 2487-06) sand used in this study could be classified as poorly graded sand (SP) as shown in Figure 3. Biaxial geogrid made of polypropylene was used in this study as planar reinforcement and for preparation of geocell. The Height of Geocell (HG) used in R_F-R-G_c was equal to the number of geogrid layers used for preparation of geocell. The photographic view of geogrid and geocell are shown in Figures 4a and 4b.

The resultant load-deformation behavior of geogrid is presented in Figure 5 as per ASTM D 6637-01. Experimental test series was designed to conduct tests on UR_F, R_F-R-G_r and R_F-R-G_c. The test series G_0 were conducted on unreinforced raft at 40% and 70% Relative Density (RD). In case of R_F-R-G_r and R_F-R-G_c, the laboratory tests were conducted under test series G_1, G_2, G_3, G_4 and G_{C1}, G_{C3}, G_{C5}, respectively, as shown in Table 1. The schematic diagram for R_F-R-G_r and R_F-R-G_c is shown in Figures 6a and 6b. For R_F-R-G_r, the design variables were N, b/B, d_r, u/B and for R_F-R-G_c, the variables were h_g/ and U_g.

2.1. Development of Neural Models

Artificial Neural Network (ANN) models using feed-forwarded and back propagated technique were used for making the neural model for this study. The basic structure of the neural network is divided into three components namely input layer, hidden neuron and output. For optimization of the ANN, fixation of neurons was done by trial-and-error method. The architecture of neural model for geogrid and geocell is shown in Figures 7a and 7b, respectively. The database consisted of matrix of outcomes of experiments for R_F-R-G_r and R_F-R-G_c for constructing neural model. For training the neural model, 70% data was used and 30% data was used for testing the model.

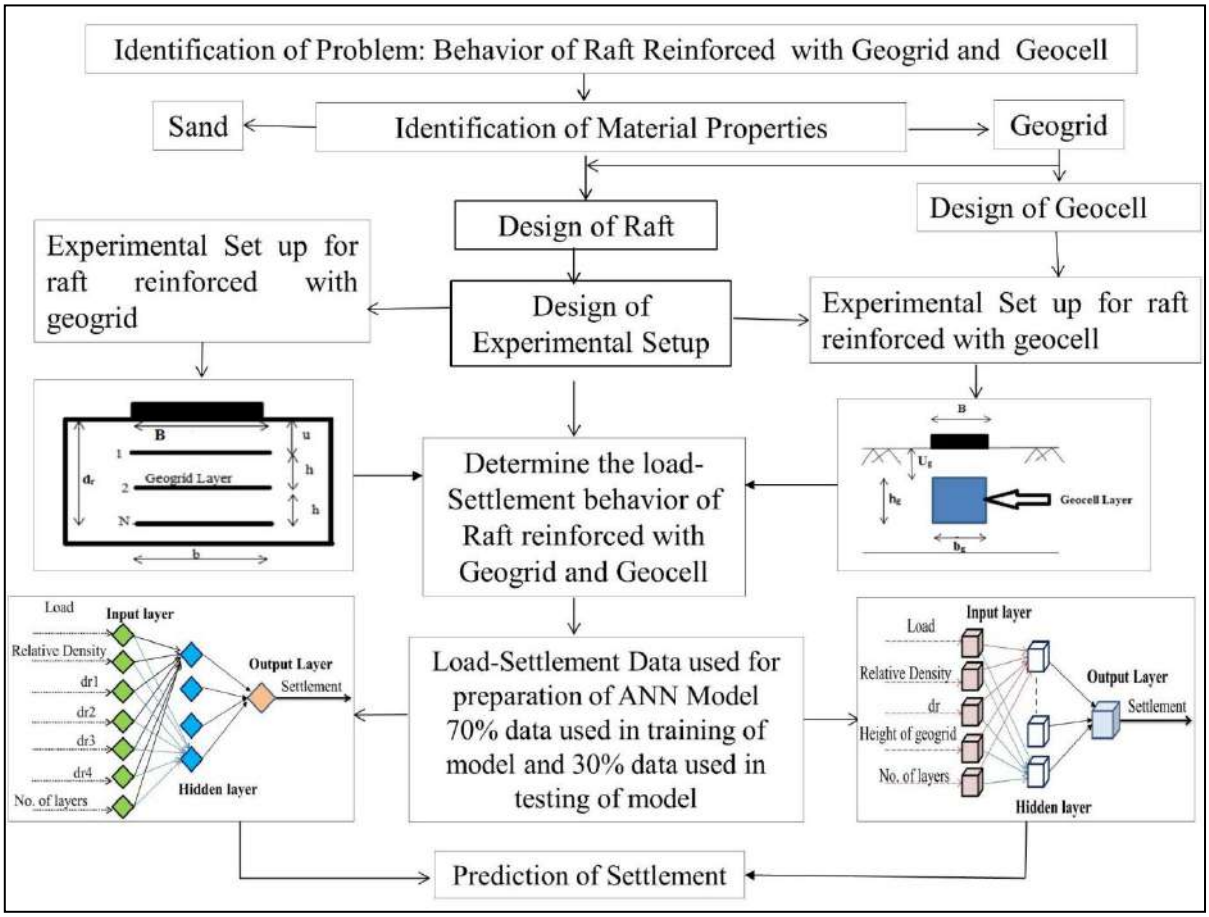

Fig. 1. Methodology employed in study

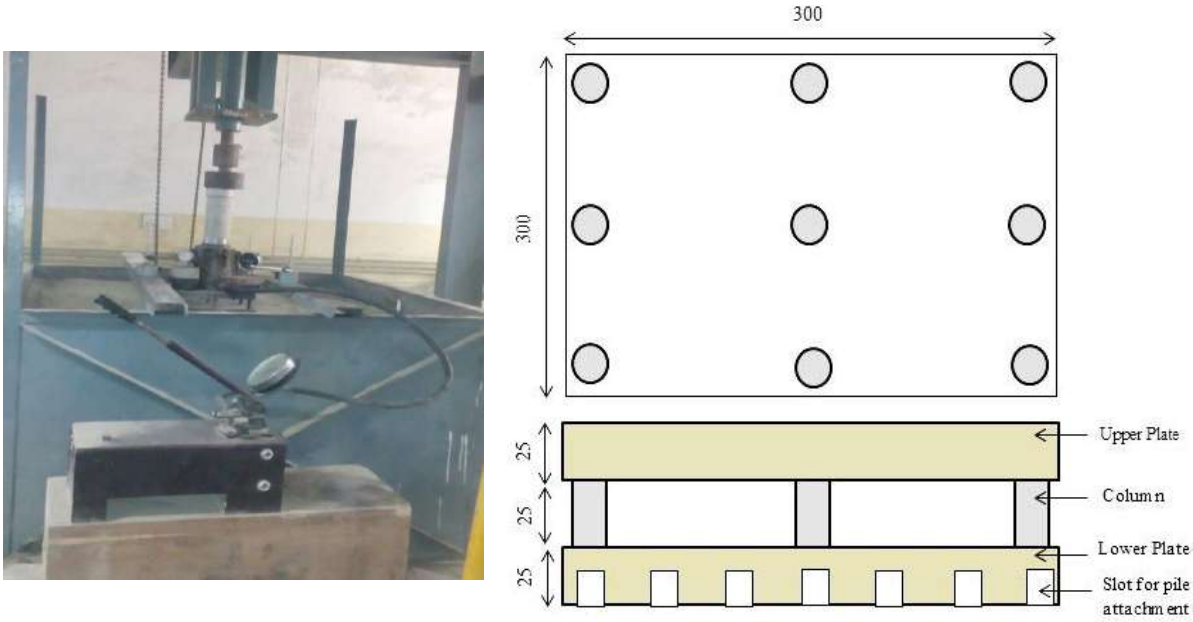

(a) Testing tank **(b)** Model raft used

Fig. 2. Test Set up and model raft used in the study

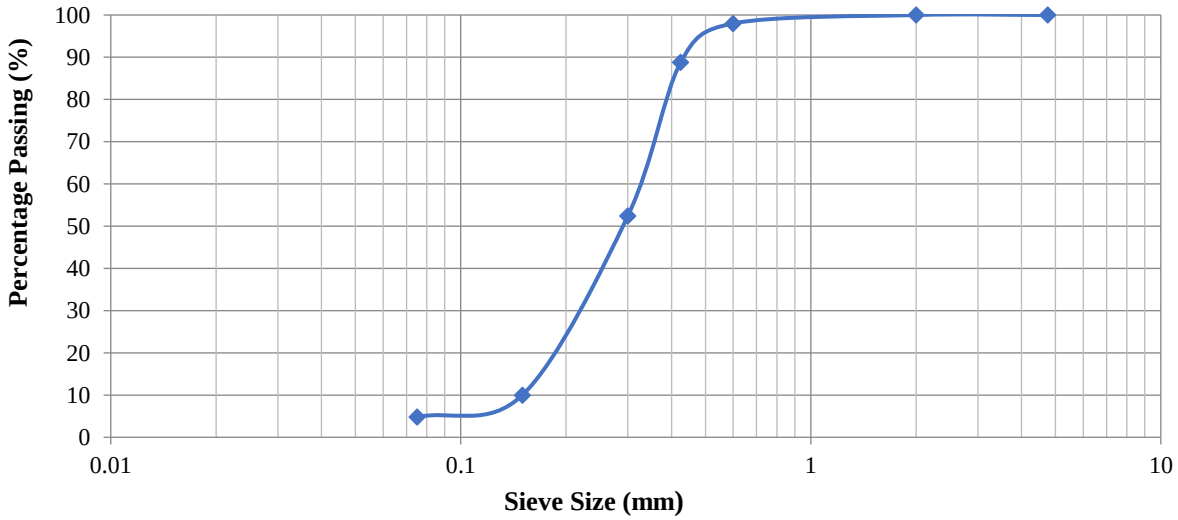

Fig. 3. Grain size distribution of sand

Table 1. Test details for U-RF, RF-R-Gr and RF-R-Gc

RD (%)	Test series	U-R_F and R_F-R-G_r Number of layer (N)	d_r/B	U/B	R_F-R-G_c Test series	U_g/B
	G_0	----	-----	----	----	---
40,70	G_1	1	0.1	0.1	G_{C1}	0.1
			0.3	0.3		0.3
			0.5	0.5		0.5
			0.7	0.7		0.7
	G_2	2	0.1 and 0.3	0.1	G_{C3}	0.1
			0.1 and 0.5	0.1		0.3
			0.1 and 0.7	0.1		0.5
			0.3 and 0.5	0.3		0.7
			0.3 and 0.7	0.3		
			0.5 and 0.7	0.5		
	G_3	3	0.1, 0.3 and 0.5	0.1	G_{C5}	0.1
			0.3,0.5 and 0.7	0.3		0.3
						0.5
						0.7
	G_4	4	0.1,0.3,0.5 and 0.7	0.1		

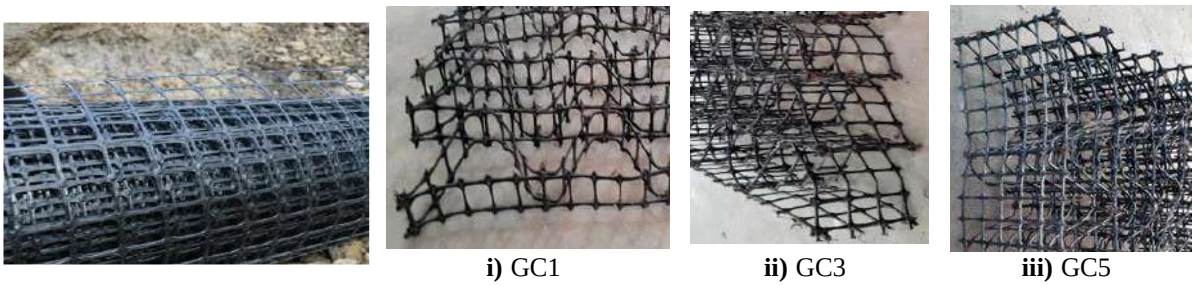

i) GC1 **ii)** GC3 **iii)** GC5

(a) Geogrid used **(b)** Geocell used for model study

Fig. 4. Geogrid and Geocell used in the study

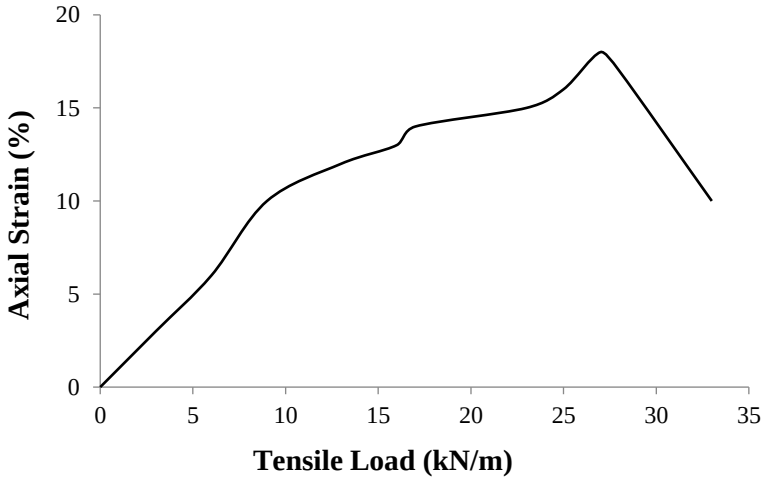

Fig. 5. Load-deformation behavior of biaxial geogrid used in the study

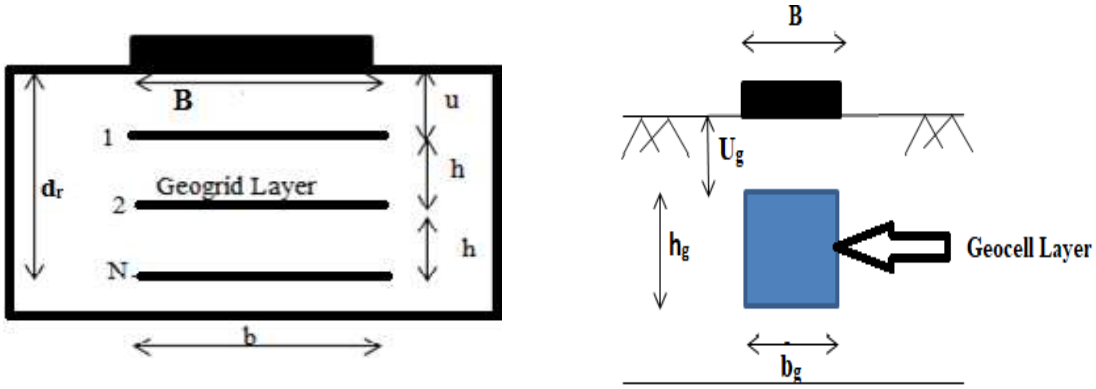

(a) Experimental set up for RF-R-Gr **(b)** Experimental set up for RF-R-Gr

Fig. 6. Experimental Setup for Reinforced foundation

3. Results and Discussion

The effect of design variables considered for U-R_F, R_F-R-G_r and R_F-R-G_c model tests are discussed in the following section. The results obtained were further used to develop a prediction neural model. For comparing the performance of reinforcements, parameters like density, type of reinforcement, reinforcement's top-spacing and number of layers are discussed.

3.1. Effect of Density

Direct Shear test was conducted to study the interaction effect of geogrid with sand. From Figure 8, it can be inferred that peak shear stress would increase with increase in the relative density of soil. This enhancement will increase with the inclusion of planar reinforcement. Peak stress was improved from 65.49 kN/m^2 to 74 kN/m^2 for unreinforced sand and from 75.54 kN/m^2 to 93.05 kN/m^2 for reinforced sand when the relative density was observed to be increased from 40% to 70%.

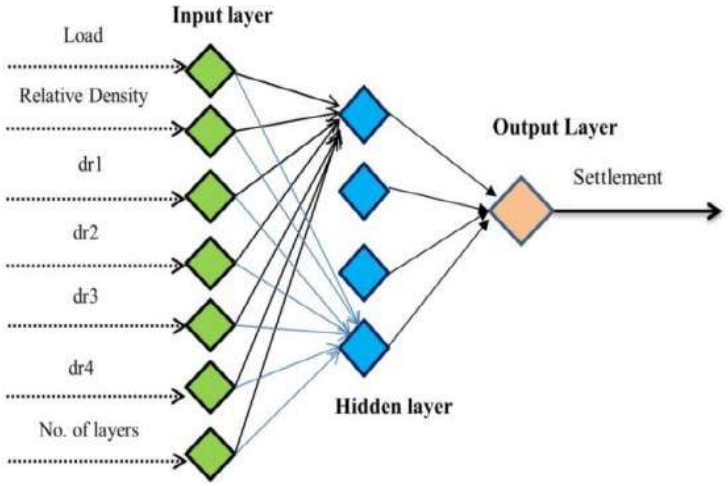

(a) ANN model for geogrid

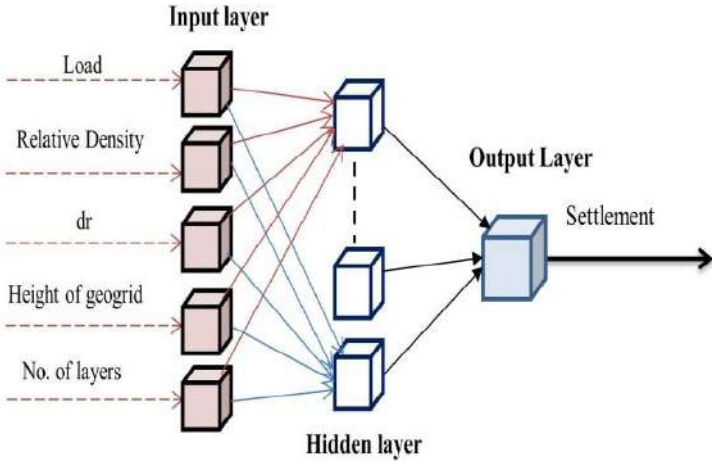

(b) Neural topology for geocell

Fig. 7. Architect of ANN model

For R_F-R-G_r: dr1, dr2, dr3 and dr4 represent different depths of reinforcement when one, two, three and four layers were used, respectively.
No. of layers = No. of geogrid layers.
For R_F-R-G_c: dr = different depth of reinforcement (30 mm, 90 mm, 150 mm).
Height of geocell = No. of layers × 30 mm

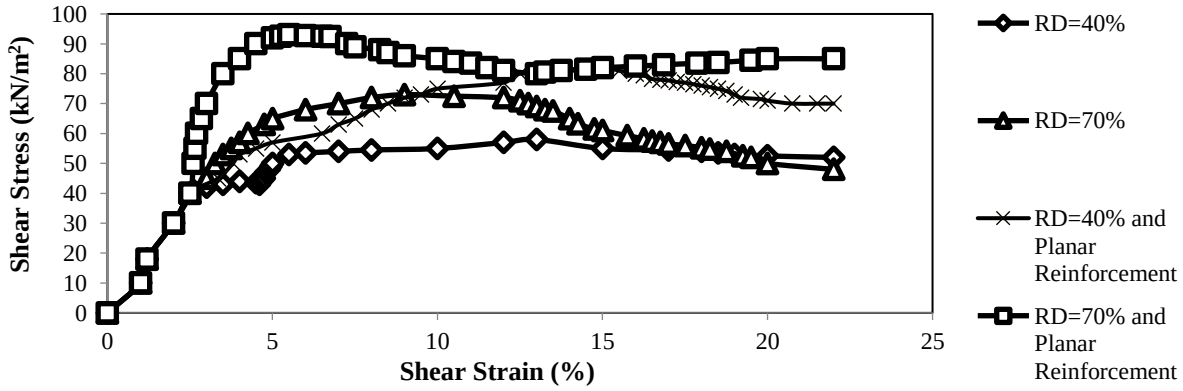

Fig. 8. Stress-strain response for reinforced and unreinforced sand at different relative densities

3.2. Effect of Reinforcement

The pressure–settlement responses were compared through a non-dimensional parameter i.e. Bearing Capacity Ratio (BCR) as in Eq. (1).

$$BCR = \frac{q_{UR}}{q_U} \quad (1)$$

where, q_{UR}: is bearing capacity of reinforced foundation and q_U: is bearing capacity of U-R_F.

The BCR for R_F-R-G_r was typically five times higher than that of U-R_F while for R_F-R-G_c it was seven times than that of U-R_F as shown in Figures 9a and 9b. This is due to the fact that geocell confine the sand more significantly as compared to geogrid. Also an anchorage action will take place if foundation is reinforced by geocell which develop the hoop stress. This combined action resulted in significant improvement in the BCR.

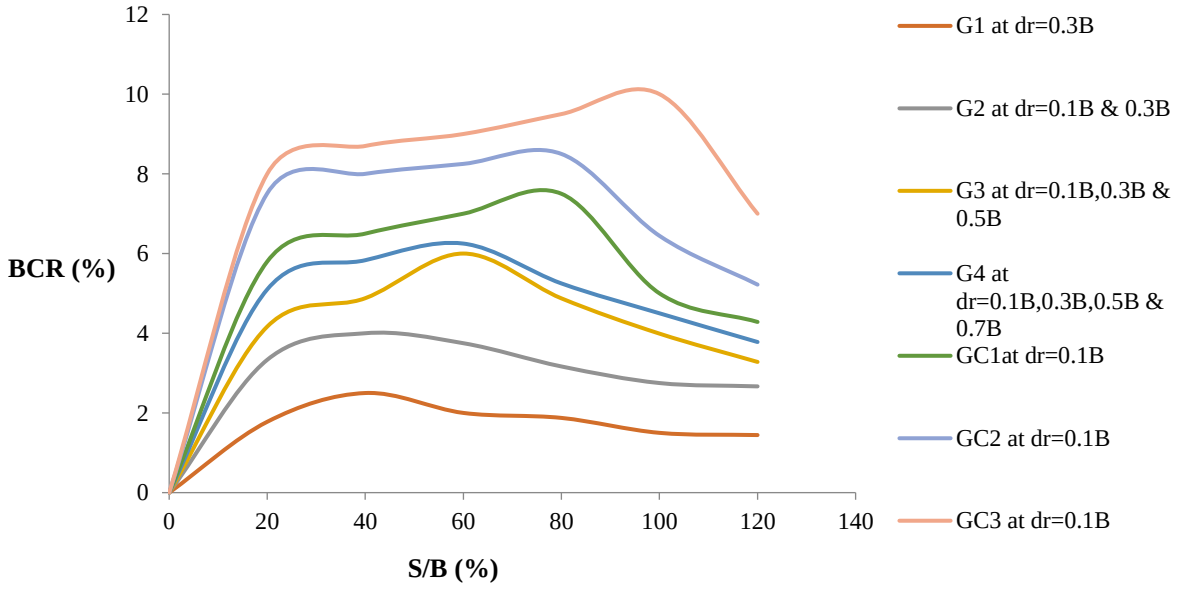

(a) Pattern of BCR for RF-R-Gr and RF-R-Gc at RD = 40%

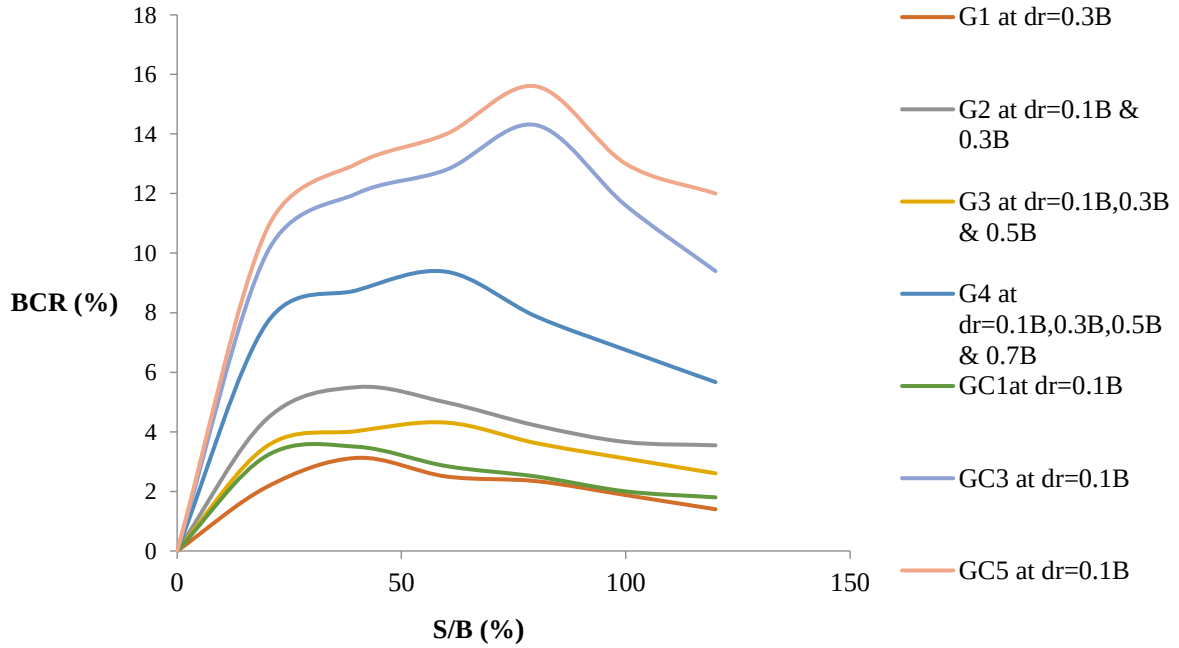

(b) Pattern of BCR for RF-R-Gr and RF-R-Gc at RD = 70%

Fig. 9. Effect of relative density on reinforced foundation

3.3. Effect of Reinforcement's Top Spacing for Geogrid and Geocell reinforced foundation

In case of R_F-R-G_r, the distance of first layer of reinforcement from the base of footing shall mobilize the tensile forces developed which are directly proportional to the depth of the reinforcement. As the

depth of reinforcement below the raft increases, these tensile forces decrease. From Figure 10a it could be inferred that for R_F-R-G_r the optimal results were achieved at u/B = 0.3 and the maximum improvement in BCR was obtained at S/B = 20%.

From test results, it is observed that R_F-R-G_c provides better performance than U-R_F and R_F-R-G_r in all cases. This improvement in performance is owing to interface friction developed between soil and 3-dimensional geocell which developed the confinement effect. From Figures 10b it is inferred that for R_F-R-G_{c1} the optimal results were achieved at U_g/B = 0.15 and the maximum improvement in BCR was obtained at S/B = 30%

3.4. Effect of Number of Layers

For R_F-R-G_r the maximum significant improvement in BCR was achieved when three layers were used as in test series G_3. Therefore, it can be concluded that further addition of number of geogrid layers does not affect the bearing capacity of soil significantly, while in case of R_F-R-G_c best results were obtained at test series GC3 as shown in Figure 11.

3.5. Neural Models

The final topology for any neural model is obtained after finalizing the parameters like activation function, neurons in middle hidden layer, stopping criteria etc. The connections between the layers were logsigmoid and purelin. The first connection was logsigmoid and purelin was a successive function. Least Root Mean Square Error (RMSE) during testing was used for neurons selection in middle layer. Therefore, for R_F-R-G_r the topology was 7-12-1 and for R_F-R-G_c it was 5-11-1 as shown in Figure 12.

3.5.1. Performance of Neural Model

For identifying the performance of ANN, different performance variables (Kumar and Kumar, 2018) as shown in Table 2 were calculated. The performance variables help in deciding the goodness of developed neural models. The predicted results from the model are shown in Figure 13.

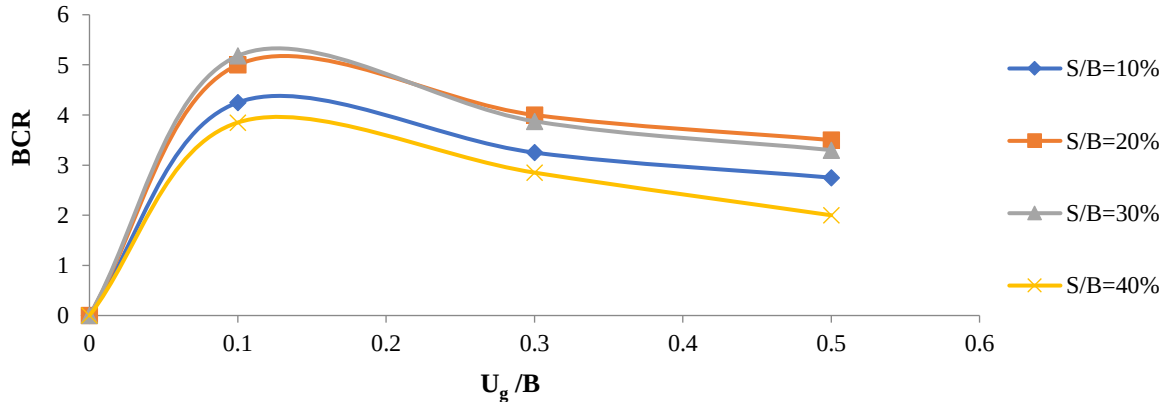

(a) BCR versus u/B for test series G1 at RD = 40%

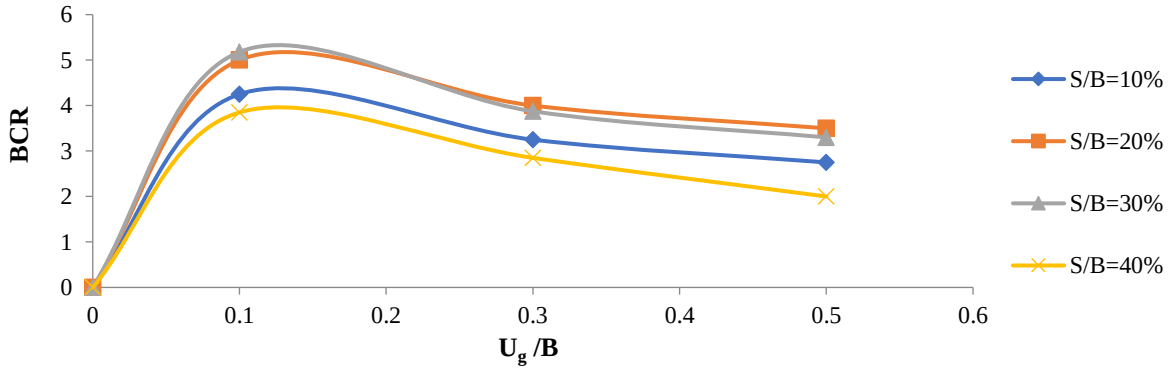

b) BCR versus Ug/B at RD = 70% for test series GC1

Fig. 10. Effect of reinforcement top spacing on reinforced foundation

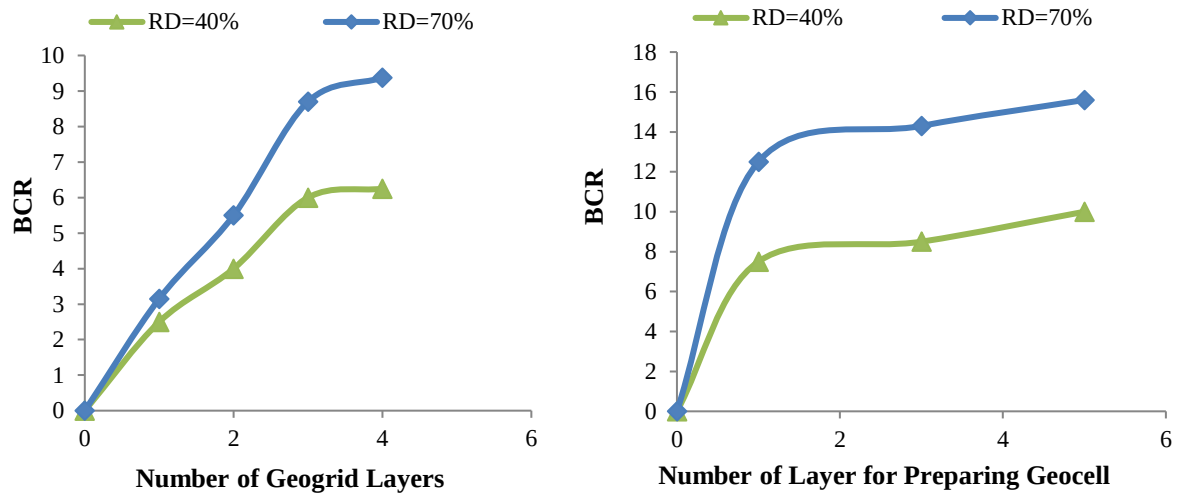

(a) Effect of N for RF-R-Gr **(b)** Effect of hg for RF-R-Gc

Fig. 11. Effect of reinforcement layer

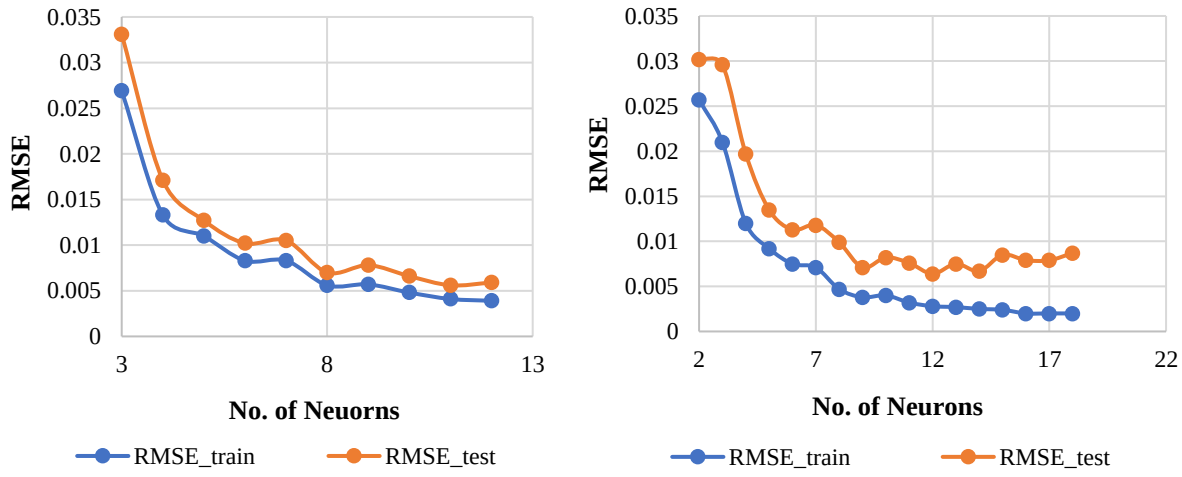

(a) For RF-R-Gr **(b)** For RF-R-Gc

Fig. 12. Pattern of RMSE during training and testing

Table 2. Assessment of performance variables for Geogrid and Geocell

	MAE	RMSE	CF	r
Geogrid				
Training	0.002	0.003	0.999	0.9998
Testing	0.004	0.006	0.999	0.9996
Geocell				
Training	0.003	0.004	0.999	0.9997
Testing	0.004	0.005	0.999	0.9995

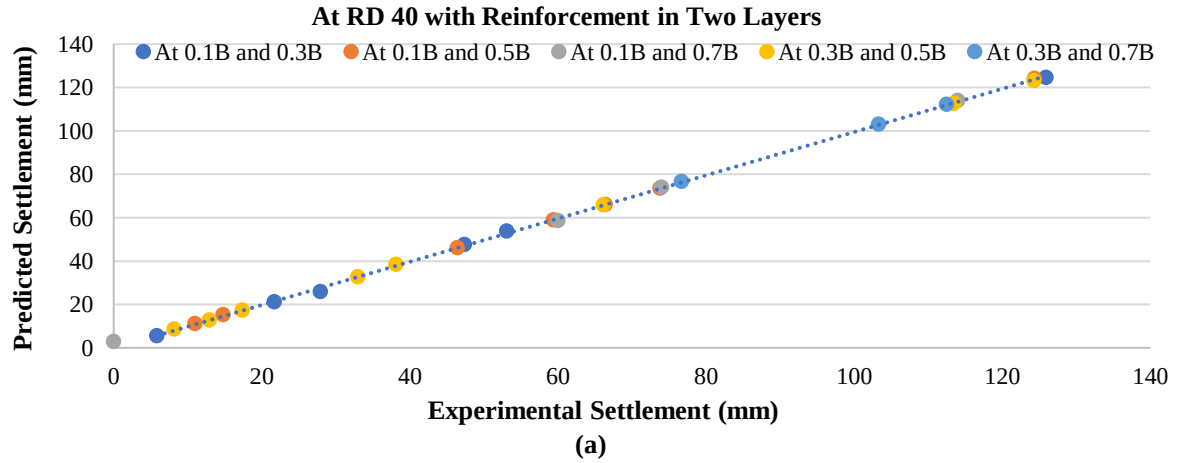

(a)

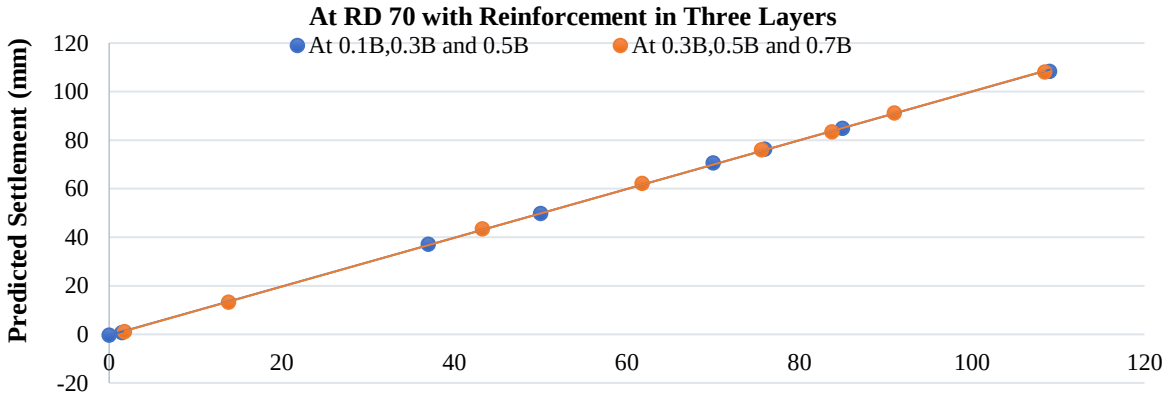

(b)

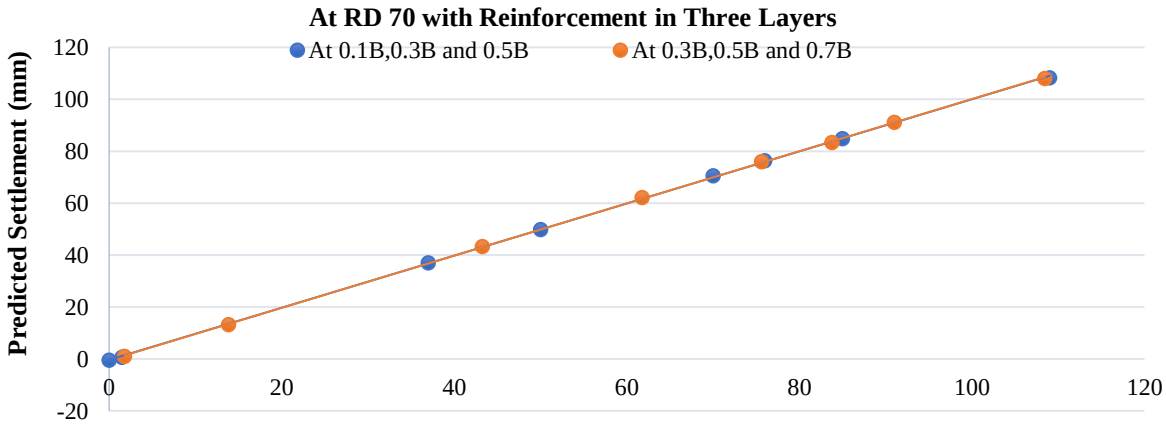

(c)

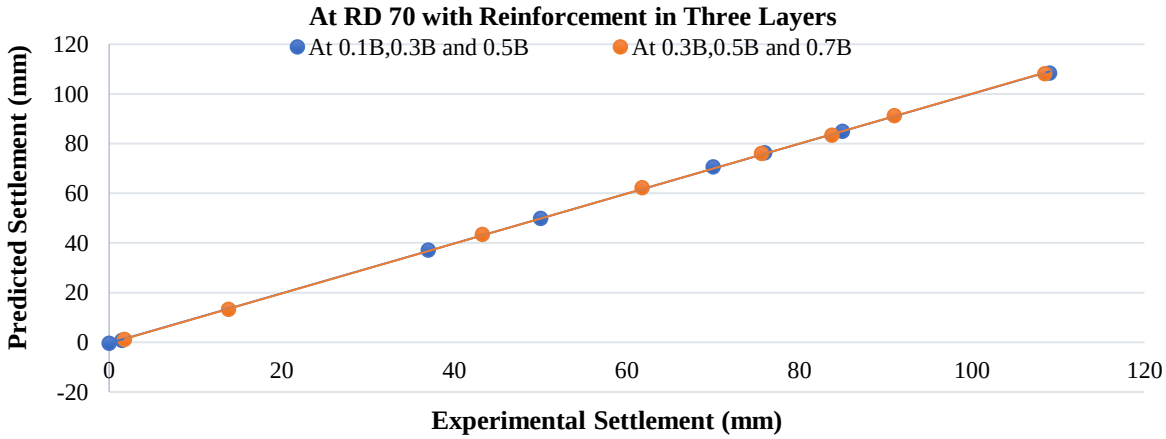

(d)

Fig. 12. Pattern of RMSE during training and testing

For R_F-R-G_r, the optimal architecture was obtained as 7-12-1 to predict settlement (S). The weights and biases obtained from trained model for geogrid are shown in Table 3. The Eq. (2) gives output (settlement) by using all input parameters (i.e. Loads (L), Relative Density (RD), dr1, dr2, dr3, dr4 and No. of layers (Nlp).

For raft reinforced with geocell the optimal architecture obtained was 5-11-1 to predict settlement (S). The weights and biases obtained from trained model for geocell had been shown in Table 4.

The normalized value of settlement (S) can be calculated using following equation.

$$Settlement = f_{sig}\{b_o + \sum_{k=1}^{h}\left[w_k f_{sig}(b_{hk} + \sum_{i=1}^{m} w_{ik} X(input)_i\right]\} \quad (2)$$

Table 3. Connection weights and biases for calculating settlement (Ygc) i.e. for raft reinforced with Geogrid

Hidden neuron	Weights								Bias	
	w_{ik}							w_k	b_{hk}	b_o
	Inputs							Output	Hidden layer	Output layer
(k = 1 to 12)	Load (L)	Relative density (RD)	dr1	dr2	dr3	dr4	No. of layers (N_{lp})	Settlement (S)		
1	2.8042	3.4678	2.1315	3.0136	3.8188	-0.2099	-3.0085	0.5280	-0.6778	0.0120
2	-8.4476	-4.2540	-4.0283	0.6813	-0.1670	-1.3368	7.3752	-0.0794	3.9817	
3	-2.4716	-8.1776	-14.7238	-0.0437	4.5439	0.7352	-11.6633	0.5249	-5.3355	
4	2.1153	-0.3233	0.3523	-2.9803	-3.7383	0.4669	3.2740	1.1401	-4.4261	
5	-1.7771	0.7992	-6.0401	-0.8943	-0.3476	0.6638	4.6114	1.2843	-3.0169	
6	2.1295	-0.2827	0.2917	0.2573	0.0546	0.6708	-1.7831	2.8495	2.2199	
7	1.9098	-0.3136	-0.0572	0.7825	0.1691	0.5006	-1.5603	4.6961	-0.9630	
8	1.2493	-0.5264	-1.3923	0.4040	-2.2094	4.4762	5.6170	-2.8879	2.4666	
9	-0.9754	0.1731	2.8333	0.4662	2.2984	-4.3208	4.5377	2.8611	0.8589	
10	0.7209	-0.5175	-2.4152	-0.7004	-1.3631	-4.1193	2.7417	-4.4829	-0.5241	
11	0.5201	0.7982	2.9534	0.5987	2.1740	0.5332	-1.4558	-1.8853	0.6765	
12	0.4852	-1.6963	3.8710	-7.8275	-0.2785	1.3689	7.4323	-1.3636	-3.5628	

where f_{sig}: represent the transfer function (here is log-sigmoid), b_o: is bias at output layer, w_k: is weight connection between 'k' of the hidden layer and the single output neuron, b_{hk} is bias at neuron 'k' of the hidden layer (k = 1, h), w_{ik}: is weight connection between input variable i and neuron k of the hidden layer and $X(input)_i$: is the input parameter.

4. Conclusions

Study showed the effectiveness of using planar reinforcement and geocell as settlement reduction measure with the rafts. In general, the extra strength was observed due to geocell-reinforcement which is to be dependent on the number of the geocell layers and thickness of geocell used to reinforce the soil. The BCR for R_F-R-G_r was typically six times higher than that of U-R_F while for R_F-R-G_c was eleven times than that of U-R_F. It was observed that relative density plays a significant role in improving the bearing capacity of soil. The effect of reinforcement was almost double in case of reinforced raft as compared to U-R_F. The optimal depth for placement of geogrid was obtained as 0.3B and for geocell it was 0.15B. In case of reinforced raft, it was observed that with increase in number of layers of geogrid, load intensity was found to be increased at RD 70% more than that for RD 40% however, this effect was observed to be insignificant after an optimum number of reinforcement layers. The lower values of the order of 10^{-3} for MAE and RMSE shows that the neural models are well trained and tested and can be used for solving complex geotechnical problems.

Table 4. Connection weights and biases for calculating settlement (Ygc) i.e. for raft reinforced with geocell

Hidden neuron	Weights						Bias	
	w_{ik}					w_k	b_{hk}	b_o
	Inputs					Output		
(k = 1 to 11)	Load (L)	Relative density (RD)	dr	Height of Geogrid (h_g)	No. of layers (N_{lg})	Settlement (S)	Hidden layer	Output layer
1	4.6619	-0.1100	0.3989	-0.5677	-1.4156	0.7687	-2.9583	2828.9116
2	-0.9584	-0.0199	1.4175	1.6667	-0.3249	-2829.0547	10.1704	
3	-1.6689	2.6778	-1.6870	-2.6193	-1.1327	-0.6833	1.0955	
4	1.0102	1.5909	0.7418	2.0951	0.3838	-153.4224	1.3146	
5	-1.6498	0.2736	-2.5507	1.0150	-0.5241	0.3931	-1.2418	
6	-5.1185	9.4275	-6.9803	-4.9604	-4.1751	0.1176	1.1746	
7	-2.6048	-1.5796	2.1554	-2.3718	-2.0127	0.2284	0.3234	
8	-1.2315	0.3857	30.4316	15.1914	16.4570	0.8228	37.0194	
9	1.0003	1.5870	0.7434	0.4169	2.0675	152.8009	1.2982	
10	-2.0663	0.0789	-0.2321	-0.4019	1.5601	-2.0521	-0.2065	
11	2.3428	2.1446	0.5364	1.4305	-0.0262	1.0644	2.2043	

5. References

Adams, M.T. and Collin, J.G. (1997). "Large model spread footing load tests on geosynthetic reinforced soil foundation", *Journal of Geotechnical and Geoenvironmental Engineering*, 123(1), 66-72, http://doi.org/10.1061/(ASCE)1090-0241(1997)123:1(66).

Bathurst, R.J. and Karpurapu, R. (1993). "Large-scale triaxial compression testing of geocell-reinforced granular soils", *Geotechnical Testing Journal*, 16(3), 296-303, http://doi.org/10.1520/GTJ10050J.

Binquet, J. and Lee, K.L. (1975). "Bearing capacity tests on reinforced earth slabs", *Journal of Geotechnical and Geoenvironmental Engineering*, 101(12), 1241-1255.

Doley, C., Das, U.K. and Shukla, S.K. (2021) "Response of square footing on geocell-reinforced sand bed under static and repeated loads", *International Journal of Geosynthetics and Ground Engineering*, 7(4), 90, https://doi.org/10.1007/s40891-021-00336.

Doley, C., Das, U.K. and Shukla, S.K. (2022) "Development of a multiple regression equation for prediction of bearing capacity of geocell-reinforced sand beds based on experimental study", *Arabian Journal of Geosciences*, 15(16), 1408, https://doi.org/10.1007/s12517-022-10652-y.

Jahed Armaghani, D., Shoib, R.S.N.S.B.R., Faizi, K. and Rashid, A.S.A. (2017). "Developing a hybrid PSO-ANN model for estimating the ultimate bearing capacity of rock-socketed piles", *Neural Computing and Applications*, 28, 391-405, https://doi.org/10.1007/s00521-015-2072-z.

Jindal, A. and G.D. Ransinchung, R.N. (2022). "Behavioural study of incorporation of recycled concrete aggregates and mineral admixtures in pavement quality concrete", *Civil Engineering Infrastructures Journal*, 55(2), 351-372, https://doi.org/10.22059/ceij.2022.326564.1766.

Kumar, K.S.R. and Thyagaraj, T. (2020). "Comparison of lime treatment techniques for deep stabilization of expansive soils", *International Journal of Geotechnical Engineering*, 15(8), 1021-1039. https://doi.org/10.1080/19386362.2020.1775359

Latha, G.M., Dash, S.K. and Rajagopal, K. (2008). "Equivalent continuum simulations of geocell reinforced sand beds supporting strip footings", *Geotechnical Geology Journal*, 26, 387-398, https://doi.org/10.1007/s10706-008-9176-5.

Priyadarshee A., Chandra S., Gupta D. and Kumar V. (2020). "Neural models for unconfined compressive strength of kaolin clay mixed with pond ash, rice husk ash and cement", *Journal of Soft Computing in Civil Engineering*, 4(2), 87-108, https://doi.org/10.22115/SCCE.2020.223774.1189.

Suman,S., Khan, S.Z., Das, S.K. and Chand, S.K. (2016). "Slope stability analysis using artificial intelligence techniques". *Natural Hazards*, 84(2),727-748, https://doi.org/10.1007/s11069-016-2454-2.

Verma, S., Kumar V. and Priyadarshee A. (2018). "An experimental test study on ring footing resting on clay bed reinforced by stone column", *Innovative Infrastructure Solutions*, 64(3),1-16, https://doi.org/10.1007/s41062-018-0169-9.

Yang, Y. and Rosenbaum, M.S. (2002). "The artificial neural network as a tool for assessing geotechnical properties", *Geotechnical and Geological Engineering*, 20(2), 149-168.

Civil Engineering Infrastructures Journal 2023, 56(2): 333-345
DOI: 10.22059/CEIJ.2023.344568.1850

RESEARCH PAPER

Ageing Resistance of Bituminous Binder Modified with Propitious Antioxidant

Chakravarty,H.[1*], Sinha, S.[2] and Gupta, S.[3]

[1] Assistant Professor, Department of Civil Engineering, National Institute of Technology Patna, Bihar, India.
[2] Professor, Department of Civil Engineering, National Institute of Technology Patna, Bihar, India.
[3] M.Tech., Department of Civil Engineering, National Institute of Technology Patna, Bihar, India.

Received: 16 Jun. 2022; Revised: 13 Sep 2022; Accepted: 22 Oct. 2022

ABSTRACT: Bituminous mixes are prepared with aggregates, filler and bitumen as binder. Ageing of bitumen due to oxidation reduces the durability of such mixes. Various research efforts are therefore put in to decrease the ageing potential of binders and use of anti-oxidants has shown substantial success. In this research, Irganox 1010 has been identified as an anti-oxidant which has been found to be economical and yet of limited use in the field of pavement engineering. Various physical and rheological tests were conducted to determine the influence of Irganox 1010 on short-termed as well as long termed aged binders and results were analyzed. Softening Point Index (SPI) and Viscosity Ageing Index (VAI) were determined to understand the influence of Irganox 1010 on bituminous mixes. It was observed that Irganox 1010 significantly reduce ageing potential with usage of 0.6% by weight of bitumen. It has been found to be cost-effective due requirement of small quantities and being of comparatively lesser cost. This material has the potential of large scale usage to increase durability of bituminous mixes.

Keywords: Ageing, Anti-Oxidant, Bitumen, Irganox 1010.

1. Introduction

The top layers of flexible pavements are made up of aggregates bonded by bitumen as a binding material and are termed as bituminous mixes. The properties of bitumen greatly influence the performance of these mixes and depend upon exposure to environmental conditions such as presence of moisture and oxidation (Chakravarty and Sinha, 2020). Ageing of bitumen is considered to be one of the important factors for deterioration of bituminous mixes. Due to simultaneous action of external factors such as temperature, moisture, oxygen, solar radiation and internal factors such as thermal conductivity, reactive oxygen species, volumetric properties etc., ageing of bitumen occurs over its useful service life which further results in various distresses leading to decrease in serviceability of pavements (Aley et al., 2021; Omairey et al., 2021; Omaimey et al., 2022). Due to

* Corresponding author E-mail: hillol.ce@nitp.ac.in

ageing, the stiffness and brittleness of the binder increases, thereby reducing the flexibility of the binder as well as the mix. Under repeated traffic loading, cracks are developed due to reduced flexibility of the bituminous mixes (Apeagyei, 2011). Ageing of bitumen occurs due to the exposure of heat, UV rays and atmospheric conditions due to thermal oxidation and photo-oxidation (Dickinson, 1980). The ageing process can be broadly subdivided into short term ageing and long-term ageing for hot mix asphalt (Singh and Kumar, 2015). Short term ageing is caused due to loss of volatile components and oxidation of bitumen due to high temperatures during storage, mixing, laying and compacting stages which happen within a span of hours. Environmental oxidation and UV radiations lead to long term ageing during service life of pavements (Hofko et al., 2017; Feng et al., 2021). Volatization of light components, physical changes of polar substances also results in micro-transformation and intricate chemical changes in the process of ageing (Wang et al., 2020). Moreover, the increase in share of asphaltene and decrease in aromatic compounds due to ageing of the bitumen matrix leads to greater stiffness (Hofko et al., 2017; Read and Whiteoak, 2003). The short-term ageing process is simulated in laboratory using Rolling Thin Film Oven (RTFO) in accordance with ASTM D2872 whereas, long-term ageing is simulated by Pressure Ageing Vessel (PAV) in accordance with ASTM D6521. The recently developed Viennese Binder Ageing (VBA) gives expected to result in realistic long term field ageing simulation by use of highly oxidative gases such as ozone and nitrogen oxides, and can be performed for both bitumen and bituminous mixes (Hofko et al., 2020; Sreeram et al., 2021; Steiner et al., 2020; Mirwald et al., 2020). Various advanced testing techniques have been used to qualitatively and quantitatively analyze chemical components, characteristic functional groups and molecular weights before and after ageing by Thin-Layer Chromatography-Flame Ionization Detector (TLC-FID) (Margaritis et al., 2020; Yao et al., 2015), Fourier Transform Infrared spectrometer (FTIR) (Yao et al., 2015) and Gel Permeation Chromatography (GPC) (Lee et al., 2008), respectively. For assessing microstructural changes that occur due to ageing, florescent microscopy (Zhang et al., 2017), Scanning Electron Microscopy (SEM) (Ji et al., 2020) and Atomic Force Microscopy (AFM) (Xu et al., 2017) have been used for assessing ageing related microstructural changes.

Delaying ageing process can lead to enhanced serviceability life for bituminous pavements. Moreover, acceptance of hot, warm as well as cold Reclaimed Aasphalt Pavement (RAP) materials which could significantly reduce environmental loads is greatly dependent upon proper understanding of the aged binder and influence of various anti-ageing additives to virgin binders (Luo et al., 2018; Wang et al., 2018; Gu et al., 2019; Qian et al., 2020). Contemporary literatures mention that various modifiers enhance the binder performance by delaying ageing caused due to oxidation (Apeagyei, 2011; Perez and Maicelo, 2021; Sirin et al., 2018). Researches on anti-oxidants to resist ageing have increased in recent times. Some of the compounds such as Vitamin E, Irganox 1010, carbon black, Hydrated Lime (HL), Di-Lauryl-Thio-Di-Propionate (DLTDP), wood lignin, Styrene-Butadine-Styrene (SBS) etc. can work as anti-oxidants (Apeagyei, 2011; Feng et al., 2011; Cong et al., 2012; Cong et al., 2013; Feng et al., 2016). Bitumen modified with a combination of furfural and DLTDP (2.0% and 1.5%) was observed to have a lower ageing tendency. A comparison was done for Vitamin E, Irganox 1010, Irgafos P-EPQ, Carbon black, hydrated lime and the combination of furfural and DLTDP (Apeagyei, 2011). The combination of Irganox 1010 and UV326, which is a UV absorber, showed good effect in resisting the thermal and photo-oxidative ageing of

bituminous binder, which results in outstanding ageing resistance behavior of modified bituminous binder (Feng et al., 2011). Usage of grape pomace antioxidant exhibited optimal behavior in all tests performed at 10% content and for all aging conditions with respect to the controls (Floody and Thenoux, 2012). Experimental results indicated that the improvement of the anti-aging resistance of asphalt binder is noticeable when anti-aging agents containing 1% antioxidant Zinc dialkyldithio phosphate (ZDDP) and UV absorbers (0.5% UV531) were used (Cong et al., 2012; Cong et al., 2013). Wood lignin at dosages of 5% and 10% were used as an anti-ageing asphalt binder substitute (Wang and Derewecki, 2013). It was found that the 2% furfural modification of bitumen had the lowest ageing index after ageing, indicating an improvement in ageing properties of binder (Fini et al., 2015). The combination of layered double hydroxide (LDHs) and Irganox 1010 (3 wt% and 0.6 wt%) modified bitumen shows outstanding anti-ageing behaviour to both thermo-oxidative ageing and UV ageing (Zhao et al., 2015). The aged epoxy natural rubber (ENR) modified binder show better physical and rheological properties than the base binder (Al-Mansob et al., 2016). The thermal- and photo-oxidative aging resistance of bitumen was improved significantly by the pyrolysis carbon black (PCBs) (Feng et al., 2016). Usage of 0.5% poly phosphoric acid (PPA) as polymer replacement indicates better anti-ageing properties of binders (Liu et al., 2018). Replacing petroleum-based binder (bitumen) with up to 6% of lignin precipitated from black liquor can be used for hot mix asphalt, and may even be feasible for lower temperature warm mix asphalt process (Arafat et al., 2019). The alternative use of waste vegetable cooking oil (WVCO) as anti-ageing agent for bitumen shows noteworthy benefits to the environment, human health, and economy (Gokalp and Uz, 2019).

As can be observed from literature, few studies have been conducted using Irganox 1010 as anti-oxidant in binders with promising results (Apeagyei 2011; Feng et al., 2011; Zhao et al., 2015). The quantity requirement for optimized performance is also observed to be quite low. Moreover, market study showed that Irganox 1010 has low cost, good availability and better compatibility with organic products. Further researches conducted on ageing resistance with anti-oxidants with viscosity grade binders are limited. These factors served as motivation for adopting Irganox 1010 in this study and determine the influence of the modifier on performance of the bituminous binder of viscosity grade (VG) 30 which is widely used in India.

2. Materials

2.1. Bitumen

Viscosity Grade (VG) 30 bituminous binder was obtained from Indian Oil, Barauni refinery, Bihar, India. Basic physical properties were determined to ascertain the quality of binder.

2.2. Anti-oxidant

Irganox 1010 was selected as the anti-oxidant as depicted in Figure 1a and the molecular structure is shown in Figure 1b. It is a high-grade antioxidant for natural and synthetic oil. Irganox 1010 was procured from Eklingjee Polymers Pvt. Ltd., Rajasthan, India. The physical properties of Irganox 1010 are presented under:

2.3. Methodology

The modified asphalt binders with antioxidant Irganox 1010 were prepared by melt blending. The contents of antioxidant are 0.2, 0.4, 0.6, 0.8 and 1.0 % by weight of bitumen had been taken as shown in Figure 2. In this way, five modified binders were prepared with different compositions. Firstly, base binder was melted by heating it at 150 ℃ in a steel container and then antioxidant Irganox 1010 added into the container of bitumen while continuously stirring it. After the complete addition of antioxidant, mixture was mechanically

blended at mixing speed of 1000 rpm for 30 min at the temperature of 150 °C for obtaining the modified bituminous binder. Short-term ageing and long-term ageing were done using RTFO and PAV testing facilities. The RTFO ageing was done as per ASTM D2872 at 163 ^{o}C for 85 minutes. The PAV ageing was performed on the RTFO aged samples at 305 psi for 20 hours in accordance to ASTM D6521. Thereafter, physical parameters such as penetration and softening point for modified and aged binders were determined. Viscosity measurement was performed using Brookfield rotational viscometer at 135 ^{o}C and 20 rpm in accordance to ASTM D4402. Complex modulus and phase angle were determined using Dynamic Shear Modulus (DSR) test with oscillation rate of 10 rad/sec and stain level of 12% in accordance to ASTM D7175-15. Comparison between these parameters were drawn to determine the influence of Irganox 1010 modifications on unaged, RTFO aged and PAV aged binders. The temperature range was in the range of 46-76 ^{o}C as this is the range of operational temperature within India. Thereafter, Softening Point Increment (SPI) and Viscosity Ageing Index (VAI) were determined. SPI is given by the difference of softening points of aged and unaged binders and VAI is given by the ratio of difference of viscosity of aged and unaged binders to the viscosity of unaged binders. Smaller values of SPI and VAI indicate better ageing resistance and are used to estimate the ageing characteristics of binder.

3. Results and Discussions

3.1. Physical Tests

3.1.1. Penetration Value

The penetration value was determined in accordance with ASTM D6. Tests were performed at a temperature of 25 ^{o}C.

Penetration test result of modified binder is plotted in Figure 3. Addition of Irganox 1010 makes binder softer, so their penetration value increases gradually for unaged and RTFO aged binders while increasing Irganox 1010 content. It is lesser in case of PAV aged binders but for PAV aged binder penetration values increase up to 0.6% Irganox 1010 and then after decreases up to some extent on further addition of antioxidant. As observed, after ageing the binder becomes stiff and thereby a reduction in penetration value is observed. It is observed that penetration value decreases upon increase in oxidative ageing. Thus, PAV aged binders have lesser penetration values as compared to RTFOT aged binders.

Table 1. Physical properties of bitumen

Physical properties	Test method	Observed value
Penetration value	ASTM D5	61
Softening point value	ASTM D36	49 ^{0}C
Specific gravity value	ASTM D70-03	1.02

(a) Irganox 1010

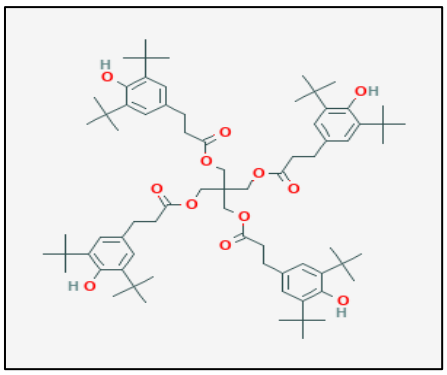

(b) Molecular Structure of Irganox1010 (Pubchem, National Centre for Biotechnology Information, 2021)

Fig. 1. Physical and chemical form for Irganox 1010

Table 2. Physical properties of Irganox 1010

Material	Appearance	Melting range	Specific gravity (g/ml, 20 ºC)	Molecular formula
Irganox 1010	White powder	110 ~ 125 ºC	1.116	$C_{73}H_{108}O_{12}$

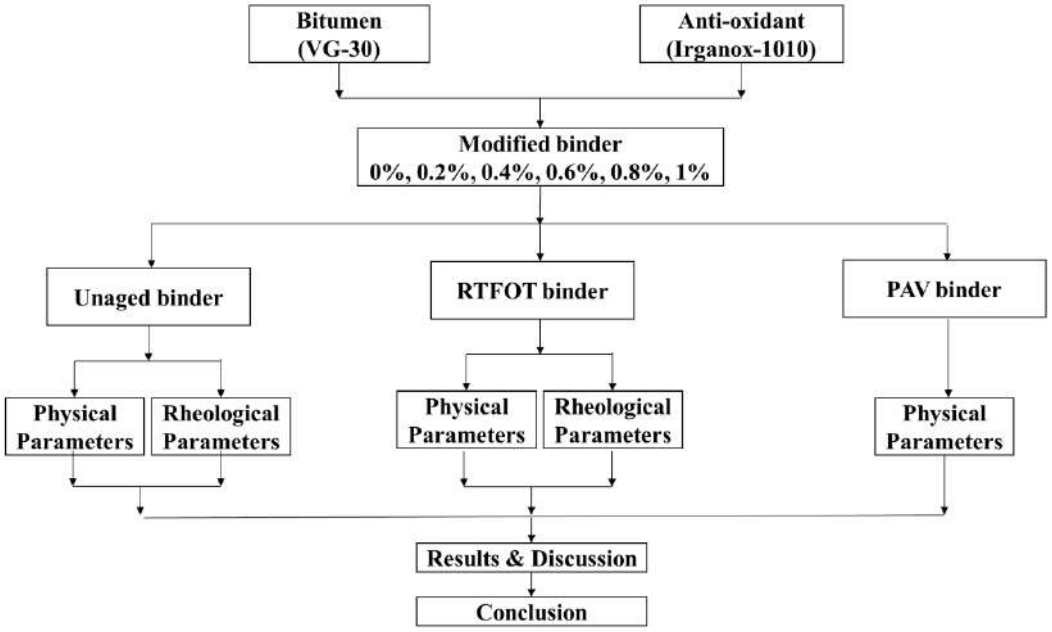

Fig. 2. Methodology for evaluation of Irganox 1010 as anti-oxidant

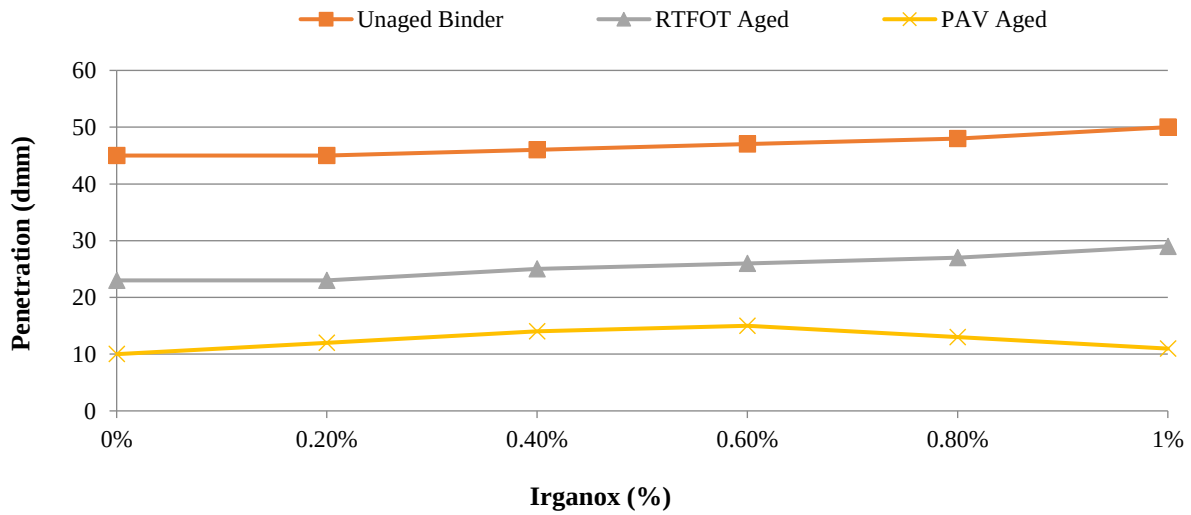

Fig. 3. Effect of Irganox 1010 on penetration values of unaged, RTFO aged and PAV aged binders

3.1.2. Softening Value

The softening point was determined in accordance with ASTM D36. The results obtained are provided in Figure 4.

After ageing of binders, they become harder in nature and their softening point increases. It can be observed from Figure 4 that softening point of base binder after RTFO ageing is more than un-aged binder. After PAV ageing, softening point is further increased. Addition of Irganox 1010 makes binder softer, so their softening point decreases gradually for un-aged and RTFO aged binders while increasing Irganox 1010 content. But for PAV aged binders softening point values decrease up to 0.6% Irganox 1010 and then after increases up to some extent on further addition of antioxidant.

Thus, observing the softening point and the penetration results, it can be concluded that after ageing, the binder becomes harder. This can be attributed to oxidative ageing due to the short-term as well as long-

term ageing simulation process.

3.2. Rheological Parameters

3.2.1. Rotational Viscosity

Bolin's viscometer was used for Rotational Viscosity (RV) tests to determine the dynamic viscosity of binder in accordance with ASTM D4402. RV test result of different binders at 135 °C is provided in Figure 5.

After ageing of binders, these become more viscous. It can be observed from Figure 5 that PAV aged binders are highly viscous followed by RTFOT aged binders and the unaged binders have the least viscosity. With the addition of Irganox 1010, it is observed that the viscosity decreases for all conditions. For PAV aged binder, however, viscosity increases after modification by 0.6% Irganox 1010 thereby setting an optimum value of modification at 0.6%.

3.2.2. Complex Modulus (G*)

Dynamic Shear Rheometer (DSR) was used for determination of complex modulus (in kPa) in accordance with ASTM D7175-15. The G* values were obtained for unaged as well as RTFO and PAV aged binders. The values obtained are plotted in Figure 6-8, representing the values in graphical format.

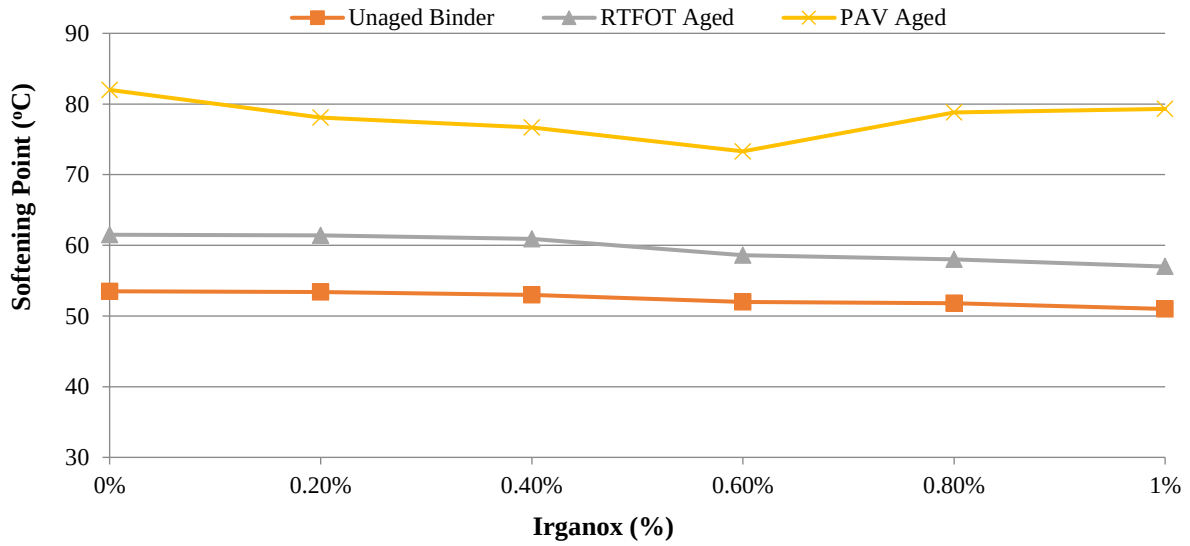

Fig. 4. Effect of Irganox 1010 on softening point of un-aged, RTFO aged and PAV aged binders at 135 °C

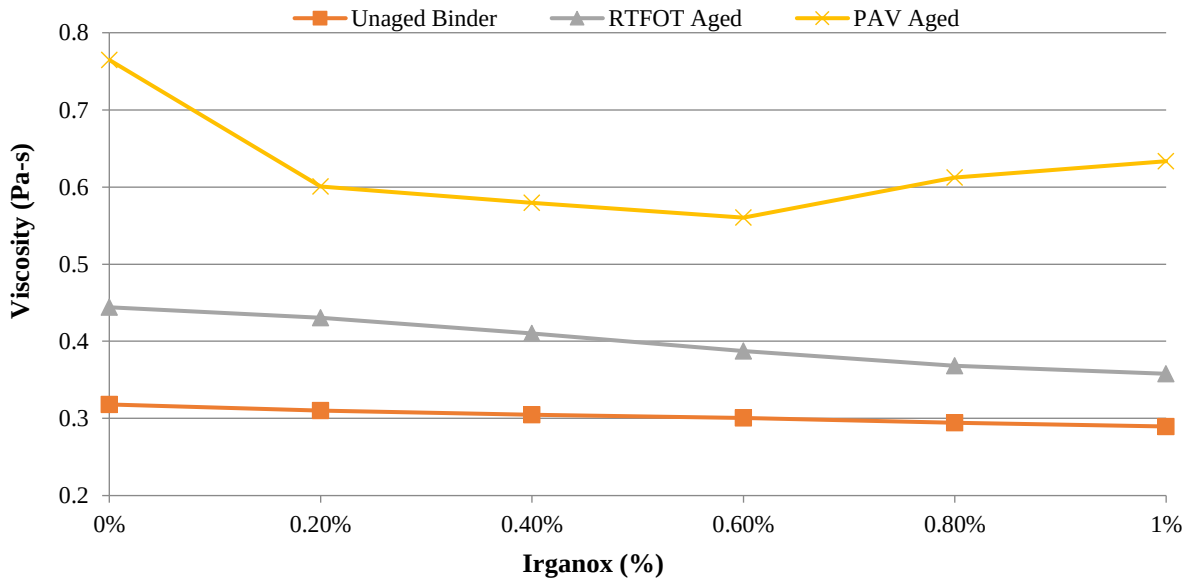

Fig. 5. Effect of Irganox 1010 contents on viscosity of un-aged, RTFO aged and PAV aged binders at 135 °C

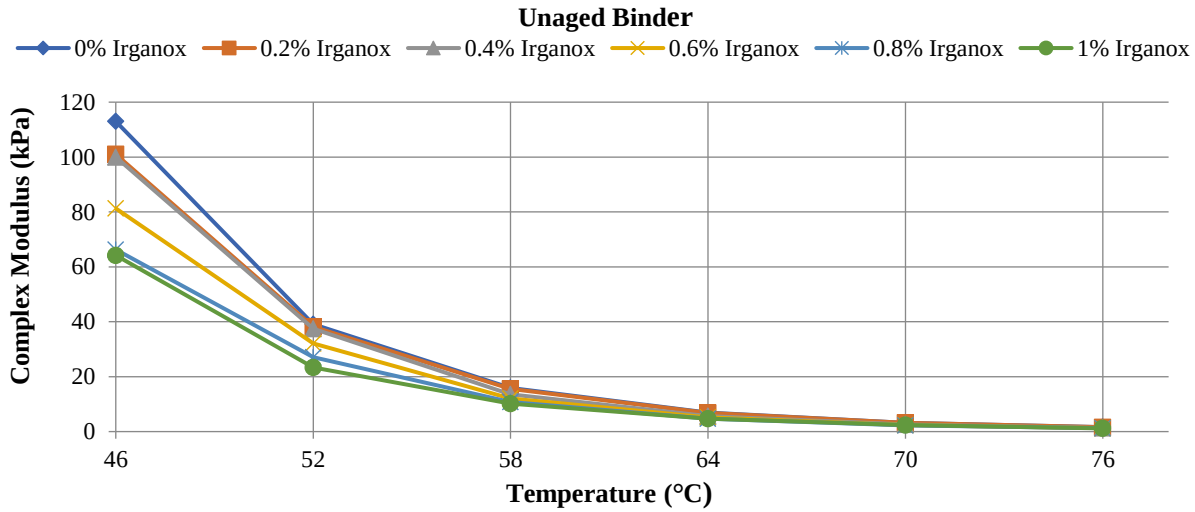

Fig. 6. Complex modulus variation of binders of unaged binders

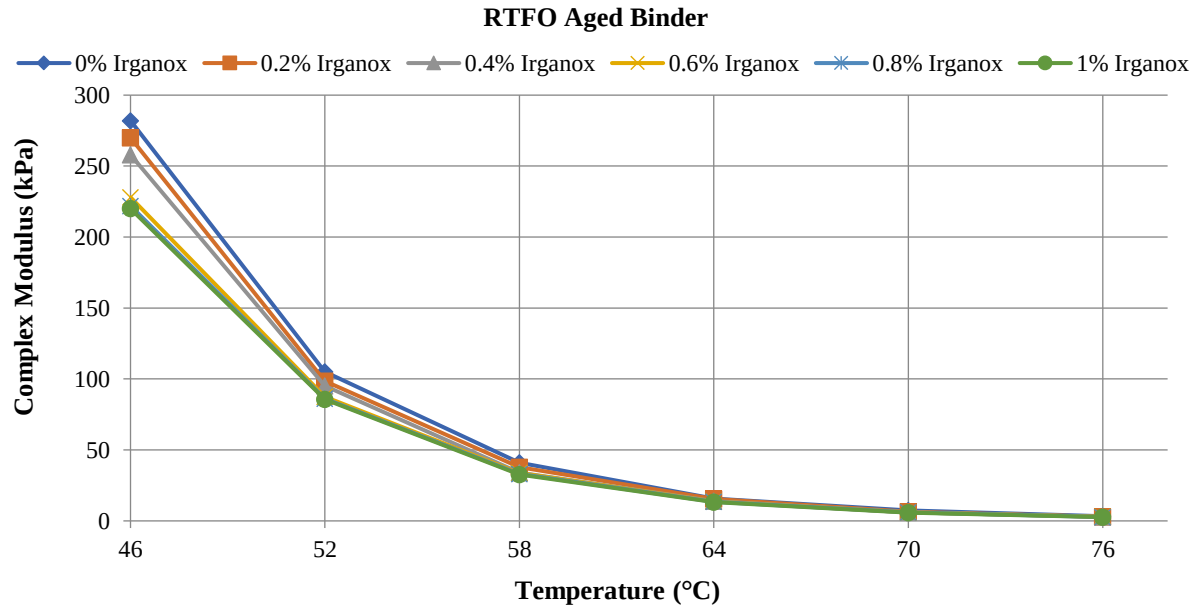

Fig. 7. Complex modulus variation of binders after RTFO ageing

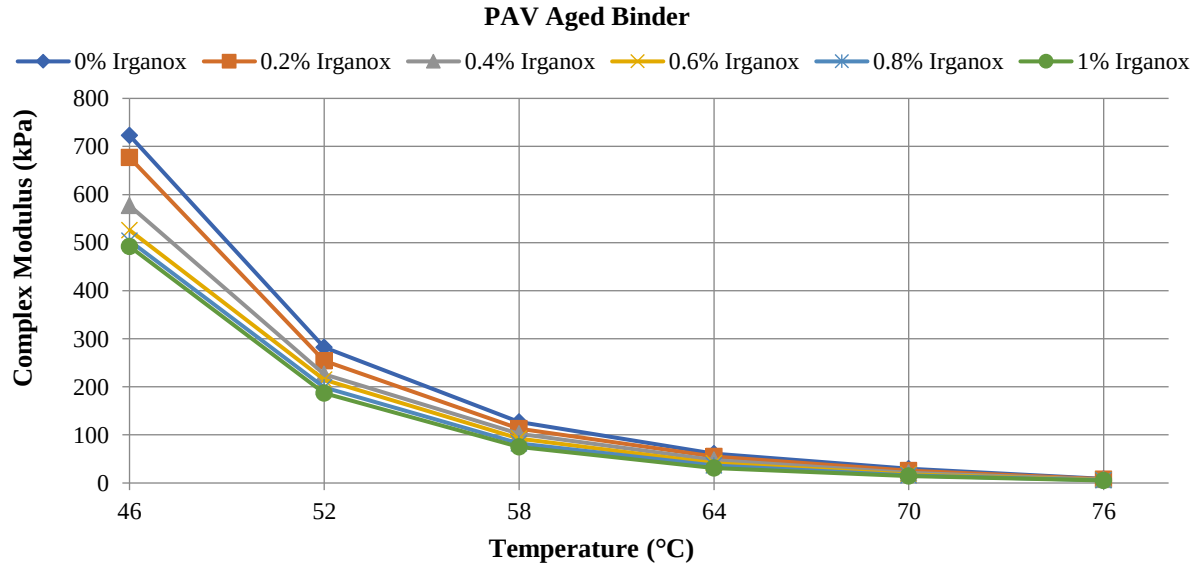

Fig. 8. Complex modulus variation of binders after PAV ageing

It can be observed that from the Figures 6-8 that for both unaged and aged binders complex modulus values decrease with subsequent introduction of Irganox 1010 signifying decrease in stiffness with Irganox 1010. The complex modulus values for PAV aged binders were higher than RTFO aged binders and both were subsequently higher as compared to unaged binders corresponding to individual temperatures meaning thereby that the binders became stiffer with ageing. The results are in line with observations made for penetration and softening point values and can be attributed to loss of volatile materials and increasing the asphaltene content leading to rise to stiffness (Hofko et al., 2017; Read and Whiteoak, 2003).

3.2.3. Phase Angle (δ)

Phase angle was also obtained from DSR results performed in accordance with ASTM 7175-15. Phase angle provides an overview about the viscous and elastic nature of binders. Higher phase angle signifies an elastic binder. The results found have been plotted in Figures 9-11. It was observed from the phase angle values that with the ageing there is a loss of binder elasticity due to decreased phase angle. The phase angles were compared for individual temperatures at different ageing conditions. This loss of elasticity or increase in brittleness subsequently promotes fatigue cracking. However, when Irganox 1010 was introduced, it was found that phase angle values increases thereby signifying a more elastic binder.

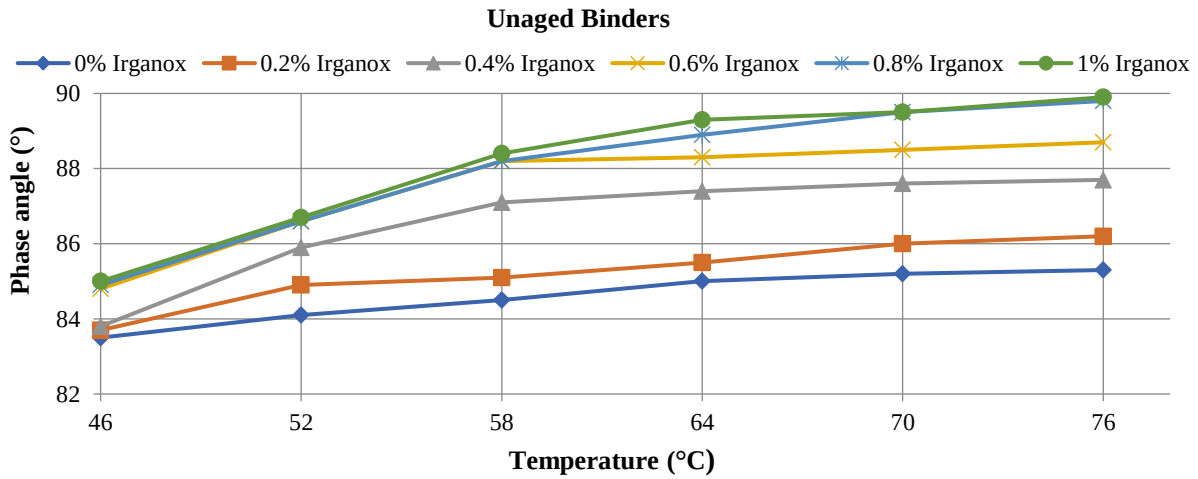

Fig. 9. Phase angle variation of unaged binders

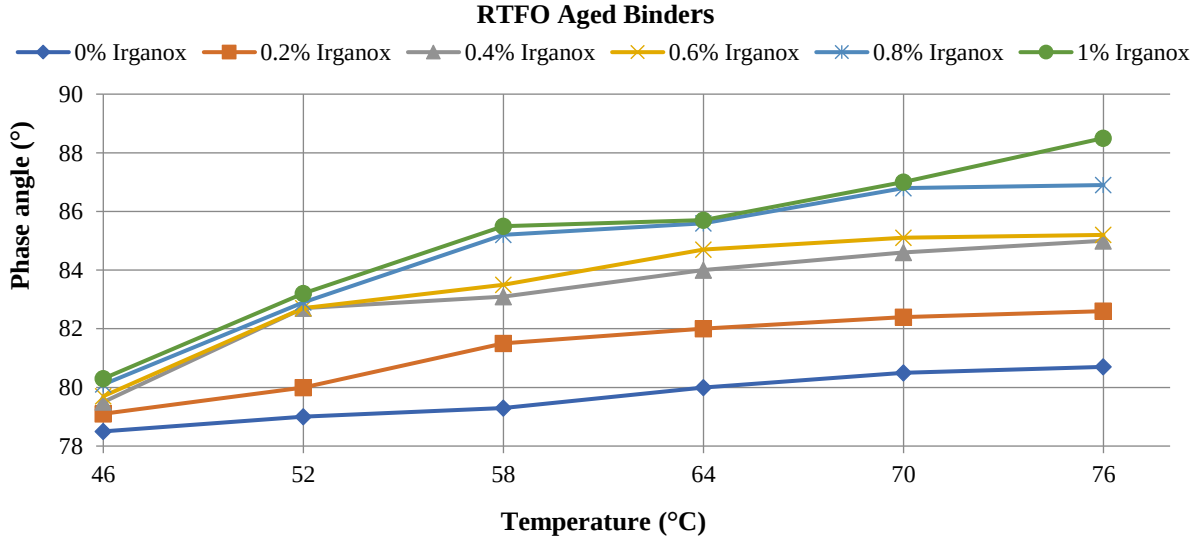

Fig. 10. Phase angle variation of binders after RTFO ageing

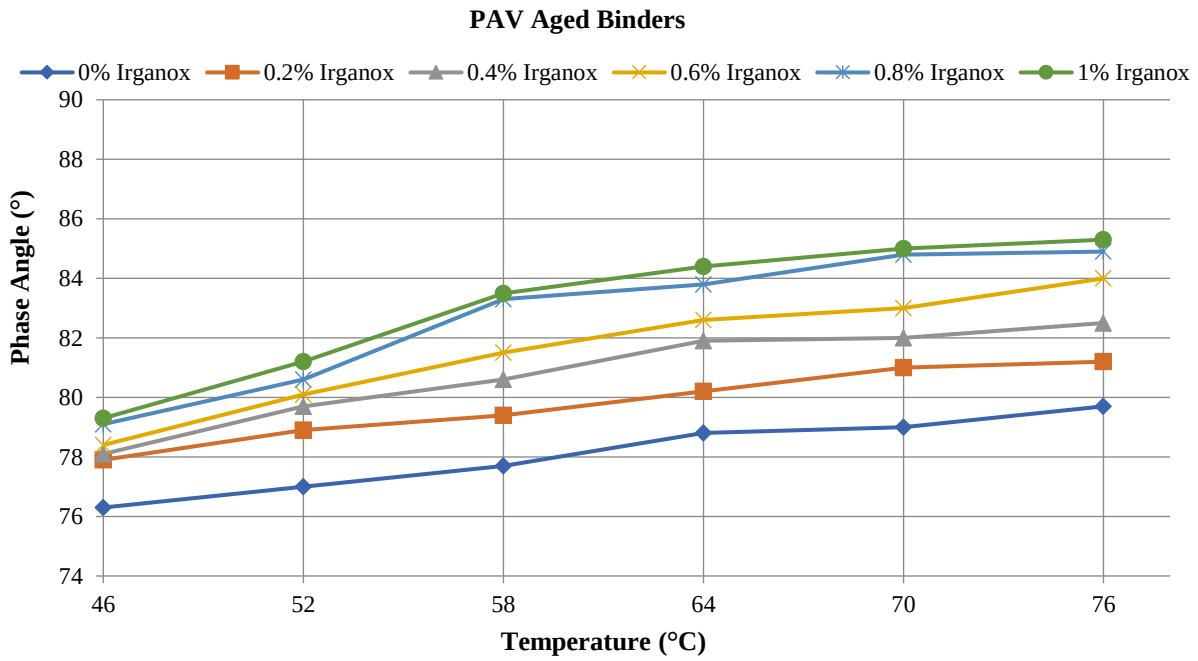

Fig. 11. Phase angle variation of binders after PAV ageing

3.2.4. Softening Point Increment (SPI) and Viscosity Ageing Index (VAI)

The ageing characteristics of bituminous binder have been estimated with the help of two indexes in this study namely the Softening Point Increment (SPI) and Viscosity Ageing Index (VAI) (Feng et al., 2011; Cong et al., 2012; Cong et al., 2013; Zhao et al., 2015). These are as can be observed in Eqs. (1) and (2).

$$SPI = SP_2 - SP_1 \quad (1)$$

$$VAI = \frac{V_2 - V_1}{V_1} \quad (2)$$

where, SP_1 and SP_2: indicate softening point of un-aged and aged bitumen, respectively; V_2 and V_1: indicate viscosity of un-aged and aged bitumen, respectively in Pa-s. Lesser values of SPI and VAI signify enhanced anti-ageing performance of bitumen (Cong et al., 2013).

The ageing characteristics of binder with different amount of Irganox 1010 are provided in Figures 12 and 13. After RTFO ageing, binders modified using Irganox 1010 show continuous decrement in SPI and VAI values when the amount of Irganox 1010 is increased gradually. It indicates the improvement of thermal-oxidative anti-ageing behaviour of bitumen. The consequence of Irganox 1010 on PAV aged binder can be observed to have decreasing trend initially. However, after 0.6% addition, a rise in values can be seen for both SPI and VAI results. The Irganox 1010 shows supporting results on the anti-ageing behaviour of PAV aged binder while the amount of Irganox 1010 is not greater than 0.6 wt%, but opposing influence on the anti-ageing behaviour is shown when the amount of Irganox 1010 is more than 0.6% weight of bitumen. This behavior is observed for PAV aged binder and not for RTFO aged binder. It can be attributed to the fact that long term ageing simulated by PAV gives a wholistic overview of the thermal oxidative ageing of binder as compared to short term aged RTFO binders.

The reason and mechanism of action of Irganox 1010 on the aged bitumen has been explained in few contemporary literatures (Feng et al., 2011; Zhao et al., 2015). It may be concluded that Irganox 1010 deflocculates the asphaltene which is responsible for imparting hardness to the aged bitumen by the process of peptization (Zhao et al., 2015; Lian et al., 1994). This action thus improves the resistance of the bitumen for both short- and long-term aging.

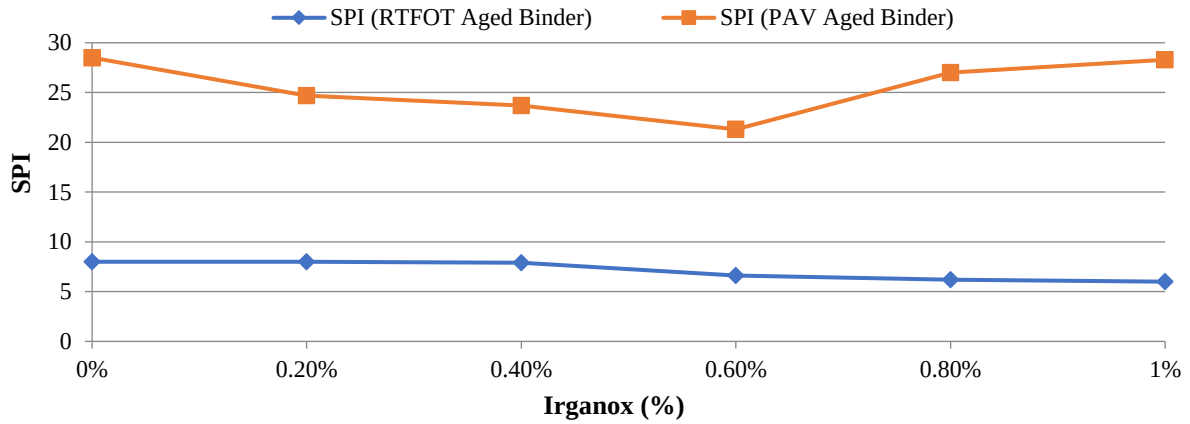

Fig. 12. Effect of Irganox 1010 contents on SPI (°C) of bitumen

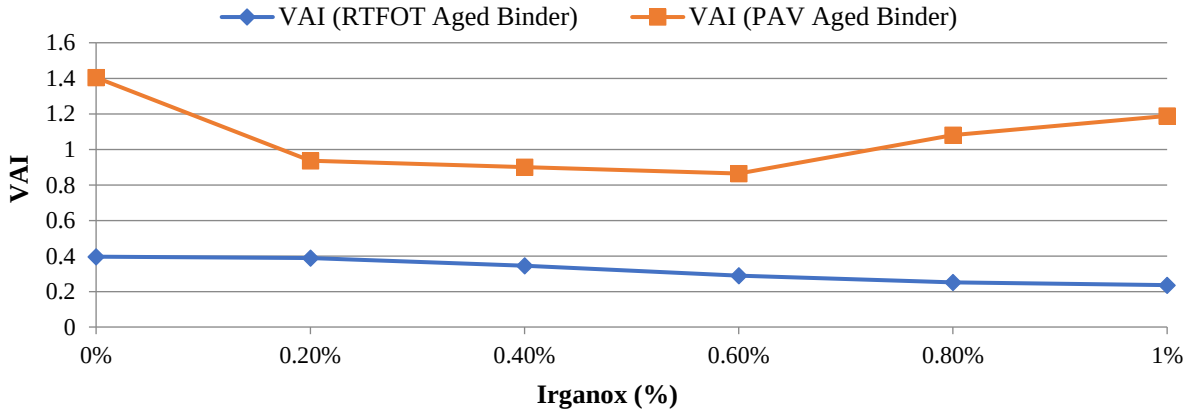

Fig. 13. Effect of Irganox 1010 contents on VAI of bitumen

4. Conclusions

The process of ageing of bitumen leads to stiffer bitumen which can be observed from respective physical and rheological tests. As observed from literature, this change is attributed to loss of volatile aromatic compounds and increase in asphaltene contents due to the process of ageing.

Various anti-ageing materials are used to mitigate the problem of ageing and Irganox1010 is one of them. The use of this anti-oxidant was found to be limited in literature. However, due to lower cost and wide scale availability this material was selected for this study. While increasing the antioxidant Irganox 1010 content in bitumen, the softening point, viscosity, complex modulus decreases gradually whereas penetration and phase angle increases gradually. After RTFO ageing, SPI and VAI values of binders gradually decrease with increase in antioxidant content, which indicates the improvement in ageing resistance of binders. SPI and VAI values of binders after PAV ageing are observed to be having slightly different nature. Firstly, both indexes decrease up to 0.6% of Irganox 1010 and then after both of them increases. It can thus be concluded that Irganox 1010 improves resistance of bituminous binders to ageing and 0.6 wt% of Irganox 1010 is the appropriate content of antioxidant for VG30 binder. Literature explains that Irganox 1010 deflocculates the asphaltene by the process of peptization and inhibits gelatinization of the binders subjected to ageing. This however, needs to be ascertained by carrying out detailed chemical analysis and studying of the microstructures of the bituminous binders and the mixes.

Thus, it can be concluded that Irganox 1010 can be considered as potential anti-ageing bitumen modifier considering smaller quantity, lower cost and wide scale availability to enhance durability of flexible pavements. However, other performance

evaluation for Irganox 1010 modified binders would further help for confirmation of appropriate content of antioxidant.

5. References

Apeagyei, A.K. (2011). "Laboratory evaluation of antioxidants for asphalt binders", *Construction and Building Materials*, 25, 47-53, https://doi.org/10.1016/j.conbuildmat.2010.06.058.

Alae, M., Zhao, Y. and Leng, Z. (2021). "Effects of ageing, temperature and frequency-dependent properties of asphalt concrete on top-down cracking", *Road Material Pavement Design*, 22(10), 2289-2309, https://doi.org/10.1080/14680629.2020.1753099.

Al-Mansob, R.A., Ismail, A., Md-Yusoff, N.I., Albrka, SI., Azhari, C.H. and Karim, M.R. (2016). "Rheological characteristics of unaged and aged epoxidised natural rubber modified asphalt", *Construction and Building Materials*, 102, 190-199, https://doi.org/10.1016/j.conbuildmat.2015.10.133.

Arafat, S., Kumarm N., Wasiuddinm, N.W., Owhem E.O. and Lynamm, J.G. (2019). "Sustainable lignin to enhance asphalt binder oxidative aging properties and mix properties", *Journal of Cleaner Production*, 217, 456-468, https://doi.org/10.1016/j.jclepro.2019.01.238.

ASTM D5. (1997). *Standard test method for penetration of bituminous materials*, American Society for Testing and Materials, Conshohocken, Pennsylvania, USA.

ASTM D36. (1995). *Standard test method for softening point of bitumen (Ring-and-Ball apparatus)*, American Society for Testing and Materials, Conshohocken, Pennsylvania, USA.

ASTM D-4402. (2000). *Standard test method for viscosity determination of asphalt at elevated temperatures using a rotational viscometer*, American Society for Testing and Materials, Conshohocken, Pennsylvania, USA.

ASTM D7175. (2015). *Standard test method for determining the rheological properties of asphalt binder using a dynamic shear rheometer*, ASTM International, West Conshohocken, Pennsylvania, USA.

ASTM D2872. (2019). Standard method of test for effect of heat and air on a moving film of asphalt (rolling thin-film oven test), ASTM International, West Conshohocken, PA, USA.

ASTM D6521. (2000). *Standard practice for accelerated aging of asphalt binder using a Pressurized Aging Vessel (PAV)*, American Society for Testing and Materials, Conshohocken, Pennsylvania, USA.

Chakravarty, H. and Sinha, S. (2020). "Moisture damage of bituminous mixes and application of nanotechnology in its Prevention", *Journal of Materials in Civil Engineering*, 32(8), 03120003, https://doi.org/10.1061/(ASCE)MT.1943-5533.0003293.

Cong, P., Wang, J., Li, K. and Chen, S. (2012). "Physical and rheological properties of asphalt binders containing various antiaging agents", *Fuel*, 97, 678-684, https://doi.org/10.1016/j.fuel.2012.02.028.

Cong, P., Wang, X., Xu, P., Liu, J., He, R., Chen, S. (2013). "Investigation on properties of polymer modified asphalt containing various antiaging agents", *Polymer Degradation and Stability*, 98, 2627-2634, https://doi.org/10.1016/j.polymdegradstab.2013.09.024.

Dickinson, E.J. (1980). "The hardening of Middle East petroleum asphalts in pavement surfacings, *Proceedings of the Association of Asphalt Paving Technologists (AAPT)*, 49, 30-57.

Feng, Z., Yu, J., Zhang, H. and Kuang, D. (2011) "Preparation and properties of ageing resistant asphalt binder with various anti-ageing aadditives", *Applied Mechanics and Materials*, 71-78, 1062-1067, https://doi.org/10.4028/www.scientific.net/AMM.71-78.1062.

Feng, Z., Rao, W., Chen, C., Tian, B., Li, X., Li, P. and Guo, Q. (2016). "Performance evaluation of bitumen modified with pyrolysis carbon black made from waste tyres", *Construction and Building Materials*, 111, 495-501, https://doi.org/10.1016/j.conbuildmat.2016.02.143.

Feng, Z., Cai, F., Yao, D. and Li, X. (2021). "Aging properties of ultraviolet absorber/SBS modified bitumen based on FTIR analysis", *Construction and Building Materials*, 273, Article 121713, https://doi.org/10.1016/j.conbuildmat.2020.121713.

Ji, X., Hou, Y., Zou, H., Chen, B. and Jiang. Y. (2020). "Study of surface microscopic properties of asphalt based on atomic force microscopy", *Construction and Building Materials*, 242, Article 118025, https://doi.org/10.1016/j.conbuildmat.2020.118025.

Floody, A.C. and Thenoux, G. (2012). "Controlling asphalt aging by inclusion of byproducts from red wine industry", *Construction and Building Materials*, 28, 616-623, https://doi.org/10.1016/j.conbuildmat.2011.08.092.

Fini, E.H., Buabeng, F.S., Abu-Lebdeh, T. and Awadallah,. F (2015). "Effect of introduction of furfural on asphalt binder ageing characteristics", *Road Materials and Pavement Design*, 17(3), 638-657,

https://doi.org/10.1080/14680629.2015.1108219.

Gokalp, I. and Uz, V.E. (2019). "Utilizing of waste vegetable cooking oil in bitumen: Zero tolerance aging approach", *Construction and Building Materials*, 227, 116695, https://doi.org/10.1016/j.conbuildmat.2019.116695.

Gu, F., Ma, W., West, R.C., Taylor, A.J. and Zhang, Y. (2019). "Structural performance and sustainability assessment of cold central-plant and in-place recycled asphalt pavements: A case study", *Journal of Cleaner Production*, 208, 1513-1523, https://doi.org/10.1016/j.jclepro.2018.10.222.

Hofko, B., Cannone Falchetto, A., Grenfell, J., Huber, L., Lu, X., Porot, L., Poulikakos, L.D. and You, Z. (2017). "Effect of short-term ageing temperature on bitumen properties", *Road Materials and Pavement Design*, 18(sup2), 108-117, https://doi.org/10.1080/14680629.2017.1304268.

Hofko, B., Maschauer,, D., Steiner D., Mirwald, J. and Grothe, H. (2020). "Bitumen ageing, Impact of reactive oxygen species", *Case Study Construction Materials*, 13, e00390, https://doi.org/10.1016/j.cscm.2020.e00390.

Lee, S.-J., Amirkhanian, S.N., Shatanawi, K. and Kim, K.W. (2008). "Short-term aging characterization of asphalt binders using gel permeation chromatography and selected superpave binder tests", *Construction and Building Materials*, 22(11), 2220-2227, https://doi.org/10.1016/j.conbuildmat.2007.08.005.

Lian, H., Lin, J. and Yen, T.F. (1994). "Peptization studies of asphaltene and solubility parameter spectra", *Fuel*, 73(3), 423-428, https://doi.org/10.1007/978-1-4899-0617-5_4.

Liu, X., Cao, F., Xiao, F. and Amirkhanian, S. (2018). "BBR and DSR testing of aging properties of polymer and polyphosphoric acid, modified asphalt binders", *Journal of Materials in Civil Engineering*, 30(10), 04018249(1)-04018249(11), https://doi.org/10.1061/(ASCE)MT.1943-5533.0002440.

Luo, X., Gu, F., Zhang, Y., Lytton, R.L. and Birgisson, B. (2018). "Kinetics-based aging evaluation of in-service recycled asphalt pavement", *Journal of Cleaner Production*, 200, 934-944, https://doi.org/10.1016/j.jclepro.2018.07.267.

Margaritis, A., Soenen, H., Fransen, E., Pipintakos, G., Jacobs, G. and Blom, J. (2020). "Identification of ageing state clusters of reclaimed asphalt binders using principal component analysis (PCA) and hierarchical cluster analysis (HCA) based on chemo-rheological parameters", *Construction and Building Materials*, 244, 118276, https://doi.org/10.1016/j.conbuildmat.2020.118276.

Mirwald, J., Maschauer, D., Hofko, B. and Grothe, H. (2020). "Impact of reactive oxygen species on bitumen aging, The viennese binder aging method", *Construction and Building Materials*, 257, 119495, https://doi.org/10.1016/j.conbuildmat.2020.119495.

Miyamoto, A. and Ximenes, H.D.C. (2021). "Development of a road-condition assessment system and application to road maintenance decision-making", *Civil Engineering Infrastructures Journal*, 54(2), 225-251, https://doi.org/10.22059/CEIJ.2021.294057.1642.

Muñoz Perez, S.P. and Onofre Maicelo, P.A.A. (2021). "Use of recycled asphalt as an aggregate for asphalt mixtures: literary review", *Innovative Infrastructure Solution*, 6, 146, https://doi.org/10.1007/s41062-021-00516-x

Omairey, E.L., Gu, F. and Zhang, Y. (2021). "An equation-based multiphysics modelling framework for oxidative ageing of asphalt pavements", *Journal of Cleaner Production*, 280, 124401, https://doi.org/10.1016/j.jclepro.2020.124401.

Omairey, E.L., Zhang, Y., Soenen, H. and Carbonneau, X. (2022). "Parametric analysis and field validations of oxidative ageing in asphalt pavements using multiphysics modelling approaches", *International Journal of Pavement Engineering*, 24(2), 1-24, https://doi.org/10.1080/10298436.2021.2020267.

Qian, Y., Guo, F., Leng, Z., Zhang, Y. and Yu, H. (2020). "Simulation of the field aging of asphalt binders in different reclaimed asphalt pavement (RAP) materials in Hong Kong through laboratory tests", *Construction and Building Materials*, 265, 120651, https://doi.org/10.1016/j.conbuildmat.2020.120651.

Read, J. and Whiteoak, D. (2003) *The shell bitumen handbook*, Thomas Telford Publishing Ltd., London.

Singh, B. and Kumar, P. (2015). "Effect of modifiers on the ageing properties of bitumen: A review", *Proceedings of 3rd Conference of Transportation Research Group of India (3rd CTRG)*, Kolkata.

Sirin, O., Paul, D.K. and Kassem, E., (2018). "State of the art study on aging of asphalt mixtures and use of antioxidant additives", *Advances in Civil Engineering*, Article ID 3428961, 18 pages, https://doi.org/10.1155/2018/3428961.

Steiner, D., Hofko, B. and Blab, R. (2020). "Introducing a nitrogen conditioning to separate oxidative from non-oxidative ageing effects of

hot mix asphalt", *Road Materials and Pavement Design*, 21(5), 1293-1311, https://doi.org/10.1080/14680629.2018.1548371

Sreeram, A., Masad, A., Sootodeh Nia, Z., Maschauer, D., Mirwald, J., Hofko, B. and Bhasin, A., (2021). "Accelerated aging of loose asphalt mixtures using ozone and other reactive oxygen species", *Construction and Building Materials*, 307, 124975, https://doi.org/10.1016/j.conbuildmat.2021.124975.

Wang, F., Xiao, Y., Cui, P., Lin, J., Li, M. and Chen, Z. (2020). "Correlation of asphalt performance indicators and aging degrees: A review", *Construction and Building Materials*, 250, 118824, https://doi.org/10.1016/j.conbuildmat.2020.118824.

Wang, Y., Leng, Z., Li, X. and Hu, C. (2018). "Cold recycling of reclaimed asphalt pavement towards improved engineering performance", *Journal of Cleaner Production*, 171, 1031-1038, https://doi.org/10.1016/j.jclepro.2017.10.132.

Wang, H. and Derewecki, K. (2013). "Rheological properties of asphalt binder partially substituted with wood lignin", *Airfield and Highway Pavement Conference*, LA, California, https://doi.org/10.1061/9780784413005.081.

Xu, M., Yi, J., Pei, Z., Feng, D., Huang, Y. and Yang, Y. (2017). "Generation and evolution mechanisms of pavement asphalt aging based on variations in surface structure and micromechanical characteristics with AFM", *Materials Today Communication*, 12, 106-118, https://doi.org/10.1016/j.mtcomm.2017.07.006.

Zhang, D., Zhang, H. and Shi, C. (2017). "Investigation of aging performance of SBS modified asphalt with various aging methods", *Construction and Building Materials*, 145, 445-451, https://doi.org/10.1016/j.conbuildmat.2017.04.055.

Zhao, Z.J., Xu, S., Wu, W.F., Yu, J.Y. and Wu, S.P. (2015). "The aging resistance of asphalt containing a compound of LDHs and antioxidant", *Petroleum Science and Technology*, 33, 787-793, https://doi.org/10.1080/10916466.2015.1014965

Civil Engineering Infrastructures Journal 2023, 56(2): 347-364
DOI: 10.22059/CEIJ.2023.345306.1855

RESEARCH PAPER

Performance of Grape Extract Addition as an Admixture in Concrete Construction

Mahmood, H.F.[1*], Dabbagh, H.[2] and Mohammed, A.A.[3]

[1] Associate Professor, Civil Engineering Department, University of Halabja, Kurdistan Region, Iraq.
[2] Assistant Professor, Civil Engineering Department, University of Kurdistan, Sanandaj, Iran.
[3] Professor, Civil Engineering Department, College of Engineering, University of Sulaimani, Kurdistan Region, Iraq.

Received: 02 Jul. 2022; Revised: 30 Nov 2022; Accepted: 30 Jan. 2023

ABSTRACT: Chemical admixtures are widely used for the production of high-performance concrete, but they are responsible for environmental pollution and health issue during construction because of their chemical nature. Also manufactured admixtures are expensive, on this base recently, researches and attempts are focused to find alternatives, and using different natural or bio admixtures for concrete is a good choice. In this study, the impact of Grape Extract (GE), a natural additive, on the properties of concrete was investigated. Various GE percentages were used to investigate the properties of fresh and hardened concrete. The results show that there is a continuous workability enhancement and continuous splitting tensile strength loss with GE increase. Improvement of 28 days compressive strength by 18.5% was observed on using 0.22% GE, while no compressive and flexural strengths loss was observed with GE addition up to 0.55%. Finally, the results of the study showed that GE dosages can strongly impact the fresh properties and mechanical strength of concrete mixtures. So there is a chance to produce self-compacting concrete using GE natural admixture instead of chemical admixture but there is a need for further experimental tests.

Keywords: Compressive Strength, Flexural Strength, Grape Extract, Slump, Water Absorption.

1. Introduction

A chemical admixture is a material besides water, aggregates, or blended cement that is used as an additive in concrete or mortar and is added to the batch directly before or during mixing. Admixtures are substances added to concrete mixes to alter or enhance the properties of fresh and/or hardened concrete, according to the ASTM C-494 standard. Typically, the admixture is added in small amounts ranging from 0.005% to 2% by weight of cement (Li, 2011). Although it is advantageous to use chemical admixtures consciously to improve the early and final properties of cementation materials, Chemical admixtures also allow for the production and construction of

* Corresponding author E-mail: e.hershfaqe@gmail.com

specialty concretes such as high fluidity concrete, high strength concrete, underwater concrete, and sprayed concrete (Plank et al., 2015).

Chemical admixtures also contribute to environmental pollution. When they are in concrete, and are released into the atmosphere, many of them are Insafe for human consumption (Faqe et al., 2020). Chemical admixtures also have leaching issues in hardened concrete where it comes into contact with drinking water, as well as in normal structures where leaching could affect the environment in which it is placed, and corrosion due to chemical content is a major problem affecting the durability, strength, and sustainability of buildings and structures (Tangtakabi et al., 2022).

Nowadays, concrete construction techniques are directed toward eco-efficiency, a technology that aims to manufacture highly durable and environmentally friendly concrete while minimizing both environmental load and production costs. (Kim and Chae, 2017). Trying to discover alternative admixtures is highly beneficial in the construction of environmentally friendly concretes.

According to historical records, ancient structures left by Egyptians, Greeks, Romans, and Indian civilizations were usually built with lime as a binding medium, and this material was a versatile material to use in traditional temples and monuments (Thirumalini and Sekar, 2013). Additionally, different bio admixtures were used by the builders to prepare their lime stuccos. The actual aim of using such admixtures is not truly recognized (ACI Education Bulletin E4-12, 2013). However, the builders were certain that using plants and animal derived as natural admixtures in lime mortar can improve the durability and strength of the mortar.

In modern concrete construction, many types of admixtures have been used to provide a more cost-effective method and enhance the properties of the concrete (Patel and Deo, 2016). Different studies have already worked on natural material as alternative for chemical admixture, which are commonly used in concrete construction. Although organic or natural admixtures may have been a viable option abundant; their production is not technologically advanced, and creates green construction (Mahmood et al., 2022).

Researchers have shown various cases with the development of bio-based admixtures that perform as well as oil-based polymers used as admixtures. The researchers drove that they have improved concrete's mechanical properties, durability, and sustainability. Based on reviewing the published works on using natural admixtures in concrete, Table 1 was prepared, from which test variables attempted and the action of admixture have been illustrated. According to the study's results, the necessity of using admixture in concrete, and the problems with using chemical admixture, which is harmful to human health and causes leaching, which is responsible for environmental pollution, natural admixture as an alternative to chemical admixture is the best way for making sustainable concrete. The main purpose behind this study is to investigate the performance of normal strength concrete containing grape extract natural admixture. The grape tree (see Figure 1), which belongs to Vitis, Species Vinifera of the family Vitaceae, has been grown and dispersed worldwide for over 2000 years. The chemical composition and nutritional condition of grape trees can be influenced by a variety of climatic, topographical, and soil conditions (Mansour et al., 2022). The fruit is generally eaten fresh or dried, and it is also used to manufacture wine, fruit juice, jam, and canned food. In the Kurdistan region, grape juice has a relatively low cost because the tree is widely planted, and on this foundation, there is an increased possibility that grape extract might be used as a natural admixture in the production of concrete in place of chemical admixtures. However, because of lack of information on this topic, there is a need for experimental laboratory works to highlight different

properties of modified concrete with this natural admixture. Unfortunately, in the author's idea there is not any research on the action of grape extract added on the hardened, and fresh properties of concrete to illustrate the action of the grape extract addition. The subject of this investigation could not be related to some studies' attempts to use natural solid waste in concrete, due to the fact that grape extract cannot be considered as waste material. The grape extract from the grape tree's fruit was used in the current investigation with the dosage of (0, 0.22%, 0.33%, 0.44%, 0.55%, and 0.66%) by cement weight, in order to assess the applicability for concrete production. Properties of fresh and hardened concrete to be examined in this study are workability using slump test, water absorption and using a scanning electron microscope device to analyze morphology. In addition, some tests on hardened concrete including compressive strength, splitting tensile strength, modulus of elasticity and modulus of rupture have been performed. Based on the results of such a laboratory work, this additive can be used in actual applications to enhance the performance of concrete production. Considering that the resource of this admixture is natural, and the production of the concrete is environmentally friendly, it can be classified as a low-cost, environmentally friendly construction material with a promising future in the construction industry.

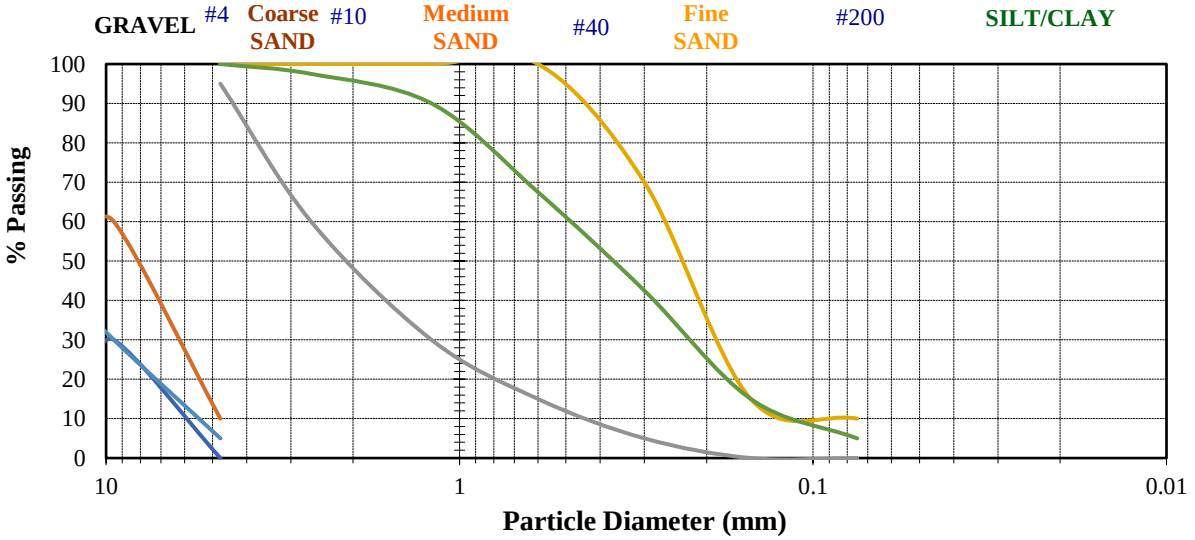

Fig. 1. Sieve analysis aggregates graph (course and fine)

Table 1. Description of test variables attempted by the past researches

Reference	Type of NA	Addition	Property studied	Action of NA in concrete
Chandra and Aavik (983)	Black gram	1,3,5% (Cement weight)	Air content, water absorption, compressive strength.	Black gram worked as air-entraining admixture, water absorption is reduced, while compressive strength is increased.
Chandra et al. (1998)	Cactus extract	50,100% (Water replacement)	Density, water absorption, compressive strength, freezing-thawing resistance.	Density and water absorption are decreased, compressive strength is reduced at early ages, and freezing-thawing resistance is increased.
Ismail et al. (2009)	Natural rubber latex (NRL)	1.5,3,5% and 2.5,5,7.5,10%	Sodium sulphate resistance (SSR), water absorption.	1.5% NRL is the optimum dosage for SSR, 5% NRL resulted in low absorption.
Otoko and Ephraim (2014)	Palm liquor (PL)	5,15,25,35% (Water replacement)	Setting time, slump, compressive strength, splitting tensile strength.	Slump, compressive strength AND tensile strength were increased up to 15% PL then decreased, initial and final setting times are increased with increasing PL.

Woldemariam et al. (2014)	Cypress tree (CT)	5,10,15% (by weight of water)	Consistency, setting time, flow table, compressive strength	Initial and final setting times increased, workability increased (OD=5%), compressive strength is increased (OD = 15%). Performance of boiled extract is better than the soaked extract.
Sathya et al. (2014)	Water hyacinth (WH)	10,15,20% (Water replacement)	Setting time, slump, compressive strength, water absorption.	Setting time, slump and compressive strength were increased (OD = 20%). Water absorption is reduced.
Woldemariam et al. (2015)	Blue gum (BG)	5,10,15% (by weight of water)	Shrinkage, cracking.	Shrinkage is reduced, OD is between 10% and 15%. Using BG will reduce shrinkage cracking even the concrete is subjected to direct heat from the sun.
Otunyo and Koate (2015)	Sugar cane juice (SCJ)	3,5,10,15% (Water replacement)	Slump, setting time, compressive strength.	Setting times were delayed. Slump was decreased. Compressive strength was reduced up to 10% SCJ.
Patel and Deo 2016)	Gram flour	1% (Cement weight)	Electrical resistivity, UPV, carbonation depth.	Electrical resistivity was increased, UPV is nearly not changed, and carbonation depth is reduced.
Muhammed et al. (2016)	Pulp black (PB)	1,1.5,2%	Slump, flow, compressive strength, splitting tensile strength.	Slump, flow value, compressive strength, splitting tensile strength are increased up to 1.5% PB then decreased.
Amaran and Ravi (2016)	Cactus (OFI)	10,20% (Water replacement)	Standard consistency, setting time, workability, compressive strength.	Standard consistency, initial and final setting times, workability, compressive strength are increased with increasing cactus up to 20%.
Paul et al. (2017)	Natural rubber latex	0.5,0.8,0.9,1,1.5% (by cement weight)	Compacting factor, compressive strength.	There was a compacting factor decrease with latex content of minimum loss at 0.9%. There was a compressive strength enhancement up to 0.9% latex followed by a strength loss.
Amrita et al. (2017)	Aqueous extract of okra	(1:10, 1:20, 1:30, 1:40, 1:50) gm(okra): liter(water)	The consistency, water retention capacity, compressive strength, and water absorption capacity and porosity with durability properties	Improved water retention capacity of cement pastes, and viscosity enhancing, also improves mechanical and durability performances of cement mortar and concrete.
Ramesh and Neeraja (2017)	Hen egg	0.25,0.5,0.75, 1,1.5% (Binders weight)	Normal consistency, setting time, slump, compressive strength.	Normal consistency is increased (OD=1%), setting time is reduced, compressive strength, tensile strength and elastic modulus are increased (OD =0.25%), slump is reduced (OD = 0.75%).
Ramesh et al. (2017)	Hen egg	0.25,0.5,1% (Concrete volume)	Water absorption, porosity, acid attack.	Water absorption and porosity are reduced; acid attack resistance is increased (OD = 0.25%).
Pathan and Singh (2017)	Molasses	0.4,0.6,0.8% (by cement weight)	Slump, setting time, compressive strength, splitting tensile strength, flexural strength.	There is a slump increase, setting time increase, slight increase of compressive, slitting tensile, flexural strengths are increased with increasing molasses up to 0.8%.
Elinwa et al. (2018)	Gum Arabic (GA)	0.25,0.5,0.75, 1% (by cement weight)	Workability, density, water absorption, compressive strength.	Slump, porosity and water absorption are increased with GA increase, Optimum dosage is 0.5% for compressive strength enhancement.
Andayani et al. (2018)	Copolymer - natural latex methacrylate (KOLAM) and copolymer	1,5,10% (by cement weight)	Compressive strength, Dynamic properties: load and energy dissipation.	There is a compressive strength reduction except for mix with 1% KOLAM. Impact load is reduced and energy dissipation is increased on using 1% KOLAM. KOLAS addition into concrete mixture does not give good performance in strength and impact properties.

	- natural latex styrene (KOLAS)			
Aquilina et al., (2018)	Cactus (OFI)	10,20,40,60% (Water replacement)	Consistency, setting time, compressive strength, UPV.	Flow is decreased, setting time is increased, compressive strength and UPV are reduced at early ages.
Azizi et al. (2019)	Opuntia ficus-indica Cladodes	1, 2.5 and 4% of Opuntia ficus-indica cladode's powder by weight of cement	Setting time and compressive strength.	Setting times were reduced significantly with the addition of Opuntia ficus-indica cladodes, and mechanical strength and resistance to acetic and hydrochloric 5% acid solution were enhanced over the control sample.
Mechaymech and Assaad (2019)	Cellulose-based VEA, modified-startch VEA	0.02,0.035,0.05and 0.08% VEA	Slump flow and J-Ring tests.	The rheological properties with VEA additions given the higher degree, The mixes prepared with cellulose VEA showed the maximum levels of stability, including deformability and resistance to bleeding and surface settlement, at a VEA dosage of 0.035%.
Torres-Acosta and González-Calderón (2021)	Opuntia ficus-indica (OFI) cactus	0%, 1.5%, 4%, 8%, 42%, and 95%, by water mass replacement Concentration.	Electrochemical Characterization. linear polarization resistance (LPR) measurements.	Because corrosion rates and cracking initiation/propagation were decreased, it was useful as a corrosion inhibitor for steel in carbonated cement-based materials.
Abana et al. (2021)	Pulverized Water Hyacinth	0.5%, and 1% of pulverized water hyacinth by weight	Setting time and strength.	Comparing a concrete cylinder containing 0.5% and 1% pulverized water hyacinth to that without, they show an improvement in compressive strength of 2.39 and 3.83%, respectively.
Paul et al. (2022)	Sugarcane Juice (SCJ)	0, 2, 5, 10, 20% (Water replacement)	Initial and final setting time, workability, compressive strength, and splitting tensile strength of concrete.	The setting time was reduced with the increased SCJ content in the mix. As an accelerator, The compressive strength of concrete increased as the SCJ content increased in the concrete mix.
Mahmood et al. (2023)	mulberry extract	0,0.22,0.33,0.44,0.55 and 0.66% of cement content	Slump test, water absorption and morphology analysis, compressive strength, splitting tensile strength, modulus of elasticity and modulus of rupture	Increase in the slump of concrete with increasing mulberry liquid up to 0.66%, and accordingly dosage of 0.33% (optimum dosage) of the mulberry extract caused a reduction in water absorption and an increase in compressive strength.

NA = natural admixture, OD = optimum dosage.

2. Materials

The concrete mixtures contain cement, fine aggregate, coarse aggregate, water and liquid grape extract. Ordinary Portland cement (Type I ASTM) was used in all concrete mixes. Which are manufactured by the Tasluja factory in Sulaimani and characterized as ordinary Portland cement-II/A-L 42.5 R. The chemical and physical properties of cement are presented in Table 2. It can be proved that the cement meets the requirements with the Iraqi specification's limits. As a coarse aggregate, particles of crushed aggregate with a maximum size of 19 mm and fine aggregate, natural river sand with a fineness modulus of 1.87 were used. The results of the sieve analysis test on the aggregates are shown in Figure 1 and Table 3. Both aggregates were checked to satisfy with the (BS 812, 1990) limitations. Clean potable water was used for mixing

concrete and curing specimens. The natural admixture employed in this study was grape liquid, which was made from the fruit of a grape tree native to Iraq's Kurdistan region (see Figure 2). The density of the liquid was determined to be 1.335 g/ml. Table 4 shows the chemical composition and mineral concentrations. The liquid was then investigated with EDX and XRD images as shown in Figures 3 and 4, respectively. Figure 5 shows the microstructure view of the dried grape juice using an SEM device.

Table 2. Properties of OPC and limits of Iraqi specification

Chemical properties	**Results**	**Limit of I.Q.S No. 5/1984**
Lime saturation factor, %	0.94	0.66 - 1.02
Magnesium oxide (MgO), %	3.58	Not more than 5%
Sulfate content (SO_3), %	2.28	Not more than 2.85%
Loss on ignition (LOI), %	3.48	Not more than 4%
Insoluble substance, %	0.78	Not more than 1.5%
Physical properties	**Results**	**Limit of I.Q.S No.5/1984**
Finesse (Blaine), m^2/Kg	345	Not less than 230 m^2/kg
Initial setting time, minute	175	Not less than 45 min.
Final setting time, hours	3:35	Not more than 10 hrs.
Soundness (expansion), %	0.22	Not more than 0.8%
Compressive strength (3 days), MN/m^2	35.6	Not less than 15 MN/m^2
Compressive strength (7 days), MN/m^2	47.3	Not less than 23 MN/m^2

Table 3. Sieve analysis of coarse and fine aggregates

Coarse aggregate			**Fine aggregate**		
Sieve size (mm)	**% passing**	**BS 882 limits**	**Sieve size (mm)**	**% passing**	**BS 882 limits**
37.5	100	100	4.75	100	95-100
19	70	90-100	2.63	97.5	60-100
12.5	42	-	1.18	90	30-100
9.5	30	30-60	0.6	67.5	15-100
4.75	5	0-10	0.3	42.5	5-70
			0.15	15	0-15

Table 4. Chemical composition and minerals content of grape liquid

Chemical composition		**Mineral contents**	
Dry Matter (%)	58.84	Al (ppm)	41.39
Moisture (%)	41.16	Ca (ppm)	589.68
Ash (%)	0.64	Fe (ppm)	58.57
Protein (%)	2.28	K (ppm)	3714.29
Fat (%)	0.12	P (ppm)	478.19
Fiber (%)	0.2	Rb (ppm)	2.94
Carbohydrate (%)	55.6	Zn (ppm)	3.17
Phosphorous (%)	0.04	Mg (ppm)	457.14
Calcium (%)	1	Na (ppm)	69.21

(a) **(b)** **(c)**

Fig. 2. View of grape: a) tree; b) fruit; and c) extract

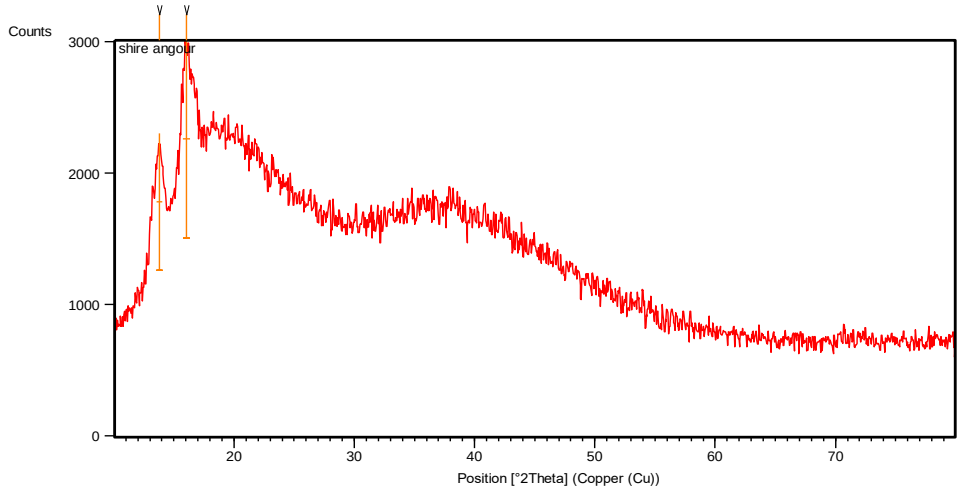

Fig. 3. EDX picture of grape extract

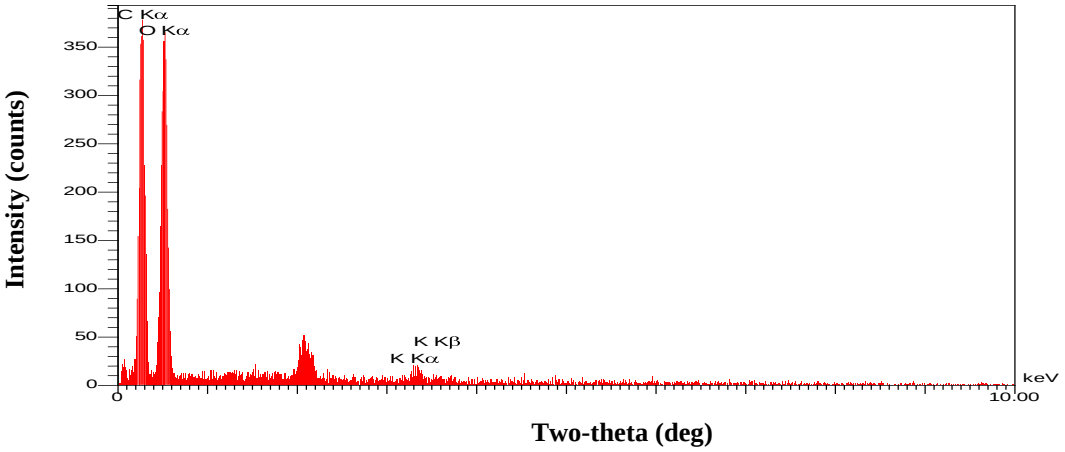

Fig. 4. XRD of grape extract

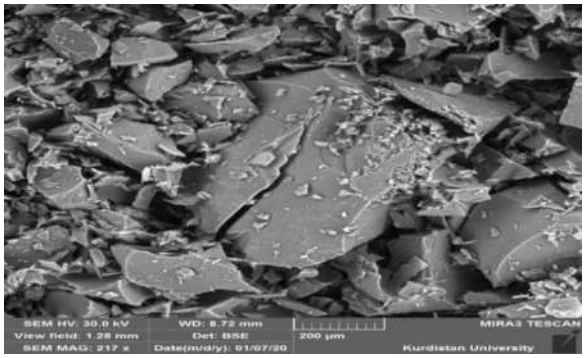

Fig. 5. SEM view of grape extract powder

3. Mix Design and Procedure

Based on the previous experience, the control concrete mixture (without any grape liquid) was chosen, and the target compressive strength was set at 35 MPa. Table 5 illustrates the proportion of the mix design, with the water/cement ratio of 0.55, and the amount of grape extract (GE) as the major variable investigated. This admixture was added to the concrete mix at a dosage of 0.22 %, 0.33 %, 0.44 %, 0.55 %, and 0.66 % by the cement weight.

For mixing concrete, an electrical tilting drum was used. Cement and other dry components were first added to the mixer and left to rotate for two minutes. After adding some mixing water, the mixture was left for another minute to combine. The remaining water containing the liquid grape extract was then added, and the concrete mixture and left to mix for three minutes

until it was homogeneous. All internal parts of steel molds were carefully lubricated before concrete casting to facilitate in the remolding of hardened concrete. The concrete specimens were compacted by external vibration (see Figure 6a). After 24 hours, the specimens were taken out of the mold and placed in a water tank to cure for 3, 7, 28, and 90 days at a temperature of roughly 25 °C. Three days before testing, the samples were taken out of the water tank and dried at the lab.

4. Instrumentation and Testing

Fresh concrete was determined by slump test, which using a standard slump cone, as recommended by (ASTM C143, 2013). At the ages of 28 and 90 days, hardened concrete cube specimens of (150 × 150 × 150) mm were used for water absorption tests. Compressive strength was determined on 150 × 300 mm cylinder specimens using the Turkey model testing machine (Figure 6b), in accordance with the (ASTM C39 specification, 2013). Splitting tensile tests on 150 × 300 mm cylinders were done in accordance with (ASTM C496 specifications, 2013), whereas the flexural strength testing was done on 100 × 100 × 400 mm concrete prisms in accordance with (ASTM C78 specification, 2013). In addition, according to ASTM C469 (2013) 150 × 300 mm cylinders were used to measure modulus of elasticity. For the tests listed above, an average of three values were obtained, and results were reported. Additionally, using an FEI QUANTA 400 model scanning electron microscopy apparatus, a morphological analysis of small portions of hardened concrete was done after compressive strength testing.

5. Results and Discussion

The results of testing specimens for different concrete properties are shown in Table 5. The sections that follow are given to a lengthy discussion of the results.

Table 5. Experimental test results

Mix code	Slump (mm)	Water absorption (%)		Compressive strength (MPa)				Splitting tensile strength (MPa)		Flexural strength (MPa)	Elastic modulus (MPa)
		28 days	90 days	3 days	7 days	28 days	90 days	28 days	90 days	28 days	28 days
MC	43	4.37	4.01	19.81	23.13	32.53	34.75	2.09	2.53	5.5	23654
MG0.22	57	4.01	3.72	24.44	33.80	38.54	40.64	2.01	2.34	5.99	25313
MG0.33	68	4.21	3.80	26.53	31.98	35.33	36.04	2.0	2.28	5.99	20594
MG0.44	83	4.33	3.89	20.58	29.66	33.23	35.36	1.99	2.19	5.55	20569
MG0.55	97	4.41	4.00	14.97	22.67	31.89	34.65	1.78	2.12	5.41	20973
MG0.66	123	4.46	4.14	1.63	4.25	25.28	25.11	1.56	1.45	5.35	21360

(a) **(b)** **(c)**

Fig. 6. Photos of: a) Specimens subjected to vibration; b) Compressive strength machine; and c) Cast specimens

5.1. Workability

Slump test results for various dosage of GE content are shown in Figure 7. When the percentage of Grape Extract (GE) in the concrete mix is increased, the slump gradually increases, from the beginning. The control mixture was made with a relatively small slump value of 43 mm. It was expected that the addition of GE can improve workability, due to the sugar content. Slump value increases with increased liquid addition, reaching 123 mm (286%) at the dosage of 0.66% GE, showing a more than twice increase in workability. The simplest group of carbohydrates, which is made of carbon, hydrogen, and oxygen is the source of the slump development in the extract liquid. As shown in Table 4, the GE used in this study includes approximately 55.6% carbohydrates (or sugar). Sugar in mixing water enhances workability (the optimal amount is 16%), according to Otoko and Ephraim (2010). Also according to Pathan and Singh (2017), adding molasses, a byproduct of sugar, improves workability by up to 0.8% of cement weight. Based on the findings, there is a possibility of using a lower water/cement ratio in the concrete mix when GE is added for a constant slump as compared to control concrete. It will produce in a concrete with a higher compressive strength. However, additional testing is required to assess this performance experimentally because the high sugar content makes concrete volume expansion and does not set as shown in Figure 10.

5.2. Water Absorption

The results of the water absorption test at 28 and 90 days are shown in Figure 8. Water absorption decreases with increased grape liquid at 28 and 90 days, reaching 8.2% and 7.2% when 0.22% GE is used, respectively. As a result, 0.22% is considered the optimum dosage of the GE additive in regards to water absorption. The factors governing hardened concrete absorption capacity generally are the same as those that modify concrete compressive strength, and the positive effects of GE addition can be compared to changes that the GE addition causes in the microstructure and pore structure of hardened cement paste. The following section provides more detail about this.

5.3. Compressive Strength

Figure 9 indicates the change in compressive strength with the addition of grape liquid for concrete tested at different ages.

The compressive strength of concrete tested at 3 days is increased by 34% when 0.33% of the GE additive is used. Maximum strength improvement relates to 0.22% GE addition, which is equal to 14.6%, 18.5%, and 16.9% at ages (7, 28, and 90) days, respectively. It should be noted that the 3 days compressive strength with 0.33% GE is higher than the 7 days control mix and that there is a continuous loss of compressive strength with increasing grape liquid content, with the maximum compressive loss of 92% occurring at the age of 3 days with the dosage of 0.66%. It should be highlighted that this may be because ages, segmentations, and filling of capillary pores are partially fulfilled by the hydration product primarily represented by the C-S-H gel, and so there is no need for significant GE addition. According to the results, a higher GE is more influence on the compressive strength of the concrete at the age of 3 days This low strength can be attributed to the fact that the existence of GE in concrete in a large amount has a vital effect against the cement hydration development. Figure 10 shows one cylinder made of concrete with 0.66% GE tested at 3 days, from which one can observe a complete distortion of concrete indicating a very low strength. The results also show that the high strength loss reduces with increasing concrete age, primarily due to cement paste hydration development, and that some of the strength loss is restored when compared to the concrete tested at 3

days. The previous discussion will lead to decide that 0.22% GE is the optimum dosage to be added to concrete, and there is a degradation of strength with increasing the extract addition. The potential and actual reasons for an increase in compressive strength as a result of GE's addition to concrete is discussed in details as follows. Three major factors can be attributed to the GE addition's improvement of pore structure, reduction of absorption, and gradual development. It is important to know that GE extract has the following components: Organic acids, nitrogenous compounds, sugars, phenolic chemicals, chemical compounds, minerals, and pectic substances. The first reason for the enhanced microstructure and strength is due to the liquid's amount of sugar. The extract consists of 94.5% carbohydrates, based on Table 4. According to Ashworth (1965) studies, adding sugar to concrete enhances compressive strength by around 8%. Deva et al. (2017) showed that using 0.06% sugar in concrete mixes at different water/cement ratios improves the strength. Second, the influence of mineral components plays a role in the increase in strength. Potassium is the most common mineral in the liquid, accounting for around 50% to 70% of the cations. Table 4 shows that the potassium amount of the GE extract is 69%. The potassium absorbed by the fruit during ripening changes to potassium bitartrate (or potassium hydrogen tartrate) ($C_4H_5O_6$), which reduces acidity and increases the pH of the juice. As a result, the GE ingredient is chemically compatible with the cement paste's hydration product. Crystals of potassium bitartrate may form within the pore structure of hardened cement paste. In addition to crystallizing during the fermentation of grape juice in containers like wine barrels and precipitating out of wine in bottles, potassium bitartrate is commonly known to be poorly soluble in water. With the development of cement paste hydration, there is a possibility that a sufficient amount of potassium mineral will crystallize inside the capillary poses within the cement paste mass, especially at early ages (3 days in this study), segmenting such pores, increasing homogeneity, and thus increasing compressive strength. The microstructure of concrete with and without the admixture, as shown by the results of the scanning electron microscope images in Figures 11a and 11b, varies. One may see an enlarged view of GE crystal precipitation completely blocking micro cracks. When Figures 11e and 11f, as well as Figures 11h and 11i, are compared, this situation appears as well. Another reason for the increased strength linked to the presence of GE in concrete is that GE contains phenolic chemicals, which are composed of two components: Anthocyanins and tannins, Tannins polymerize and age, which causes an increase in molecule size. On this basis, tannins may have the ability to fill in micro-cracks caused by cement hydration. Figure 11i may show the process of polymerization in which the produced chains tend to fill the existed crack gap. The results of Figure 9 also show that with a relatively large GE content (0.55%), 28 and 90 days compressive strength is quite similar to that of control concrete, knowing that on using such ratio there is about 126% increase in the slump of fresh concrete. As a result, there is an excellent chance that this natural additive will be used in the construction of self-compacting concrete. However, more experimental work is required to verify this. When 0.66% GE is used, there is a compressive strength loss, which can be attributed to the admixture's extremely strong thickening effect, which leads to a weaker material structure. Izaguirre et al. (2010) observed this impact while using potato starch in lime-aggregate mortar, or the strength loss may be attributed to the high sugar content related to the use of high GE content. Ahmad et al. (2020) showed compressive strength decreases when 0.2% sugar was used in concrete.

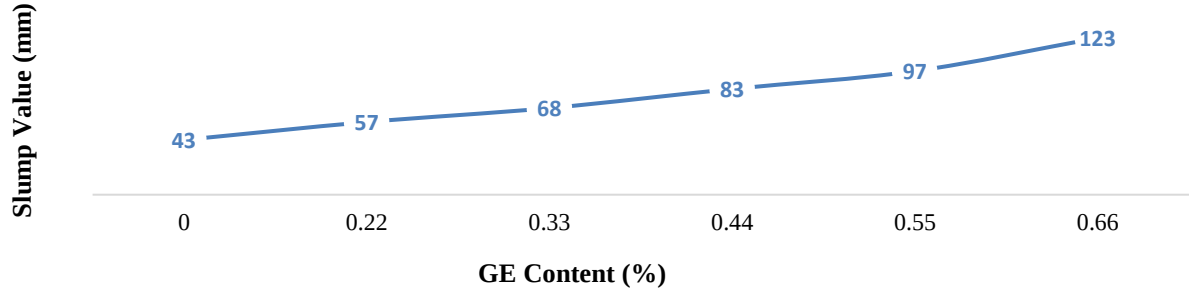

Fig. 7. Slump value with different ratio of grape content

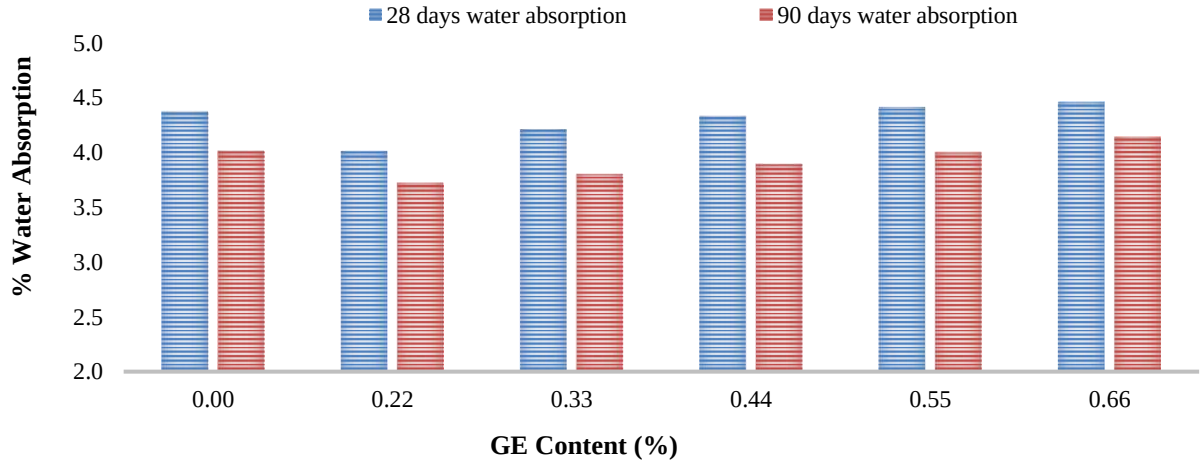

Fig. 8. Water absorption variation with GE contents

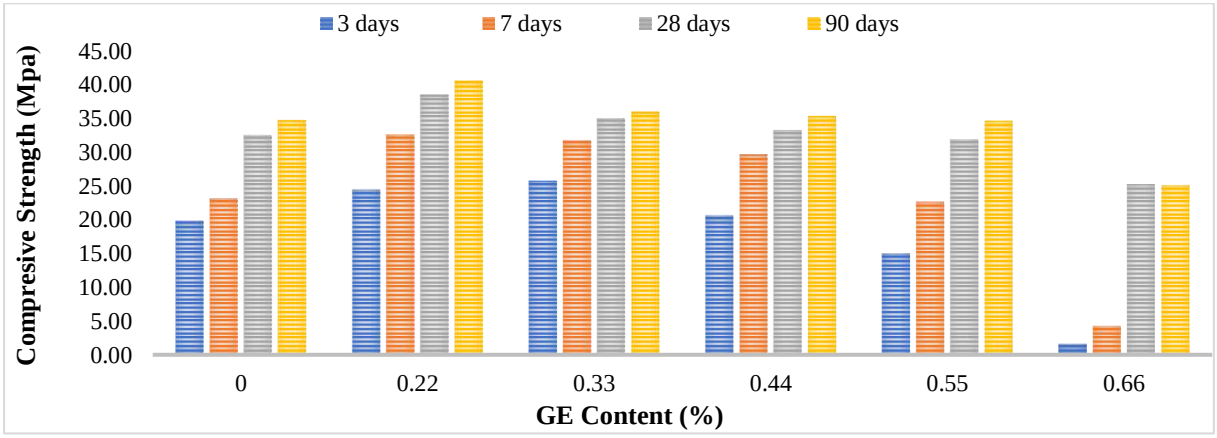

Fig. 9. Compressive strength variation with GE content

Fig. 10. View of a cylinder tested in compression (GE = 0.66%)

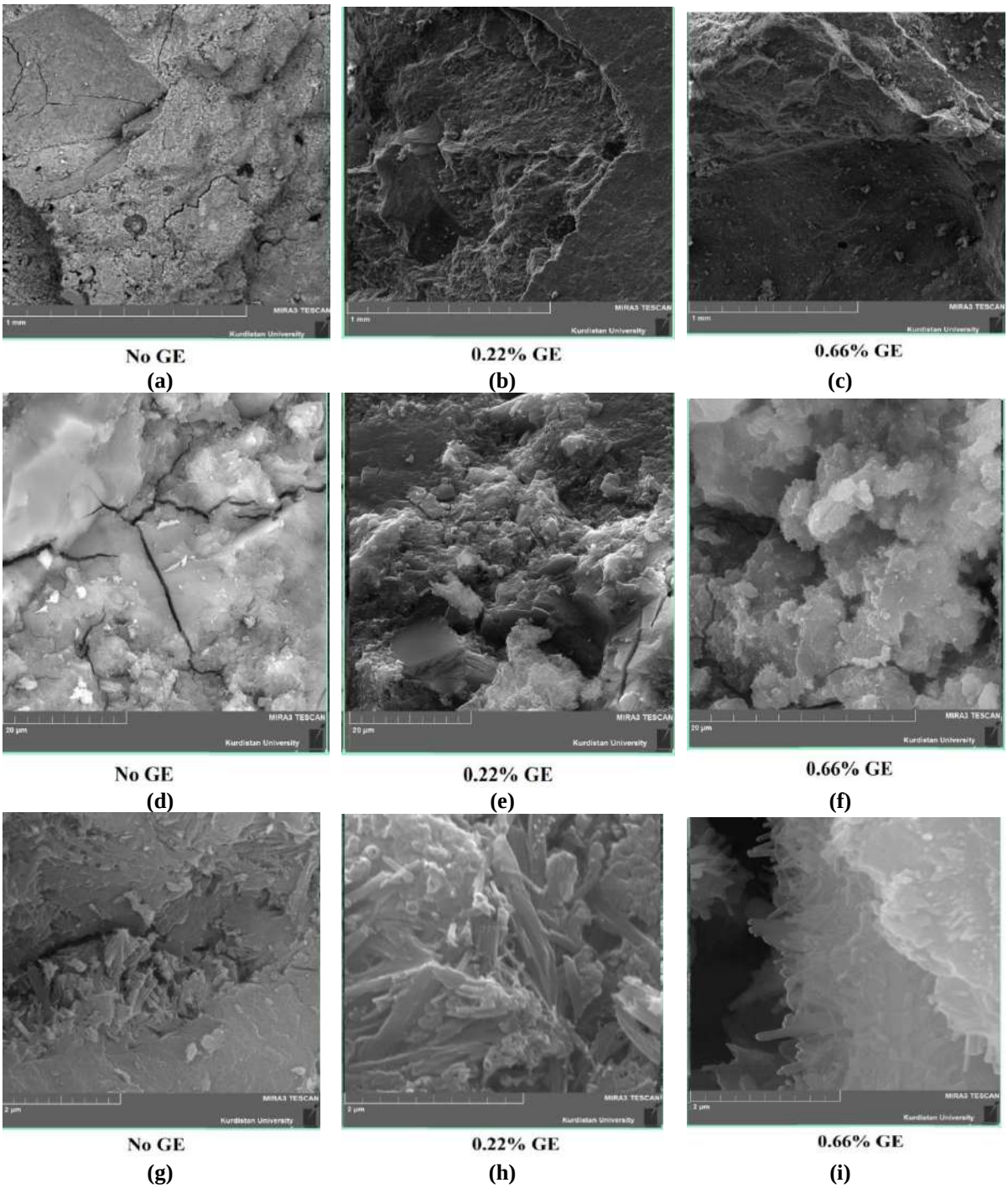

Fig. 11. Microstructure of concrete obtained by SEM analysis (28 days age)

5.4. Splitting Tensile Strength

Figure 12 shows the variation of the splitting tensile strength percentage with grape extract percentage. A constant decline of splitting tensile strength can be seen, reaching 25.4% and 42.9% at ages 28 and 90 days, respectively. Due on this, there is no optimum GE dosage for improving tensile strength as compared to compressive strength. At the age of 90 days, there is a 16.2% reduction in tensile strength when the liquid is used at an optimum dosage (0.22% based on compressive strength). In the practical applications of concrete based on using the GE natural admixture, this tensile strength loss as a result of GE addition to concrete should be taken into consideration. Totally, grape liquid has no beneficial effect to increase splitting tensile strength compared to the case of

compressive strength. The relationship between the splitting tensile strength and compressive strength of concrete mixes analyzed at 28 and 90 days is presented in Figure 13. Because there is no statistically significant improvement in splitting tensile strength with the improvement in compressive strength, the correlation is not strong. The equations that were basically proposed for normal concrete to calculate splitting tensile strength based on compressive strength cannot be applied on this approach.

5.5. Flexural Strength

Figure 14 shows the change of flexural strength with GE ratio, indicating a strength development at all grape juice ratios except 0.55% and 0.66%. The maximum flexural strength obtained with 0.22% and 0.33% admixture is 9%, while the strength reduction with 0.66% GE is only 2.7%. In general, the behavior of concrete in flexure is similar to that in compression, but lower flexural strength enhancement is observed for the optimum dosage of grape liquid, and on using 0.66% GE, there is a lower flexural strength loss. Figure 15 shows flexural strength- compressive strength relationship, from which one can find that the correlation is similar to that of splitting tensile strength-compressive strength. Also, it will be observed that the equation given by ACI 318 Code (2015) is conservative for all ratios of GE admixture of average test/calculated value equal to 1.59.

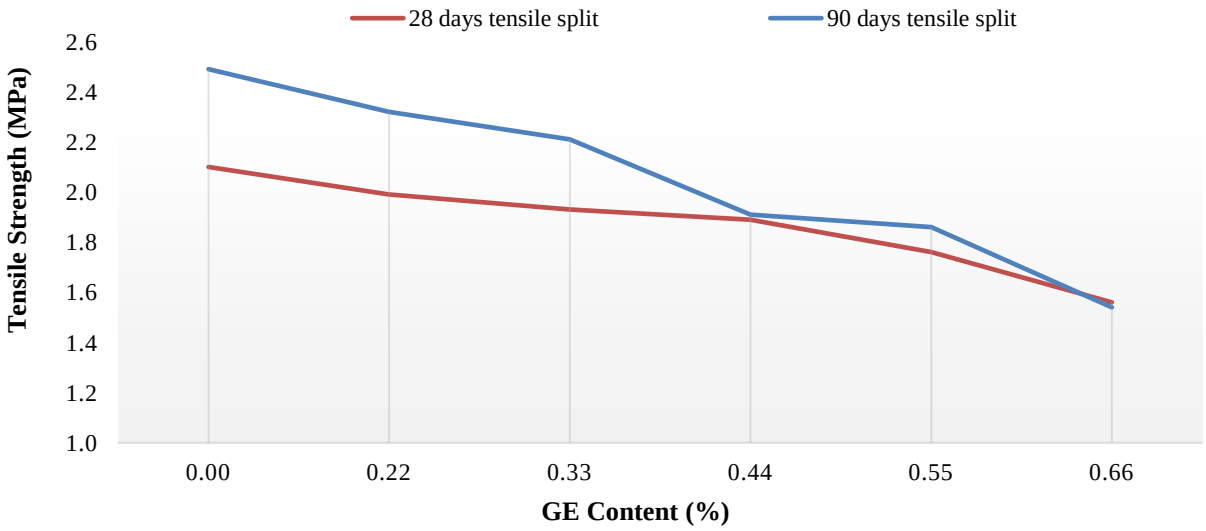

Fig. 12. Splitting tensile strength variation with GE content

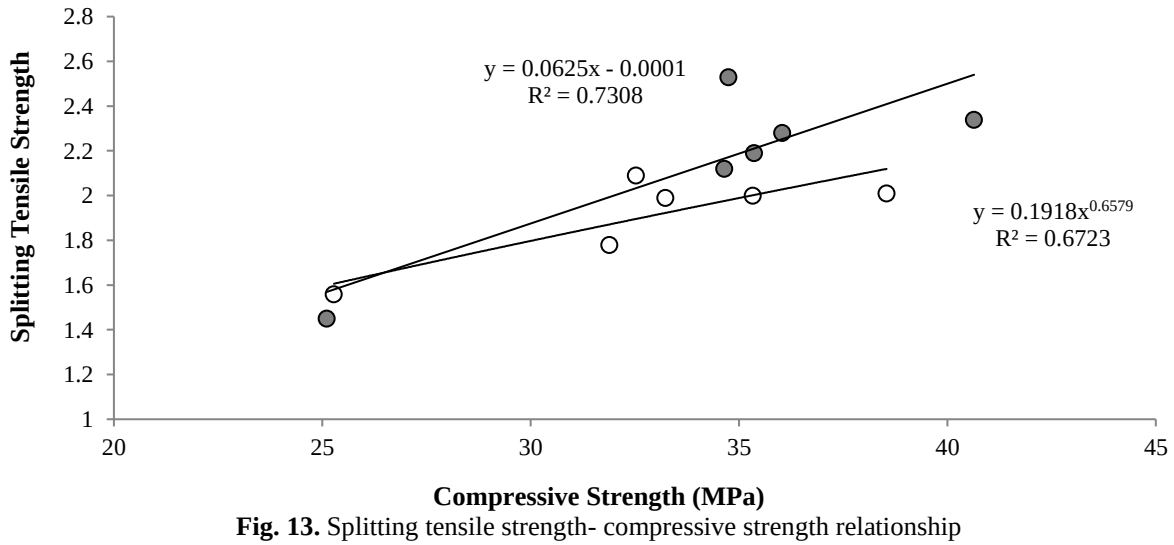

Fig. 13. Splitting tensile strength- compressive strength relationship

5.6. Modulus of Elasticity

The modulus of elasticity as a result of the concrete sample with different percentages of GE is shown in Figure 16. With the addition of GE, the elastic modulus increases slightly reaching its maximum value of 7% at a GE dosage of 0.22%. However, when the admixture increases to 0.66%, some elastic modulus is lost. The results line up with the observed compressive strength, therefore the optimum dose for enhancement is 0.22%, and at 28 days of age, 0.55% GE causes very little loss. The relationship between elastic modulus and compressive strength has weak correlation, as shown in Figure 17. Furthermore, it has been proven that the ACI 318 Code (2015) equation, which averages test/calculated values of 0.82, greatly overestimates test data when calculating the elastic modulus of concrete with GE admixture.

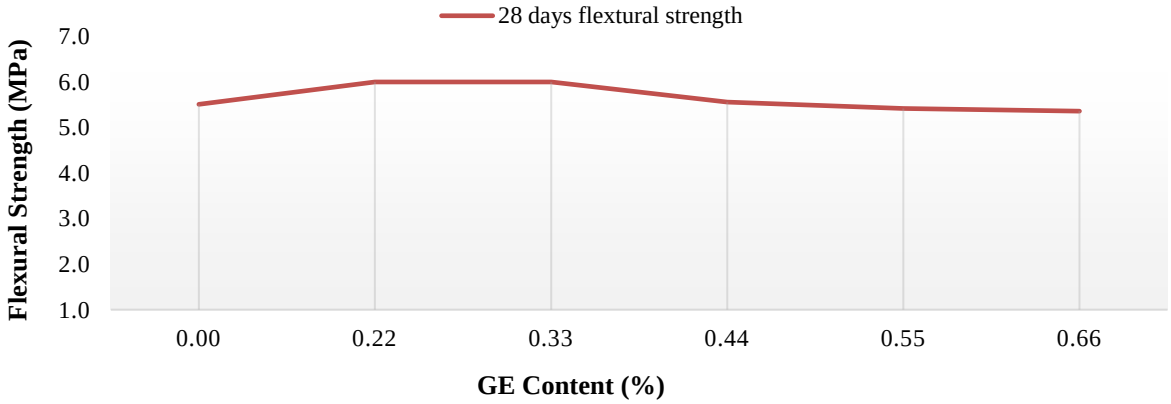

Fig. 14. Flexural strength variation with GE content

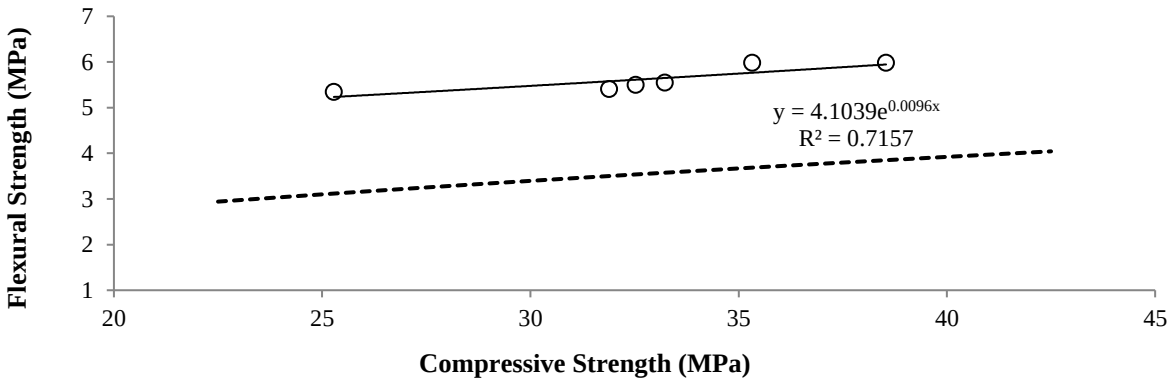

Fig. 15. Flexural strength- compressive strength relationship

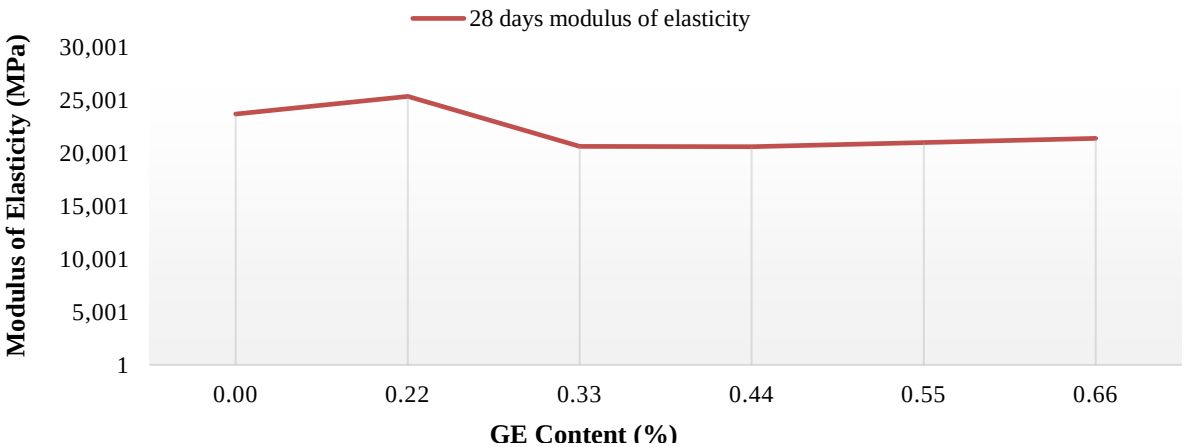

Fig. 16. Elastic modulus variation with GE content

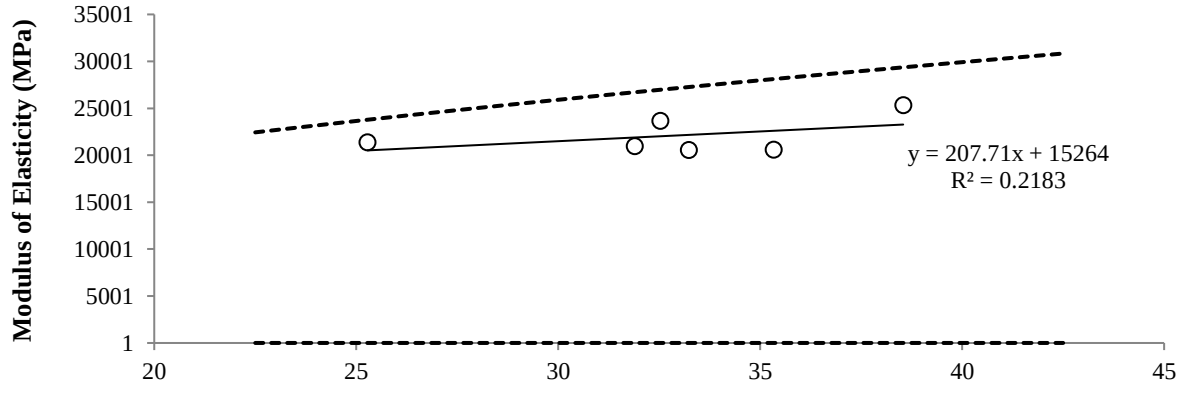

Fig. 17. Modulus of elasticity- compressive strength relationship

When 0.55% GE is used as a natural admixture, it will be noted that, there is a negligible water absorption loss, compressive and flexural strengths loss, while there is 16.2% splitting tensile strength loss and 11.33% elastic modulus loss as compared with the control concrete without GE. Fortunately, there is flow enhancement represented by the slump value equal to 126%, therefore one can conclude that there is a good chance to manufacture green self-compacting concrete using GE natural admixture added to concrete by 0.55% instead on using chemical admixtures.

6. Conclusions

The results of this experimental investigation into the properties of fresh and hardened normal strength concrete using grape extract as a natural admixture led to the following conclusions.

- Increasing the Grape Extract (GE) up to 0.66% produces a continuous increase in the slump of concrete, and as a conclusion, this natural admixture is working as flowing agent admixture. Using up to 0.55% GE in concrete resulted in no loss of compressive or flexural strength, but a 16.2% loss of splitting tensile strength and an 11.33% loss of elastic modulus. On this basis, there is a good chance that GE could be used instead of chemical additive in the construction of green self-compacting concrete.
- Using 0.33% GE, water absorption was reduced while compressive strength increased at age of 3-days, and the compressive strength was observed to be greater than control concrete of the age 7-days. When 0.22% GE is used in concrete, the 28-days compressive strength increases by 18.5%, and GE could be utilized to produce high-strength concrete when properly designed. The increased strength is mostly due to an improvement in the microstructure of the cement paste (seen from SEM test results), which is attributable to calcium precipitation in the porous structure of the cement paste.
- As additional GE is added to concrete, flexural strength follows the same trend as compressive strength, but with a less valuable strength increase, a slight elastic modulus loss, and a continual splitting tensile strength decrease.
- This study suggests engineers to use GE rather than chemical admixture because natural grape extract does not need advanced technology to produce, and the amount of optimum dosages is very small (0.22%) compared to chemical admixture 10-20%. So it is cost-effective, and the product will be more environmentally sustainable when using natural admixture.

7. Future Work

The properties of concrete products are improved by the use of GE as an admixture

in the production of concrete. For evaluation and observation, more studies must be done on all types of concrete used in the construction of concrete structures. The effects of this additive on the properties of concrete that contained this admixture need to be studied further, and tests such as fire resistance and durability improvement, etc. were not implemented for this study.

Based on the outcomes of this study, it has been found that the effects of GE liquid on the properties of normal concrete can be used, especially for self-compacting concrete, due to the good workability results obtained in this study.

8. References

Abana, E., Vega, W., Gacias, J., John RaÃ±on, P., Talattad, J.D., Orata, H. and Perez, J. (2021). "Pulverized water hyacinth as an admixture for concrete", *International Journal of Integrated Engineering*, 13(4), 298-303, https://doi.org/10.30880/ijie.2021.13.04.028.

ACI Committee 318. (2015). *Building code requirements for structural concrete*, American Concrete Institute, Farmington Hills, First Printing.

ACI Education Bulletin E4-12. (2013). *Chemical admixtures for concrete*, American Concrete Institute.

Ahmad, S., Lawan, A. and Al-Osta, M. (2020). "Effect of sugar dosage on setting time, microstructure and strength of Type I and Type V Portland cements", *Case Studies in Construction Materials*, 13, e00364. https://doi.org/10.1016/j.cscm.2020.e00364.

Amaran, R. and Ravi, R. (2016). "Effect of cactus on the rheological properties of cement", *International Journal of Chemical Sciences*, 14, 203-210.

Amrita, H., Indranuj, H., Mumee, G., Shilpi, S.B., Rashmi, R.B., Prasanta, J.G. and Nabajyoti, S. (2018). "Use of a plant based polymeric material as a low cost chemical admixture in cement mortar and concrete preparations", Journal of Building Engineering, 15, 194-202, https://doi.org/10.1016/j.jobe.2017.11.017.

Andayani, S.W., Suratman, R., Imran, I. and Mardiyati (2018). "Copolymer natural latex in concrete: Dynamic evaluation through energy dissipation of polymer modified concrete", *3rd International Conference on the Science and Engineering of Materials (ICoSEM 2017)*, 24–25 October, Kuala Lumpur, Malaysia, https://doi.org/10.1063/1.5034543.

Aquilina1, A., Borg, R.P. and Buhagiar, J. (2018). "The application of natural organic additives in concrete: Opuntia ficus-indica", *IOP Conference Series: Materials Science and Engineering*, Volume 442, FIB Conference: Sustainable Concrete: Materials and Structures, 10 April, Malta, https://doi.org/10.1088/1757-899X/442/1/012016.

Ashworth, R. (1965). "Some investigations into the use of sugar as an admixture to concrete", *Proceedings of the Institution of Civil Engineers*, 31(2), 129-145, https://doi.org/10.1680/iicep.1965.9477.

ASTM Designation C143. (2013). *Standard test method for slump of hydraulic- cement concrete*, Annual Book of ASTM Standard.

ASTM Designation C39. (2013). *Standard test method for compressive strength of cylindrical concrete specimens*, Annual Book of ASTM Standard.

ASTM Designation C469. (2013). *Standard test method for static modulus of elasticity and Poisson's ratio of concrete in compression*, Annual Book of ASTM Standard.

ASTM Designation C496. (2013). *Standard test method for splitting tensile strength of cylindrical concrete specimens*, Annual Book of ASTM Standard.

ASTM Designation C78. (2013). *Standard test method for flexural strength of concrete (using simple beam with third-point loading)*, Annual Book of ASTM Standard.

Azizi, C.E., Hammi, H., Chaouch, M.A., Majdoub H. and Mnif, A. (2019). "Use of Tunisian Opuntia Ficus-Indica cladodes as a low cost renewable admixture in cement mortar preparations", *Chemistry Africa*, 2, 135-142, https://doi.org/10.1007/s42250-019-00040-7.

BS 882. (2002). *Specification for aggregates from natural sources for concrete*, BSI 6, BSI publications, London.

Chandra, S. and Aavik, J. (1983). "Influence of black gram (natural organic material) addition as admixture in cement mortar and concrete", *Cement and Concrete. Research*, (13):, 423-430. https://doi.org/10.1016/0008-8846(83)90043-1.

Chandra, S., Eklund, L. and Villarreal, R.R. (1998). "Use of cactus in mortar and concrete", *Cement and Concrete Research*, 28(1), 41-51. https://doi.org/10.1016/S0008-8846(97)00254-8.

Deva, K.A.B., Acharya, V.T. and Keerthi, G.B.S. (2017). "Effect of sugar on setting-time and compressive strength of concrete", *Conference Mangalore Institute of Technology and Engineering, ICGCSC*, 17-18 March, Moodbidri, India.

Elinwa, A.U., Abdulbasir, G. and Garba, A.G. (2018). "Gum Arabic as an admixture for cement concrete production", Construction and Building Materials, 176, 201-212,

https://doi.org/10.1016/j.conbuildmat.2018.04.160.

Faqe, H., Dabbagh, H. and Mohammed, A. (2020). "Natural admixture as alternative for chemical admixture in concrete technology, A review", *Duhok University*, 23(2), 301-308, https://doi.org/10.26682/csjuod.2020.23.2.24.

Ismail, M., Muhammad, B. and Mohamad, N.A. (2009). "Durability performance of natural rubber latex modified concrete", *Malaysian Journal of Civil Engineering*, 21(2), 195-203.

Izaguirre A., Lanas J., and Álvarez J.I. (2010). "Effect of a biodegradable natural polymer on the properties of hardened lime-based mortars", *Materiales de Construcción*, 61(302), 257-274, https://doi.org/10.3989/mc.2010.56009.

Kim, T.H. and Chae, C.U. (2017). "Proposal of eco-efficiency evaluation method for concrete using equivalent durability on carbonation", In: *Applied Mechanics and Materials*, (Vol. 864, pp. 284-289), Trans Tech Publications, Ltd., https://doi.org/10.4028/www.scientific.net/amm.864.284.

Li, Z. (2011). *Advanced concrete technology*, John Wiley & Sons, Inc., Hoboken, New Jersey.

Mahmood, F.H, Dabbagh, H. and Mohammed, A. (2021). "Comparative study on using chemical and natural admixtures (grape and mulberry extracts) for concrete", *Case Studies in Construction Materials*, 15(37) https://doi.org/10.1016/j.cscm.2021.e00699.

Mahmood, F.H., Dabbagh, H. and Mohammed, A.A. (2023) "Improvement of mechanical and physical properties of normal concrete using mulberry extract as an admixture", *Asian Journal of Civil Engineering*, 24, 1309-1321, https://doi.org/10.1007/s42107-023-00570-z.

Mahmood, H.F., Dabbagh, H. and Mohammed, A. A. (2022). "Fresh, mechanical, and durability properties of concrete contains natural material as an admixture, An overview", *Journal of Studies in Science and Engineering*, 2(3), 66-86, https://doi.org/10.53898/josse2022235.

Mansour, G., Ghanem, C., Mercenaro, L., Nassif, N., Hassoun, G. and Del Caro, A. (2022). "Effects of altitude on the chemical composition of grapes and wine: A review", *OENO One*, 56(1), 227-239, https://doi.org/10.20870/oeno-one.2022.56.1.4895.

Mechaymech, A. and Assaad, J. (2019). "Stability of self-consolidating concrete containing different viscosity modifiers", *Civil Engineering Infrastructures Journal*, 52(2), 245-263, https://doi.org/10.22059/ceij.2019.262859.1502.

Muhammed, S.K., Navaneeth, A.P., Bhavia, K.K., Harikrishna, A.S., Mohammed Anas, P.P. and Maya, P. (2016). "Pulp black liquor, An admixture in concrete", International Journal of Civil Engineering, 3(3), 48-55, https://doi.org/10.14445/23488352/IJCE-V3I3P109.

Otoko, G.R. and Ephraim, M.E. (2014). "Concrete admixture and set retarder potential of palm liquor", *European International Journal of Science and Technology*, 3(2),74-80.

Otunyo, A.W. and Koate, A.I. (2015). "Sugar cane juice as a retarding admixture in concrete production", *Global Journal of Research in Engineering*, 14(1), 17-23, https://doi.org/10.4314/gjer.v14i1.3.

Patel, G.K. and Deo, S.V. (2016). "Effect of natural organic materials as admixture on properties of concrete", Indian Journal of Science and Technology, 9(37), 1-5, https://doi.org/10.17485/ijst/2016/v9i37/93541.

Pathan, B. and Singh, V.V. (2017). "Using molasses in concrete as a time retarding admixture", *International Journal of Engineering Research and Technology*, 6(11), 509-513

Paul, S., Aswathi, K.P., Hanna, P., George, J.K. and Shameer, K. (2017). "Effect of natural rubber latex as admixtures in concrete", *International Research Journal of Engineering and Technology (IRJET)*, 4, 2031-2034.

Paul, S.C., Adewumi, J.B., Miah, M.J., Abdul Basit, M., Noor, M.S.H. and Sih, Y.K. (2022). "Role of sugarcane juice as a natural admixture on setting time and hardened properties of cementitious materials", Infrastructures, 7(10), 145, https://doi.org/10.3390/infrastructures7100145.

Plank, J., Sakai, E., Miao, C.W., Yu, C. and Hong, J.X. (2015). "Chemical admixtures, Chemistry, applications and their impact on concrete microstructure and durability", *Cement and Concrete Research*, 78(Part A), 81-99, https://doi.org/10.1016/j.cemconres.2015.05.016.

Ramesh, B.T.S. and Neeraja, D. (2017). "An experimental study of natural admixture effect on conventional concrete and high volume class F fly ash blended concrete", *Case Studies in Construction Materials*, 6, 43-62, https://doi.org/10.1016/j.cscm.2016.09.003.

Ramesh, B.T.S., Neeraja, D., Daniel, M. and Waraboa, U. (2017). "Effect of natural admixture on durability properties of conventional and class C fly ash blended concrete", *American Journal of Engineering Research (AJER)*, 6, 321-333,

Sathya, A., Bhuvaneshwari, P., Niranjan, G. and Vishveswaran, M. (2014). "Influence of bio admixture on mechanical properties of cement and concrete", *Asian Journal of Applied Sciences*, 7(4), 205-214, https://doi.org/10.3923/ajaps.2014.205.214.

Tangtakabi, A., Ramesht, M.H., Golsoorat pahlaviani, A. and Pourrostam, T. (2022). "Assessment of corrosion in offshore R.C. piers and use of microsilica to reduce corrosion induced oxidation (A case study of Wharves 11

and 12 in Imam Khomeini Port, Iran)", *Civil Engineering Infrastructures Journal*, 55(2), 333-350, https://doi.org/10.22059/ceij.2021.325670.1761.

Thirumalini, P. and Sekar, S.K. (2013). "Review on herbs used as admixture in lime mortar used in ancient structures", *International Journal of Applied Engineering Research*, 3(8), 295-298, https://doi.org/10.15373/2249555X/AUG2013/93.

Torres-Acosta, A.A. and González-Calderón, P.Y. (2021). "Opuntia Ficus-Indica (OFI) mucilage as corrosion inhibitor of steel in CO_2-contaminated mortar", *Materials*, 14(5), 1316, https://doi.org/10.3390/ma14051316.

Woldemariam, A.M., Oyawa, O.W.O. and Abuodha, S.O. (2014). "Cypress tee extract as an eco-friendly admixture in concrete", *International Journal of Civil Engineering and Technology (IJCIET)*, 5(6), 25-36.

Woldemariam, A.M., Oyawa, W.O. and Abuodha, S.O. (2015). "The use of plant extract as Shrinkage Reducing Admixture (SRA) to reduce early age shrinkage and cracking on cement mortar", *Internati*onal *Journal of Innovation and Scientific Research*, 13(1), 136-144.

Civil Engineering Infrastructures Journal 2023, 56(2): 365-379
DOI: 10.22059/CEIJ.2022.345402.1856

RESEARCH PAPER

Experimental Study of Properties of Green Concrete Based on Geopolymer Materials under High Temperature

Mansourghanaei, M.H.[1*], Biklaryan, M.[2] and Mardookhpour, A.[3]

[1] Ph.D., Department of Civil Engineering, Chalous Branch, Islamic Azad University, Chalous, Iran.
[2] Assistant Professor, Department of Civil Engineering, Chalous Branch, Islamic Azad University, Chaloous, Iran.
[3] Assistant Professor, Department of Civil Engineering, Lahijan Branch, Islamic Azad University, Lahijan, Iran.

Received: 04 Jul. 2022; Revised: 12 Sep 2022; Accepted: 08 Oct. 2022

ABSTRACT: Geopolymer Concrete (GPC) are known as green and nature-friendly concretes. In the current research, GPC based on Granulated Blast Furnace Slag (GBFS) was used with 0-2% Polyolefin Fibers (POFs) and 0-8% Nano Silica (NS) to improve its structure. After curing the specimens under dry conditions at a temperature of 60 °C in an oven, then subjected to permeability test, water absorption test and Uultrasonic Pulse Velocity (UPV) test at the ages of 7, 28 and 90 days. On the other hand, NS reduced the amount of water absorption and water permeability in concrete by 24 and 44%, this is due to the property of filling the pores with NS. Moreover, by conducting the ultrasonic, X-Ray Fluorescence (XRF), X-Ray Diffraction (XRD), and Scanning Electron Microscope (SEM) tests, a microstructure investigation was carried out on the concrete samples. In addition to their overlapping with each other, the results indicate the GPC superiority over the regular concrete. Besides, it demonstrated the positive influence of NS addition on the UPV and microstructural properties concretes against the heating treatment at the age of 90 days. Heat caused a drop in the results by destroying the concrete microstructure.

Keywords: Concrete Microstructure, Geopolymer Concrete, Granulated Blast Furnace Slag, Nano Silica, Polyolefin Fibers.

1. Introduction

Geopolymers are newly emerging adhesive materials that are able to replace ordinary Portland cement (OPC), while producing less toxic gas CO_2 and consuming less energy in the production process. (Ahmed et al., 2022). For this reason, this type of concrete is known as green and nature-friendly concrete. Geopolymers are materials with cement properties that are comparable to OPC due to environmental benefits (Lyu et al., 2022). GPC is one of the innovative eco-friendly materials that has gained the attention of many researchers in the sustainable development of the construction industry (Sathish Kumar et al., 2022). GPC are known as a suitable alternative to Ordinary Portland Cement Concrete (OPCC) due to their superior

* Corresponding author E-mail: mhm.ghanaei@iauc.ac.ir

mechanical properties and durability. (Verma and Dev, 2022). Green concrete based on GPC has many environmental advantages. So that, geopolymer concretes have lower CO_2 emissions than conventional concrete and Portland cement (Asadi et al., 2022; Memiş et al., 2022; Jindal et al., 2022; Kanagaraj et al., 2022; Erfanimanesh and Sharbatdar, 2020). Research shows that in order to reduce toxic gas CO_2 up to 55%, it is necessary to use sustainable materials such as GPC (Asadi et al., 2022). In the last three decades, the gigantic demand for sustainable and environmentally friendly concrete with reduced environmental footprints has resulted in the development of low carbon concretes such as GPC (Jindal et al., 2022). GPC is economical, stable, environmentally friendly and durable concrete (Verma et al., 2022). GPC is produced under the process of geopolymerization, in which a molecular network is formed with Coulancy bonds (Wong, 2022). GPC has superior mechanical properties and durability compared to conventional concrete (Srividya et al., 2022). In GPC, GBFS were used as binder material, along with sodium hydroxide and sodium silicate solutions as activator solutions (Kanagaraj et al., 2022). Geopolymer adhesive materials are recognized as a potential and sustainable alternative to conventional concrete (Albidah et al., 2022). Increasing the concentration of the molarity of active alkali solution in the composition of GPC leads to the improvement of the properties of GPC to a certain extent (Shilar et al., 2022). SEM images of the microstructure of GPC show the superiority of this type of concrete compared to ordinary concrete (Amin et al., 2022).

Recently, many efforts have been made to use nanoparticles such as NS in GPC to improve the properties of this type of concrete (Ahmed et al., 2022). These nanoparticles improve the properties of concrete by increasing the speed of the geopolymerization process (Shilar et al., 2022). Nanoparticles, by producing a large volume of hydrated gels such as C-S-H, N-A-S-H and C-A-S-H by filling holes and pores, improve durability and strength in hardened concrete (Ahmed et al., 2022). Several factors such as the proportion of active alkali solution, age of concrete curing and heat curing temperature in concrete are effective on the quality of GPC containing NS (Ahmed et al., 2022). In addition, the presence of NS particles in the composition of GPC leads to the acceleration of the geopolymerization process (Assaedi et al., 2019).

According to the studies, using macro plastic fibers for concrete improvement instead of metal mesh and fibers has captured researchers' attention (Abbasi Nattaj Omran., 2022). The concrete-related industries widely use polyolefin-based fibers (Alberti et al., 2015). By bridging the cracks in the hardened concrete mix, POF sprevent the development of cracks against the incoming loads (Yousefvand., 2019). By performing Crack Mouth Opening Displacement (CMOD) analysis, POFs with proper connection in the concrete composition and due to the high strength of these fibers lead to the improvement of concrete properties (Adhikary, 2019).

Although the use of GPC as one of the emerging building materials is expanding, but the resistance of this type of concrete against high heat in the long term needs to be known more (Amran et al., 2022). In this regard, research has shown that geopolymers, in addition to environmental properties, have good resistance to high temperatures (Albidah et al., 2022).

The properties and the bonding type are different in regular and GPCs. The bonding in regular concretes is based on calcium oxide hydration and silicon dioxide reactions in order to form calcium silicate hydrate. However, the GPC bonding is established via alkaline activator contact with the Aluminosilicate raw materials, reshaped in the polymerization reaction product, and slowly cooled in a high pH medium and hydrothermal condition (hydrothermal condition is referred to the

chemical reactions in the presence of solvent in higher pressure and temperature). This structure (related to the GPC) has some merits compared to the regular concrete, e.g. it provides better resistance performance at higher temperatures (Aslani, 2016).

A higher temperature brings about physical and chemical changes in the concrete structure, accompanied by resistance performance decline and concrete destruction. Although concrete is one of the insulating building materials against heat, if it is exposed to a higher temperature, irreversible physical and chemical changes will take place. Some damages created as a result of concretes placement against the heat exposure are indicated as follows. Resistance performance decline, weight loss, and the formation of large cracks and cavities in the micro and macrostructure of concrete.

- The removal of evaporative water at 100 °C.
- Calcium Silicate Hydrates hydration starts at 180 °C; as the temperature increases to 200 °C, the vapor pressure continuously elevates in the geopolymer structure.
- The OH hydroxyl groups are evaporated at 500 °C. The dihydroxylation changes the Aluminosilicate structure, reducing the resistance level.
- An intensely porous ceramic structure is formed at 800 °C.

The changes occurring at a temperature higher than 500 °C in concrete are irreversible, and the changes made in the concrete behavior are more obvious at such temperatures. Some researchers have reported that reduction in resistance is mainly attributed to the breakdown of calcium hydroxide, and this phenomenon usually takes place in the temperature range between 450 to 500 °C (Bentz et al., 2000).

This study mainly aims to investigate the durability and microstructural properties of the GPCs based on the GBFS containing NS and also reinforced with POFs. In this way, while producing green concrete based on GPC, concrete with superior advantages over OPCC can be produced. For this purpose, the water absorption and water permeability tests under room temperature and UPV, SEM, XRD and XRF tests under room temperature and high heat have been conducted.

2. Experimental Program and Test Methods

2.1. Materials

In this experimental study, according to other articles (Mansourghanaei et al., 2022), the Portland cement type II with a 2.35 g/cm^3 of specific weight according to standard En 197-1 and the GBFS was with the density of 2.79 g/cm^3 according to ASTM C989/C989M standard. The chemical properties of these materials are indicated in Table 1. The used fine aggregates with a density of 2.75 g/cm^3, and the coarse aggregates with a maximum size of 19 mm and a density of 2.65 g/cm^3 according to ASTM-C33. The curing was performed at a temperature of 60 °C. NS was used with a purity of 99.9% and a particle size of 15-25 nm. POFs were used in a wavy form with a length of 30 mm under the standard ASTM D7508/D7508M, whose physical properties are shown in Table 2.

Table 1. Chemical compositions of materials

Component	GBFS (%)	Portland cement type II (%)
SiO_2 (%)	29.2	21.3
Al_2O_3 (%)	19.4	4.7
Fe_2O_3 (%)	5.8	4.3
CaO (%)	38.6	62.7
MgO (%)	2.8	2.1
SO_3 (%)	2.6	2
K_2O (%)	0.1	0.65
Na_2O (%)	0.2	0.18
TiO_2 (%)	0.6	-
Free Cao	-	1.12
Blaine (cm^2/gr)	2200	3200
LOI (%)	0.3	1.84

Table 2. Physical properties of the POFs

Tensile Strength (N/mm^2)	**> 500**
Length (mm)	30
Diameter (mm)	0.8
Elasticity Modulus (GPa)	>11
Bulk Density (Kg/m^3)	2400

2.2. Mix Design

According to other articles (Mansourghanaei et al., 2022), GPC under the standard is made in 6 mixing designs, the first design is made of ordinary concrete and the 2nd to 5th designs are made of geopolymeric concrete based on the slag of the slag containing different percentages of NS and polyolefin fibers. A 12 M active alkali solution of NaOH and Na_2SiO_3 was used. Table 3 lists the mix designs of the specimens.

2.3. Test Methods

After fabricating the samples, for better curing and increasing the durability and microstructural properties, the samples were at 80 °C with a thermal rate of 4.4 °C/min for 48 h. After curing the samples and before performing the tests, the samples were placed in an oven at 500 °C for 1 h at the age of 90 days. In the end, by opening the oven door, the samples reached the ambient temperature (Wong, 2022). Then, the necessary tests were performed on concrete samples according to the relevant standards at ambient temperature and under high temperature.

The water absorption test was carried out according to the standard ASTM C1585-04 and at first the concrete samples were dried under 50±5 °C temperature for three days. Then, after cooling, the samples were kept at room temperature for 15 days. A plastic cover was used to prevent water evaporation (Albitar et al., 2017). The water absorption coefficient was calculated based on the following equation (De Beer et al., 2005):

$$S = \frac{(Q/A)}{\sqrt{t}} \quad (\frac{\mathrm{m}}{\sqrt{t}}) \tag{1}$$

where Q: is volume of the absorbed water, A: is area of the concrete in contact with water, and t: is time.

The water permeability test under the EN 12390-8 standard was performed on 15 cm cubic samples, in which the concrete samples were subjected to water pressure 50±500 kPa for 72 hours. The water penetration coefficient was calculated according to Eq. (2) (Ahmad et al., 2017):

$$K = \frac{e^2 v}{2ht} (m/s) \tag{2}$$

where e: is penetration depth (m), v: is volume fraction of concrete, h: is hydraulic length of concrete, and t: is the duration it is under water pressure.

The UPV tests (Galan, 1967) were conducted according to ASTM C597 using a non-destructive ultrasonic electronic apparatus, PUNDIT MODEL PC1012, with an accuracy of ±0.1 μs for a transformator with a vibrational frequency of 55 kHz and a movement time accuracy of ±2% for the distance.

3. Results and Discussion

3.1. The Results of The Water Absorption Test

The results of the water absorption test in concrete are shown in Figure 1. Increasing the curing age in concrete has led to a decrease in water penetration in concrete. In this regard, the age of 28 days compared to the age of 7 days has experienced the superiority of the results between 11-32% and the age of 90 days compared to the age of 28 days has experienced the improvement of the results of 2-18%. At the age of 90 days, GPC has 40% less water absorption than normal concrete. Adding silica nanoparticles to the GPC mix up to 24% and adding POFs to the GPC mix up to 24% improved the results.

3.2. The Results of The Water Permeability Test

The results of the water permeability test in concrete are shown in Figure 2. Based on these results, normal concrete is in the poor classification and GPC is in the average classification of concrete quality (Rendell et al., 2010). The results of this section indicate that GPC has 16% less water permeability than normal concrete. The

addition of NS particles to the composition of geopolymeric concrete has improved the results of water permeability in this type of concrete by 44%. On the other hand, adding up to 2% of POFs in the composition of geopolymeric concrete has led to an improvement of the results by 55% (compared to samples of geopolymeric concrete without fibers). The permeability of water in concrete has a direct relationship with the amount of porosity in the concrete composition, so that with the increase of porosity in concrete, the penetration of water in concrete increases.

Figure 3 shows the concrete sample measuring the amount of water penetration in the concrete. The relationship between the capillary water absorption coefficient and the water permeability coefficient in concrete is shown in Figure 4.

Table 3. Details of the mix designs

Mix No.	Mix ID	OPC (Kg/m^3)	GBFS (Kg/m^3)	Water (Kg/m^3)	Alkaline solution	NS (Kg/m^3)	NS %	Coarse aggregates (Kg/m^3)	Fine aggregates (Kg/m^3)	POFs (Kg/m^3)	POFs %	Superplasticizer (Kg/m^3)
1	**OPCC**	450	0	202.5	0	0	0	1000	761	0	0	9
2	**GPCNS0PO0**	0	450	0	202.5	0	0	1000	816	0	0	9
3	**GPCNS4PO0**	0	432	0	202.5	18	4	1000	767	0	0	10
4	**GPCNS8PO0**	0	414	0	202.5	36	8	1000	718	0	0	11
5	**GPCNS8PO1**	0	432	0	202.5	36	8	1000	672	24	1	11
6	**GPCNS8PO2**	0	432	0	202.5	36	8	1000	646	48	2	11

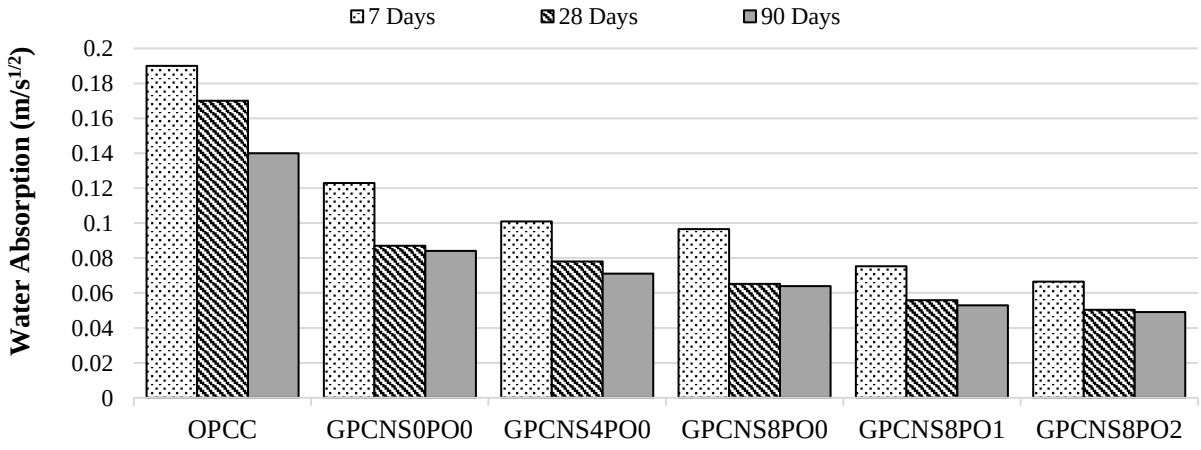

Fig. 1. Water absorption variations in specimens

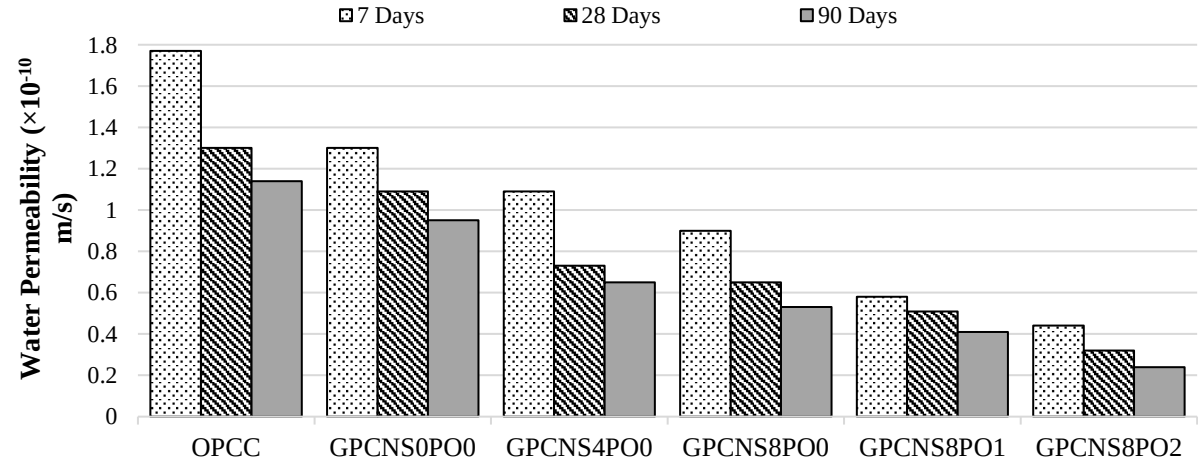

Fig. 2. Variations in the permeability coefficients of the specimens

Fig. 3. The amount of water permeability in the specimens

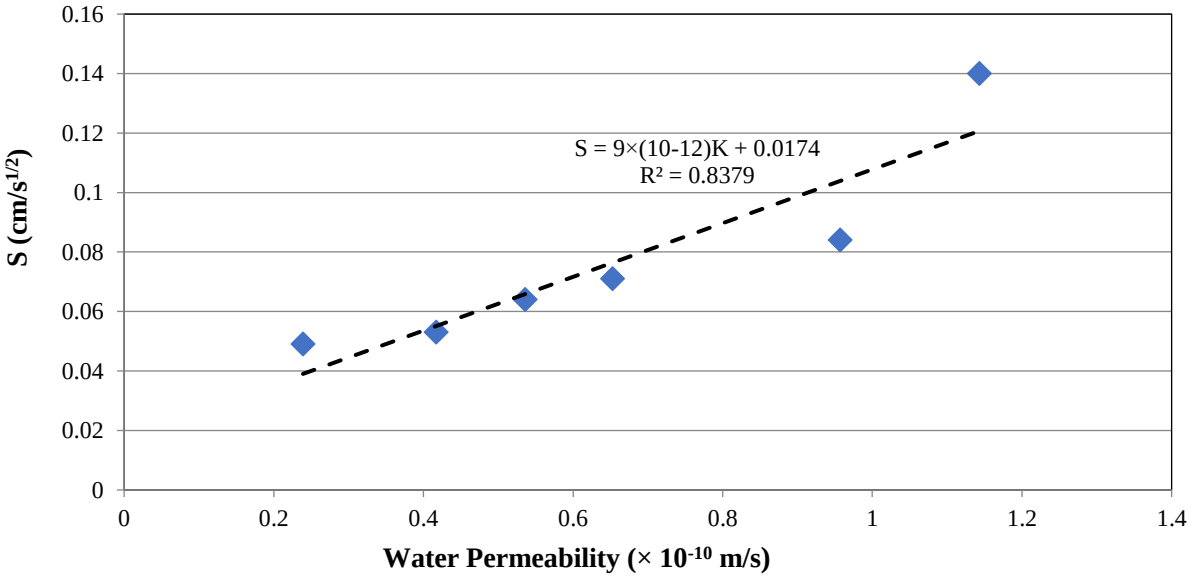

Fig. 4. The relationship between permeability and water absorption

3.3. The Results of The Ultrasonic Pulse Velocity (UPV) Test

The velocity of the ultrasonic waves passing through the samples can be seen at ambient temperature (7,28,90 days) in Figure 5 and under heat (90 days) in Figure 6. The speed quality of ultrasonic waves based on IS 13311-1 standard in four levels as follows: Doubtful with a speed below 3000 m/s, Moderate with a speed of 3000 to 3500 m/s, Good with a speed of 3500 to 4500 m/s and Excellent with a speed of more than 4500 m/s is divided.

The results obtained in this section indicate a decline in transient ultrasonic wave velocity after putting concrete samples under heating treatment such that transition velocity of ultrasonic waves decreased by 37% and 46% in regular concrete and GPC at 500 °C, respectively. By the addition of 4% and 8% NS to the GPC compound, the transition velocity of ultrasonic pulse declined by 40% and 37%, respectively. The results indicated that the addition of fibers reduced the UPV. This reduction was not significant being in the range lower than 12.5%. The small effect of fibers on the pulse velocity was also reported, this rise can be originated from the fact that the pulse velocity in steel is 1.2-1.9 times more than that in GPC (Reufi et al., 2016). According to the obtained results in this investigation, all designs at room temperature have "superior" quality, and all samples at 500 °C have average and good quality (Whitehurst, 1951). As long as the UPV values are classified as "excellent", the concrete has no large cracks or pores that

can affect the integrity of the specimen structure (Kwan et al., 2012). On the other hand, the obtained results revealed that the addition of NS increased the pulse velocity by filling the pores and densifying and integrating the concrete. Due to the curing in the dry environment of the oven, some fine cracks and pores were formed in the GPC preventing its full integrity, which allows for the transmission of ultrasonic pulses with higher velocities. Therefore, the obtained velocities were slightly lower than those of OPCC. Nevertheless, these cracks had very fine dimensions and could only influence the UPV having no remarkable effect on the compressive strength of the specimens (Ren et al., 2016). The presence of NS in mix design GPCNS8PO0 was very effective in making the velocity of the passing pulses close to those of the OPCC.

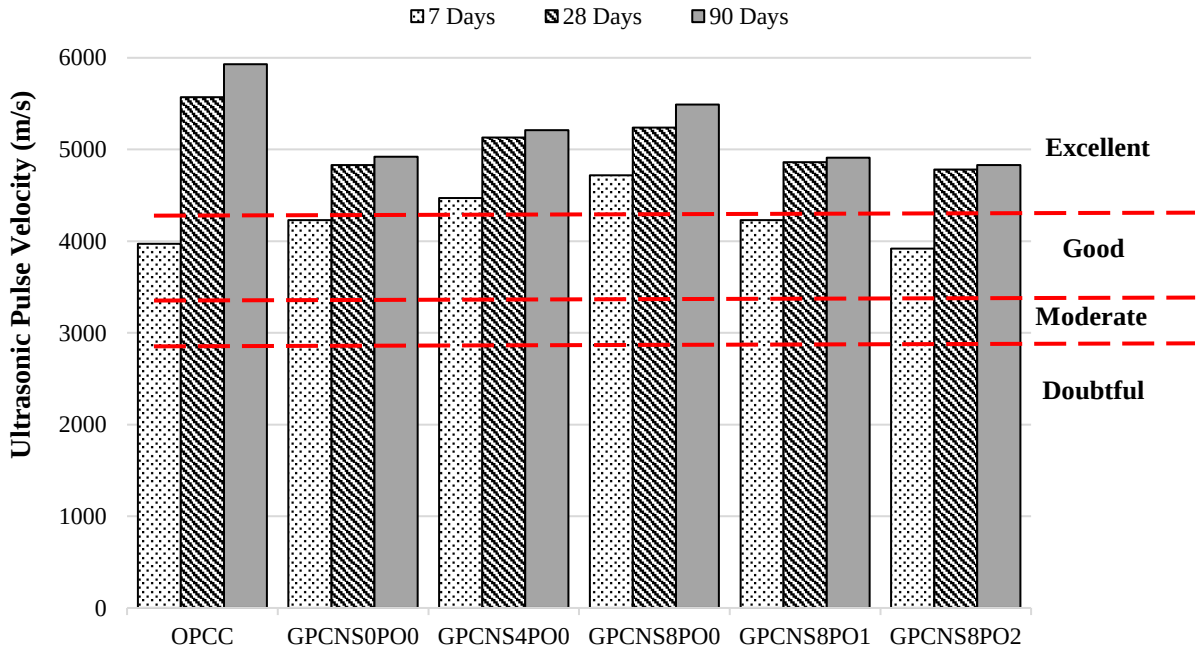

Fig. 5. The variations in the ultrasonic pulse velocities of the specimens

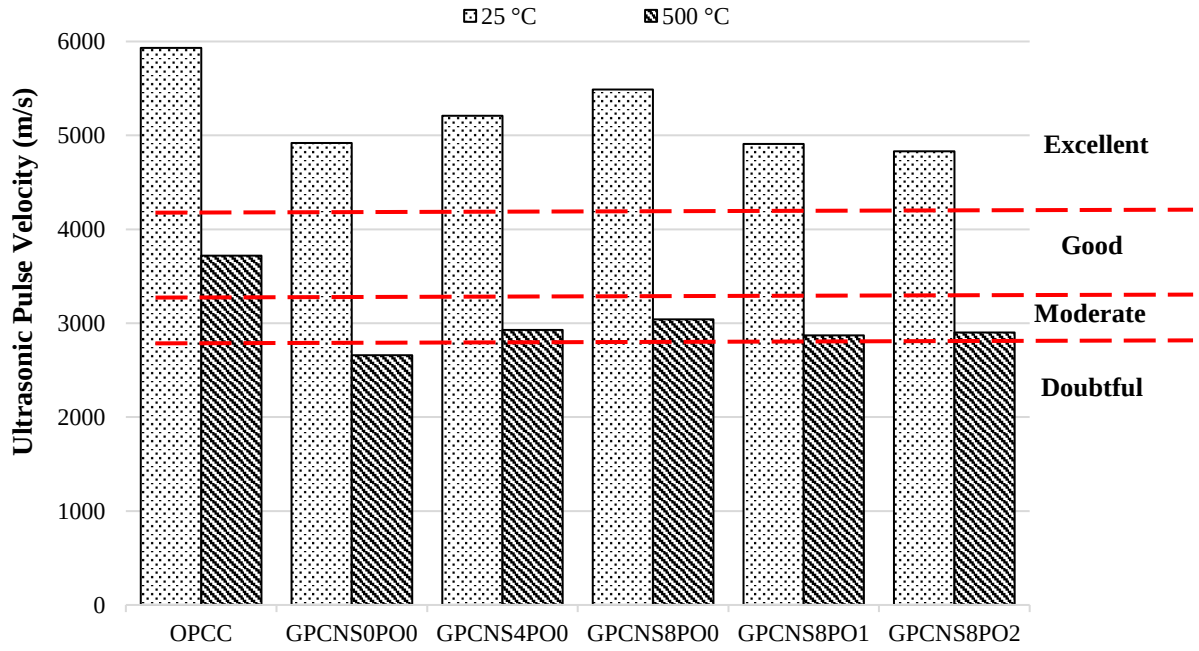

Fig. 6. The variation in ultrasonic wave velocity of samples

4. The Results of the SEM, XRD and XRF Tests

Figure 7 demonstrates microscopic images of regular concrete containing Portland cement at different temperatures. Figure 8 indicates microscopic images of GPC based on GBFS at different temperatures. The chemical reaction process in GPC is more than normal concrete (Du et al., 2014). Due to the porous structure of geopolymer and micro pores at micro and nano scales, GPC allows water evaporation without damaging the Aluminosilicate network, leading to the greater durability of geopolymers than regular concrete high temperatures. Various chemical compounds can be seen in the Figure 9. Microcracks, cavities, amorphous structure of Aluminosilicate, and ceramic structure in GPC can be seen. Compact and homogenous Aluminosilicate structure in geopolymer sample at room temperature, which is the results of geopolimarization process, is indicated. GBFS is full of calcium. In geopolymeric concrete based on blast furnace slag, geopolymerization products include hydrated gels such as C-S-H, A-S-H, C-A-S-H and N-A-S-H. These gels are the main factor of strength in hardened geopolymer paste. On the other hand, these gels improve durability in concrete. With the passage of time, the geopolymerization process and the volume production of hydrated gels develop in the concrete composition (Mansourghanaei et al., 2022).

As can be seen in Figure 8 for geopolymer samples at 500 °C, OH of hydroxyl groups dehydrate at this temperature, and OH is located on the surface and edges of each geopolymer micelle. The dehydroxylation process affects and declines durability properties. As the dehydroxylation process begins, the structure of Aluminosilicate is changing to calcium carbonate and appears in the form of crystal and semi-crystal structures. As crystal structures increases, microcracks and cavities expand. An increase in temperature leads to the formation and destruction of new carbonate minerals. On the other hand, as crystal structures decrease, cavities and cracks increase on geopolymer structure. Dehydration takes place between 100 °C and 300 °C, and Dehydroxylion takes place between 500 °C and 900 °C. On the other hand, heat destroys C-A-S-H and C-S-H microstructures in GPC. Applying a great deal of heat converts amorphous geopolymer Aluminosilicate to a ceramic-like structure.

At a temperature higher than 100 °C, the sample shrinks, and cracks appear since water leaves geopolymer structures and the hydration process begins. According to studies conducted by other researchers, when vapor pressure reaches its maximum value, the compact structure of geopolymer with low permeability will not be able to control thermal stresses. This will lead to the creation of thermal cracks on the sample surface due to shrinkage. This phenomenon is known as the "vapor effect" (Hu et al., 2009). Besides, water evaporation from the geopolymer structure is accompanied by weight reduction, leading to the creation of thermal cracks due to shrinkage.

At a temperature condition of 500 °C, geopolymer microstructures change and become destroyed, leading to crystal structure formation. In addition, at high temperatures, superficial and internal cracks are created on the geopolymer structure. It is attributed to calcite decomposition and carbon dioxide release. Carbon dioxide release creates cracks on samples. High expansion and extended cracks change the size and shape of samples. According to SEM images, the formation of extremely porous ceramic structures, water evaporation, and the dehydroxylation process are the main reasons behind the destruction of physical structures. Another reason behind the reduction in resistance of GPC at high temperatures can be attributed to the fact that the presence of strong alkaline activator in GPC under laboratory conditions produces a matrix of highly reactive

Aluminosilicate gels, while a great number of unreacted silicate forms, which undergoes densification and swelling processes at the temperature range of 500 to 800 °C.

Even though fibers change the pathway of cracks or prevent them from developing, the lack of chemical composition between fibers and materials in GPC reduces durability. Fibers completely burn at 500 °C, and their empty spaces become pores and cavities. On the one hand, this phenomenon reduces durability features. On the other hand, these pores and cavities create a way for gases and water vapor formed inside concrete to leave it and prevent spalling and disintegration of concrete at high temperatures.

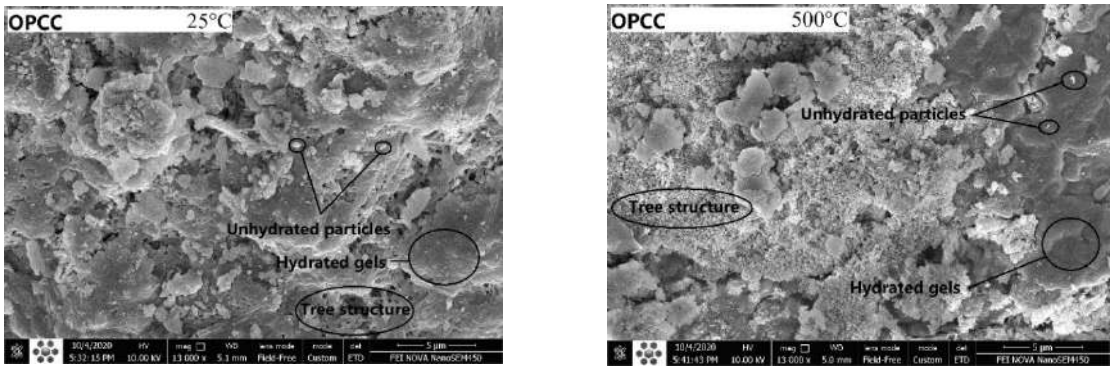

Fig. 7. SEM for the OPCC at different temperatures

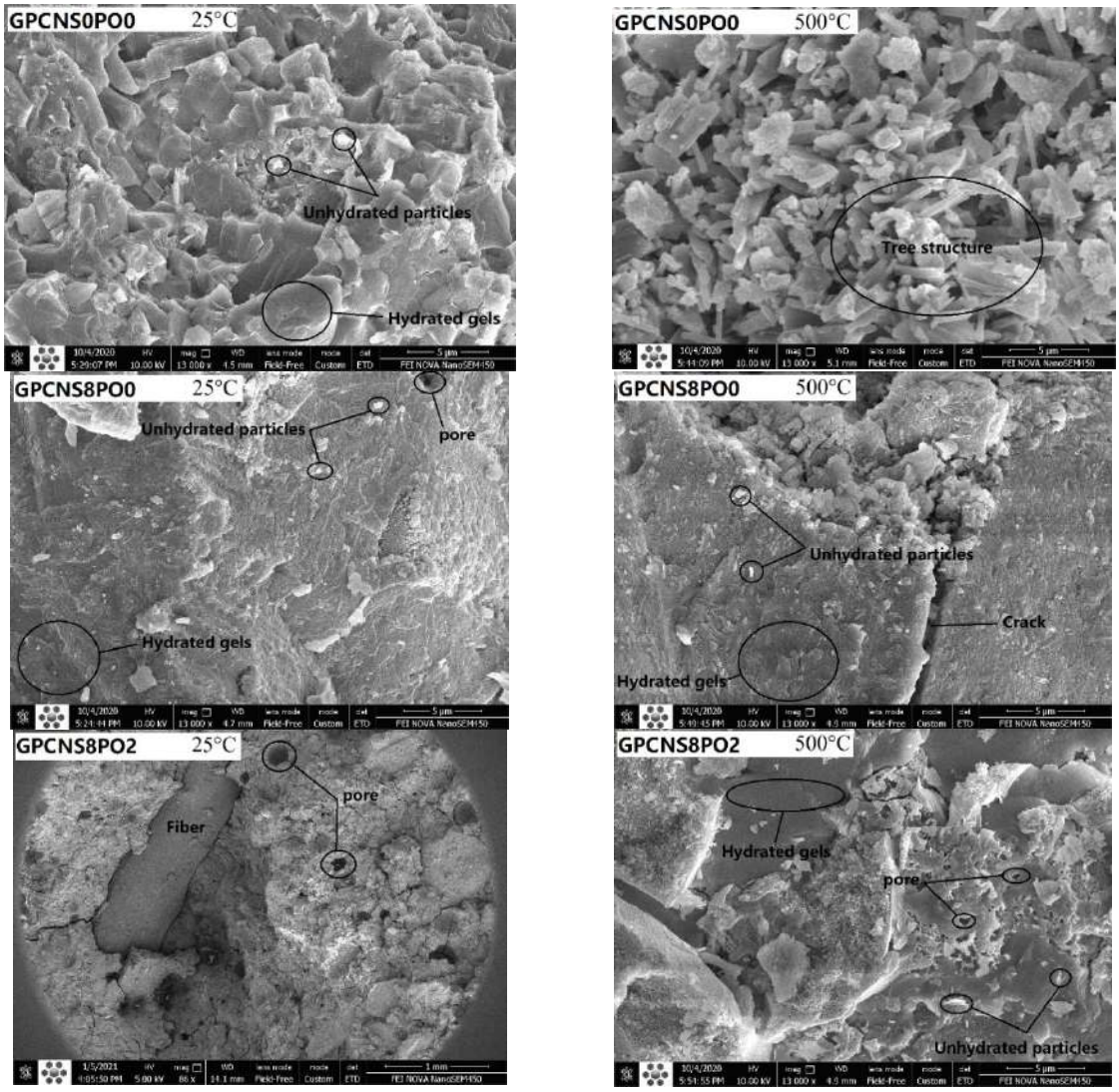

Fig. 8. SEM for the GPC at different temperatures

The results of spectrometry are shown in Figure 9, which illustrates the regular concrete XRD graph at 25 and 500 °C. At 25 °C, the crystal and quasicrystal phases of Aluminum Phosphate, Calcium Hydroxide, Titanium Oxide, Calcite, and Dolomite were observed. Besides, at 500 °C, Magnesium Calcium Carbonate, Carbon, Potassium Iron Magnesium Aluminum Silicate, and Calcium Aluminium Silicate Hydrate were observed.

At a higher temperature, CH gel does not turn into Calcium Carbonates, e.g. Calcite. As indicated in the graph, the CH disappears at a higher temperature, turning into Carbon and C-A, the main reason behind concrete's weakness at a high temperature (Rashad and Zeedan, 2012; Morsy et al., 2012). In the range of 29, 27, 25, and 60 angles, a number of peaks with 2200, 2000, 3000, and 3000 cm^{-1} heights are observed. After being exposed to heating treatment, a number of peaks were created at 27, 28, and 29 angles and 1250, 2800, 2300 cm^{-1} heights. In part b, the XRD graph is indicated for the NS-free GPC at two 25 and 500 °C. At 25 °C, the crystal and quasicrystal phases of Magnesium Calcium Carbonate, Silicon Oxide, Cristobalite, and Sodium Aluminum Silicate were observed. In addition, at 500 °C, Magnesium Calcium Carbonate, Silicon Oxide, Sodium Aluminium Silicate, and Calcium Carbonate Silicate were observed. These findings are consistent with the other researchers' findings (Fan et al., 2018; Türkmen et al., 2016).

The XRD analysis indicates that most existing peaks at greater than 1000 in the GPC graph have taken place in a region with 26-30 = 2θ angles. However, for regular concrete, the peak region is larger, and peaks at 15-35 = 2θ and 60 angles can be observed. This issue can be due to the configuration and the difference in atomic structure among the concrete samples. Therefore, the materials type and the XRD peak phases can be identified by examining the peaks' formation angle and their relative intensity. By placing the samples under the heating treatment, it can be seen that the volume and height of the peaks are dramatically declined, demonstrating the weakening of the concrete structure in encountering heat. The GPC peaks range is in the range of 27, 28, and 29 angles. The maximum peak value for the NS-free GPC is 1300 and 1950. By being exposed to a heating treatment, it reaches 1500, 1700, and 1300.

The XRD graph for GPC containing 8% NS is demonstrated in parts 25 and 500 °C. At 25 °C, the crystal and quasicrystal phases of Calcium Carbonate, Silicon Oxide, Pyroxene, Aluminum Phosphate, and Calcite were observed. Besides, at 500 °C, Silicon Oxide, Sodium Calcium Aluminium Carbonate Silicate were observed (Adak et al., 2017; 2014; Mustakim et al., 2021).

With the increase of NS to the composition of geopolymeric concrete, the volume of hydrated gels increases, this process leads to an improvement in the strength of hardened geopolymeric concrete (Ahmed et al., 2022). With the increase of silica nanoparticles in the composition of geopolymeric concrete, geopolymeric mortar changes from crystalline to amorphous phase (Phoo-ngernkham et al., 2014; Nazari and Sanjayan, 2015).

The peaks occur at angles 27, 28, and 29, and its value is 1800, 4500, and 2200 cm^{-1} at an ambient temperature. The strong peak at 1800 to 1900 cm^{-1} is known as the major fingerprint for the geopolymer matrix, occurring at angles 26 to 29 degrees (Phair and Van Deventer, 2002). Additionally, the 4500 peak took place at angle 28 due to NS addition. Due to being exposed to heating treatment, the peaks reach 2100, 1350, and 1050.

In this research, XRF spectroscopy was performed under ASTM C989 standard. According to XRF results in Tables 4 and 5, compared to mixture OPCC, the SiO_2 and CaO elements are declined by 28% in mixture design GPCNS0PO0 and the Na_2O content has increased from 1.1 to 15.1%. By adding 8% of NS, the SiO_2 content increases by 85%, compared to mix 2.

It is worth mentioning that by comparing the samples XRF in Tables 4 and 5 at different temperatures, it can be concluded that as the temperature increases, the CaO content declines dramatically, such that this level of decrease has been 53% in design OPCC, 31% in design GPCNS0PO0, and 0.5% in design GPCNS0PO0. Besides, the temperature rise increases the SiO_2 percentage, such that this enhancement reaches 41% in design OPCC, 85% in design GPCNS0PO0, and 1% in design GPCNS8PO2. Concerning the mentioned reasons in the SEM part, the reason behind these changes is totally rational. In this case, the lower resistance loss against the heat in design four can be due to more stability of the constituents when exposed to the heating treatment.

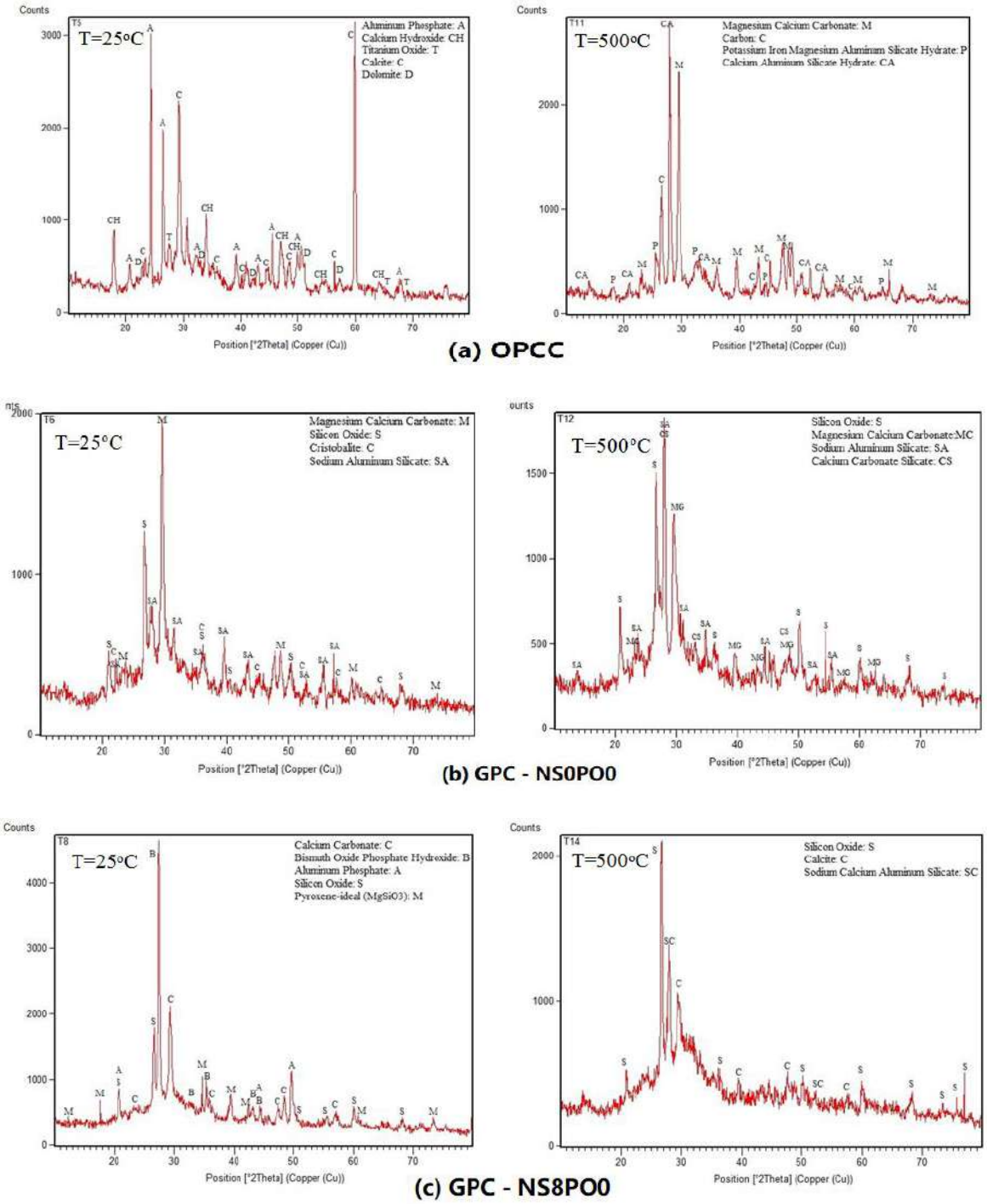

Fig. 9. XRD patterns for samples at different temperatures

Table 4. XRF test values for samples at ambient temperature

SO_3	TiO_2	LOI	Fe_2O_3	Na_2O	K_2O	MgO	CaO	AL_2O_3	SiO_2	
1.59	0.47	16.4	7.2	1.1	0.91	2.11	37.16	5.63	27.12	**Mix1**
1.16	0.961	16.04	5.64	15.1	1.01	5.05	26.81	8.07	19.57	**Mix2**
2.8	1.17	15.7	3.94	12.87	1.05	3.01	15.2	7.01	36.33	**Mix4**

Table 5. XRF test values for samples at 500 °C

SO_3	TiO_2	LOI	Fe_2O_3	Na_2O	K_2O	MgO	CaO	AL_2O_3	SiO_2	
2.41	0.52	16.77	9.85	1.32	1.34	1.95	17.41	9.87	38.25	**Mix1**
2.52	0.74	19.48	7.92	2.1	1.41	2.32	18.41	8.41	36.32	**Mix2**
3.54	0.87	12.95	8.24	4.87	1.5	3.14	15.12	8.21	39.87	**Mix4**

5. Conclusions

A major advantage of lab testing is that the samples are tested under controlled conditions (Fallah Hosseini and Hajikarimi, 2019). The addition of NS and POFs in GPC based on slag of forging furnace leads to improvement of mechanical properties and durability in this type of concrete (Mansourghanaei et al., 2022).

- In most of the tests of this laboratory research, the superiority of the properties of green concrete based on GPC compared to OPCC was obtained under ambient temperature and high temperature.
- Applying heat of 500 ℃ has caused fundamental changes in the microstructure of OPCC and GPC, these changes are due to evaporation of water from chemical bonding spaces in hydrated gels, which has weakened the durability properties of concrete.
- In the water permeability test in concrete, the addition of NS up to 55% and the addition of POFs up to 44% improved the results.
- Reduction of capillary water adsorption results and water permeability in fiber-containing samples can be attributed to fiber type, bonding in interfacial transfer zones and non-uniform distribution of fibers in geopolymer cement paste. Research has shown that excessive use of fibers (more than 2%) in concrete composition may lead to uneven distribution of fibers and consequently weaken the concrete structure against the forces (Connolly et al., 2014).
- The ultrasonic wave velocity determining test indicates the high quality of all concrete samples at an ambient temperature and its higher than medium quality at 500 °C. Accordingly, NS addition increased the velocity of the waves by filling the cavities and concretes uniformity.
- The results of SEM, XRD and XRF tests well demonstrated the filling of the pores by the nanoparticles and densification of the concrete structure and bridging between the cracks by the fibers and were in coordination with the results of all tests performed in this study.

8. References

Abbasi Nattaj Omrani, I., Ardeshir-Behrestaghi, A. and Saeedian, A. (2022). "Influences of Polyvinyl Alcohol Fiber Addition on the specimen size effect and energy absorption of self-consolidating Concrete", *Civil Engineering Infrastructures Journal*, 55(1), 59-74, https//doi.org/10.22059/ceij.2021.310356.1705.

Adak, D., Sarkar, M. and Mandal, S. (2017). "Structural performance of nano-silica modified fly-ash based geopolymer concrete", *Construction and Building Materials*, 135, 430-439, https://doi.org/10.1016/j.conbuildmat.2016.12.111.

Adhikary, S.K., Rudzionis, Z., Balakrishnan, A. and Jayakumar, V. (2019). "Investigation on the mechanical properties and post-cracking behavior of polyolefin fiber reinforced concrete", *Fibers*, 7(1), 8, https://doi.org/10.3390/fib7010008.

Ahmad, S.I. and Hossain, M.A. (2017). "Water permeability characteristics of normal strength concrete made from crushed clay bricks as coarse aggregate", *Advances in Materials Science and Engineering*, 2017, 1-9, https://doi.org/10.1155/2017/7279138

Ahmed, H.U., Mohammed, A.A. and Mohammed, A.S. (2022). "The role of nanomaterials in geopolymer concrete composites: A state-of-the-art review", *Journal of Building Engineering*, 49, 104062,

https://doi.org/10.1016/j.jobe.2022.104062.

Ahmed, H.U., Mohammed, A.S., Faraj, R.H., Qaidi, S.M. and Mohammed, A.A. (2022). "Compressive strength of geopolymer concrete modified with nano-silica: Experimental and modeling investigations", *Case Studies in Construction Materials*, 16, e01036, https://doi.org/10.1016/j.cscm.2022.e01036.

Ahmed, H.U., Mohammed, A.S. and Mohammed, A.A. (2022). "Proposing several model techniques including ANN and M5P-tree to predict the compressive strength of geopolymer concretes incorporated with nano-silica", *Environmental Science and Pollution Research*, 29(47), 71232-71256. https://doi.org/10.1007/s11356-022-20863-1.

Alberti, M.G., Enfedaque, A. and Gálvez, J.C. (2015). "Improving the reinforcement of polyolefin fiber reinforced concrete for infrastructure applications", *Fibers*, 3(4), 504-522, https://doi.org/10.3390/fib3040504.

Albitar, M., Ali, M.M., Visintin, P. and Drechsler, M. (2017). "Durability evaluation of geopolymer and conventional concretes", *Construction and Building Materials*, 136, 374-385, https://doi.org/10.1016/j.conbuildmat.2017.01.056.

Albidah, A., Alqarni, A.S., Abbas, H., Almusallam, T. and Al-Salloum, Y. (2022). "Behavior of Metakaolin-Based geopolymer concrete at ambient and elevated temperatures", *Construction and Building Materials*, 317, 125910, https://doi.org/10.1016/j.conbuildmat.2021.125910.

Amin, M., Elsakhawy, Y., Abu el-hassan, K. and Abdelsalam, B.A. (2022). "Behavior evaluation of sustainable high strength geopolymer concrete based on fly ash, metakaolin, and slag", *Case Studies in Construction Materials*, 16, e00976, https://doi.org/10.1016/j.cscm.2022.e00976.

Amran, M., Huang, S.S., Debbarma, S. and Rashid, R.S. (2022). "Fire resistance of geopolymer concrete: A critical review", *Construction and Building Materials*, 324, 126722, https://doi.org/10.1016/j.conbuildmat.2022.126722.

Asadi, I., Baghban, M.H., Hashemi, M., Izadyar, N. and Sajadi, B. (2022). "Phase change materials incorporated into geopolymer concrete for enhancing energy efficiency and sustainability of buildings: A review", *Case Studies in Construction Materials*, 17, e01162, https://doi.org/10.1016/j.cscm.2022.e01162.

Assaedi, H., Alomayri, T., Shaikh, F. and Low, I.M. (2019). "Influence of nano silica particles on durability of flax fabric reinforced geopolymer composites" *Materials*, 12(9), 1459, https://doi.org/10.3390/ma12091459.

Aslani, F. (2016). "Thermal performance modeling of geopolymer concrete", *Journal of Materials in Civil Engineering*, 28(1), 04015062, https://doi.org/10.1061/(ASCE)MT.1943-5533.000129.

Bentz, D.P. (2000). "Fibers, percolation, and spalling of high-performance concrete", *Materials Journal*, 97(3), 351-359, https://www.researchgate.net/publication/234155149.

Connolly, D.P., Kouroussis, G., Woodward, P.K., Giannopoulos, A., Verlinden, O. and Forde, M. C. (2014). "Scoping prediction of re-radiated ground-borne noise and vibration near high speed rail lines with variable soils", *Soil Dynamics and Earthquake Engineering*, 66, 78-88, https://doi.org/10.1016/j.soildyn.2014.06.021.

Deb, P.S., Sarker, P.K. and Barbhuiya, S. (2016). "Sorptivity and acid resistance of ambient-cured geopolymer mortars containing nano-silica", *Cement and Concrete Composites*, 72, 235-245, https://doi.org/10.1016/j.cemconcomp.2016.06.017.

De Beer, F.C., Le Roux, J.J. and Kearsley, E.P. (2005). "Testing the durability of concrete with neutron radiography", *Nuclear Instruments and Methods in Physics Research Section A: Accelerators, Spectrometers, Detectors and Associated Equipment*, 542(1-3), 226-231, https://doi.org/10.1016/j.nima.2005.01.104.

Du, H., Du, S. and Liu, X. (2014). "Durability performances of concrete with nano-silica", *Construction and Building Materials*, 73, 705-712, https://doi.org/10.1016/j.conbuildmat.2014.10.014.

Erfanimanesh, A. and Sharbatdar, M.K. (2020). "Mechanical and microstructural characteristics of geopolymer paste, mortar, and concrete containing local zeolite and slag activated by sodium carbonate", *Journal of Building Engineering*, 32, 101781, https://doi.org/10.1016/j.jobe.2020.101781.

Fan, F., Liu, Z., Xu, G., Peng, H. and Cai, C.S. (2018). "Mechanical and thermal properties of fly ash based geopolymers", *Construction and Building Materials*, 160, 66-81, https://doi.org/10.1016/j.conbuildmat.2017.11.023.

Fallah Hosseini, S. and Hajikarimi, P. (2019). "Investigation on the effect of volume, length and shape of Polyolefin Fibers on mechanical characteristics and fracture properties of high-strength concrete", *Concrete Research*, 12(1), 59-70, https://jcr.guilan.ac.ir/article_3176.html.

Galan, A. (1967). "Estimate of concrete strength by ultrasonic pulse velocity and damping constant", *Journal Proceedings*, 64(10), 678-684.

Hu, S.G., Wu, J., Yang, W., He, Y.J., Wang, F.Z. and Ding, Q.J. (2009). "Preparation and properties of geopolymer-lightweight aggregate refractory concrete", *Journal of Central South University of Technology*, 16(6), 914-918, https://link.springer.com/article/10.1007/s11771-009-0152-x.

Jindal, B.B., Alomayri, T., Hasan, A. and Kaze, C. R. (2022). "Geopolymer concrete with metakaolin for sustainability: A comprehensive review on raw material's properties, synthesis, performance, and potential application", *Environmental Science and Pollution Research*, 30, 25299-25324, https://doi.org/10.1007/s11356-021-17849-w.

Kanagaraj, B., Anand, N., Alengaram, U.J., Raj, R. S. and Kiran, T. (2022). "Exemplification of sustainable sodium silicate waste sediments as coarse aggregates in the performance evaluation of geopolymer concrete", *Construction and Building Materials*, 330, 127135, https://doi.org/10.1016/j.conbuildmat.2022.127135.

Kwan, W.H., Ramli, M., Kam, K.J. and Sulieman, M.Z. (2012). "Influence of the amount of recycled coarse aggregate in concrete design and durability properties" *Construction and Building Materials*, 26(1), 565-573, https://doi.org/10.1016/j.conbuildmat.2011.06.059.

Law, D.W., Adam, A.A., Molyneaux, T.K., Patnaikuni, I. and Wardhono, A. (2015). "Long term durability properties of class F fly ash geopolymer concrete", *Materials and Structures*, 48(3), 721-731, https://doi.org/10.1617/s11527-014-0268-9.

Lyu, X., Robinson, N., Elchalakani, M., Johns, M. L., Dong, M. and Nie, S. (2022). "Sea sand seawater geopolymer concrete", *Journal of Building Engineering*, 50, 104141, https://doi.org/10.1016/j.jobe.2022.104141.

Mansourghanaei, M., Biklaryan, M., and Mardookhpour, A. (2022). "Experimental study of the effects of adding silica nanoparticles on the durability of geopolymer concrete", *Australian Journal of Civil Engineering*, 1-13, https://doi.org/10.1080/14488353.2022.2120247.

Memiş, S. and Bılal, M.A.M. (2022). "Taguchi optimization of geopolymer concrete produced with rice husk ash and ceramic dust", *Environmental Science and Pollution Research*, 29(11), 15876-15895, https://doi.org/10.1007/s11356-021-16869-w.

Mansourghanaei, M. (2022). "Experimental evaluation of compressive, tensile strength and impact test in blast furnace slag based geopolymer concrete, under high temperature", *Journal of Civil Engineering Researchers*, 4(2), 12-21, https//doi.org/10.52547/JCER.4.2.12.

Mansourghanaei, M. (2022). "Experimental study of compressive strength, permeability and impact testing in geopolymer concrete based on Blast furnace slag", *Journal of Civil Engineering Researchers*, 4(3), 31-39, https://doi.org/10.52547/JCER.4.3.31.

Morsy, M.S., Al-Salloum, Y.A., Abbas, H. and Alsayed, S.H. (2012). "Behavior of blended cement mortars containing nano-metakaolin at elevated temperatures", *Construction and Building Materials*, 35, 900-905, https://doi.org/10.1016/j.conbuildmat.2012.04.099.

Mustakim, S.M., Das, S.K., Mishra, J., Aftab, A., Alomayri, T.S., Assaedi, H.S. and Kaze, C.R. (2021). "Improvement in fresh, mechanical and microstructural properties of fly ash-GBFS based geopolymer concrete by addition of nano and micro silica", *Silicon*, 13(8), 2415-2428, https://doi.org/10.1007/s12633-020-00593-0.

Nazari, A. and Sanjayan, J.G. (2015). "Hybrid effects of alumina and silica nanoparticles on water absorption of geopolymers: Application of Taguchi approach", *Measurement*, 60, 240-246, https://doi.org/10.1016/j.measurement.2014.10.004.

Phoo-ngernkham, T., Chindaprasirt, P., Sata, V., Hanjitsuwan, S. and Hatanaka, S. (2014). "The effect of adding nano-SiO_2 and nano-Al_2O_3 on properties of high calcium fly ash geopolymer cured at ambient temperature", *Materials and Design*, 55, 58-65, https://doi.org/10.1016/j.matdes.2013.09.049.

Phair, J. W. and Van Deventer, J.S.J. (2002). "Effect of the silicate activator pH on the microstructural characteristics of waste-based geopolymers", *International Journal of Mineral Processing*, 66(1-4), 121-143, https://doi.org/10.1016/S0301-7516(02)00013-3.

Rashad, A.M. and Zeedan, S.R. (2012). "A preliminary study of blended pastes of cement and quartz powder under the effect of elevated temperature", *Construction and Building Materials*, 29, 672-681, https://doi.org/10.1016/j.conbuildmat.2011.10.006.

Rendell, F., Jauberthie, R. and Grantham, M. (2002). *Deteriorated concrete: Inspection and physicochemical analysis*, Thomas Telford.

Ren, W., Xu, J. and Bai, E. (2016). "Strength and ultrasonic characteristics of alkali-activated fly ash-slag geopolymer concrete after exposure to elevated temperatures", *Journal of Materials in Civil Engineering*, 28(2), 04015124, https://doi.org/10.1061/(ASCE)MT.1943-5533.000140.

Reufi, E., Marku, J. and Bier, T. (2016). "Ultrasonic pulse velocity investigation of Polypropylene

and steel fiber reinforced concrete", *International Journal of Civil and Environmental Engineering*, 10(3), 332-335, https://doi.org/10.5281/zenodo.1112125.

Sathish Kumar, V., Ganesan, N., Indira, P.V., Murali, G. and Vatin, N.I. (2022). "Flexural behaviour of hybrid fibre-reinforced ternary blend geopolymer concrete beams", *Sustainability*, 14(10), 5954, https://doi.org/10.3390/su14105954.

Shilar, F.A., Ganachari, S.V., Patil, V.B., Khan, T. Y. and Dawood, S. (2022). "Molarity activity effect on mechanical and microstructure properties of geopolymer concrete: A review", *Case Studies in Construction Materials*, 16, e01014, https://doi.org/10.1016/j.cscm.2022.e01014.

Shilar, F.A., Ganachari, S.V., Patil, V.B., Khan, T. Y., Almakayeel, N.M. and Alghamdi, S. (2022). "Review on the relationship between nano modifications of geopolymer concrete and their structural characteristics", *Polymers*, 14(7), 1421, https://doi.org/10.3390/polym14071421.

Srividya, T., PR, K.R., Sivasakthi, M., Sujitha, A., and Jeyalakshmi, R. (2022). "A state-of-the-art on development of geopolymer concrete and its field applications", *Case Studies in Construction Materials*, 16, e00812, https://doi.org/10.1016/j.cscm.2021.e00812.

Türkmen, İ., Karakoç, M B., Kantarcı, F., Maraş, M.M. and Demirboğa, R. (2016). "Fire resistance of geopolymer concrete produced from Elazığ ferrochrome slag", *Fire and Mmaterials*, 40(6), 836-847, https://doi.org/10.1002/fam.2348.

Verma, M. and Dev, N. (2022). "Effect of liquid to binder ratio and curing temperature on the engineering properties of the geopolymer concrete" *Silicon*, 14(4), 1743-1757, https://doi.org/10.1007/s12633-021-00985-w.

Verma, M., Dev, N., Rahman, I., Nigam, M., Ahmed, M. and Mallick, J. (2022). "Geopolymer concrete: A material for sustainable development in Indian construction industries", *Crystals*, 12(4), 514, https://doi.org/10.3390/cryst12040514.

Whitehurst, E.A. (1951). "Soniscope tests concrete structures", *Journal Proceedings*, 47(2), 433-444.

Wong, L.S. (2022). "Durability performance of geopolymer concrete: A review", *Polymers*, 14(5), 868, https://doi.org/10.3390/polym14050868.

Yousefvand, M., Sharifi, Y. and Yousefvand, S. (2019). "An analysis of the shear strength and rupture modulus of Polyolefin-Fiber reinforced concrete at different temperatures", *Journal of Civil Engineering and Materials Application*, 3(4), 225-233, https://doi.org/10.3390/polym14050868.

Civil Engineering Infrastructures Journal 2023, 56(2): 381-392
DOI: 10.22059/CEIJ.2023.345511.1857

RESEARCH PAPER

Use of Reclaimed Asphalt Pavement (RAP) in Concrete in Perspective of Rigid Pavements

Jadoon, N.[1], Ullah, I.[2], Sarir, M.[3*], Noman, M.[4] and Shah, A.A.[5]

[1] M.Sc., Civil Engineering Department, University of Engineering and Technology, Peshawar, Pakistan.
[2] M.Sc., Department of Civil Engineering, Faculty of Engineering and Technology, International Islamic University Islamabad, Pakistan.
[3] Ph.D. Candidate, Department of Civil Engineering, Faculty of Engineering and Technology, International Islamic University Islamabad, Pakistan.
[4] Ph.D., Instructor, Department of Civil Engineering, Faculty of Engineering and Technology, International Islamic University Islamabad, Pakistan.
[5] Professor, Department of Civil Engineering, Faculty of Engineering and Technology, International Islamic University Islamabad, Pakistan.

Received: 06 Jul. 2022; Revised: 14 Nov. 2022; Accepted: 26 Nov. 2022

ABSTRACT: The demolishing of roads for repair and reconstruction produces an ample amount of Recycled Asphalt Pavement (RAP) which, if not utilized, may cause depletion of aggregate sources and pollution. The use of RAP in the plain cement concrete (PCC) is sustainable use of road waste material. However, the potential of incorporating RAP to replace natural aggregate needs to evaluate. This research targets the evaluation of mechanical properties of PCC made with extracted RAP materials through laboratory experiments and to achieve the optimized replacement of natural aggregate for rigid pavement composite design. The Virgin Coarse Aggregate (VCA) in PCC was replaced with RAP at 0:25:100 percent by weight. Results show that incorporating RAP in PCC causes a gradual decrease in mechanical properties. However, the decrease in compressive strength is more (57%) than the flexural and splitting tensile strength. RAP up to 25% was found as an optimum allowable replacement with VCA in the rigid pavement. From the Modulus Of Elasticity (MOE), it was detected that with the incorporation of RAP the ductility of PCC improved slightly.

Keywords: Concrete, Recycled Asphalt Pavement (RAP), Virgin Coarse Aggregate (VCA).

1. Introduction

Reclaimed Asphalt Pavement (RAP) is the waste material produced as a result of removal of asphalt concretes from the existing infrastructure and to a minor extent, of wasted or rejected mixes during the production process of asphalt concrete mixtures (Tarsi et al., 2020). In 2018, about 88% wt. and 72% wt. of RAP were utilized in USA and Europe, respectively as an aggregate for cold, warm and hot asphalt

* Corresponding author E-mail: muhammad.sarir@iiu.edu.pk

mixtures and for unbound layers (Tarsi et al., 2020). The asphalt concrete that has been removed as a waste material form an existing road pavement is a fully recyclable material for construction (EAPA, 2014; AAPA, 2018). The removed asphalt concrete consists of non-renewable resources such as approximately 95% wt. of aggregated and 5% wt. of bituminous binder. It has the ability to be re-used, reducing the demand for virgin aggregates or it can be re-used to produce unbound layers of pavements (SABITA, 2019). The mechanical properties such as stiffness modulus, indirect tensile strength, and cracking and fatigue characteristics were studied. The results showed that high amount of RAP up to 60% can be incorporated into bituminous mixtures to obtain satisfactory results (Valdés et al., 2011). The RAP content was used ranging from 0% to 40% in Warm-Mix Asphalt (WMA) and Hot-Mix Asphalt (HMA) and comparison were made by performing different tests such as rut resistance, fatigue resistance and moisture susceptibility. The results indicated that WMA with high RAP content exhibited less rutting and moisture resistance that HMA with high RAP content. Moreover, WMA-high RAP content mixes exhibit better fatigue resistance than HMA-high RAP content (Zhao et al., 2013). Laboratory investigations on asphalt mixes prepared with RAP and rejuvenating agent have been carried out and then compared with asphalt mixtures made with virgin aggregates. Different performance tests such as indirect tensile strength, retained stability, creep test, beam fatigue test, resilient modulus and wheel tracking test have been conducted and compared. The results showed that the asphalt mixtures with RAP and rejuvenating agent ended with better performance as compared to virgin asphalt mixtures (Pradyumna et al., 2013). The replacement of conventional stone dust with sugarcane bagasse ash has improved the performance characteristics of asphalt concrete mixtures (Sarir et al., 2022). The effect on the mechanical properties of hot mix asphalt mixtures partially and fully replaced with RAP were assessed. The results indicated that 100% replacement of granular material by RAP produced highest indirect tensile strength and resilient modulus in both dry and wet condition (Reyes-Ortiz et al., 2012). When the RAP, which was combination of two different sources in Latvia, was added at rates of 30% and 50% in local aggregates, the wheel tracking test results indicated that all the mixtures bear high rutting resistance and fatigue test results using four-point bending beam were similar to those of virgin asphalt mixtures (Izaks et al., 2015). The rheological and chemical analysis of the 100% RAP using rejuvenators was done by (Rathore et al., 2022) which concluded that the bitumen having rejuvenators possesses acceptable rutting performance. Laboratory performance tests such as asphalt pavement analyzer rutting test, wheel tracking test, tensile strength ratio test, indirect tension test and the beam fatigue test were carried out on asphalt mixtures having RAP ranging from 0% to 50%. The test results showed that mixtures with high percentages of RAP exhibit higher resistance to rutting, moisture damage and possessed better fatigue performance (Zhao et al., 2012). Moreover, the mechanical performance, environmental impacts and economic benefit criteria are assessed by (Jahanbakhsh et al., 2020) to introduce the use of RAP in asphalt concrete mixtures. The mechanical properties of asphalt concrete mixtures containing RAP in various percentages i.e. 30%, 60% and 100% along with other supplementary materials were better that or equal to that of the conventional asphalt mixtures. On the other hand, the blending process of RAP with virgin mixture was analyzed by (Huang et al., 2005) in which a blended mixture containing 20% of screened RAP was subjected to staged extraction and recovery. The result showed improved performance of the hot-mix asphalt mixture. The RAP was utilized in rubberized asphalt

mixtures that contains crumb rubber. The results of experimental investigations indicated that the utilization of RAP and crumb rubber in the hot mix asphalt had the ability to effectively improve the rut resistance of the asphalt mixtures (Xiao et al., 2007). The laboratory investigation of high modulus asphalt concrete mixtures was done by (Izaks et al., 2022) having high content of RAP materials. Different tests such as wheel tracker test, water sensitivity test, four-point bending test etc. were performed. The tests performed indicated satisfactory results. The performance of high modulus asphalt mixtures containing RAP was examined. Different percentages of RAP was incorporated and was found that 40% RAP content resulted in optimal mixture in terms of dynamic modulus and moisture damage susceptibility (Zhu et al., 2020). The morphological study of RAP induced concrete was conducted by (Jindal and Ransinchung, 2022) apart from evaluation of mechanical properties which concluded that the addition of mineral admixtures at 15% amount refined the pore structure making the concrete less permeable. The RAP possesses particles of different sizes. Some of them are coarse particles while some are fine particles coated with asphalt binder around them. This phenomenon led to the agglomeration of RAP thus reducing the strength of the concrete modified with RAP (Zhu et al., 2020). However, with the ever-increasing concern about solid waste disposal and the sustainable use of natural resources, the incorporation of recycled materials in Portland Cement Concrete (PCC) has become increasingly popular in recent years. This research has aimed to make it possible the use of RAP as aggregate in rigid pavements.

Out of 276.4 million tons of black-top in Europe, available RAP was 49.6 million tons (17.94%). Similarly, Pakistan has an estimated 100,000 km of road network, mostly asphaltic roads; tonnes of RAP from it are being unearthed and dumping it elsewhere will pose serious environmental risks. The utilization of RAP in rigid (concrete) asphalts not just lessens the cost yet additionally builds strength. After the beginning of the Bus Rapid Transit (BRT) venture in Peshawar, Pakistan, huge amounts of black-top streets were peeled off for the laying of new tracks for the transports. The material is not being reused for any reason and goes to squander.

This research investigated the feasibility of using Reclaimed Asphalt Pavement (RAP) to replace virgin aggregates in concrete pavements. Specifically, this research considered using minimally processed RAP (i.e., simply fractionating into fine and coarse components) in this capacity for roadways in Pakistan.

2. Material and Methods

2.1. Cement

Ordinary Portland Cement (OPC), locally available with the brand name of Kohat cement complying with ASTM C 150 and having a specific gravity of 3.15, was used. The consistency, initial setting time, final setting time, and fineness of cement were found to be 30%, 45 min, 120 min, and 6.9%, respectively.

2.2. Fine Aggregate

The fine aggregate (sand) used in this research was Galbai river sand having Fineness Modulus (FM), specific gravity (by water pycnometer) of 2.76 and 2.78 respectively, while the water absorption was found 1.27 percent according to ASTM C128.

2.3. Coarse Aggregates

The VCA used in this research was acquired from a local quarry site had a size range of 4.75- 25.4 mm. The bulk density as per ASTM C39 (ASTM C39/C39M, 2003) was found to be 1550.1 kg/m^3 (96.77 lb/ft^3). The saturated surface dry (SSD) specific gravity, absorption, and abrasion loss (class B) were 2.70 and 0.60% and 23.72%, respectively.

2.4. Reclaimed Asphalt Pavement (RAP)

RAP aggregates were obtained by breaking the junk from the demolished pavement disposed near M-1 motorway (Peshawar-Islamabad Motorway) into pieces, shown in Figures 1a and 1b, which reportedly was lying in the dumb site for almost 2 years; hence it was exposed to the external weathering conditions. The specific gravity of RAP was 2.9 and determined 4.40% of bitumen content by centrifugal extractor as shown in Figure 1c. The result of VCA and RAP sieve analysis according to ASTM C136 is shown in Table 1. Figure 2 shows the gradation of VCA and RAP aggregate.

Table 1. Sieve analysis

Sieve sizes (inches)	Weight retained on each sieve (g)		Individual percent retained on each sieve		Cumulative weight retained		Percent passing	
	VCA	RAP	VCA	RAP	VCA	RAP	VCA	RAP
1	0	121	0	6.12	0	6.12	100	93.88
¾	628	786	28.88	39.78	31.4	45.9	68.60	54.1
½	768	1039	45.76	52.58	69.80	98.48	30.20	1.52
3/8	280	16	14.56	0.81	83.80	99.29	16.20	0.71
No.4	324	10	10.48	0.51	100	99.8	0	0.2

(a) **(b)** **(c)**

Fig. 1. a) RAP chunks; b) RAP aggregate; and c) Centrifugal extractor

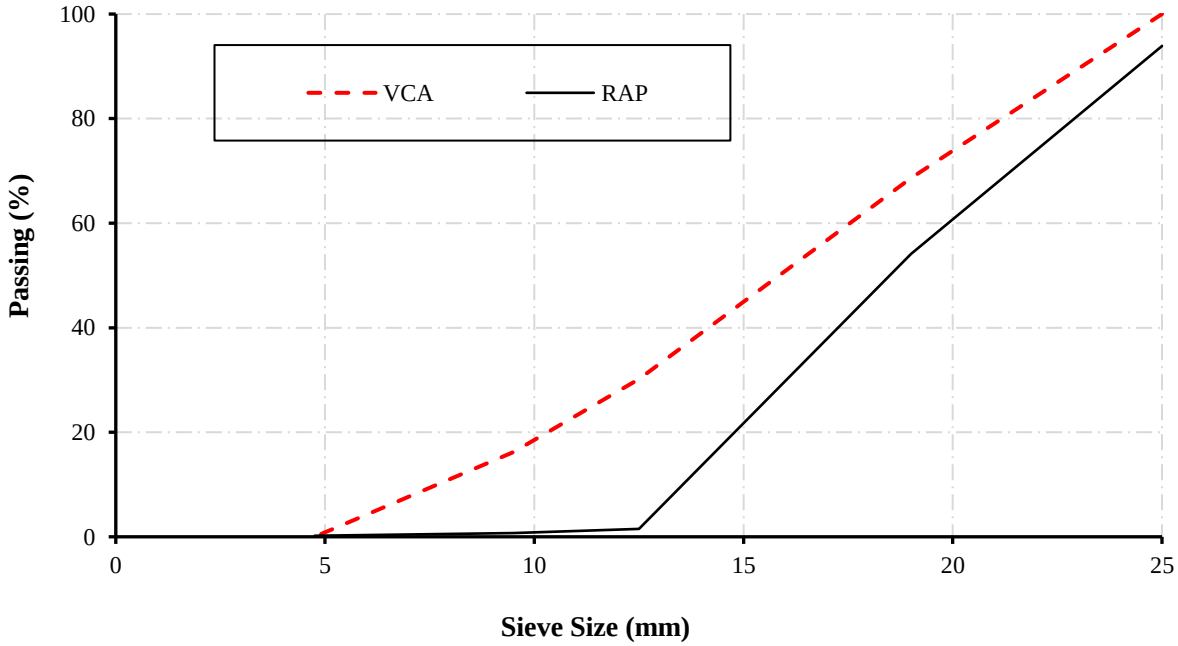

Fig. 2. RAP and VCA gradation

2.5. Mix Design

The controlled mix was designed to achieve class A3 concrete for design strength of 4000 psi compressive strength with water-cement ratio of 0.57 as per National Highway Authority of Pakistan Standards (NHA, 1998). A total of 30 test specimens were prepared in the lab at an average temperature of 26.4 °C, with VCA being replaced by RAP at 0, 25, 50, 75, and 100 % by weight of VCA, with an average slump of 3.5 inches (90 mm). The nomenclatures of an alphabet preceding by a digit, whereas the alphabet represents the type of test and the digit represents the percent replacement of VCA, and proportions of mixes are provided in Table 2. The mix design ratio for 75% and 100% RAP replacement was different from others to avoid honeycombing in concrete specimens. The specimens were cured in a chamber containing fresh drinking water for 28 days.

3. Experimental Investigation

The VCA was replaced with RAP at an increment of 0, 25, 50, 75, and 100 percent by weight. Tests were performed to investigate the concrete specimens' compression strength, splitting tensile strength, flexural strength, and modulus of elasticity. The average value of three specimens was taken to avoid human or machine error. For the investigation of compression and splitting tensile strength, cylindrical specimens with dimensions of 12 × 6 inches (300 × 150 mm) were cast and tested according to ASTM C39 (ASTM C39/C39M, 2003) and ASTM C496 (ASTM C496/C496M-17, 2011), respectively, as shown in Figures 3 and 4. Flexural tests were performed on beams of length 12 inches and 4 × 4 inches cross-sections. The beams were tested using the 3-point loading method (Figure 5) according to ASTM C78 (ASTM C78/C78M-22, 2010).

Two cylinders were tested for MOE under UTM connected to the data logger and strain gauges (Figure 6). UCAM software was used to find the modulus of elasticity. Used sidekick guides to choose the compressive quality according to test method ASTM C39 preceding the test for modulus of elasticity.

Table 2. Mix design detail

Sr. No.	Mix design name	VCA (kg/m^3)	RAP (kg/m^3)	Materials Fine Aggregate (kg/m^3)	Cement (kg/m^3)	Water (kg/m^3)	Ratio
1	CR0	981.9	0.0	811.9	353.9	201.7	
2	CR25	736.4	245.5	810.4	353.9	201.7	1:2.29:2.77
3	CR50	491.0	491.0	810.4	353.9	201.7	
4	CR75	230.9	692.7	870.5	353.9	201.7	1:2.46:2.61
5	CR100	0.0	923.6	870.5	353.9	201.7	
6	TR0	981.9	0.0	811.9	353.9	201.7	
7	TR25	736.4	245.5	810.4	353.9	201.7	1:2.29:2.77
8	TR50	491.0	491.0	810.4	353.9	201.7	
9	TR75	230.9	692.7	870.5	353.9	201.7	1:2.46:2.61
10	TR100	0.0	923.6	870.5	353.9	201.7	
11	FR0	981.9	0.0	811.9	353.9	201.7	
12	FR25	736.4	245.5	810.4	353.9	201.7	1:2.29:2.77
13	FR50	491.0	491.0	810.4	353.9	201.7	
14	FR75	230.9	692.7	870.5	353.9	201.7	1:2.46:2.61
15	FR100	0.0	923.6	870.5	353.9	201.7	

Fig. 3. Compression test

Fig. 4. Splitting tensile test

Fig. 5. Flexural test

Fig. 6. Compression test in UTM

4. Results and Discussion

4.1. Damage Pattern

The damage pattern of specimens under loading was diverse. The cylinders CR0 and CR25 showed cracks under the compression strength test from top to bottom. It showed that there might be a continuous bond between the aggregates. The spalling of concrete in CR25 at the mid-span as shown in Figure 7a, is possibly due to the presence of RAP because these cracking and spalling were noted in all specimens containing RAP. The CR50 specimen had a wider crack opening on its top side shown in Figure 7b. The cracks in CR75 and CR100 were much wider compared to other specimens due to the presence of more RAP aggregates depicted in Figure 8.

(a) Damage/Crack pattern in CR25 **(b)** Damage/Crack pattern in CR50

Fig. 7. Damage/Crack pattern during the compression tests

(a) Damage/Crack pattern in CR75 **(b)** Damage/Crack pattern in CR100

Fig. 8. Damage/Crack pattern during the compression tests

Upon applying loads for the flexural test, the rupture in FR0, FR25, and FR50 was sudden, and the failure was brittle represented in Figure 9. On the other hand, FR75 and FR100 showed ductile failure due to the presence of more RAP shown in Figure 10. Likewise, the greater RAP percentage in the beams contributed to reducing brittleness. The failure was at the middle third of the beam in this case.

During the splitting tensile test, the cracks in the specimen were quite visible. In the case of TR0, there was only a single crack initiated from the top of the cylinder's circular cross-section. The crack initiated in TR25 was similar but was a bit wider revealed in Figure 11. Wide and multiple crack failure was observed in the case of TR50, TR75 and TR100 as shown in Figure 12. These cracks show that aggregates' binding ability was reduced with an increase in RAP contents. During the MOE test, the cracks in R0, R25, and R50 were wider and saturated at the upper loading portion, while R75 and R100 revealed significant cracks from top to bottom and multiple cracks in every direction throughout the circumference as shown in Figure 13.

(a) Damage/Crack pattern in FR25 **(b)** Damage/Crack pattern in FR50

Fig. 9. Damage/Crack pattern during flexural tests

(a) Damage/Crack pattern in FR75 **(b)** Damage/Crack pattern in FR100

Fig. 10. Damage/Crack pattern during flexural tests

(a) Damage/Crack pattern in TR0 **(b)** Damage/Crack pattern in TR25

Fig. 11. Damage/Crack pattern during splitting tensile tests

(a) Damage/Crack pattern in TR50 **(b)** Damage/Crack pattern in TR100

Fig. 12. Damage/Crack pattern during splitting tensile tests

(a) Damage/Crack pattern in R25 **(b)** Damage/Crack pattern in R75 **(c)** Damage/Crack pattern in R100

Fig. 13. Damage/Crack pattern during MOE tests

4.2. Test Results of Hardened Concrete Upholding RAP

4.2.1. Compressive Test

The compressive strength of the conventional concrete i.e., CR0 was more than 4000 psi, and the compressive strength of concrete made after certain replacement of VCA with RAP decreased. The results show a decrease in compressive strength of the modified concrete. The percent reduction in compressive strength of RAP-modified concrete varies from 28% for 25% replacement to a maximum of 57% for 100% replacement. This reduction in compressive strength is mainly attributed to the presence of agglomerated particles containing lumps of different sizes of particles. Moreover, the RAP contains aged asphalt which makes the asphalt film harder and stiffer. This may also be the possible reason for the reduction of compressive strength of the RAP induced concrete.

4.2.2. Flexural Test

The results obtained from flexural test also showed a decrease in flexural strength of concrete with the increase in replacement of VCA with RAP. The results showed a maximum decrease of approximately 40% in flexural strength for 100% RAP replacement and a minimum decrease of approximately 10% for 25% replacement. The incorporation of RAP in concrete has

also reduced the flexural strength however the reduction is comparatively lower than the compressive strength. This reduction might also be the reason of the presence of agglomerated particles. Moreover, the presence of particles coated with bitumen might have reduced the bond between the RAP and VCA due to which the flexural strength has reduced.

4.2.3. Split Tensile Test

The trend of strength loss in split tensile strength was somehow identical to that of compressive strength. The decrease was minimum at 25% RAP replacement showing 21% decrease while for 100% replacement, it showed a decrease of 51%. The strength reduction pattern was somehow similar to that of compressive strength. However, the percentage reduction in split tensile strength is lower than that of compressive strength. This might be due to the fact that the RAP is obtained from flexible pavement which possesses flexibility thus inhibiting tensile strength.

4.2.4. Modulus of Elasticity (MOE)

The Modulus Of Elasticity (MOE) is a very important property considered for concrete samples. Minimum decrease of 25% had been observed for RAP replacement of 25% while a maximum decrease of 84% had been observed for RAP replacement of 100%. Moreover, the ductility being more makes R75 less brittle. The ductility path followed by the graph came out to be the highest for R100 sample. It shows that the ductility increases with an increase in RAP content and vice versa. The increase in elasticity is due to the presence of RAP which is obtained from flexible pavement. The RAP possesses elasticity thus making the RAP induced concrete more ductile as the RAP content is increased.

Table 3. Mechanical properties of RAP modified concrete samples

RAP (%)	Compression average (psi)	Flexure average (psi)	Splitting tensile average (psi)	Modulus of elasticity average (psi)
0	4023	630	347	175440
25	2905	566	274	131069
50	2401	508	267	125390
75	1965	467	190	33150
100	1715	376	168	28500

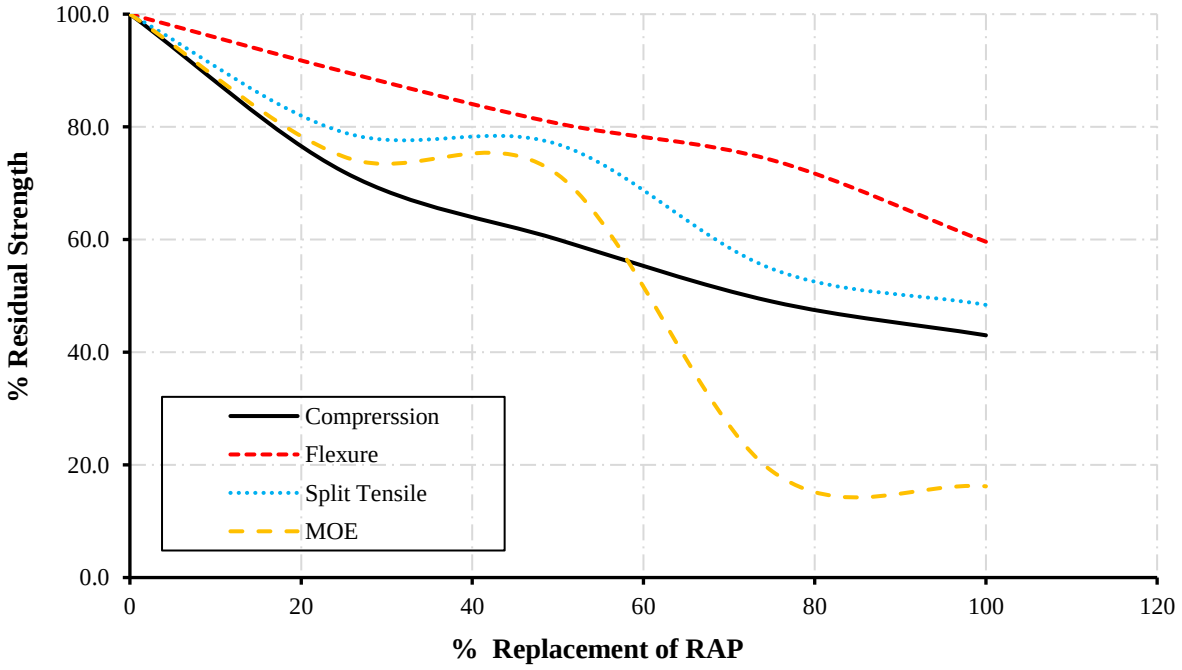

Fig. 14. Percentage residual strength vs percent RAP replacement

5. Conclusions

RAP material is a waste product produced after the demolishing of old pavements. The utilization of RAP in concrete is an innovative technique. This paper addresses the use of RAP in concrete as an alternative way of disposal of waste. The mechanical properties such as compressive strength, flexural strength, split tensile strength and modulus of elasticity decrease with the increase in the percent replacement of RAP in virgin concrete aggregates. The decrease was maximum at replacement of 100% of VCA with RAP. Minimum percent decrease was observed at 25% replacement. At all replacements, RAP concrete mixes had lower strength parameters such as compressive strength, flexural strength, and splitting tensile strength as compared to control concrete mixes. However, mixes with 25% replacement achieved characteristic compressive strength of 2900 psi. Concerning the percentages of RAP content, the extent of the reduction in strengths was investigated. The maximum reduction in compressive, flexural, and splitting tensile strengths at 100% replacement of RAP was 57 %, 40.4%, and 51.6%, respectively. However, the optimum replacement of RAP aggregate is found to be 25% replacement.

6. References

ASTM C39/C39M. (2003). *Standard test method for compressive strength of cylindrical concrete specimens*, ASTM Standard Book, (pp. 1-5), ASTM International, West Conshohocken, PA, United States.

ASTM C78/C78M-22. (2010). *Standard test method for flexural strength of concrete (using simple beam with third-point loading) 1*, ASTM Standard Book, (pp. 1-4), ASTM International, West Conshohocken, PA, United States, https://doi.org/10.1520/C0078_C0078M-22.

ASTM C496/C496M-17. (2011). *Standard test method for splitting tensile strength of cylindrical concrete specimens ASTM C-496*, ASTM International, (pp. 1-5), ASTM Standard Book, (pp. 1-5), ASTM International, West Conshohocken, PA, United States.

Australian Asphalt Pavement Association (AAPA). (2018). *Reclaimed Asphalt Pavement (RAP) management plan*, National Technology and Leadership Committee, Port Melbourne, Australia.

European Asphalt Pavement Association (EAPA). (2014). *Asphalt the 100% recyclable construction product*, EAPA, Brussels, Belgume.

Huang, B., Li, G., Vukosavljevic, D., Shu, X. and Egan, B.K. (2005) "Laboratory investigation of mixing hot-mix asphalt with reclaimed asphalt pavement", *Journal of Transportation Research Board*, 1929(1), 37-45, https://doi.org/10.3141/1929-05.

Izaks, R., Rathore, M., Haritonovs, V. and Zaumanis, M. (2022). "Performance properties of high modulus asphalt concrete containing high reclaimed asphalt content and polymer modified binder", *International Journal of Pavement Engineering*, 23(7), 2255-2264, https://doi.org/10.1080/10298436.2020.1850721.

Izaks, R., Haritonovs, V., Klasa, I. and Zaumanis, M.J.P.E. (2015). "Hot mix Aasphalt with high RAP content", *Procedia Engineering*, 114, 676-684, https://doi.org/10.1016/j.proeng.2015.08.009.

Jahanbakhsh, H., Karimi, M.M., Naseri, H. and Nejad, F.M. (2020). 'Sustainable asphalt concrete containing high reclaimed asphalt pavements and recycling agents: Performance assessment, cost analysis, and environmental impact", *Journal of Cleaner Production*, 244, 118837, https://doi.org/10.1016/j.jclepro.2019.118837.

Jindal, A. and Ransinchung, G.D. (2022). "Behavioural study of incorporation of recycled concrete aggregates and mineral admixtures in pavement quality concrete", *Civil Engineering Infrastructures Journal*, 55(2), 351-372, https://doi.org/10.22059/CEIJ.2022.326564.1766.

National Highway Authority (NHA). (1998). *General specifications*, Islamabad, Pakistan.

Pradyumna, T.A., Mittal, A. and Jain, P.K. (2013). "Characterization of Reclaimed Asphalt Pavement (RAP) for use in bituminous road construction", *Procedia, Social and Behavioral Sciences*, 104, 1149-1157, https://doi.org/10.1016/j.sbspro.2013.11.211.

Rathore, M., Haritonovs, V., Meri, R.M. and Zaumanis, M. (2022). "Rheological and chemical evaluation of aging in 100% reclaimed asphalt mixtures containing rejuvenators", *Construction and Building Materials*, 318, 126026, https://doi.org/10.1016/j.conbuildmat.2021.126026.

Reyes-Ortiz, O., Berardinelli, E., Alvarez, A.E., Carvajal-Muñoz, J. and Fuentes, L.G. (2012). "Evaluation of hot mix asphalt mixtures with

replacement of aggregates by Reclaimed Asphalt Pavement (RAP) material", *Procedia, Social and Behavioral Sciences*, 53, 379-388, https://doi.org/10.1016/j.sbspro.2012.09.889.

Sarir, M., Khan, R., Alam, M., Khan, M.T. and Imran, W. (2022). 'Performance evaluation of asphalt concrete mixtures using bagasse ash as filler", *Iranian Journal of Science and Technology, Transactions of Civil Engineering*, 46(2), 1553-1570, https://doi.org/10.1007/s40996-021-00641-8.

Southern African Bitumen Association (SABITA). (2019). *Use of reclaimed asphalt in the production of asphalt MANUAL 36/TRH 21*, SABITA: Western Cape, South Africa.

Tarsi, G., Tataranni, P. and Sangiorgi, C. (2020). "The challenges of using reclaimed asphalt pavement for new asphalt mixtures: A review", *Materials*, MDPI AG., 13(18), 4052, https://doi.org/10.3390/ma13184052.

Valdés, G., Pérez-Jiménez, F., Miró, R., Martínez, A. and Botella, R. (2011). "Experimental study of recycled asphalt mixtures with high percentages of Reclaimed Asphalt Pavement (RAP)", *Construction and Building Materials*, 25(3), 1289-1297, https://doi.org/10.1016/j.conbuildmat.2010.09.016.

Xiao, F., Amirkhanian, S. and Juang, C.H. (2007). "Rutting resistance of rubberized asphalt concrete pavements containing reclaimed asphalt pavement mixtures", *Journal of Materials in Civil Engineering*, 19(6), 475-483, https://doi.org/10.1061/(ASCE)0899-1561(2007)19:6(475).

Zhao, S. Huang, B., Shu, X. and Woods, M. (2013). "Comparative evaluation of warm mix asphalt containing high percentages of reclaimed asphalt pavement", *Construction and Building Materials*, 44, 92-100, https://doi.org/10.1016/j.conbuildmat.2013.03.010.

Zhao, S., Huang, B., Shu, X., Jia, X. and Woods, M. (2012). "Laboratory performance evaluation of warm mix asphalt containing high percentages of RAP", *Journal of the Transportation Research Board*, 2294(1), 98-105, https://doi.org/10.3141/2294-11.

Zhu, J., Ma, T., Fan, J., Fang, Z., Chen, T. and Zhou, Y. (2020). 'Experimental study of high modulus asphalt mixture containing reclaimed asphalt pavement", *Journal of Cleaner Production*, 263, 121447, https://doi.org/10.1016/j.jclepro.2020.121447.

Zhu, J., Ma, T. and Fang, Z. (2020). "Characterization of agglomeration of reclaimed asphalt pavement for cold recycling", *Construction and Building Materials*, 240, 117912, https://doi.org/10.1016/j.conbuildmat.2019.117912.

Civil Engineering Infrastructures Journal 2023, 56(2): 393-414
DOI: 10.22059/CEIJ.2023.347012.1861

RESEARCH PAPER

Evaluating UHP-SFRCs Performance under Flexural and Tensile Loadings and Aggressive Environment by Assessing the Applicability of Different Constituent Materials in UHPC Production

Pourjahanshahi, A.[1], Madani, H.[2*] and Khaghani Boroujeni, A.[1]

[1] M.Sc., Department of Civil and Surveying Engineering, Graduate University of Advanced Technology, Kerman, Iran.
[2] Associate Professor, Department of Civil and Surveying Engineering, Graduate University of Advanced Technology, Kerman, Iran.

Received: 12 Aug. 2022; Revised: 20 Jan. 2023; Accepted: 27 Feb. 2023

ABSTRACT: Ultra-High Performance Concrete (UHPC), known for its superior mechanical and durability properties, is an appropriate material for different applications such as building and bridge construction. Investigating the possibility of UHPC production using available materials is an engineering challenge. This paper evaluates the applicability of some materials in making UHPC and the effectiveness of several parameters on the compressive strength of UHPCs. Then, by choosing the mixture yielding the highest compressive strength, the durability and mechanical properties of the mixture with 0-2.5% crimped steel fiber are investigated. The tests include compressive strength, flexural and tensile parameters, length change, rapid chloride ion migration, sorptivity, porosity, and sulfate resistance. The results reveal that the pozzolanic activity of silica fume and its synergetic effect with glass powder lead to the highest compressive strength. Moreover, it makes it possible to easily obtain a strength higher than 150MPa. Utilization of 2.5% crimped steel fiber in UHPC mixtures remarkably enhanced mechanical performance so that the flexural and tensile strength were increased by about 95% and 25% compared to the plain UHPC, respectively. However, the incorporation of fibers increased the UHPC permeability.

Keywords: Chloride Ion Diffusivity, Flexural and Tensile Performance, SEM Image, Supplementary Cementitious Materials, UHPC Constituents.

1. Introduction

Ultra-High Performance Concrete (UHPC) is defined as a cement composite with a minimum compressive strength of 120 MPa, as described in ASTM C1856. Compared to other concrete types, the UHPC has enhanced energy absorption and mechanical properties due to the high volume content of supplementary cementitious materials, relatively high volume fraction of fibers, and low water-to-binder ratio (Hung et al., 2021). In addition, the low permeability of UHPCs, especially in sulfate and chloride environments, has increased the service life of such concretes and reduced their maintenance costs. The self-compacting characteristic of UHPCs

* Corresponding author E-mail: h.madani@kgut.ac.ir

and the ability to eliminate the need for reinforcing steel simplify its construction (Ferdosian and Camões, 2021). Tall structures, bridge construction, structural and non-structural elements, rehabilitation works, machine parts, and military structures are important applications of UHPC (Bajaber and Hakeem, 2021).

Cement production generates 7% of the worldwide CO_2 emission and is the largest carbon-emitting industrial. This production process releases about one ton of CO_2 per ton of cement into the atmosphere (Shubbar et al., 2020). Hence, cement production causes great damage to the environment. A possible sustainable solution to reduce cement consumption in the concrete production industry is partially replacing the cement content with Supplementary Cementitious Materials (SCMs), especially in UHPCs, which use a high volume of cement in production (800 - 1100 kg/m^3, about three times more than ordinary concretes) (Hung et al., 2021). SCMs are often used in concrete mixtures to improve workability, enhance durability and increase strength through hydraulic or pozzolanic activity as well as filling ability. The study by Wu et al., (2016) showed that 15 - 25% silica fume in the UHSC matrix accelerated cement hydration and increased compressive and flexural strength by about 10 - 25% after 28 days; higher utilization of silica fume (more than 25%) reduced flowability and decreased strength. Limestone powder provided nucleation sites for Calcium Silicate Hydrate (C-S-H) precipitation and accelerated cement hydration at early ages. It also reacted with tricalcium silicate and calcium aluminates to produce calcium carbosilicate hydrate and calcium carboaluminates. The mixtures with 5% coal waste powder had the highest compressive strength (about 10%) in comparison with the plain mixture at 90 days and higher substitution of coal waste powder (more than 20%) led to lower compressive strength (Modarres et al., 2018). Van Tuan et al. (2011) indicated that adding 30% rice husk ash had a compressive strength comparable with that of silica fume mixtures. However, the combination of 10% rice husk ash and 10% silica fume provided a synergistic effect to obtain optimum strength. Glass powder increased the dissolution rate of cement so that the reacted cement in the mixture with glass powder was considerably higher than the one without glass powder (Jain et al., 2020). The concrete mixtures with copper slag presented an improved durability performance and greater splitting tensile strength (Wang et al., 2021).

Although many researchers have examined the applicability of SCMs in different concrete types, more research is required to investigate the replacement ability of cement with industrial wastes or natural materials in UHPC production. This research provides comprehensive information on some materials used in UHPCs, effective parameters on the compressive strength, and performance of UHP-FRCs under different mechanical and durability tests. The current study includes two parts. First, the effects of several parameters such as types of aggregate grading, aggregate size, cement type, and aggregate type are investigated. The replacement ability of some materials such as silica fume, copper slag, coal waste, silica flour, and pumice is also evaluated. In addition, the materials' pozzolanic activity and the synergistic effect are investigated. Finally, the optimum mixture which yielded the maximum compressive strength is proposed as the final UHPC. Then, the performance of the UHPC with 0 - 2.5% crimped steel fiber is evaluated under compressive strength, flexural and tensile parameters, length change, rapid chloride ion migration, sorptivity, porosity, and sulfate resistance tests.

2. Materials

Three types of Portland cement (I-52.5, I-42.5 and II, categorized with the EN 197-1 standard) with the chemical composition and physical properties represented in Table

1 were used. Two types of sand, garnet and silica sand, were also investigated. Table 2 shows the dimension range and physical properties of the sands. The 7 Mohs hardness of garnet sand makes it an appropriate material for different applications such as water jet cutting, glass polishing, sandblasting, and abrasion-resistant concrete production (Muttashar et al., 2018); compared with silica sands, it has higher specific gravity and hardness and is relatively resistant to alterations (Olson, 2001). Table 3 lists the chemical composition and physical properties of the used SCMs. The materials were respectively supplied from: a) silica fume: Azna Ferroalloy Company, b) pumice: natural pozzolan of Khash; c) coal waste: Zarand Coal Washing; d) copper slag: Sarcheshmeh Copper Industries; E) silica flour: Kerman Stone Mines; and F) glass powder: Glass Recycling Companies. All materials were supplied from Iran. The copper coating of crimped steel fiber avoids corrosion problems (Figure 1) and has excellent potential to enhance interface bonding (Mandal et al., 2008).

Table 1. Chemical composition and physical properties of the cement (based on EN 197-1)

Chemical and physical parameters	Quantity (%)		
	Type II	**Type I-42.5**	**Type I-52.5**
SiO_2	21.74	20	22.8
AL_2O_3	5	4.9	4.2
Fe_2O_3	4	5.5	0.42
CaO	63.04	62	65.2
MgO	2	1.8	2.5
SO_3	2.3	2.9	2
C_3S	45.5	53	58.1
C_2S	28	24	25.2
C_3A	6.5	8	11.1
C_4AF	12.2	17	1.37
LOI (%)	1.3	1.5	1.5
Blain (cm^2/g)	2900	2800	3850
Compressive Strength (MPa)	38	46	55

Table 2. Physical properties of the aggregates

ID	Material	SSD (%)	Specific gravity (Kg/m^3)	Rang of aggregate(mm)
SS1	Silica sand	0.94	2570	0.2-2.36
SS2	Silica sand	1.05	2565	0.08-1.18
SS3	Silica sand	0.51	2550	0.001-0.05
GS1	Garnet sand	0.87	3200	0.6-2.36
GS2	Garnet sand	1.35	3230	0.08-1.18

Table 3. Chemical composition and physical properties of the supplementary cementitious materials

Chemical composition	Quantity (%)					
	Silica fume	**Glass powder**	**Coal waste**	**Copper slag**	**Silica flour**	**Pumice**
SiO_2	93	66.5	34.8	34	98	63.4
AL_2O_3	0.9	0.64	14.53	2	0.2	18.45
Fe_2O_3	0.8	0.44	3.89	47	0.32	1.2
CaO	1	11.5	0.513	6.5	0.06	5.44
MgO	1.25	4.4	0.868	-	0.01	0.9
K_2O	0.3	0.39	2.39	-	0.05	2.06
NaO_2	0.4	15.8	0.27	-	0.05	3.57
MnO	0.5	-	0.02	3	0.005	-
L.O.I	1.7	0.1	40.96	0.1	0.3	2.88
Physical characterize						
Blain (m^2/g)	20	0.34	0.84	0.68	0.91	3.9
Density (g/cm^3)	2.2	2.52	2.15	3.4	2.65	2.71

Properties:
Length (mm): 25
Diameter (mm): 0.7
Aspect ratio: 36
Tensile strength (MPa):1150
Form: Crimped

Fig. 1. Type and properties of the fiber

3. Experimental Program

3.1. Mechanical Tests

3.1.1. Compressive, Flexural and Tensile Tests

Compressive strength was determined per the ASTM C109 standard method using cube molds at 3, 7 and 28 days. Moreover, a uniform loading rate of 180 kg/s was adopted.

The prism specimens were molded to determine flexural parameters. Figure 2 depicts the important data obtained from the flexural test, including first-crack strength, MOR (modulus of rupture: the stress corresponding to the peak force), load drop (occurring after cracking), and flexural toughness in different deflections. The I5, I10, and I20 are defined as flexural toughness indices. The flexural parameters were evaluated based on ASTM C78 and ASTM C1018 methods. In addition, according to the details provided in Figure 3, dog bone specimens were employed to determine the tensile performance of UHP-FRCs. Tensile toughness was also evaluated based on the ASTM C1018 standard test method. An INSTRON device with a capacity of 300 kN was used to perform the flexural and tensile tests.

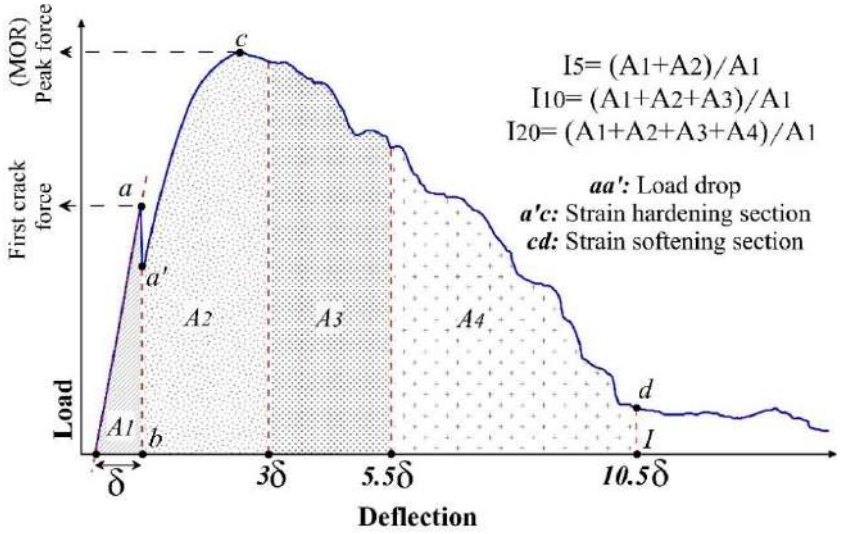

Fig. 2. Schematic diagram of flexural behavior of the UHP-FRC specimen

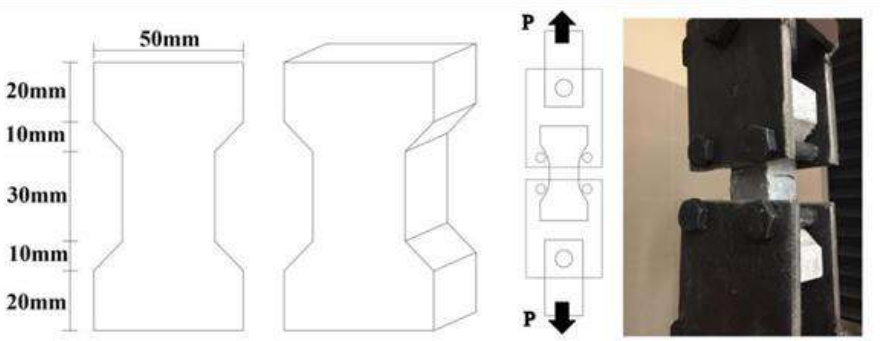

Fig. 3. Schematic presentation and an image of the tensile test

3.1.2. Length Change

The Length change of UHPC was measured using prismatic specimens of 25 × 25 × 285 mm in accordance with ASTM C490. After demolding the specimens, 24 h after casting, they were cured in a standard curing room with Relative Humidity (RH) of 98% ± 2% and a temperature of 20 ± 1 ℃ for 48 h. Afterwards, they were transferred to a chamber with a controlled RH of 50 ± 5% and temperature of 20 ± 2 ℃ until the testing age. The length change values calculated based on Eq. (1) were defined as the length change at different ages.

$$L = \frac{(L_x - L_i)}{G} \quad (1)$$

where: L: is the change in length at a specified age (x); %, Lx: is the comparator reading of specimen at age x minus comparator reading of reference bar at age x; in millimeters, Li: is the initial comparator reading of specimen minus comparator reading of reference bar at the same time; in millimeters; and G: is the nominal gauge length, 250 mm.

3.2. Durability Tests

3.2.1. Rapid Chloride Migration Test (RCMT)

The Rapid Chloride Migration Test (RCMT) method as per the NT BUILD 492 standard was used to evaluate the durability of concrete against diffusion of chloride ions. In this test, the cylindrical specimens were secured with two clamps after fitting in a rubber sleeve. The sealed specimens were placed on plastic support in a reservoir with 10% NaCl solution (Figure 4). Afterwards, 300 mL of 0.3-M NaOH solution was poured inside part of the rubber sleeves. The voltage magnitude was set to 60 V for 96 h, based on the initial voltage and the electrical current. The RCMT coefficient was determined according to Eq. (2):

$$D_{nssm} = \frac{0.0239(273+T)\times L}{(U-2)\times t} \times (X_d - 0.0238) \times \sqrt{\frac{(273+T)\times L \times X_d}{U-2}} \quad (2)$$

where $Dnssm$: is the non-steady state migration coefficient ($\times 10^{-12}$ m^2/s), U: is the applied voltage (V), T: is the average value of the initial and final temperatures in the anolyte solution (°C), L: is the thickness of the specimen (mm), X_d: is the average value of the penetration depth (mm), and t: is the test duration (hour).

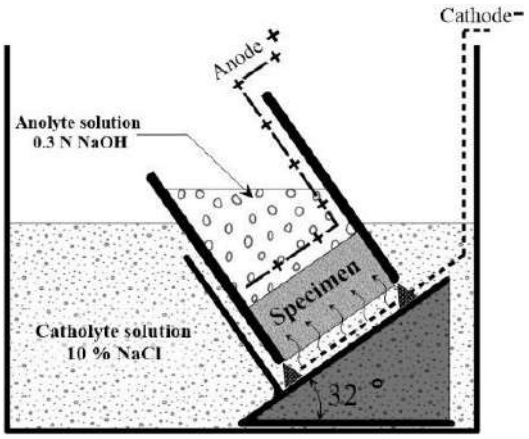

Fig. 4. Schematic presentation of the RCMT test

3.2.2. Sorptivity Test

Based on the standard test method of ASTM C1585, the sorptivity of the concrete mixtures was measured. In this test, the specimens were oven dried at 100 °C until they reached a constant weight. Afterwards, the lateral surfaces of the specimens were coated with a sealer to prevent lateral water absorption. Subsequently, they were submerged in water at a depth of 3 mm. Before and after submerging, the weight of UHPC specimens was determined in time intervals from 1.5 to 360 min. Finally, the water absorption rate was estimated utilizing Eq. (3).

$$I = \frac{m_t}{a.d} \quad (3)$$

where I: is the rate of water absorption, m_t: is the change in specimen mass (g) at time t, a: is the exposed area of the specimen in mm^2, and d: is the density of the water in g/mm^3. The initial water absorption rate ($mm/s^{1/2}$) is defined as the slope of the line with the best fit to I plotted against the square root of time using all the points from 1 min to 6 h. Calculating the secondary

water absorption rate (mm/s$^{1/2}$) is similar to the initial one, but the water absorptions from days 1 to 7 days were used.

3.2.3. Permeable Pore Volume

Cylindrical specimens were used to determine the permeable pore volume (porosity) based on ASTM C642. In this method, the specimens were oven-dried at 100 °C to reach constant weight. Subsequently, the dried specimens were immersed in water until no significant increase in weight was obtained. Eq. (4) was used to calculate the permeable void contents of UHPCs.

$$\text{Permeable voids} = (1 - \frac{g_b}{g_a}) \times 100 \quad (4)$$

where g_b: is the dry bulk density (T/m^3) and g_a: is the apparent density (T/m^3). Three specimens were used to obtain a reliable value for each variable.

3.2.4. Resistance to Sulfuric Acid Attack

Aggressive environments such as chemical waste, sewage systems, and groundwater can cause significant damage to the concrete and decrease durability (Jeon et al., 2020). In order to evaluate the resistance of UHPCs against external sulfuric acid attack, three 50 mm cubic specimens were cured under standard conditions for 28 days. Afterwards, the specimens were immersed in 5% (v/v) aqueous sulfuric acid solution and their weight loss at different times was recorded from the age of 28 days to 56 days.

3.3. SEM Micrographs

SEM images were employed to evaluate the ITZ (interfacial transition zone) of concrete. To this end, the SEM samples containing fiber were removed from flexural specimens and soaked in acetone in order to stop hydration. Next, after drying in an oven at 60 ◦C for 24 h, they were covered with aluminum foil. The SEM images were used to confirm the other test results.

3.4. Pozzolanic Activity of Materials

An electrical conductivity method was adopted to evaluate the pozzolanic activity of the materials. For this purpose, an unsaturated lime solution was prepared by dissolving 120 mg of Ca $(OH)_2$ in 150 mL of deionized water. Then, under constant stirring, 5 g of pozzolanic material was added to the solution, and variations in pH and electrical conductivity of the solution with time (B_t) were recorded. The procedure was done again for the pozzolanic material added into 250 mL of deionized water (A_t). The corrected conductivity curve (Ca_t) was obtained by the equation of $(Ca)_t = B_t - A_t$. Eventually, LC (relative loss in corrected conductivity) was calculated as the percentage with respect to the initial conductivity value of lime-water solution, the solution before the addition of pozzolanic material.

$$LC_t(\%) = \frac{(Ca)_0 - (Ca)_t}{(Ca)_0} \quad (5)$$

where (LC_t): is the percentage of loss in conductivity for a given time t, $(Ca)_0$: is the conductivity of lime solution before the addition of pozzolanic materials, and $(Ca)_t$: is the absolute loss in conductivity for materials/lime suspension at a given time t.

4. Investigating the Effectiveness of Some Parameters on the Compressive Strength of UHPC

Achieving an optimized particle packing of solid concrete constituents with superior mechanical and durability performance has been the target of studies such as Liu et al. (2019) and De Larrard and Sedran (2002). In this research, all efforts were made to investigate the effectiveness of some parameters on the UHPC mix design. Several experiments were performed for this purpose. The findings of other researchers were also used to support the results. Considering the most important characteristic of UHPCs, high compressive strength, all attempts were made to improve

this characteristic. After reaching the final mixture, the durability and mechanical properties of the final UHPC mixture with 1.5 and 2.5% crimped steel fiber were evaluated.

4.1. Aggregate Dimension, Aggregate Gradation Curve, and Aggregate to Binder Ratio

Based on research on ultra-high performance concretes (Pourjahanshahi and Madani, 2021; Wille et al., 2012), the supplementary cementitious material of silica fume is a main part of UHPC. At the first attempt, using the results of other studies (Wille et al., 2012; Wille and Boisvert-Cotulio, 2015), a proportion of 0.9:0.1:1.2 (cement: silica fume: sand) was chosen as the basic mix proportion. Then, the effect of three dimensions of silica sand (SS1 to SS3) introduced in Table 2 was investigated.

The results of Table 4 show that the aggregate size changes did not remarkably affect the compressive strength. However, the high strengths were attributed to the aggregate size of SS3, SS2, and SS1, respectively. Based on the diameter range of the aggregates and the results, choosing an aggregate grading rich in fine particles is very likely to help achieve an aggregate packing with minimum voids or maximum density.

Choosing the appropriate aggregate grading is a key point in making concrete with high durability and mechanical properties (Hunger, 2010; Brouwers and Radix, 2005). The first attempts to achieve this goal date back to about 100 years ago. Fuller and Thomsen (1907) proved that using a continuous geometric grading of aggregates in concrete mixtures could enhance concrete properties. Based on the investigations by Fuller and Thompson (1907) and Andreasen and Andersen (1930), achieving minimum porosity in concrete could theoretically result from Eq. (6).

$$P(D) = (\frac{D}{D_{max}})^q \quad (6)$$

where $P(d)$: is the percentage of aggregates passing through a sieve with the nominal mesh size of d (mm), $d_{\max}$ (mm): is the nominal maximum aggregate size, and q: is the distribution modulus.

The minimum particle size of aggregate was not considered in the equation, while in reality, it must be limited to a specific size. Therefore, based on Andreasen and Andersen's Equation, Funk and Dinger (2013) proposed a modified model. Based on the model (Eq. (7)), the proportion of aggregate particles could be specified.

$$p(D)=\frac{D^q-D_{min}^q}{D_{max}^q-D_{min}^q} \quad (7)$$

where d_{min} (mm): is the nominal minimum aggregate size.

Nowadays, the model is widely used for grading aggregate materials or concrete constituents in designing different concretes such as normal density concretes (Hunger, 2010) and lightweight concretes (Yu et al., 2013). The q parameter in Eq. (7) shows the proportion between the fine and coarse aggregate particles. By changing the value of q, different aggregate materials grading can be provided. The high values of the distribution modulus (more than 0.5) lead to a coarse mixture, and the low values (less than 0.25) result in aggregate grading riched in fine particles (Hüsken and Brouwers, 2008). The investigations by Brouwers and Radix (2005) and Hunger (2010) showed that using q in the range of 0.22 - 0.25 leads to optimal concrete packing for UHPC. Thus, in this research, the value of q = 0.23 was applied in Funk and Dinger's model to grade the aggregate materials (mixture F23). In order to check the validity of these hypotheses, two mixtures of F35 and F50 with a distribution modulus of 0.35 and 0.50 were also examined. On the other hand, the aggregate-to-binder ratio is another important parameter that influences concrete characteristics. The mixtures of A0 to A6 were examined using the ratio of 1 to 6, respectively.

Table 4. Effect of aggregate dimension

Mixture	Type of cement	ID (diameter range)	Cement	Silica fume	Sand	W/B*	C.Strength (Mpa)
A1	II	SS1 (0.2-2.36)	0.9	0.1	1.2	0.25	88
A2	II	SS2 (0.08-1.18)	0.9	0.1	1.2	0.25	89
A3	II	SS3 (0.001-0.05)	0.9	0.1	1.2	0.25	91

***** Water to binder ratio

Table 5. Effect of aggregate gradation curve and aggregate to binder ratio on compressive strength

Mixtures	Type of cement	Cement	Silica fume	Sand	W/B*	C.Strength (MPa)
F23	**II**	**0.9**	**0.1**	**1.2**	**0.25**	**94**
F35	II	0.9	0.1	1.2	0.25	86
F50	II	0.9	0.1	1.2	0.25	78
A0	II	0.9	0.1	1.0	0.25	92
A1	II	0.9	`0.1	1.1	0.25	94
A2	II	0.9	0.1	1.2	0.25	94
A3	II	0.9	0.1	1.3	0.25	99
A4	**II**	**0.9**	**0.1**	**1.4**	**0.25**	**102**
A5	II	0.9	0.1	1.5	0.25	98
A6	II	0.9	0.1	1.6	0.25	97

***** Water-to-binder ratio

Comparing the results of Tables 4 and 5 shows that higher compressive strength resulted from mixtures using the modified Funk and Dinger model in the grading aggregate materials than mixtures with single-size aggregates (about 3 - 6%). In addition, using a lower distribution modulus value (q) leads to higher compressive strength. The enhancement was attributed to the decreasing maximum aggregate size and increasing fine particles in aggregate grading, resulting in a dense microstructure and decreased crack width (Brouwers, 2006). On the other hand, the aggregate-to-cement ratio of 1.4 led to the highest compressive strength. It indicates that the best packing density of concrete was achieved when the weight of aggregate materials in the mixture was 40% more than the binder weight.

4.2. Effect of Type and Replacement Percentage of Different Supplementary Cementitious Materials

The Supplementary Cementitious Materials (SCMs) consist of a wide range of materials used in concrete. Generally, the SCMs include industrial waste products, natural pozzolans, and minerals (Skibsted and Snellings, 2019). SCMs can alter hardened concrete properties through pozzolanic or hydraulic activity. In addition, the fine particles of SCMs could enhance the packing density of concrete mixtures through the filling effect. The pozzolanic materials as a partial replacement of Portland cement in blended cement are siliceous or siliceous and aluminous materials that have little or no chemical reactivity. However, in the presence of moisture, they react with calcium hydroxide $Ca(OH)_2$ (the hydration product of Portland cement) in the concrete environment and form Calcium Silicate Hydrate gel (C–S–H) (pozzolanic activity). Some materials, like blast furnace slag, have varying self-cementitious properties (hydraulic activity) (Skibsted and Snellings, 2019). In addition, inert materials such as silica flour physically improve the gradation of aggregates and reduce the permeability of concrete (filling effect) (Lawrence et al., 2005; Celik and Marar, 1996).

The methods used to assess the pozzolanic activity of materials are categorized into direct and indirect methods (Pourkhorshidi, 2013). In direct methods, the presence of $Ca(OH)_2$ is monitored by time as the pozzolanic reaction proceed. X-ray diffraction (XRD) and thermo-gravimetry (TG) are examples of these methods. Indirect methods measure a property of samples or materials that shows

the extent of pozzolanic activity. Tests such as compressive strength and electrical conductivity are in this category (Pourkhorshidi, 2013).

In this research, five SCMs were investigated: Silica Fume (SF), Copper Slag (CS), Coal Waste (CW), Silica Flour (SL), and pumice (PU). The mixtures containing the SCMs are presented in Table 6. In the mixtures, the SCMs were substituted with cement at the percentages of 0, 10, 20, and 30%. The spread value of the mixes was adapted in the range of 190 - 20 mm using a superplasticizer. Furthermore, the control mixtures of C1 to C5 were prepared on five different days. The investigation focused on the optimal percentage of SCMs and their pozzolanic activity potential in UHPC.

Table 6 shows that the utilization of 10% silica fume, 10 to 30% copper slag, and 10% silica flour led to higher compressive strength compared to the plain mixture. Substitution of 10 to 30% copper slag and pumice resulted in lower strength. The compressive strength enhancement provided by the replacement of cement with different SCMs is due to two major reasons: 1) high rate of pozzolanic reactivity; 2) filling effect, whereby the fine particles of SCMs physically fill the void space in the aggregate skeleton effectively and lead to a dense packing of aggregate materials in concrete. Previous studies did not report hydraulic activity for the five materials investigated in this research (Thomas, 2013; Ambily et al., 2015).

An electrical conductivity test was carried out to investigate the pozzolanic activity of SCMs. The LC parameter in Figure 5 demonstrates the reactivity potential of the material with calcium hydroxide with time. The SCMs led to higher LC values, implying that both Ca^{2+} and OH^- ions concentrations were decreased. The results showed that, after 120 minutes, the value of relative loss in conductivity (LC) reached 32%, 26%, 20%, and 15% by adding silica fume, coal waste, pumice, and copper slag/silica flour, respectively.

Table 6. Compressive strength of specimens with different dosages and types of SCM at 28 days

Mixtures	Type of cement	Pozzolanic material	Cement	Pozzolan	Sand	W/B*	C.Strength (MPa)
C 1	II	-	1	0	1.4	0.25	86
SF 10	**II**	**Silica fume**	**0.9**	**0.1**	**1.4**	**0.25**	**102**
SF 20	II	Silica fume	0.8	0.2	1.4	0.25	74
SF 30	II	Silica fume	0.7	0.3	1.4	0.25	63
C 2	II	-	1	0	1.4	0.25	84
CS 10	II	Copper slag	0.9	0.1	1.4	0.25	97
CS 20	II	Copper slag	0.8	0.2	1.4	0.25	101
CS 30	II	Copper slag	0.7	0.3	1.4	0.25	92
C 3	II	-	1	0	1.4	0.25	85
CW10	II	Coal waste	0.9	0.1	1.4	0.25	76
CW20	II	Coal waste	0.8	0.2	1.4	0.25	65
CW30	II	Coal waste	0.7	0.3	1.4	0.25	59
C4	II	-	1	0	1.4	0.25	88
SP 10	II	Silica flour	0.9	0.1	1.4	0.25	91
SP 20	II	Silica flour	0.8	0.2	1.4	0.25	78
SP 30	II	Silica flour	0.7	0.3	1.4	0.25	76
C 5	II	-	1	0	1.4	0.25	85
NP 10	II	Pumice	0.9	0.1	1.4	0.25	63
NP 20	II	Pumice	0.8	0.2	1.4	0.25	72
NP 30	II	Pumice	0.7	0.3	1.4	0.25	69

***** Water-to-binder ratio

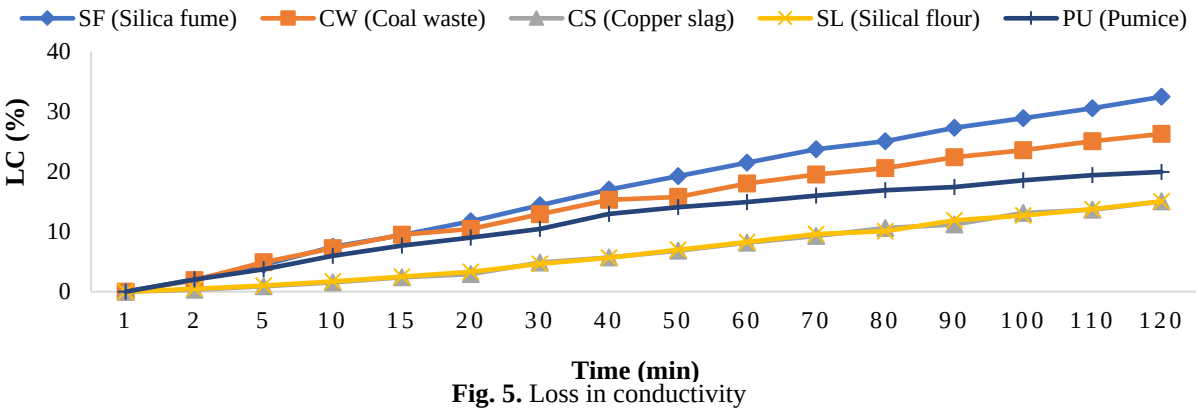

Fig. 5. Loss in conductivity

Silica fume is a by-product of the smelting process in the silicon and ferrosilicon industry. The particle size range of silica fume is between 0.1 µm to 0.2 µm. In addition, silica fume contains over 93% SiO_2 active ingredient with an amorphous structure which can cause a high level of pozzolanic activity, as could be concluded in Figure 5 and other studies (McCarthy and Dyer, 2019; Nedunuri et al., 2020). Table 6 shows that the optimal percentage of silica fume in UHPC mixtures is 10% of cementitious materials weight. However, different quantities of silica fume were proposed by other researchers (Amin et al., 2022; Wu et al., 2019). The investigation by Van and Ludwig (2012) showed that the optimum silica fume content in a mixture was highly dependent on the water to cement (w/c) ratio so that a higher w/c required a higher silica fume content. At any rate, when the W/B was 0.25, the highest compressive strength was achieved with 10% replacement of silica fume.

In the separation of copper, slag is a by-product obtained during the matte smelting and refining of copper. Research has usually focused on copper slag to replace concrete aggregates or cement (Wang et al., 2021). Nevertheless, the application of copper slag as supplementary cementitious materials (SCMs) has a higher priority than its usage as aggregates. Replacement of 10 and 20% copper slag with cement in concrete improved compressive strength by about 15 and 20%, respectively (Table 6). beyond this value, the compressive strength was reduced. The above observations are supported by other studies (Sharma and Khan, 2017; Gupta and Siddique, 2020). On the other hand, since copper slag contains a low CaO content and other oxides such as Al_2O_3, SiO_2, and Fe_2O_3, a low pozzolanic activity was expected from this material, as depicted in Figure 5. Thus, the high compressive strength of the UHPCs containing copper slag could be ascribed to the filling effects of this material.

Coal wastes are solid industrial by-products stockpiled around washing plants and coal mines. They are mostly composed of clay and carbon minerals. As noted in the literature, coal wastes were partially replaced in mortars and concrete with a replacement level of 0% to 20% of cementitious material's weight (Modarres et al., 2018). As could be deduced from Table 6, the utilization of coal waste and increasing the level of replacement from 10 to 30% had lower compressive strength than plain UHPC. This result was confirmed by similar works (Modarres et al., 2018; Karimaei et al., 2020). Figure 5 shows the high pozzolanic activity potential of coal waste which is higher than pumice and lower than silica fume. However, this effect could not be observed from compressive strength results. This contradiction could be due to several reasons: a) The indirect pozzolanic test results could not be a base for the pozzolanic reactivity of materials in the cement environment; b) the pozzolanic activity of such materials takes place in the long term, not in 28 days (McCarthy and Dyer, 2019); and c) the optimum content of coal waste in concrete is lower than 10% of

the cementitious material weight (Modarres et al., 2018).

Silica flour is a mineral produced by grinding quartz stone. The results show that replacing 10% of cementitious material weight with silica flour leads to a 5% increase in compressive strength. It was believed that the particles of fine silica flour provided a large amount of substrate surface for portlandite to crystallize at the early stages of cement hydration (Lawrence et al., 2005). On the other hand, under ambient temperature, silica flour is an inert material, and its fine particles physically improve the gradation of the aggregate (Celik and Marar, 1996). Thus, no pozzolanic activity could be imagined for silica flour. Furthermore, the lowest LC value was attributed to silica flour and copper slag among the materials investigated in this research (Figure 5).

Natural pozzolans are raw or calcined natural materials that show pozzolanic properties. Tuffs, shales, opaline cherts, volcanic ash or pumice, and diatomaceous earth are examples of natural pozzolans. Among the five SCMs investigated in this research from high pozzolanic activity materials such as silica fume to low ones such as silica flour, the natural pozzolan pumice demonstrated medium pozzolanic activity. However, the results at 28 days in Table 6 indicate that the compressive strengths were reduced at different pumice replacement levels. The reduction of compressive strength in mixtures with pumice was also reported by Madani et al. (2018).

4.3. Effect of Aggregate Type

As depicted in Table 7, two types of sand (silica and garnet) were used to produce mixes. The results in the table show that the UHPC with garnet sand had just an enhancement of 3% compared to the one with silica sand. It may be deduced that the ITZ of binder/sands is a more critical factor than the type of sand in enhancing UHPC compressive strength. However, the garnet sand was used for the following experimental program.

4.4. Effect of Cement Type

The cement content in UHPC mixture is normally about 600 - 1000 kg/m^3. The use of high quantity of cement content affects hydration heat, production costs, and dimensional stability. It is also believed that the cementitious components in UHPC mixtures could not completely hydrate and act as a filler (Fehling et al., 2008). Table 8 shows the compressive strength of UHPCs with three types of cement (S1: white cement type I-52.5, S2: Portland cement type I-42.5, and S3: Portland cement type II). The highest compressive strength of UHPC was obtained using white cement type I-52.5. The high compressive strength of the S3 mixture, which used white Portland cement in the mix design, was due to the moderate C_3A content and the very low amount of C_4AF, leading to the highest values of C_2S + C_3S, up to 84%. Thus, cement type I-52.5 was the most appropriate one to produce UHPC mixtures.

4.5. The Synergistic Effect of Silica Fume and Glass Powder

Using some materials as partial cement replacement, the dissolution of which has a lower effect on pore solution alkalinity reduction, could significantly increase the dissolution rate of cement (Vaitkevičius et al., 2014). Glass powder generally consists of sodium oxide, calcium oxide, non-crystalline silica, and other components and is prepared from various types of recycled bottles. It has been shown that the coarse particles of glass powder could initiate an alkali-silica reaction (ASR). However, using pozzolanic materials impedes the ASR. In other words, pozzolans increase the alkali fixation of C-S-H, reduce the pore solution's alkalinity, and consequently mitigate ASR. Note that the fine particle of glass powder smaller than 0.25 mm, form an alkali-silica gel that does not have any negative expansion and could act as a chemical activator (Vaitkevičius et al., 2014).

Figure 6 depict the pH value of different materials with time. The measure of pH values was the part of loss on the conductivity test described in Section 3.4. The pH range of silica fume, copper slag, silica flour, and pumice was about 7.2 to 7.6. Thus, the dissolution of the materials in the concrete environment did not significantly affect the pore solution alkalinity. The low pH value of coal waste may be a reason for the low compressive strength of the mixtures (Section 4.2). Nevertheless, glass powder had the highest alkali value. The dissolution of glass powder releases a high amount of alkali, which acts as a catalyst for the decomposition of cement and other materials. Shi and Zheng (2007) showed that among various alkali activators (like sodium and potassium hydroxides, carbonates, sulfates and silicates), sodium silicate is the most effective activator.

Considering 10% silica fume as the optimum replacement percentage of SCMs in making UHPC (as resulted from Table 6), the synergistic effect of silica fume and glass powder was investigated in Table 9. As depicted in the table, incorporating 5% and 10% glass powder accompanied by 10% silica fume resulted in 10 and 15% higher compressive strength, respectively. In addition, higher-level replacement of glass powder and silica fume at the dosages of 20 to 30% enhanced compressive strength by about 25 - 35% in comparison with the mixture with only 10% silica fume. Due to the high pH of glass powder mixtures, this material maintained pore solution alkalinity at a high level when used in concrete mixes. Thus, the solubility of clinker phases and silica fume drastically increased, and eventually, higher compressive strength could be expected.

Table 7. Effect of aggregate type on compressive strength

Mixture	Type of cement	Kind of sand	Cement	Silica fume	Sand	W/B	C.Strength (Mpa)
A2	II	Silica sand	0.9	0.1	1.4	0.25	102
G2	**II**	**Garnet sand**	**0.9**	**0.1**	**1.4**	**0.25**	**105**

Table 8. Effect of cement type on compressive strength

Mixture	Type of cement	Cement	Silica fume	Sand	W/B*	C.Strength (Mpa)
S1	Type II	1	0.1	1.4	0.25	105
S2	Type I-42.5	1	0.1	1.4	0.25	86
S3	**Type I-52.5**	**1**	**0.1**	**1.4**	**0.25**	**112**

***** Water-to-binder ratio

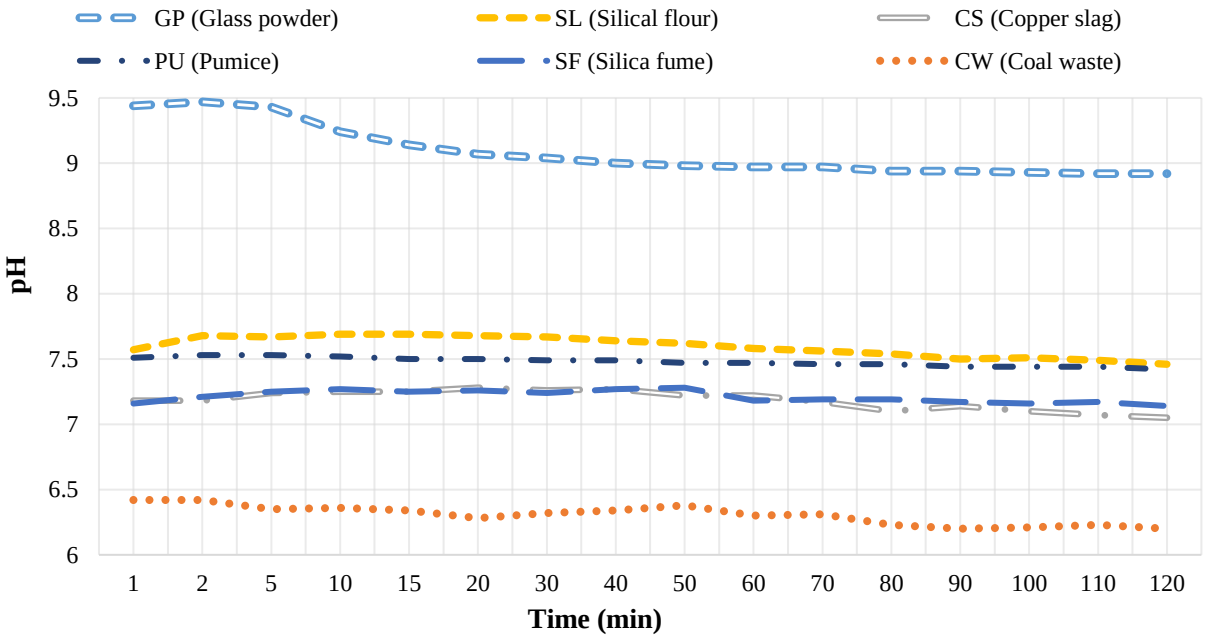

Fig. 6. pH Values of different supplementary cementitious materials

Table 9. The synergistic effects of silica fume and glass powder on compressive strength at 28 days

Mixtures	Type of cement	Cement	Supplementary cementitious materials		Sand	W/B*	C.Strength (at 28 days)
			Silica fume	Glass powder			
SF10-GP0	I-52.5	0.90	0.10	0.00	1.4	0.25	112
SF10-GP5	I-52.5	0.85	0.10	0.05	1.4	0.25	122
SF10-GP10	I-52.5	0.80	0.10	0.10	1.4	0.25	129
SF20-GP20	**I-52.5**	**0.60**	**0.20**	**0.20**	**1.4**	**0.25**	**139**
SF25-GP25	I-52.5	0.50	0.25	0.25	1.4	0.25	146
SF30-GP30	I-52.5	0.40	0.30	0.30	1.4	0.25	152

***** Water-to-binder ratio

4.6. Final Mixture

According to the cases studied in the previous sections, the following mix design is proposed to make UHPCs. The final mixture used cement type I-52.5 with an aggregate-to-binder ratio of 1.4. The replacement of glass powder and silica fume, higher than 20%, led to a rough concrete texture. Therefore, the final mixture consisted of 20% silica fume and 20% glass powder (by cementitious material weight). Due to the importance of the water-to-binder ratio in achieving higher strength, the water to binder ratio (W/B) of 0.17 was chosen to make ultra-high performance fiber-reinforced concrete (UHP-FRC). The mix proportions of UHP-FRCs are represented in Table 10. Furthermore, the flowability of fresh mixtures was measured as per ASTM C230 and ASTM C1437. A polycarboxylate ether superplasticizer was used to adjust the spread value of the mixtures in the range of 180 - 210 mm using.

The next section examines the mechanical, durability, and microstructure characteristics of UHPCs reinforced with crimped steel fiber at the dosages of 1.5 and 2.5% (by volume of concrete). This iss accomplished by analyzing compressive, flexural and tensile strength test results, flexural and tensile toughness, length change, Rapid Chloride Migration Test (RCMT), porosity, water sorptivity, and stability in a sulfate environment. In addition, a microstructural analysis is carried out using Scanning Electron Microscopy (SEM).

5. Results and Discussion

5.1. Compressive Strength

Figure 7 illustrates the compressive strength of the UHP-FRCs at ages 3, 7, and 28 days. The incorporation of steel fiber led to higher compressive strength. Moreover, 1.5% (by volume of concrete) steel fiber enhanced the strength by about 15% compared to the plain mixture. Higher substitution of the fiber up to 2.5% decreased compressive strength. However, the achieved strength of S-2.5 was still more than the plain mixture. Under axial loading, the intrinsic rigidity of stiff fibers such as steel leads to a higher bearing capacity. However, the balling effect and perturbation effect of the high content of fibers on the packing density of particles prevented compressive strength from rising. Some previous studies have reported similar findings (Ramezani and Esfahani, 2018; Wille et al., 2012). Figure 7 also illustrates that the development of compressive strength at different ages has not shown remarkable differences among the mixtures. The highest compressive strength of 165 MPa belonged to the 1.5% steel fiber mixture.

Table 10. Final mix design (kg/m^3)

Composite	Cement	Supplementary cementitious materials		Sand 0-1 mm	Sand 0.6-2.36 mm	W/B*	Steel fiber (%VOL.)
		Silica fume	Glass powder				
Plain	630	210	210	1003	334	0.17	-
S-1.5	630	210	210	967	322	0.17	1.5
S-2.5	630	210	210	943	314	0.17	2.5

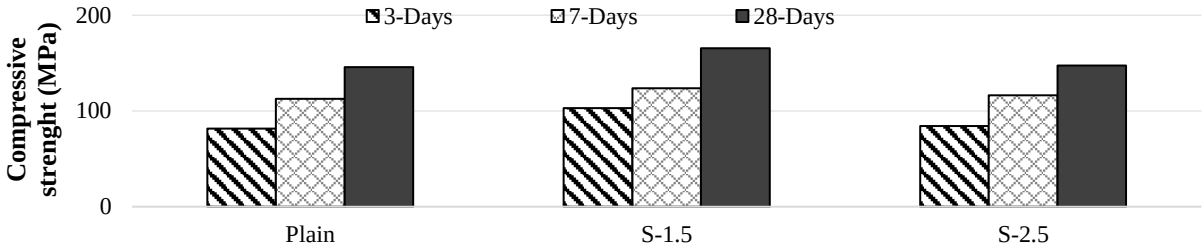

Fig. 7. Compressive strength at the age of 3, 7, and 28 days (MPa)

5.2. Flexural Performance

The flexural parameters of UHP-FRCs are tabulated in Table 11. It is assumed that before concrete cracking, the first crack strength is mainly affected by the characteristics of the concrete matrix rather than the type of fibers (Yoo et al., 2017). The improvement of the first crack strength in 28 days compared to 7 days is about 45% for all the specimens, which is a strong reason for this hypothesis. However, by controlling lateral deformation, fibers can somewhat increase flexural strength. The first crack strength increases by about 15 and 20% by incorporating 1.5 and 2.5% steel fiber, respectively.

After cracking concrete, the fibers play a remarkable role in enhancing the MOR (modulus of rupture). When a load acts on a concrete element reinforced with fiber, the fibers do not directly sustain the load. Through the interface transition zone between the fibers and the matrix, the fibers sustain the load applied to the concrete matrix. In this regard, several load transfer mechanisms can be considered. During load carrying, the fibers can rupture, pull out from the interface transition zone, or have a bridging effect.

The bridging capacity of fiber-reinforced concrete is mostly affected by mechanical anchorage, static friction, and chemical adhesion between the fiber and concrete matrix (Wu et al., 2018). After cracking of concrete, the mechanical anchorage of fiber is the most important factor in increasing flexural load-bearing capacity. Using 1.5 and 2.5% steel fiber in UHPC, the MOR was enhanced by about 40 and 95% compared to the plain mixture at 28 days, respectively. The crimped surface geometry of steel fiber led to a suitable anchorage with concrete matrix and remarkably enhanced the strain hardening section, (Figure 8). In addition, the load drop section after cracking was intensively decreased by increasing the volume of fibers.

The toughness index is obtained from the load-deflection graph and defined as the ratio of absorbed energy up to a specified deflection (3δ, 5.5δ and 10δ) to absorbed energy at the first crack deflection (δ). Table 11 illustrates that steel fiber significantly enhanced the toughness index. The energy absorption for the mixtures with 1.5 and 2.5% steel fiber was 8 and 19 times more than that of the plain mixture. This trend could be obviously seen in Figure 8. In addition, increasing the volume content of steel fiber from 1.5 to 2.5% enhanced the toughness indices of I5, I10, and I20 by about 80%, 115%, and 145%. By controlling crack formation and propagation in the concrete via bridging effect, the fibers alter the failure mechanism of concrete specimens and dramatically increase the energy absorption capacity.

Table 11. Flexural test results at the age of 7 and 28 days

Item	Plain	S -1.5	S -2.5
First crack strength at 7 days (MPa)	11.88	13.44	14.16
First crack strength at 28 days (MPa)	17.31	19.59	20.11
Modulus of rupture (MOR) at 7 days (MPa)	11.88	19.38	26.71
Modulus of rupture (MOR) at 28 days (MPa)	17.31	24.00	33.54
Flexural toughness index at 28 Days			
I5	1.00	4.32	7.83
I10	1.00	9.64	20.85
I20	1.00	16.46	40.61

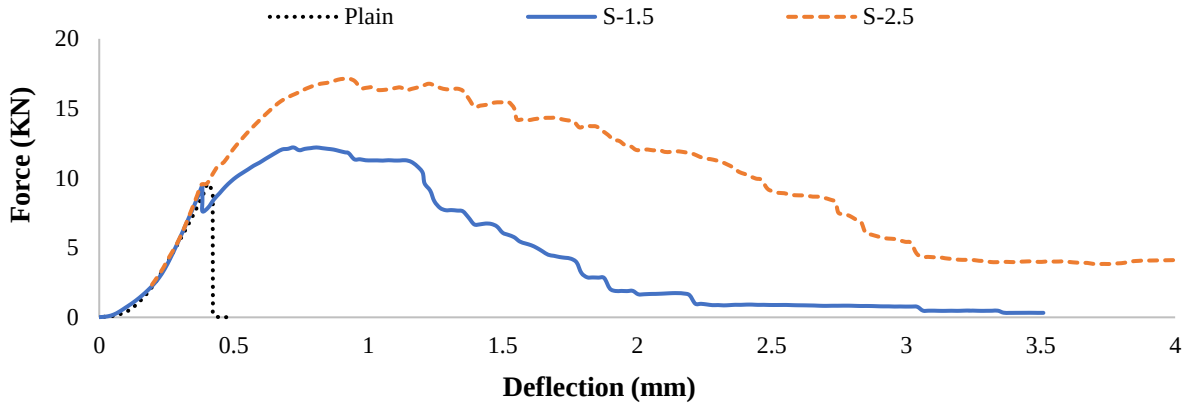

Fig. 8. Load-deflection curves of UHP-FRC specimens

5.3. Tensile Performance

To investigate the tensile performance of UHP-FRCs, a direct tensile strength test was carried out. As could be deduced from Table 12, adding steel fibers enhance tensile strength. The improvement in tensile strength for the specimens made with 1.5 and 2.5% steel fiber was 15 and 25% at 28 days, in that order. In addition, steel fiber significantly increased tensile toughness by more than three times in comparison with the plain mixture. The enhancement of tensile strength in 28 days compared to 7 days was 10 to 15%.

Comparing the tensile toughness index (I5) of the specimens made with 1.5 and 2.5% steel fibers revealed no significant differences between the results. However, a higher tensile toughness value was achieved by incorporating steel fiber in the plain mixture (more than 200%). By comparing the test results of flexural and tensile performance, it could be inferred that the enhancement in the tensile strength of UHP-FRCs was lower than flexural strength. This performance was because after cracking the flexural specimen, the flexural strength mainly reflects the fiber bridging at the tensile side; the fiber in the edge of the cross section was often better than the one in the middle due to wall effect. The bridging effect of fibers in the tensile side of flexural specimen is greater than in the tensile specimen in the whole cross section.

5.4. Length Change

The length change of concrete elements, which is the main reason for concrete cracking, mainly occurs due to the loss of moisture by evaporation and chemical alteration due to the hydration of cement. The effect of fiber content on the length change of UHPC is depicted in Figure 9. The length change of the specimens was about 600 microstrains at 70 days. The incorporation of steel fiber had an insignificant effect on length change. The length change rapidly increased in 1 to 30 days, and then slowly continued.

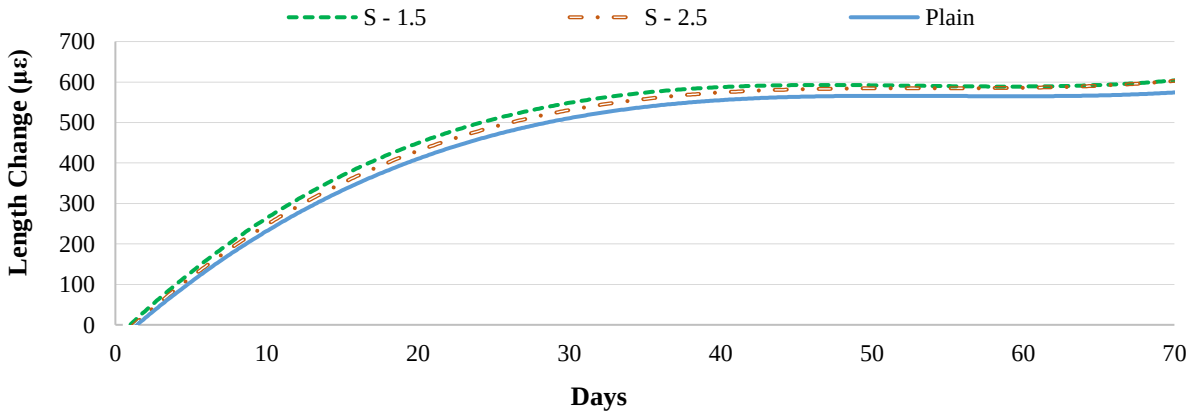

Fig. 9. Length change of the UHP-FRCs

Table 12. Tensile test results at the ages of 7 and 28 days

Item	Plain	S -1.5	S -2.5
Tensile strength at 7 days (MPa)	4.02	5.14	5.53
Tensile strength at 28 days (MPa)	5.12	5.78	6.35
Tensile toughness index at 28 Days			
I5	1.00	3.09	3.25

5.5. Durability and Microstructures

Compared to normal concretes, UHPCs, show remarkably improved durability characteristics due to low water-to-binder ratio and high amount of pozzolanic materials in the mix design. They also have negligible diffusivities. Permeability is one of the most important factors in evaluating concrete durability in long-term and severe conditions. An appropriate way to assess concrete permeability, especially in coastal or marine zones, is to examine chloride ion diffusivity in concrete. Other permeability tests, such as determining the permeable pore volume (porosity) and water sorptivity, also help investigate the durability of UHPCs.

Table 13 summarizes the porosity and chloride ion diffusivity results. The utilization of 1.5 and 2.5% of steel fiber in UHPC increased the RCMT coefficient by about 33 and 60% compared to the plain UHPC, respectively. These increasing values were 21 and 30% in the porosity test. Figure 10 displays the sorptivity rate of the specimens. The rate of sorptivity also increased by incorporating and increasing the volume content of steel fiber in the UHPC. For example, the absorption rate of the S-2.5 mixture was 60% higher than the plain mixture after 7 days. It is probable that the smooth surface of steel fiber prevents hydrate products from creating a homogeneous microstructure and acts as a wall against their precipitation. Thus, the weak interfacial transition zone of steel fibers and the cement matrix is the main reason for the higher permeability of steel fiber-reinforced UHPCs. On the other hand, stiff fibers such as steel, especially in high-level incorporation, prevent the concrete matrix from compacting. Therefore, an increase in permeability due to increasing entrapped air in the concrete mixtures is expected.

Table 13. RCMT and porosity of UHP-FRCs at 28 days

Item	Plain	S-1.5	S-2.5
Volume of permeable pore space (%)	4.19	5.07(21%)	5.45(30%)
RCMT Coefficient ($10e^{-12}$ m^2/s)	0.52	0.69(33%)	0.83(60%)

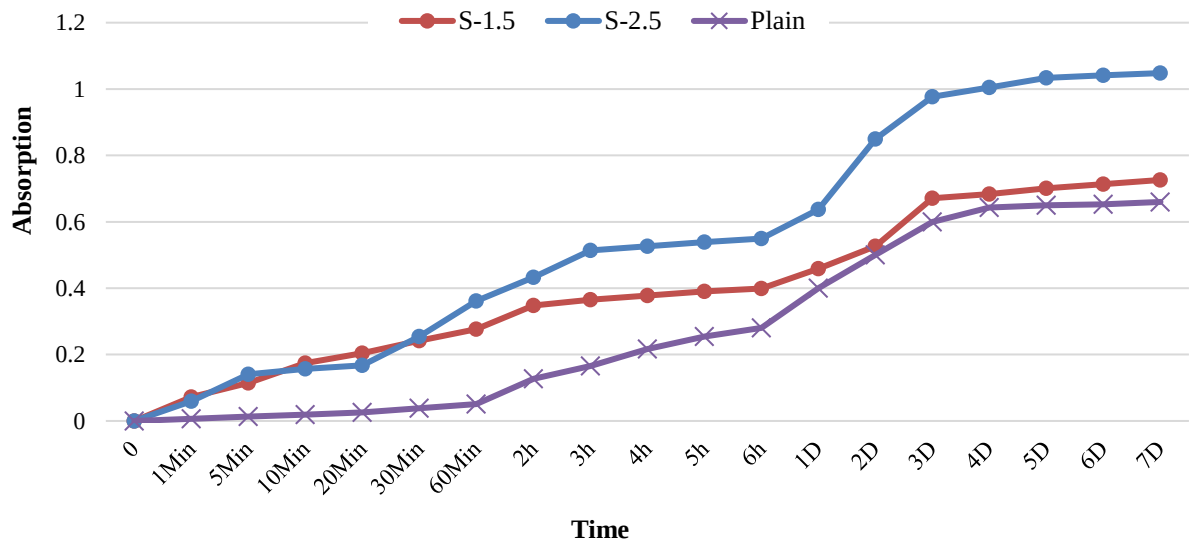

Fig. 10. Sorptivity rate of UHP-FRC specimens

5.6. Sulfuric Acid Attack

A possible degradation mechanism of concrete is sulfuric acid attack, which mainly occurs when concrete is exposed to an aggressive environment such as wastewater and sewage. This mechanism consists of two steps. First, sulfate ions react with the portlandite ($Ca(OH)_2$) and calcium silicate hydrates (C-S-H) of cement hydration products, leading to gypsum ($CaSO_4$ $(2H_2O)/CSH_2$) (Jeon et al., 2020), as depicted in Eqs. (8) and (9). Gypsum produced inside concrete induces volume expansion and causes tensile stresses and cracks in the concrete.

$$Ca(OH)_2 + H_2SO_4 \rightarrow CaSO_4.2H_2O \quad (8)$$

$$C\text{-}S\text{-}H + SO^{2-}_4 + H2O \rightarrow CaSO_4.2H_2O \quad (9)$$

Second, gypsum reacts with calcium aluminates compounds, including monosulfoaluminate (C_4ASH_{12}), unreacted tricalcium aluminate (C_3A) grains, tetracalcium aluminate hydrate (C_4AH_{13}), and alumino-ferrite phase (C_4AF), leading to the formation of ettringite ($C_6AS_3H_{32}$), which is an expansive product. In comparison with gypsum, ettringite induces higher expansion and causes more macro-cracking inside the concrete and micro-cracking (Jeon et al., 2020).

$$C_4A\overline{S}H_{12} + 2C\overline{S}H_2 + 16H \rightarrow C_6A\overline{S}_3H_{32} \quad (10)$$

$$C_3A + 3C\overline{S}H_2 + 26H \rightarrow C_6A\overline{S}_3H_{32} \quad (11)$$

$$C_4AH_{13} + 2CH + 3S + 17H \rightarrow C_6A\overline{S}_3H_{32} \quad (12)$$

$$3C_4AF + 12C\overline{S}H_2 + xH \rightarrow 4(C_6A\overline{S}_3H_{32}) + 2[(A,F)H_3] \quad (13)$$

The above reactions propagate from the surface towards the concrete core during an external attack. While the ettringite crystals exert an expansive force within the concrete, damage to the concrete occurs. The material volume expansions cause concrete to crack and scale. The effect of sulfate attack on concrete depends on the permeability of concrete and the concentration of sulfate ions (Ren et al., 2020). However, experimental studies have shown that using aggregate surface coating with mineral admixtures and improving ITZ microstructure could significantly enhance the corrosion resistance and strength of concrete (Ping and Beaudoin, 1992).

This section examines the mass loss of the specimens immersed in the 5% (v/v) aqueous sulfuric acid solution for 28 days. As shown in Figure 11 presenting the average results of three specimens, the mass loss of the specimens increased as time elapsed. Besides, the higher substitution of fiber led to higher mass loss. For example, the mass loss of the S-2.5 mixture was 20% higher than that of the plain one. The mass loss process happened by destroying and eliminating the cement paste around the aggregates. In this stage, the interfacial bond failure between aggregate and cement paste and the aggregate surface was visible.

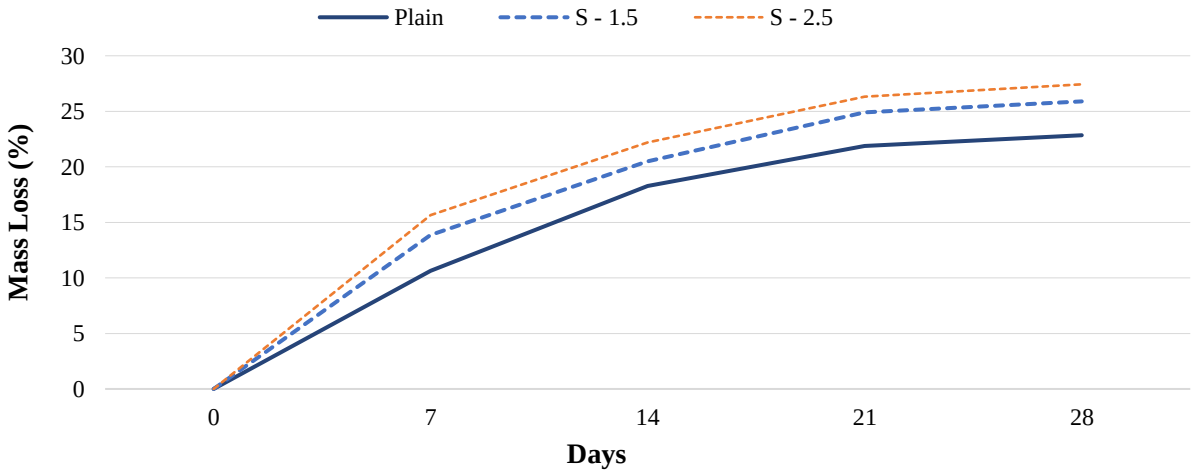

Fig. 11. Mass loss of UHP-FRC specimens under sulfuric acid solution

5.7. Microstructure

As seen in the microstructure of the plain UHPC in Figure 12, the portlandite crystals could not be detected in the interfacial transition zone of concrete matrix. It is probable that the SCMs, particularly silica fume, were the main reason for the enhanced microstructure of the concrete mixture. Silica fume is a good pozzolanic material, and its reactivity is significantly enhanced by increasing the alkalinity of pore space. However, the remaining air bubbles may be due to the insufficient compaction of the mixture.

A discontinuous region was found in the interface between the concrete matrix and steel fiber (Figure 13). this could be due to the wall effect and the smooth surface of fibers. The wall effect caused the lost packing of hydrate products around the fiber. Furthermore, the smooth surface of the fiber induced a weak interfacial transition zone between the concrete matrix and the fiber. As reported in the porosity, sorptivity, and RCMT results, the discontinuous region around the steel fibers could be a reason for higher permeability in concrete mixtures. However, the appropriate anchorage of steel fiber with the concrete matrix improved strain-hardening branch in the flexural load-deflection diagrams, despite the weak ITZ of steel fibers.

6. Conclusions

This research consisted of two parts. First part carried out an investigation to identify the best materials' proportions yielding maximum compressive strength. additionally, the pozzolanic activity, synergistic effect, and cement replacement capability of some materials such as silica fume, copper slag, coal waste, silica flour, and pumice with cement were evaluated in ultra -high performance concretes. In the second part, the performance of the UHPC with 1.5 and 2.5% crimped steel fiber was evaluated under the tests of compressive strength, flexural and tensile parameters, length change, rapid chloride ion migration, sorptivity, porosity and sulfate resistance. The following conclusions can be drawn from the current study:

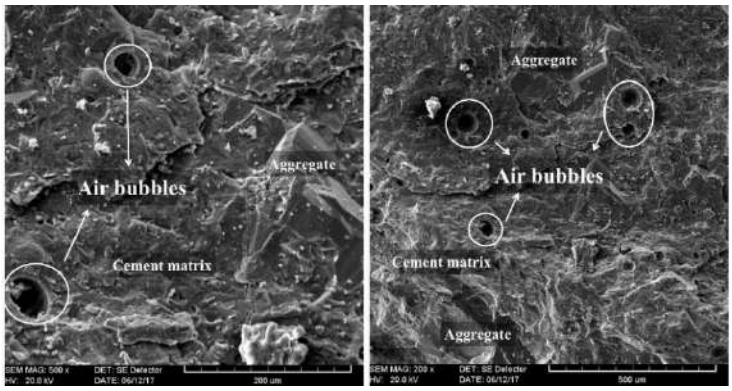

Fig. 12. SEM images of the plain UHPC

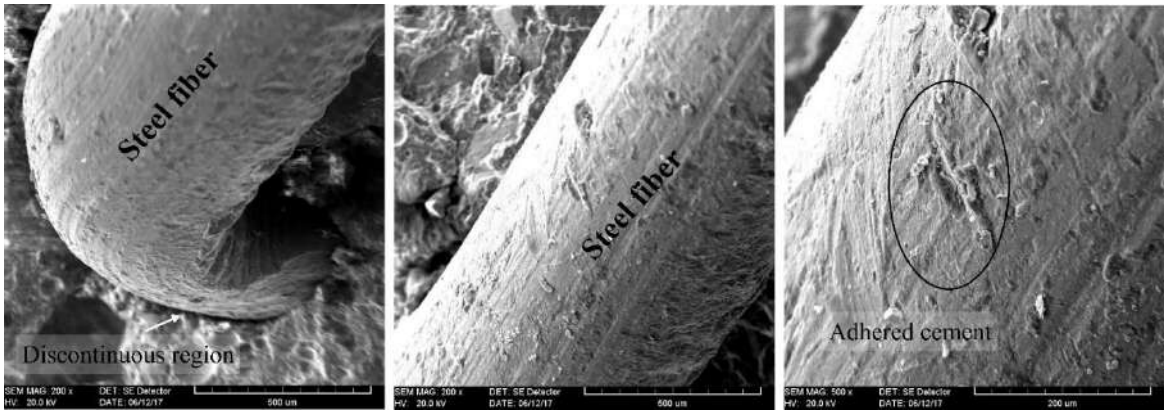

Fig. 13. SEM images of steel fiber-reinforced UHPC

- Using garnet sand, Portland cement type I-52.5, an aggregate-to-binder ratio of 1:1.4, a water-to-binder ratio of 0.17, silica fume and glass powder at the substitution level of 20% by the cementitious materials weight, Funk and Dinger's model for grading aggregates with a distribution modulus of 0.23 resulted in the highest compressive strength of 143 MPa at 28 days.
- Utilization of 10% silica fume, 10 - 30% copper slag, and 10% silica flour enhanced the compressive strength of ultra-high performance concretes.
- The interface transition zone between the aggregate and binder was more important than the type of sand; using garnet aggregate with higher hardness had no significant effect on compressive strength.
- When glass powder was used with silica fume at the same cement replacement level, an enhancement of up to 35% was obtained compared to the mix with only 10% silica fume.
- Based on the electrical conductivity test results, silica fume, coal waste, pumice, and silica flour/copper slag had the highest pozzolanic activity, respectively.
- Incorporating 1.5% crimped steel fiber increased compressive strength by about 15%. The enhancement was insignificant for the mix with 2.5% steel fiber.
- Higher incorporation of crimped steel fiber improved the post-crack behavior of UHP-FRCs. The I20 toughness index of the S-2.5 mixture increased by about 40 times under flexural loading.
- Compared to the plain UHPC, an improvement of 40 and 95% was obtained for the mixes with 1.5 and 2.5% crimped steel fiber (by volume of concrete) in the flexural strength, respectively. A 10 and 20% enhancement was also observed for the same mixes in the tensile strength.
- Steel fiber had an insignificant effect on the length change of UHPC specimens.
- The permeability of UHP-FRCs was obviously increased by incorporating steel fiber and increasing their volume fraction. This increase was 20%, 30%, and 10% in the mix with 1.5% fiber under porosity, RCMT, and sorptivity tests, in that order.
- Immersing the UHP-FRCs specimens in the 5% (v/v) aqueous sulfuric acid solution caused a 25% mass loss.

7. References

Ambily, P.S., Umarani, C., Ravisankar, K., Prem, P.R., Bharatkumar, B.H. and Iyer, N.R. (2015). "Studies on ultra-high performance concrete incorporating copper slag as fine aggregate", *Construction and Building Materials*, 77, 233-240, https://doi.org/10.1016/j.conbuildmat.2014.12.092.

Amin, M., Zeyad, A.M., Tayeh, B.A. and Agwa, I. S. (2022). "Effect of ferrosilicon and silica fume on mechanical, durability, and microstructure characteristics of ultra-high-performance concrete", *Construction and Building Materials*, 320, 126233, https://doi.org/10.1016/j.conbuildmat.2021.126233.

Andreasen, A.H.M. (1930). "Über die Beziehung zwischen Kornabstufung und Zwischenraum in Produkten aus losen Körnern (mit einigen Experimenten)", *Kolloid-Zeitschrift*, 50(3), 217-228, https://doi.org/10.1007/BF01422986.

Bajaber, M.A. and Hakeem, I.Y. (2021). "UHPC evolution, development, and utilization in construction: A review", *Journal of Materials Research and Technology*, 10, 1058-1074, https://doi.org/10.1016/j.jmrt.2020.12.051.

Brouwers, H.J.H. (2006). "Particle-size distribution and packing fraction of geometric random packings", *Physical Review E*, 74(3), 31309, https://doi.org/10.1103/PhysRevE.74.031309.

Brouwers, H.J.H. and Radix, H.J. (2005). "Self-compacting concrete: theoretical and experimental study", *Cement and concrete research*, 35(11), 2116-2136, https://doi.org/10.1016/j.cemconres.2005.06.002.

Celik, T. and Marar, K. (1996). "Effects of crushed stone dust on some properties of concrete", *Cement and Concrete Research*, 26(7), 1121-1130, https://doi.org/10.1016/0008-8846(96)00078-6.

Fehling, E., Schmidt, M. and Stürwald, S. (2008). *Ultra High Performance Concrete (UHPC), Proceedings of the Second International Symposium on Ultra High Performance Concrete*, Kassel, Germany, March, Kassel

University Press GmbH.
Ferdosian, I. and Camões, A. (2021). "Mechanical performance and post-cracking behavior of self-compacting steel-fiber reinforced eco-efficient ultra-high performance concrete", *Cement and Concrete Composites*, 121, 104050, https://doi.org/10.1016/j.cemconcomp.2021.104050.
Fuller, W.B. and Thompson, S.E. (1907). "The laws of proportioning concrete", *Transactions of the American Society of Civil Engineers*, 59(2), 67-143, https://doi.org/10.1061/TACEAT.0001979.
Funk, J.E. and Dinger, D.R. (2013). *Predictive process control of crowded particulate suspensions: Applied to ceramic manufacturing*, Springer Science & Business Media.
Gupta, N. and Siddique, R. (2020). "Durability characteristics of self-compacting concrete made with copper slag", *Construction and Building Materials*, 247, 118580, https://doi.org/10.1016/j.conbuildmat.2020.118580.
Hung, C.-C., El-Tawil, S. and Chao, S.-H. (2021). "A review of developments and challenges for UHPC in structural engineering: Behavior, analysis, and design", *Journal of Structural Engineering*, 147(9), 3121001, https://doi.org/10.1061/(ASCE)ST.1943-541X.0003073.
Hunger, M. (2010). "An integral design concept for ecological self-compacting concrete", Ph.D. Thesis, Eindhoven University of Technology. https://doi.org/10.6100/IR674188.
Hüsken, G. and Brouwers, H.J.H. (2008). "A new mix design concept for earth-moist concrete: A theoretical and experimental study", *Cement and Concrete Research*, 38(10), 1246-1259. https://doi.org/10.1016/j.cemconres.2008.04.002.
Jain, K.L., Sancheti, G. and Gupta, L.K. (2020). "Durability performance of waste granite and glass powder added concrete", *Construction and Building Materials*, 252, 119075, https://doi.org/10.1016/j.conbuildmat.2020.119075.
Jeon, I.K., Qudoos, A., Jakhrani, S. H., Kim, H.G. and Ryou, J.-S. (2020). "Investigation of sulfuric acid attack upon cement mortars containing silicon carbide powder", *Powder Technology*, 359, 181-189, https://doi.org/10.1016/j.powtec.2019.10.026.
Karimaei, M., Dabbaghi, F., Sadeghi-Nik, A. and Dehestani, M. (2020). "Mechanical performance of green concrete produced with untreated coal waste aggregates", *Construction and Building Materials*, 233, 117264, https://doi.org/10.1016/j.conbuildmat.2019.117264.
De Larrard, F. and Sedran, T. (2002). "Mixture-proportioning of high-performance concrete", *Cement and Concrete Research*, 32(11), 1699-1704, https://doi.org/10.1016/S0008-8846(02)00861-X.
Lawrence, P., Cyr, M. and Ringot, E. (2005). "Mineral admixtures in mortars effect of type, amount and fineness of fine constituents on compressive strength", *Cement and Concrete Research*, 35(6), 1092-1105, https://doi.org/10.1016/j.cemconres.2004.07.004.
Liu, K., Yu, R., Shui, Z., Li, X., Guo, C., Yu, B. and Wu, S. (2019). "Optimization of autogenous shrinkage and microstructure for Ultra-High Performance Concrete (UHPC) based on appropriate application of porous pumice", *Construction and Building Materials*, 214, 369-381, https://doi.org/10.1016/j.conbuildmat.2019.04.089.
Madani, H., Norouzifar, M.N. and Rostami, J. (2018). "The synergistic effect of pumice and silica fume on the durability and mechanical characteristics of eco-friendly concrete", *Construction and Building Materials*, 174, 356-368, https://doi.org/10.1016/j.conbuildmat.2018.04.070.
Mandal, D., Dutta, B.K., and Panigrahi, S.C. (2008). "Effect of copper and nickel coating on short steel fiber reinforcement on microstructure and mechanical properties of aluminium matrix composites", *Materials Science and Engineering: A*, 492(1-2), 346-352, https://doi.org/10.1016/j.msea.2008.03.031.
McCarthy, M.J. and Dyer, T.D. (2019). "Pozzolanas and pozzolanic materials", *Lea's Chemistry of Cement and Concrete*, Kidlington, 363-467.
Modarres, A., Hesami, S., Soltaninejad, M. and Madani, H. (2018). "Application of coal waste in sustainable roller compacted concrete pavement-environmental and technical assessment", *International Journal of Pavement Engineering*, 19(8), 748-761, https://doi.org/10.1080/10298436.2016.1205747.
Muttashar, H.L., Ariffin, M.A.M., Hussein, M.N., Hussin, M.W. and Ishaq, S.B. (2018). "Self-compacting geopolymer concrete with spend garnet as sand replacement", *Journal of Building Engineering*, 15, 85-94, https://doi.org/10.1016/j.jobe.2017.10.007.
Nedunuri, S.S.S.A., Sertse, S.G. and Muhammad, S. (2020). "Microstructural study of Portland cement partially replaced with fly ash, ground granulated blast furnace slag and silica fume as determined by pozzolanic activity", *Construction and Building Materials*, 238, 117561, https://doi.org/10.1016/j.conbuildmat.2019.117561.

Olson, D.W. (2001). *Garnet, industrial*, US Geological Survey Minerals Yearbook, 30-31.

Ping, X. and Beaudoin, J.J. (1992). "Modification of transition zone microstructure silica fume coating of aggregate surfaces", *Cement and Concrete Research*, 22(4), 597-604, https://doi.org/10.1016/0008-8846(92)90010-S.

Pourjahanshahi, A. and Madani, H. (2021). "Chloride diffusivity and mechanical performance of UHPC with hybrid fibers under heat treatment regime", *Materials Today Communications*, 26, 102146, https://doi.org/10.1016/j.mtcomm.2021.102146.

Pourkhorshidi, A.R. (2013). "Tests to evaluate pozzolanic activity in eco-efficient concrete", *Eco-Efficient Concrete*, 123-137, https://doi.org/10.1533/9780857098993.2.123.

Ramezani, A.R. and Esfahani, M.R. (2018). "Evaluation of hybrid fiber reinforced concrete exposed to severe environmental conditions", *Civil Engineering Infrastructures Journal*, 51(1), 119-130, 10.7508/CEIJ.2018.01.007.

Ren, Q., Zeng, Z., Jiang, Z. and Li, H. (2020). "Functionalization of renewable bamboo charcoal to improve indoor environment quality in a sustainable way", *Journal of Cleaner Production*, 246, 119028, https://doi.org/10.1016/j.jclepro.2019.119028.

Sharma, R. and Khan, R.A. (2017). "Sustainable use of copper slag in self-compacting concrete containing supplementary cementitious materials", *Journal of cleaner production*, 151, 179-192, https://doi.org/10.1016/j.jclepro.2017.03.031.

Shi, C. and Zheng, K. (2007). "A review on the use of waste glasses in the production of cement and concrete", *Resources, Conservation and Recycling*, 52(2), 234-247, https://doi.org/10.1016/j.resconrec.2007.01.013.

Shubbar, A.A., Sadique, M., Nasr, M.S., Al-Khafaji, Z.S. and Hashim, K.S. (2020). "The impact of grinding time on properties of cement mortar incorporated high volume waste paper sludge ash", *Karbala International Journal of Modern Science*, 6(4), 7, https://doi.org/10.33640/2405-609X.2149.

Skibsted, J. and Snellings, R. (2019). "Reactivity of Supplementary Cementitious Materials (SCMs) in cement blends", *Cement and Concrete Research*, 124, 105799, https://doi.org/10.1016/j.cemconres.2019.105799.

Thomas, M. (2013). *Supplementary cementing materials in concrete*, CRC Press.

Van Tuan, N., Ye, G., Van Breugel, K., Fraaij, A.L. A. and Dai Bui, D. (2011). "The study of using rice husk ash to produce ultra-high performance concrete", *Construction and Building Materials*, 25(4), 2030-2035, https://doi.org/10.1016/j.conbuildmat.2010.11.046.

Vaitkevičius, V., Šerelis, E. and Hilbig, H. (2014). "The effect of glass powder on the microstructure of ultra-high performance concrete", *Construction and Building Materials*, 68, 102-109, https://doi.org/10.1016/j.conbuildmat.2014.05.101.

Van, V. and Ludwig, H. (2012). "Proportioning optimization of UHPC containing rice husk ash and ground granulated blast-furnace slag", *Proceedings of the 3rd International Symposium on UHPC and Nanotechnology for High Performance Construction Materials*, Kassel, Germany, pp. 197-205.

Wang, R., Shi, Q., Li, Y., Cao, Z. and Si, Z. (2021). "A critical review on the use of copper slag (CS) as a substitute constituent in concrete", *Construction and Building Materials*, 292, 123371, https://doi.org/10.1016/j.conbuildmat.2021.123371.

Wille, K. and Boisvert-Cotulio, C. (2015). "Material efficiency in the design of ultra-high performance concrete", *Construction and Building Materials*, 86, 33-43, https://doi.org/10.1016/j.conbuildmat.2015.03.087.

Wille, K., Naaman, A.E., El-Tawil, S. and Parra-Montesinos, G.J. (2012). "Ultra-high performance concrete and fiber reinforced concrete: achieving strength and ductility without heat curing", *Materials and Structures*, 45(3), 309-324, https://doi.org/10.1617/s11527-011-9767-0.

Wu, Z., Khayat, K.H., and Shi, C. (2018). "How do fiber shape and matrix composition affect fiber pullout behavior and flexural properties of UHPC?", *Cement and Concrete Composites*, 90, 193-201, https://doi.org/10.1016/j.cemconcomp.2018.03.021.

Wu, Z., Khayat, K.H. and Shi, C. (2019). "Changes in rheology and mechanical properties of ultra-high performance concrete with silica fume content." *Cement and Concrete Research*, 123, 105786, https://doi.org/10.1016/j.cemconres.2019.105786.

Wu, Z., Shi, C. and Khayat, K.H. (2016). "Influence of silica fume content on microstructure development and bond to steel fiber in Ultra-High Strength Cement-based Materials (UHSC)", *Cement and Concrete Composites*, 71, 97-109, https://doi.org/10.1016/j.cemconcomp.2016.05.005.

Yoo, D.-Y., Kang, S.-T., Banthia, N. and Yoon, Y.-S. (2017). "Nonlinear finite element analysis of ultra-high-performance fiber-reinforced concrete

beams", *International Journal of Damage Mechanics*, SAGE Publications, 26(5), 735-757, https://doi.org/10.1177/1056789515612559.

Yu, Q.L., Spiesz, P. and Brouwers, H.J.H. (2013). "Development of cement-based lightweight composites, Part 1: Mix design methodology and hardened properties", *Cement and Cconcrete Composites*, 44, 17-29, https://doi.org/10.1016/j.cemconcomp.2013.03.030.

Civil Engineering Infrastructures Journal 2023, 56(2): 415-438
DOI: 10.22059/CEIJ.2023.347246.1862

RESEARCH PAPER

Seismic Fragility Analysis of Torsionally-Coupled Steel Moment Frames Against Collapse

Mesr Habiby, Y.[1] and Behnamfar, F.[2*]

[1] M.Sc., Department of Civil Engineering, Isfahan University of Technology, Isfahan, Iran.
[2] Professor, Department of Civil Engineering, Isfahan University of Technology, Isfahan, Iran.

Received: 16 Aug. 2022; Revised: 22 Dec. 2022; Accepted: 16 Jan. 2023

ABSTRACT: In this study, nonlinear dynamic response of 4, 7, and 10-story moment frame steel structures is investigated under seismic ground motions. An incrementally increasing intensity is accounted for to evaluate the collapse fragility curves of the same buildings under different values of torsional eccentricity. The site soil of the buildings is assumed to be composed once of a firm and then of a soft soil. As a distinction of this study, the realistic maximum possible value of eccentricity ratio for moment frames, including both stiffness and mass eccentricities, is shown to be 10-15% that is much less than peak values of the past studies. Because of the three-dimensional aspect of the study, the eccentricity is selected to be bi-directional and the horizontal components of the earthquake motion are applied concurrently. It is exhibited that while torsional eccentricity lowers the median collapse probability of the studied buildings, it does not have a sensible effect up to the eccentricity ratios not larger than 10%. Besides, the taller structures on the firm soil are affected more strongly from torsional eccentricity, as the median collapse acceleration decreases up to 46% for the 10-story building suffering from 15% eccentricity ratio on the firm soil.

Keywords: Collapse, Eccentricity, Seismic Fragility, Steel Structure, Torsion.

1. Introduction

Buildings having torsional eccentricity in plan have been known to suffer more from earthquake damage. The horizontal displacement of the plan of a torsionally-coupled building is not uniform during an earthquake even if the story diaphragms are rigid. This is turn results in accumulation of ductility demands at the soft side, i.e. part of the plan where the peak horizontal displacement happens. Then, seismic damage begins to develop at a large extent from the same location instead of being uniformly distributed among all resisting elements, at much smaller intensity.

In response to the above negative observations on seismic torsional response, strict regulations have been developed in building codes to lower torsional eccentricity and its consequences. For instance, ASCE 7-16 (2016) sets certain constraining regulations to amplify torsional demands. When the torsional

* Corresponding author E-mail: farhad@cc.iut.ac.ir

eccentricity exceeds a predefined threshold, it necessitates the spectral analysis for critically torsional buildings, and prohibits designing buildings with large eccentricities for more important building in highly seismic areas (ASCE/SEI 7-16, 2016). The point here is that abiding by these regulations results in buildings with much less eccentricities than what appears in the initial architectural drawings of the building. Then, assuming extremely large values of the eccentricity ratio in research studies is only of academic value.

Due to its importance, many researchers have embarked on the effects of torsional response of building in highly seismic areas. More than 70 of these studies, performed between 1990-2020, have been identified and reviewed in a relevant work (Habiby, 2020). Only a number of the more important works are mentioned here to form a general idea.

Mazzolani and Piluso (1996) and Gioncu and Mazzolani (2010) compiled the temporary knowledge on earthquake engineering and design of steel structures to withstand earthquakes in the form of two interesting textbooks. On critical examination of the Eurocode 8, Elghazouli (2010) assessed the seismic regulations of steel structures, Ferraioli et al. (2014) evaluated the appropriateness of the code-based behavior factor for steel structures, and Landolfo (2018) introduced the ongoing trends of the code improvement regarding seismic design of steel structures.

Patel et al. (2016), Xu et al. (2018), Dehghani and Soltanimohajer (2022), Zeng et al. (2022), and Ashwini and Stephen (2022) are among the authors who worked on developing the seismic fragility of frame structures considering various parameters including engineering demand parameters, height of the building, and supplemental damping.

Chen and Collins (2001) modified the method developed by Collins et al. (1996) for reliability-based seismic design of torsional structures. According to their study, the only necessary change in the previous process was the use of 3D pushover analysis to calibrate the parameters of the equivalent Single Degree Of Freedom model (SDOF), and the general form of the design equations did not change. The results indicated that the uncertainty amplification in the SDOF model considering the torsion was not significant. It also seemed that the design parameters were not sensitive to changes in the statistical values used to quantify the approximate nature of the SDOF method. The reason for this was that the other two sources of uncertainty (seismic hazard and site soil effects) dominated the uncertainty of the analysis and design values. However, results of the study need further investigation, because it was based on very simple analytical models and some restrictive assumptions.

Puppio et al. (2017), Seo (2018), Moon et al. (2018), Anvarsamarin et al. (2020), and Razmkhah et al. (2021) determined the seismic fragility curves by accounting for torsional irregularity in plan of the buildings. Generally, they concluded that torsional irregularity increases the seismic fragility to a considerable level.

Marušić and Fajfar (2005), evaluated the linear and nonlinear seismic response of asymmetric five-story steel buildings under bi-directional excitation. Asymmetric buildings were created with the eccentricity of the mass in both main directions. In torsionally stiff structures, the nonlinear torsional response was qualitatively similar to the linear response, except for the stiff edge in the strong direction, i.e. the direction in which the component with higher peak ground velocity was applied to the structure. Generally, formation of the plastic hinges reduced the torsional effect. It was concluded that displacement of the mass center in the asymmetric building and the symmetrical building was approximately equal. Amplitude of the displacement calculated by linear analysis was a proper approximation for the corresponding value in the nonlinear region. Any desirable torsional effect on the

stronger edge of the torsionally stiff structure, i.e. a displacement reduction relative to the symmetric structure, was due to linear analysis, and this effect might be eliminated in nonlinear analysis.

De Stefano and Pintucchi (2008) reviewed the research works on seismic behavior of torsionally-coupled buildings since 2002 having different structures. They examined the main features of the seismic response of irregular buildings and provided certain recommendations and future directions. Aziminejad and Moghadam (2010) evaluated the seismic performance of asymmetric single-story buildings under near-field and far-field earthquakes based on the fragility concept. They showed that in general, the optimal location of centers of stiffness and strength was a function of the characteristics of ground motion and nonlinear responses of structure. In their study, by evaluating the nonlinear response of one-story building models with a wide range of rotational to lateral frequency ratios, the optimal location of these centers was investigated. Diaphragm rotation, interstory drift, hinge rotation and ductility demand have been selected as damage indices. Results showed that the proper configuration of structural centers in a torsionally stiff building mainly depended on the selected demand parameter. For a specific demand parameter, such a proper configuration could lead to convergence of damage probability to that of the symmetrical building. Therefore, by identifying the critical demand parameter for a particular case, it was possible to detect the suitable arrangement of the centers and by rearranging the centers accordingly, the negative effects of asymmetry could be avoided.

Bensalah et al. (2013) studied the effect of torsion on the behavior of three-story reinforced concrete structures with rigid slabs. Uncertainty of input parameters such as Arias intensity, Peak Ground Acceleration (PGA), principal period and outputs such as interstory drift and torsional eccentricity were investigated. Time history and pushover analyses were performed under 116 earthquake records. They concluded that in low-rise multistory structures, the torsional response during an earthquake depended on many factors and the most effective parameter was the PGA with the highest correlation.

In the study implemented by Fujii (2014), a pushover-based method was proposed to estimate the maximum seismic response of an asymmetric building under an excitation with an arbitrary angle of incidence. The specifications of the two independent SDOF models were determined according to the main direction of the first modal response in each nonlinear phase, unlike the usual method that uses a fixed direction based on the linear mode shape. In the numerical example, six 4-story torsionally stiff buildings under seismic excitations at various angles were subjected to nonlinear dynamic. The results showed that the maximum displacement response of the soft edge of the torsionally stiff building obtained from the proposed method had a good accuracy. Orthogonality of the main directions of the modal response of the first and second modes of the structure was true for torsionally stiff structures, but in the torsionally flexible structures these responses were not independent of each other.

Sharifi and Sakulich (2014) studied the effects of torsion on the nonlinear response of steel structures. A number of 4, 8 and 12-storey steel moment frame structures were considered with various eccentricities. Intensity of eccentricity was an important parameter that changed the degree of participation of different transition and rotation modes in the total response. It was observed that increasing eccentricity of the structures increased participation of the floor rotation in the total response. In addition, in torsionally flexible structures when the first or second mode was mainly composed of torsional vibration, the rate of floor rotation participation could be even higher. This indicated that the torsional

mode of the structure must be controlled, by means of damping systems and control devices, to effectively reduce lateral displacement.

In the study by De Stefano and Mariani (2014) the positive and negative aspects of different analysis methods appropriate for torsional structures were described and recommendations for improving the existing building codes were proposed.

DeBock et al. (2014) investigated the importance of seismic design accidental torsion criteria of ASCE 7-16 on the collapse capacity of RC buildings with ordinary and special moment frame lateral systems. Their study, which was performed using 22 pairs of earthquake records, showed that the requirements of accidental torsion do not have much effect on increasing the collapse capacity of buildings. For example, according to their results, these criteria improve only the collapse behavior of buildings located in moderate seismic regions suffering from Torsional Irregularity Ratio (TIR) greater than 1.4 and buildings located in high seismic regions with TIR greater than 1.2.

In a case-study presentation, Ferraioli (2015) provided a comprehensive seismic performance assessment of an irregular hospital building, embarking on its nonlinear response and the main involving factors.

Manie et al. (2015) probabilistically studied the collapse behavior of low-rise asymmetric plan buildings under bi-directional ground motions. The nonlinear model of the structural members included concentric inelastic rotational springs at the ends of the otherwise elastic members. Degradation of stiffness and strength was included in the nonlinear springs. The torsional eccentricity was made by dislocating the center of mass in one direction. It was concluded that by increasing the eccentricity, a smaller margin of safety is resulted against seismic collapse. For values of the eccentricity ratio over 20%, the safety margin fell below the minimum value required for fulfilling the life safety performance level. They observed a decreasing trend of the safety margin with increasing the number of stories of the studied buildings.

Badri et al. (2016) studied the effect of deteriorating parameters on the collapse capacity of asymmetric low-rise buildings. The studied five-story buildings were of RC moment frame type and had a one-way mass eccentricity in the plan. One-directional far-field ground motions was selected for dynamic analysis. Buildings were divided into two groups: torsionally stiff and torsionally flexible. Torsionally stiff building had their periods of the translational mode to be significantly larger than their period of torsional mode in opposite to the torsionally flexible buildings. Results of the analysis showed that increasing the torsional eccentricity of ductile moment frames can slightly increase or even reduce the collapse probability of structures, which was due to stiffer torsional behavior of the studied structures. Also, as the mass eccentricity increased, the uncertainty of modeling parameters had a smaller effect on the safety margin of collapse.

Han et al. (2017) investigated the nonlinear seismic response of special steel moment frame buildings having torsional irregularity and evaluated the effects of torsional regulations of the sample building codes on the collapse safety margin of such structures. They displaced one of the moment frames at predefined values to impose torsional response due to stiffness eccentricity. It was shown that torsional irregularity increases the collapse probability in general. They developed a method for limiting the drift demand of stories such that the collapse probability of unsymmetric structures equaled that of their regular counterparts.

Eivani et al. (2018) studied the seismic behavior of asymmetric single-story structures with flexible diaphragms having different configurations of centers of mass, stiffness and strength. Effect of asymmetry on diaphragm deformation as well as effect

of diaphragm flexibility on seismic demands were studied. The optimal configuration of centers of mass, stiffness and resistance was also investigated to limit the critical engineering demand parameters. The results showed that the predominant shear deformation of the diaphragms depended on both structure asymmetry and flexibility of the diaphragm. It was also found that the proper configuration of the centers in torsionally stiff structures depended on the level of flexibility of diaphragm in addition to the intensity of earthquake and the engineering demand parameters.

Hentri et al. (2018) evaluated the seismic behavior of asymmetric RC structures using a Displacement-based Adaptive Pushover (DAP) method. Fragility curves were determined for various performance states. The results indicated that height of the asymmetric structures significantly affected their response and the strength and stiffness of the structures were a function of their slenderness ratio, especially in taller buildings. It was concluded that in asymmetric structures, more displacement and ductility capacities were required to achieve the same behavior as the symmetrical structures.

Das et al. (2021) examined an exhaustive number of studies in the literature of asymmetric and irregular structures. Because of the varied nature of the results, the guidelines are not yet well developed. In fact, distinctions in results observed even in the behavior of a single-story asymmetric structure, especially for regulation of inelastic behavior, is a major obstacle to reach the comprehensive guidelines.

Hwang et al. (2021) developed a machine learning-based methodology for reliably predicting the seismic response and structural collapse classification of RC buildings by using four component- and system-level modeling uncertainties. The RC beam modeling parameters (i.e., plastic deformation properties) of low- to mid-rise structures were the primary predictors of seismic response due to capacity design rules. In addition, models that ignore the uncertainties of the structural modeling-related parameter seem to underestimate collapse risk of low- to mid-rise RC buildings.

Moradi et al. (2022) evaluated the collapse probability of a 4-Story RC frame under post-earthquake fire scenario. The results showed that increasing PGA makes the building behavior more critical and decreases collapse time in these buildings under post-earthquake fire loading.

Tavakoli et al. (2022) investigated outrigger braced system placement effect on seismic collapse probability of tall buildings. For this goal, two structures of 50 floors were chosen. The results showed that the placement optimization of outrigger braced system enhances all structural parameters and decreases the collapse probability. Furthermore, the fragility curves derived from plastic strain energy were quite similar to the fragility curves generated from the story drifts.

Kazemi and Jankowski (2023) proposed machine learning-based algorithms to predict seismic limit-state capacity of steel MRFs considering soil-structure interaction. This study enhanced data-driven decision method in python software, known as supervised machine learning algorithms, to find median IDA curves for predicting seismic limit-state capacities. The results of the analysis confirmed that there is no specific model for anticipating the IDA curves of structures; therefore, the best algorithms to diminish high computational costs were proposed.

It is observed by the above literature review that the nonlinear seismic response of torsionally eccentric steel structures is yet to be fully known. Especially, probabilistic assessment of such a behavior and evaluation of the seismic safety margin of the steel moment frames to the extent of building code modification need much more study. This is an important aspect that the related literature lacks enough consideration. The present study is a step toward filling this gap by examining the

probabilistic features of the seismic response of torsionally-coupled buildings. Moreover, it is aimed to probabilistically find the threshold of the eccentricity ratio over which the building code should beware the designer to be concerned over the consequences. Obviously, vital to such a study is taking realistic assumptions for the eccentricity ratio of the centers of mass and stiffness. This study critically touches this very important point to find the reliable range of the ratio to make the findings meaningful. In most of the past studies, the collapse behavior of asymmetric buildings has been investigated assuming irregularity of mass in the plan. It also seems that the assumed values of eccentricity in previous research works has been sometimes much higher than the possible values. In the present study, first, the maximum feasible values of the eccentricity of torsionally-coupled buildings are determined and then the safety margin against seismic collapse of such buildings is evaluated. The wider range of cases studied, leads to more comprehensive results. Here, low and medium rise steel structures having 4, 7, and 10 stories consisting of special moment frames are studied using Incremental Dynamic Analysis (IDA) to draw their fragility curves. When designing these structures, a firm and then a soft soil site are considered. In nonlinear analysis, different values of mass eccentricity in a stiffness-eccentric plan are considered. Variation of the collapse safety margin and the median spectral acceleration with the eccentricity ratio, building height, and the soil type are discussed.

2. The Realistic Range of Eccentricity

This research study is recognized from the majority of the similar studies in the past by the fact that it evaluates the response of multistory buildings having conventional beams, columns, and diaphragms in contrast to the ones embarking only on mathematical models of real buildings by working only with stiffness and mass parameters. Therefore, it is necessary beforehand to configure the arrangement of the building frames to arrive at a certain value of eccentricity. In the past studies, values of eccentricity ratio, i.e. distance of the mass and stiffness (as opposed to strength) centers divided by the plan dimension along a major axis, up to values over 30% have been assumed. It is shown here that such large eccentricities are not possible in practice and a more realistic bound is derived. Three critical examples are considered as follows. It is to be noted that only conceptual facts are important here. Then, extensive details of the example buildings, designed based on AISC 360-16 (2016), are not given to save space for the next parts of the paper.

2.1. Example 1

In this example a mass-eccentric moment frame building is considered (Figure 1).

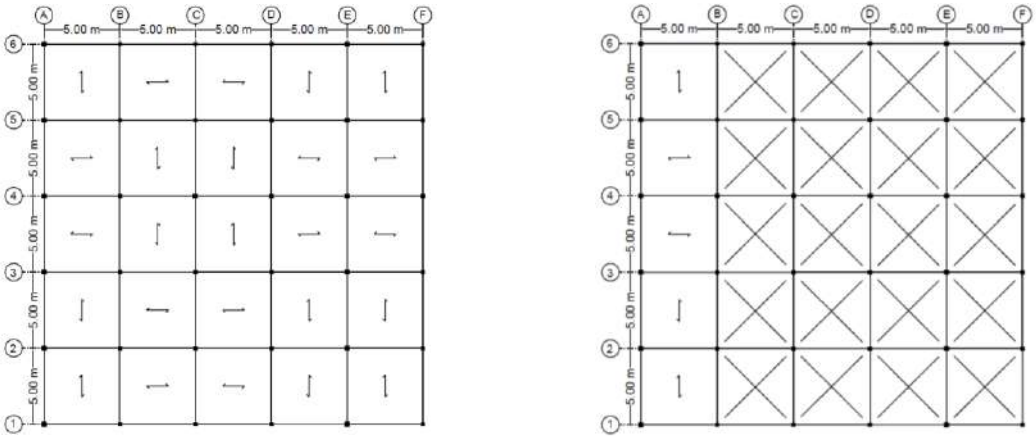

(a) **(b)**

Fig. 1. The story plan considered in Example 1: a) Regular case; and b) Irregular case

According to Figure 1b, as an extreme case, it is assumed that a large part of the plan (indicated by crosses) is void. On the remaining part, a large live load of 12 KN/m^2 is applied that can be due to a heavy storage area. The building consists of 5 stories. At the first step, for modeling using a commercial design program, identical frames are considered throughout the plan. The mass eccentricity ratio along the y-axis is calculated to be about 34%. Then the building is analyzed assuming a highly seismic zone in ASCE 7-16. For such a large torsional eccentricity, the frames under the covered part of the plan undergo much larger displacements than the opposite frames and accept amplified lateral loads when using spectral analysis. After the first round of analysis and design, the mentioned frames prove to need larger sections than the other frames. Then the eccentricity ratio reduces to about 16% based on stress limitation and only 5% based on both stress and drift limitations. For the regular building, the beams sections emerge to vary from IPE160 to IPE360. The columns are 180 × 20 to 320 × 25 boxes. In the irregular building, designed sections vary from IPE160 to IPE400 for the beams and from 180 × 20 to 380 × 25 boxes for the columns.

2.2. Example 2

In this example, the torsional eccentricity originates from non-uniform arrangement of uniformely-sectioned steel moment frames (Figure 2).

It is perceived that locating two frames at such a close proximity in a direction having only three frames is not conventional. However, the example goes on to study a very extreme case to reach to an upper bound of eccentricity.

Using conventional dead and live loads and a highly seismic zone within ASCE 7-16, the frames are designed according to AISC 360-16. Before the first round of analysis, by assuming uniform stiffness for the frames, the eccentricity ratio emerges to be 17%. After finalizing the design process through a few iterations, the eccentricity ratio reduces to about 5%. In this example, for the regular building case, the beam sections appear to vary from IPE240 to IPE360 and the columns are 180 × 20 to 300 × 20 boxes. In the irregular building, sections vary from IPE240 to IPE400 for the beams and from 240 × 20 to 400 × 40 boxes for the columns.

As the above two examples prove, real contemporary seismic design of moment frames, even in the most extreme cases, does not allow the final torsional eccentricity to be larger than, perhaps, about 10-15%. Assuming larger eccentricities, therefore, will not have a considerable practical value.

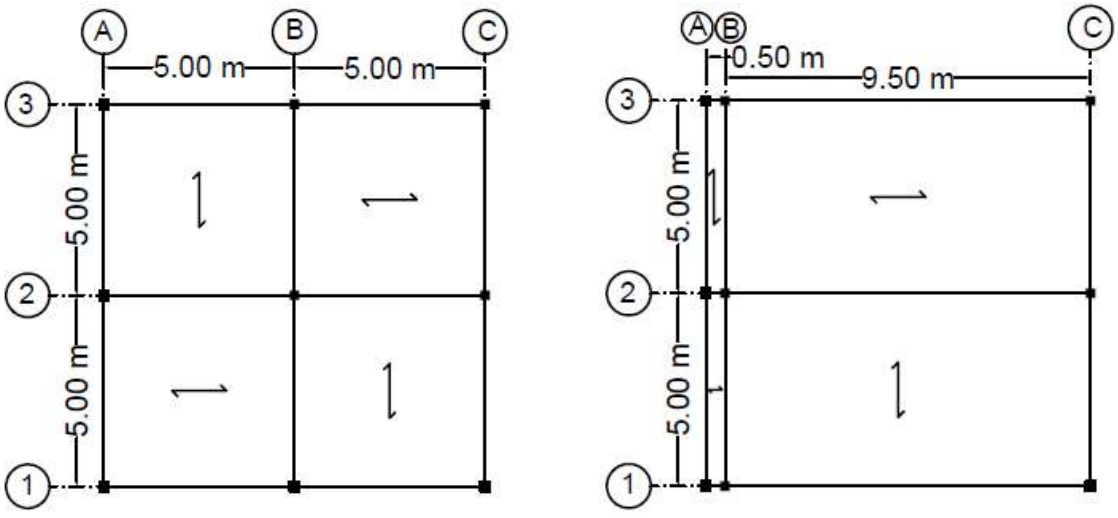

a) **b)**

Fig. 2. Arrangement of the moment frames in Example 2: a) Regular case; and b) Irregular case

2.3. Example 3

In order to generate high torsional eccentricities, braces that have more stiffness than moment frames can also be used (Figure 3). Thus, in the third example, one-way eccentricity is made in a building equipped with a dual lateral load bearing system. The plan and other specifications are similar to Example 2. In the mentioned building, the B axis is shifted to the west side while it is braced between 1-2 axes. The mass distribution on the plan is considered to be uniform. By choosing uniform initial sections for the members without regard for the inherent torsion (with member section being similar to a regular building), the one-way eccentricity ratio reaches to 38%. After the final round of analysis and design including abiding by the weak beam-strong column requirement, the dual system specific controls and drift limitation, eventually the eccentricity ratio only decreases to 35%. In this example, for the regular building case, the beam sections appear to vary from IPE240 to IPE300, the columns are 180 × 20 to 240×20 boxes and the braces are 120 × 20 box. In the irregular building, sections vary from IPE160 to IPE360 for the beams, from 220 × 20 to 340 × 25 boxes for the columns and 120 × 10 box for the braces.

By designing the structure with a dual system of moment frame and bracing in one direction, two results can be obtained in comparison to the previous examples:

a) In structures with irregularity due to displaced braced frames, after finalizing the design process, the stiffness center shifts only slightly and the change in the initial value of eccentricity is not significant. On the opposite, in structures with irregularity due to displaced moment frames, the value of eccentricity is extremely reduced by the design process. The reason for this is dependence of stiffness of moment frames on the dimensions of the beams and columns sections, while for the braced frames, stiffness of the braced bays is normally much higher than the otherwise moment frames.

b) In the irregular structures with the dislocated braced frames, the process of repetitive analysis and design has a small effect on the position of the stiffness center because of the concentrated large stiffness of the braced bays.

Then, unlike most of the previous studies where virtual structures with deliberate eccentric arrangement of members were studied without performing actual design of the buildings for those presumed eccentricities, any kind of the assumed eccentricity should be regarded in design and proportioning of the members to arrive at a final reduced eccentricity. This important fact is fulfilled in this study.

3. Introducing the Studied Buildings

Configuration of the buildings selected for the current study is shown in Figure 4.

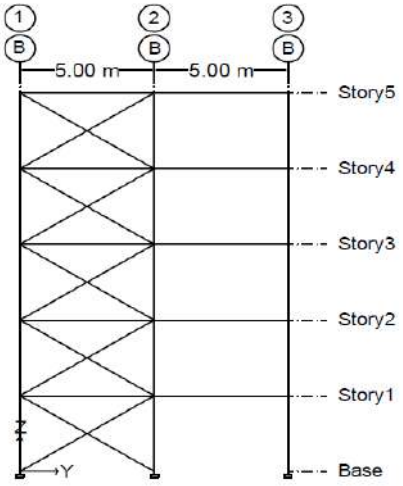

Fig. 3. Braced frame of the building in Example 3

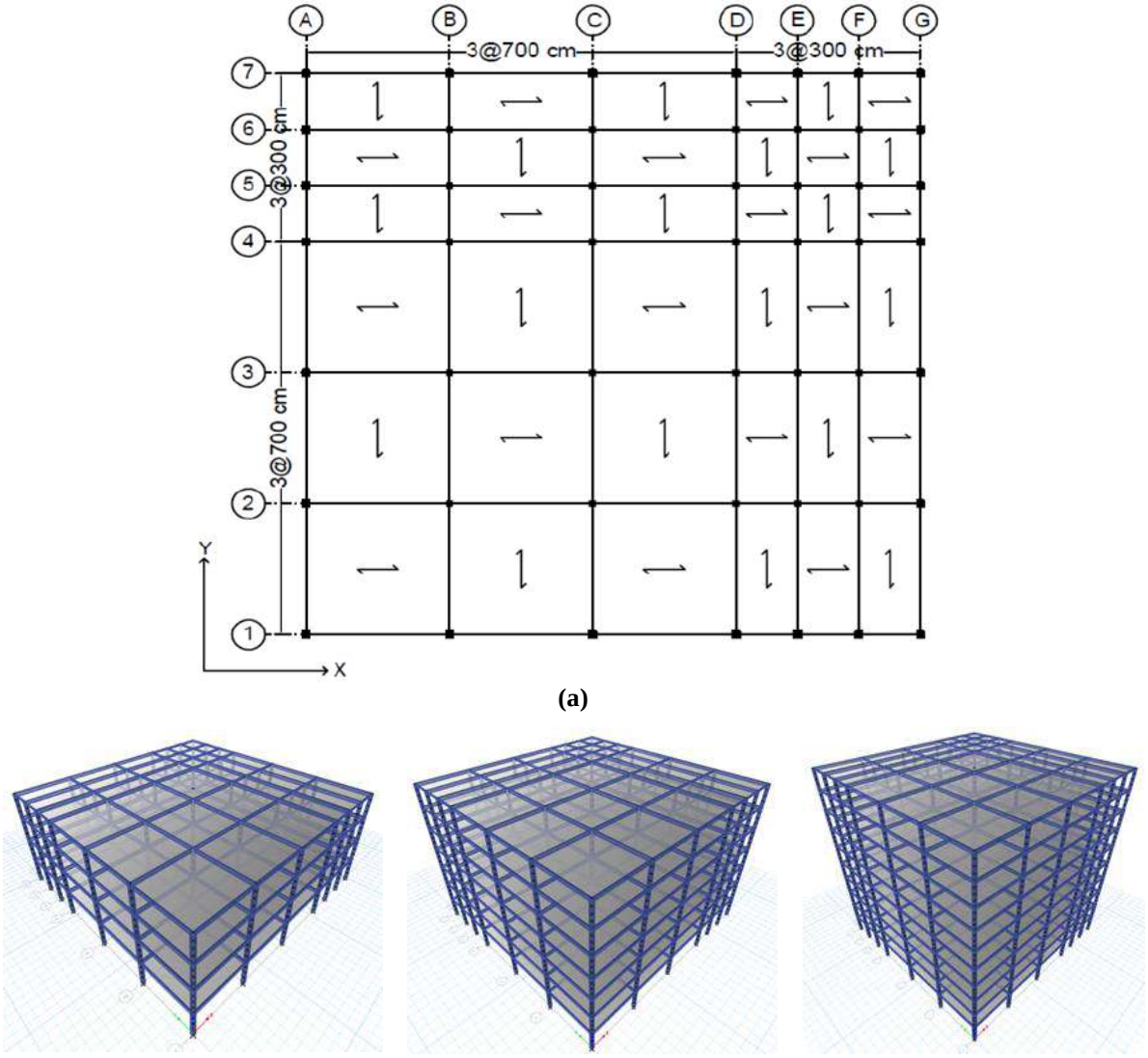

(a)

(b)

Fig. 4. The studied buildings: a) The common story plan; and b) The perspective

The structures shown in Figure 4 are in 4, 7, and 10 stories. They are composed of special steel moment frames with rigid diaphragms. The common story plan shows that the frame arrangement is irregular and the adjacent frame distances are smaller at the right and up sides of the plan. Then, if uniform frames are used, the center of stiffness will be at the North-East of the plan. In the design stage, the live load, similar to the dead load, is assumed to be uniformly distributed over the plans. However, at the stage of nonlinear dynamic analysis, the random nature of the live load will be considered by assuming different unsymmetric distribution of the same.

The common story height is 3.2 m. Values of the gravity loads are shown in Table 1.

Table 1. The gravity loads

Load type	Load intensity (KN/m^2)
Floors dead load	5.5
Roof dead load	6.0
Floors live load	2.0
Roof live load	1.5
Partition load	1.0
Snow load	1.0

In addition to the values mentioned in Table 1, a line load of 7 kN/m is used at the location of the perimeter walls.

The site soil once is taken to be of the "C" type (stiff soil) and the other time is of the "D" type (firm soil) (ASCE/SEI 7-16, 2016). The buildings are located in a highly seismic area having the design spectra for the two soil types as shown in Figure 5 (ASCE/SEI 7-16, 2016).

Design of the structural frames is performed using AISC 360-16 (AISC360-16, 2016). The steel type used is St-37 having a yield strength of 240 MPa. At each story only two beam sections and four column sections are considered for keeping in line with practical considerations, as shown in Figure 6.

For the 4-story building, B1 beams appear to be IPE400 and B2 beams vary from IPE270 to IPE330. The C1-C4 columns are 320 × 25 to 340 × 25 boxes. In the 7-story building, the same members vary from IPE240 to IPE400 for the beams and from 260 × 20 to 340 × 25 boxes for the columns. For the 10-story building, the variation is from IPE240 to IPE400 for the beams and from 300 × 20 to 400 × 25 boxes for the columns. The fundamental periods of the designed buildings on the two soil types are mentioned in Table 2.

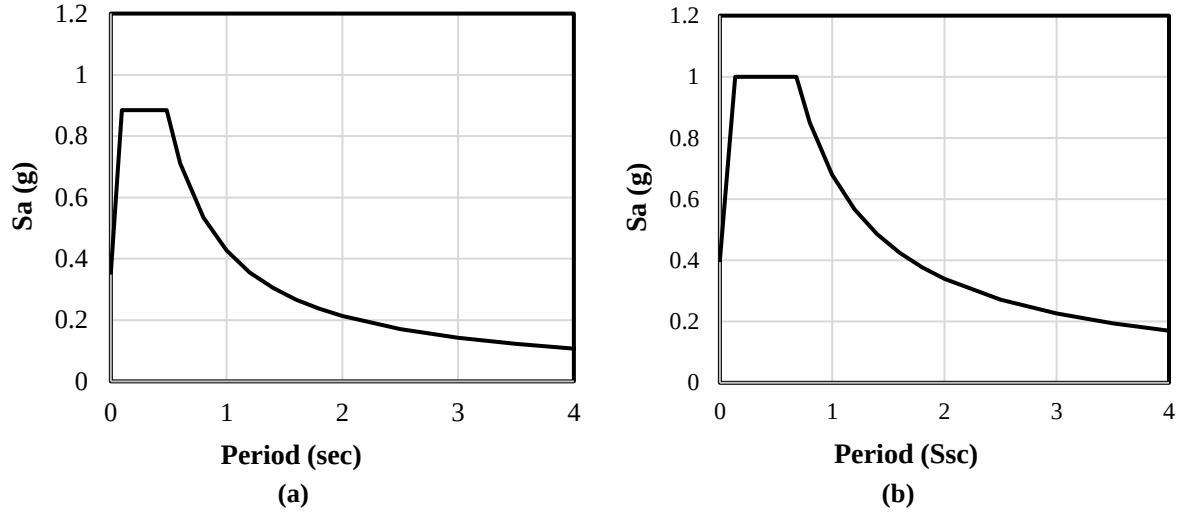

Fig. 5. The design spectra: a) For the "C" type soil; and b) For the "D" type soil

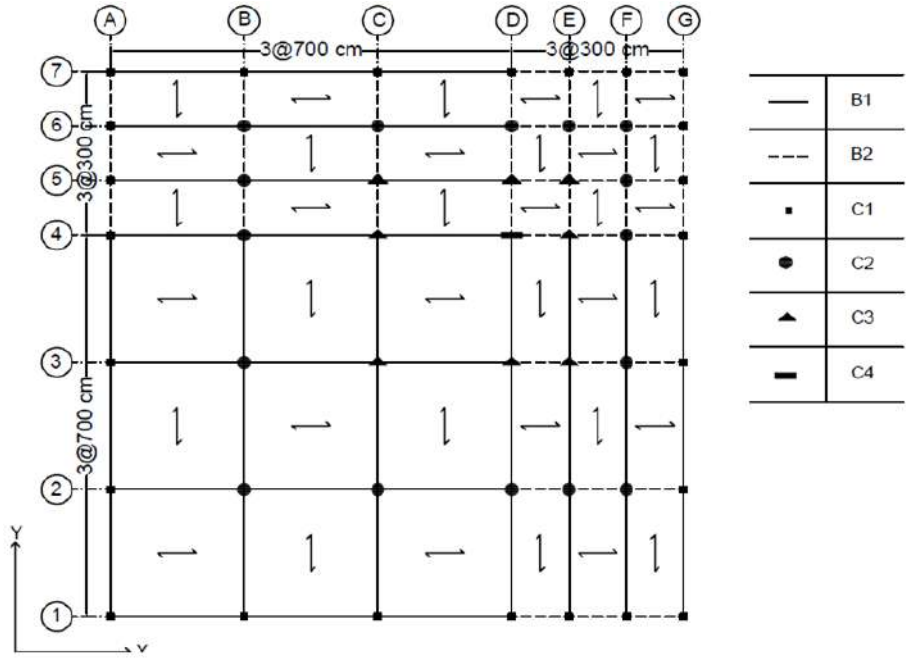

Fig. 6. Beam and column types

Table 2. Fundamental periods of the buildings on each soil type.

No. of stories	Soil C	Soil D
4	0.839	0.741
7	1.480	1.269
10	2.073	1.763

4. Nonlinear Modelling of the Structures

The basic elements of a moment frame are its beams, columns, and panel zones. From the viewpoint of nonlinear modeling, the beams are different from the columns regarding the fact that they are mainly under a two-dimensional (2D) set of a single bending moment in addition to a vertical shear force. In contrast, the internal loads of a columns belong to a three-dimensional (3D) set of forces where in addition to the axial force, a pair of bi-directional bending moments act over the horizontal axes. Then, the nonlinear modelling of columns is much more complex than beams because the interaction between all three internal loads has to be taken into account. The third element, the panel zone, is a 2D medium under a set of 2D loads including an axial force, a bending moment, and horizontal and vertical shear forces acting over its four sides. Because of its small aspect ratio, its behavior is mainly governed by shear deformations.

Considering the above facts, the OpenSees software (McKenna, 2017) has been selected for this study. For modeling of line elements, i.e. beams and columns, it is possible to use the concepts of concentrated and/or distributed plasticity along the length of the members. Since the maximum bending moment under the combination of gravity and seismic loads generally happens only at the end points of the beams and columns, it is customary to assume that selecting a concentrated plasticity approach at such locations, while the rest of the members being free to act elastically, will suffice for engineering applications. The concentrated plasticity approach itself comes in two variations in OpenSees, including the completely-nonlinear moment-rotation (M-θ) spring and the bi-linear longitudinal fibers. The nonlinear M-θ spring has the advantage of modeling the post-elastic and stiffness/strength degradation of the member section. On the other hand, it cannot deal with bi-directional bending. Therefore, it is suitable for modeling the nonlinear flexural behavior of beams only. The one-dimensional fiber elements are introduced by dividing the cross-section into several small areas and defining a fiber at each central point of the area elements along the member axis. Each fiber is known by its specific bi-linear stress-strain behavior. Altogether, the fibers comprise the whole cross section and its mechanical behavior. It is an ideal element for complex cross sections and loadings, but it can only result in a bi-linear behavior without stiffness/strength degradation. However, it is accurate enough if the flexural deformation, i.e. plastic hinge rotations, are not larger than small-enough values. Since in special moment frames the strong column-week beam rule applies, it is logical to anticipate that the inelastic action in the columns, if it happens ever in the frames under study, will not be much demanding. Therefore, the fiber elements are utilized for modelling the nonlinear behavior at the column ends. The fibers can be of steel01 or steel02 types; here the steel02 element is opted because of the more realistic gradual transition of stiffness between its two branches. The M-θ spring and the steel02 elements are shown in Figure 7.

For defining the steel02 material, the Young modulus and the yield strength of steel, E and F_y, respectively, and the post-yield elastic modulus reduction factors, b, have to be introduced. In fact, the b-factor shows the slope of the line connecting the yield point to the point of ultimate strength in the plane of stress-strain. Values of F_y, E, and b taken for St-37 steel in this study are 240 MPa, 206 GPa and 0.007, respectively.

The M-θ behavior shown in Figure 7 is defined by knowing M_y (yield moment), M_c (ultimate moment), c (residual moment factor), θ_y (yield rotation), θ_c (failure rotation), and θ_u (ultimate rotation), out of which, θ_c and θ_u are known by introducing the parameters a and b. This model is known as Bilin, or the modified Ibarra-Krawinkler model in OpenSees, and forms the basic backbone curve in ASCE 41-17

(2017). Its deterioration parameters are defined based on the works of Lignos and Krawinkler (2011). The relations and their numerical values for the above parameters based on the mentioned references as used in this study, are as follows.

The parameters *a*, *b*, and *c* in Figure 7, for the beams are functions of compactness of the section, shear characteristics and unbraced length. According to ASCE 41-17, for a beam with an I-shape and seismically compact section having sufficiently close lateral bracings, values of the mentioned parameters are a = $9\theta_y$, b = $11\theta_y$, and c = 0.6. The yield rotation θ_y, the shear effect factor η and the rate of cyclic deterioration Λ, can be calculated by Eqs. (1-3), respectively. Numerical values of the parameters are mentioned in Table 3.

The rate of stiffness and strength cyclic deterioration is determined using the rule developed by Rahnama and Krawinkler (1993), which is defined on the basis of the hysteretic energy dissipated during the cyclic loading of the component. Each member is assumed to have a reference hysteretic energy dissipation capacity E_t, which is an intrinsic property of the components regardless of the applied loading history. The reference hysteretic energy dissipation capacity of the member is expressed as a multiple of Λ and M_y, where Λ and M_y are the reference cumulative rotation capacity and the effective yield strength of the component, respectively.

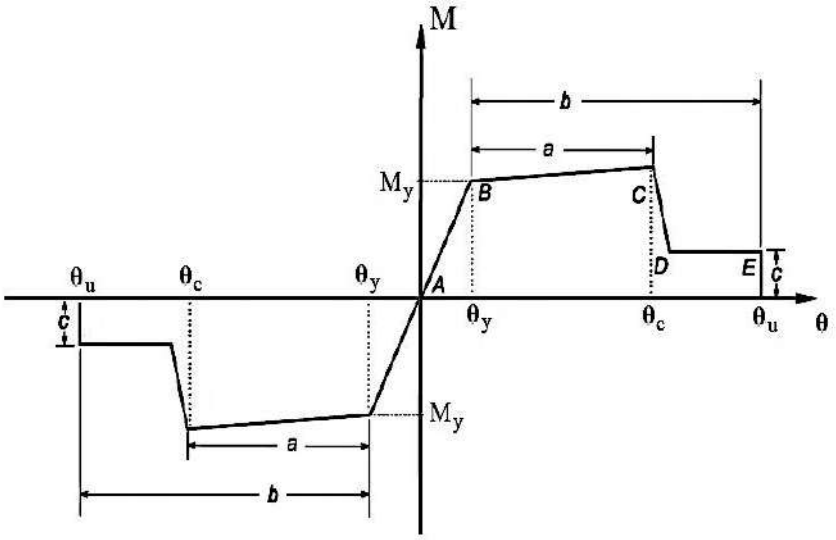

(a)

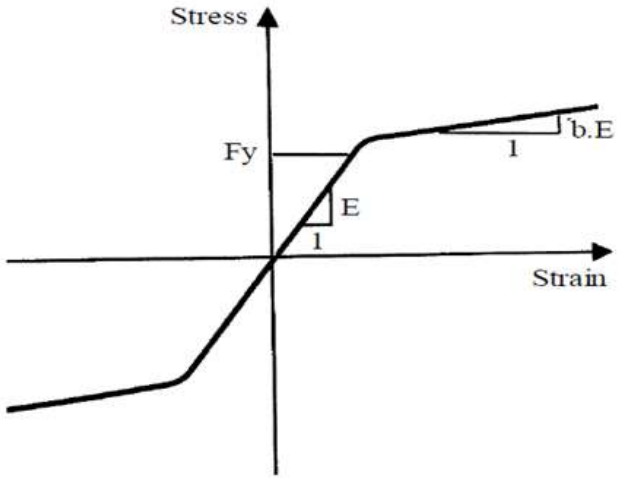

(b)

Fig. 7. a) The M-θ model for the beams per ASCE 41-17 (2017); and b) The steel02 material for the columns

Table 3. Nonlinear modeling parameters of the beams.

Beam section	Modeling parameters						
	a	***b***	***c***	θ_y	θ_c	θ_u	Λ
IPE240	0.041	0.050	0.600	0.005	0.046	0.055	1.631
IPE270	0.037	0.045	0.600	0.004	0.041	0.049	1.434
IPE300	0.033	0.041	0.600	0.004	0.037	0.044	1.319
IPE330	0.030	0.037	0.600	0.003	0.033	0.040	1.252
IPE360	0.028	0.034	0.600	0.003	0.031	0.037	1.244
IPE400 (spanning 3 m)	0.025	0.030	0.600	0.003	0.028	0.033	1.188
IPE400 (spanning 7 m)	0.058	0.071	0.600	0.006	0.064	0.077	1.188
IPE450	0.052	0.064	0.600	0.006	0.058	0.069	1.155

$$\theta_y = \frac{M_{pe} L(1+\eta)}{6EI} \quad (1)$$

$$\eta = \frac{12EI}{L^2 G A_s} \quad (2)$$

$$\Lambda = \frac{E_t}{M_y} = 495\left(\frac{h}{t_w}\right)^{-1.34}\left(\frac{b_f}{2t_f}\right)^{-0.595}\left(\frac{c_{unit}^2 F_y}{355}\right)^{-0.360} \quad (3)$$

Since the studied structures have been designed using contemporary building codes, it can be assumed that the panel zones will not suffer from bending or shear failure because of the use of appropriate continuity and (if needed) doubler plates. Then, it will be only necessary to take into account their flexibility as it can amplify the story drifts and consequently, add to the plastic hinge rotations. This effect can be dealt with either by continuing the beam line to the axis of columns in each span or by introducing a panel zone that includes elastic elements at the ends of beams through the column depth (Altoontash, 2004). In this study, the second approach has been selected to gain more accuracy. The elastic elements consist of a section including the continuity plates and the column web. Also, by assuming direct connection of the beam to the column, the distance from face of column to plastic hinge is considered to be zero.

5. The Ground Motions

The input records are used for IDA analysis. It means that first a set of appropriate earthquake records has to be selected for each building. Then, it should be scaled down and then gradually up, to be input to the model buildings to calculate their desirable responses at each scaled level of ground shaking. Therefore, at the first step the suitable ground motions have to be selected. The procedure recommended by ASCE 7-16 is followed for this purpose. Here it is meant to have a mean response spectrum of the selected earthquake records that does not fall below 90% of the design spectrum of Figure 5. The selection process is fulfilled in two steps. At the first step, all of the earthquake records that satisfy the criteria for three characteristics are chosen. The first step criteria are:

Magnitude between 6.5-7.5 (to be large enough), epicentral distance between 20-50 km (near-field effects are not meant), average shear wave velocity of the site soil being corresponding to the soil type C (366-762 m/sec) or D (183-365 m/sec) per case.

Following the above procedure, 131 and 193 pairs of earthquake records are found for the soil types C and D, respectively, using the PEER NGA database.

ASCE 7-16 requires that number of earthquake record pairs to be at least 11 for the nonlinear dynamic analysis of each building. It also recommends use of the records of only one station for each earthquake to prevent the analysis from being biased toward that seismic motion. Then, since number of the selected earthquakes is more than 11 for each soil type, and there are multiples of stations for a certain earthquake, the second step is taken by calculating the Square Root of Sum of the Squares (SRSS) of the pair of

response spectra of each ground motion. For each SRSS spectrum, a scale factor is calculated such that nowhere between 0.2T-2T, it falls below 90% of the corresponding design spectrum of Figure 5, where T: is the fundamental period of the building under study. It means that after scaling, at the lowest point each SRSS spectrum will only touch the 90% design spectrum. Between different stations of a specific earthquake, the one having the nearest scale factor to unity is selected. Again, between different earthquakes, the first 11 ground motions with their selected SRSS spectra having scale factors closer to unity are chosen. This way, the records with maximum similarity to the seismic nature, i.e. design spectrum, of the site are selected for analysis.

The earthquakes records selected for each building as a result of the above procedure are listed in Table 4. The SRSS response spectra of the selected records are shown in Figure 8.

Table 4. The selected earthquake records: a) For the C type soil; and b) For the D type soil

Order	NGA No.	Earthquake name	Year	Magnitude	PGA (g)	For buildings having No. of stories equal to:
(a)						
1	15	Kern County	1952	7.36	0.180	4, 7, 10
2	78	San Fernando	1971	6.61	0.151	10
3	79	San Fernando	1971	6.61	0.109	4, 7
4	755	Loma Prieta	1989	6.93	0.485	4
5	787	Loma Prieta	1989	6.93	0.277	7, 10
6	963	Northridge-01	1994	6.69	0.568	4, 7, 10
7	1762	Hector Mine	1999	7.13	0.182	4, 7, 10
8	3750	Cape Mendocino	1992	7.01	0.265	4, 7, 10
9	3756	Landers	1992	7.28	0.188	4, 7
10	3757	Landers	1992	7.28	0.139	10
11	4016	San Simeon_ CA	2003	6.52	0.165	4, 7, 10
12	4213	Nigata	2004	6.63	0.405	4, 7, 10
13	4858	Chuetsu-Oki_ Japan	2007	6.80	0.251	4, 10
14	4868	Chuetsu-Oki_ Japan	2007	6.80	0.180	7
15	6891	Darfield_ New Zealand	2010	7.00	0.109	7
16	6948	Darfield_ New Zealand	2010	7.00	0.146	4
17	6971	Darfield_ New Zealand	2010	7.00	0.116	10
(b)						
1	20	Northern Calif-03	1954	6.50	0.203	4, 7, 10
2	169	Imperial Valley-06	1979	6.53	0.350	4, 7, 10
3	730	Spitak_ Armenia	1988	6.77	0.200	4, 7, 10
4	776	Loma Prieta	1989	6.93	0.370	4, 7, 10
5	958	Northridge-01	1994	6.69	0.125	4, 7, 10
6	1100	Kobe_ Japan	1995	6.90	0.231	4
7	1110	Kobe_ Japan	1995	6.90	0.210	7, 10
8	3754	Landers	1992	7.28	0.310	7, 10
9	3758	Landers	1992	7.28	0.116	4
10	4849	Chuetsu-Oki_ Japan	2007	6.80	0.250	10
11	4853	Chuetsu-Oki_ Japan	2007	6.80	0.274	4, 7
12	5780	Iwate_ Japan	2008	6.90	0.354	4
13	5814	Iwate_ Japan	2008	6.90	0.320	7, 10
14	5988	El Mayor-Cucapah_ Mexico	2010	7.20	0.280	7, 10
15	5990	El Mayor-Cucapah_ Mexico	2010	7.20	0.255	4
16	6923	Darfield_ New Zealand	2010	7.00	0.360	7, 10
17	6953	Darfield_ New Zealand	2010	7.00	0.220	4

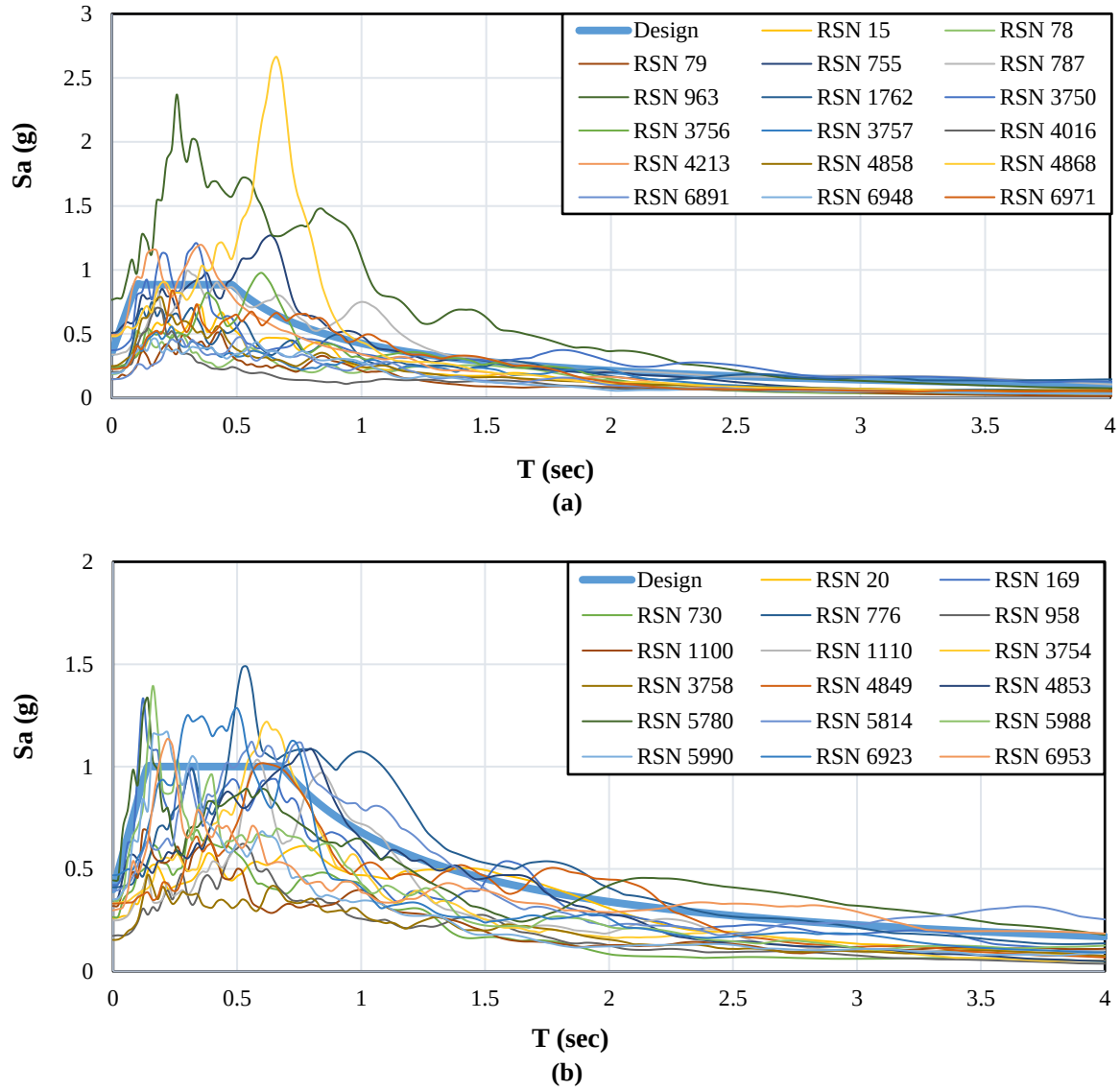

Fig. 8. The SRSS response spectra of the selected records: a) For the "C" type soil; and b) For the "D" type soil

6. Results of the Analysis

The nonlinear dynamic analysis results are presented in this section. In the first part, a verification study is accomplished. Then, the various cases of torsional eccentricity are introduced. Finally, nonlinear dynamic responses are presented.

6.1. The Verification Study

To assess the accuracy of the nonlinear modeling as described in Section 4, the 4-story building of Farahani et al. (2019) is selected. The configuration of that building is very similar to the 4-story structure of the current study. In Figure 8, time history of the lateral displacement of the roof is shown under the Loma Prieta earthquake, NGA No. 755. A very good similarity of responses between the original and current study is observed. The maximum relative differences between the responses is only about 10%.

6.2. Torsional Eccentricity Cases

According to the common plan of the buildings (Figure 4), center of stiffness is deviated toward North-East. Also, as explained in Section 2, assuming eccentricity ratios larger than 10-15% is not realistic for moment frame buildings. Then, the study is implemented for the eccentricity ratios 0%, 5%, 10%, and 15%. To make for such eccentricities, the plan is divided into some subdomains and a certain part of the total partition and live loads is

applied on each area such that the presumed torsional eccentricity is attained. It is to be noted that the total value of the partition plus live loads is the same in all of the cases. It is equal to the total load mentioned in Section 3.

The plan configuration and each superimposed load in each area are shown in Figure 9.

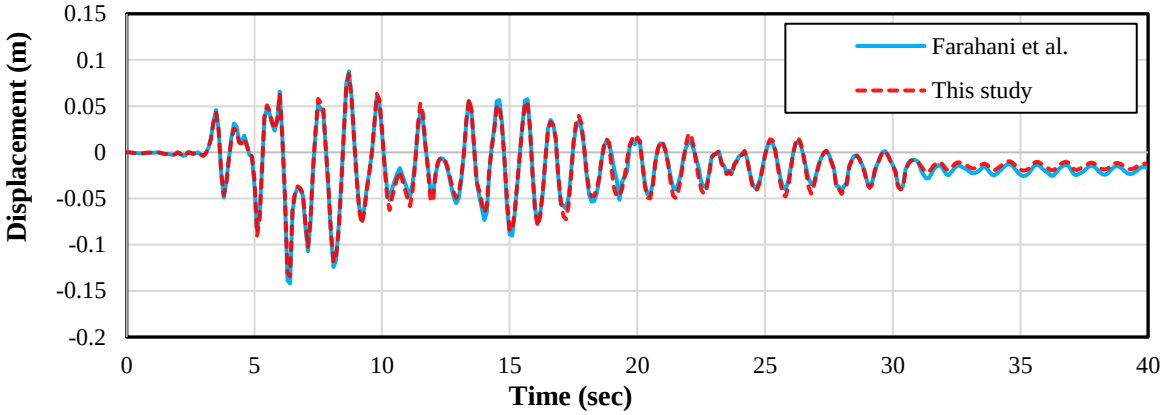

Fig. 9. Time history of the roof displacement of the 4-story building of Farahani and Behnamfar (2019)

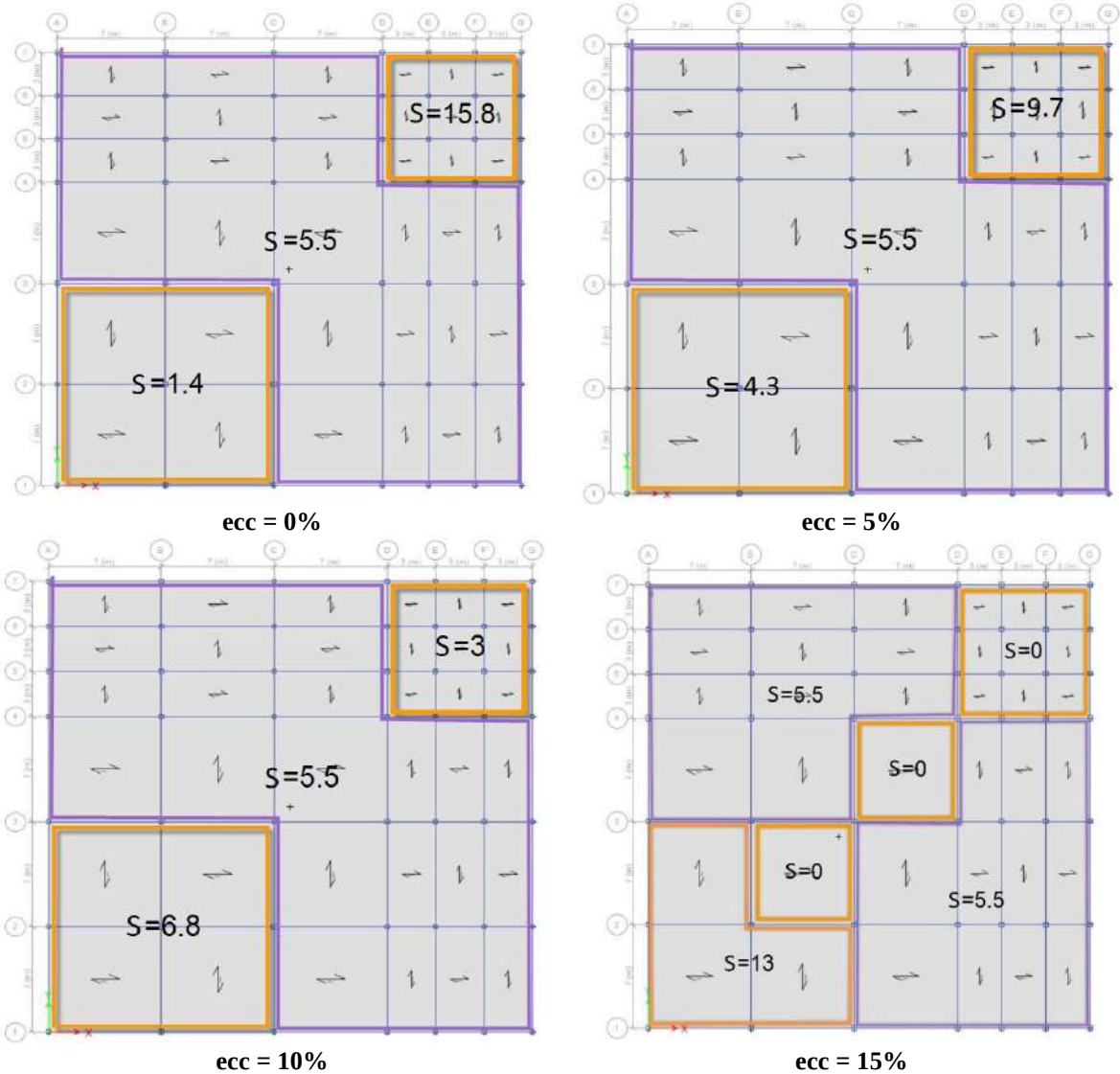

ecc = 0% **ecc = 5%**

ecc = 10% **ecc = 15%**

Fig. 10. Value of the superimposed loads in each part of the plan and the corresponding torsional eccentricity (ecc). S is for superimposed and each number is the load intensity in KN/m^2

It is to be reminded that the buildings were designed for a uniform superimposed load. It is assumed that change in the load distribution happens afterwards during service.

6.3. The Analysis Results

The IDA and fragility curves have been calculated for the 4, 7, and 10-story buildings having four cases of torsional eccentricity on two types of soils. Therefore, presenting all of the calculated results is not possible. Instead, it is opted to present details of the computation for the 4-story building on the soil type C for example, and then the final results for other buildings and for the soil type D.

6.3.1. Analysis Results of the 4-Story Building on the Soil Type C

The IDA curves of the 4-story building are illustrated in Figure 10. In this figure, each seismic record is amplified in sequences almost 20 times to finally make the building to reach its collapse state, where the lateral stiffness is almost zero. At each intensity level for each earthquake, the maximum interstory drift is determined for the building and marked as a point on the IDA plot against the first-mode spectral acceleration of the same building at the same shaking level. The IDA curve if drawn by connecting these points together. It should be noted that the maximum drift happens at a certain story on the soft side of the plan.

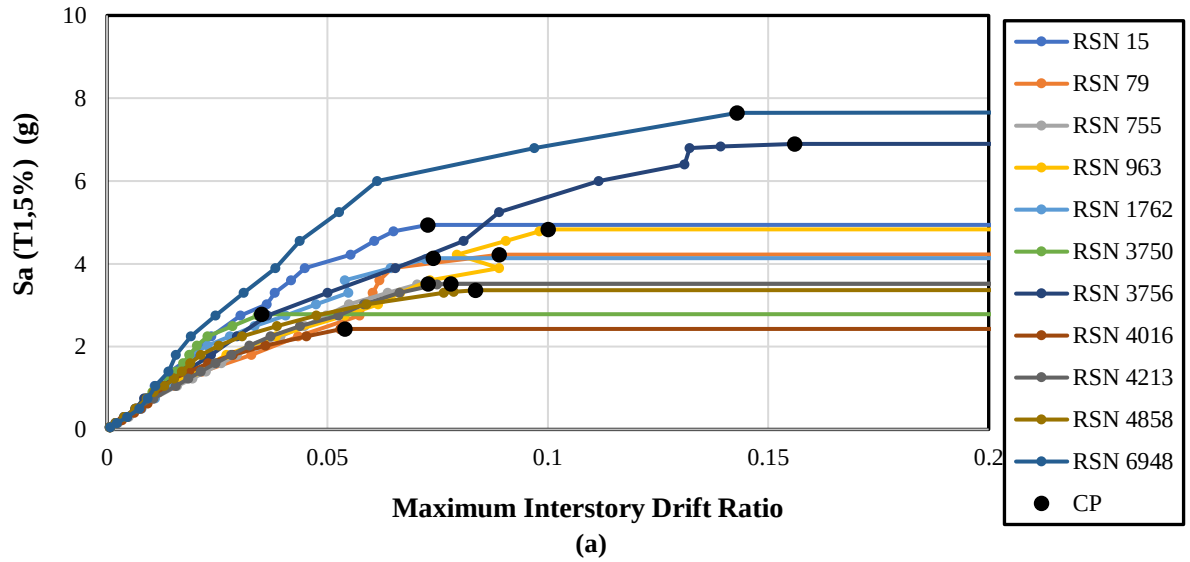

(a)

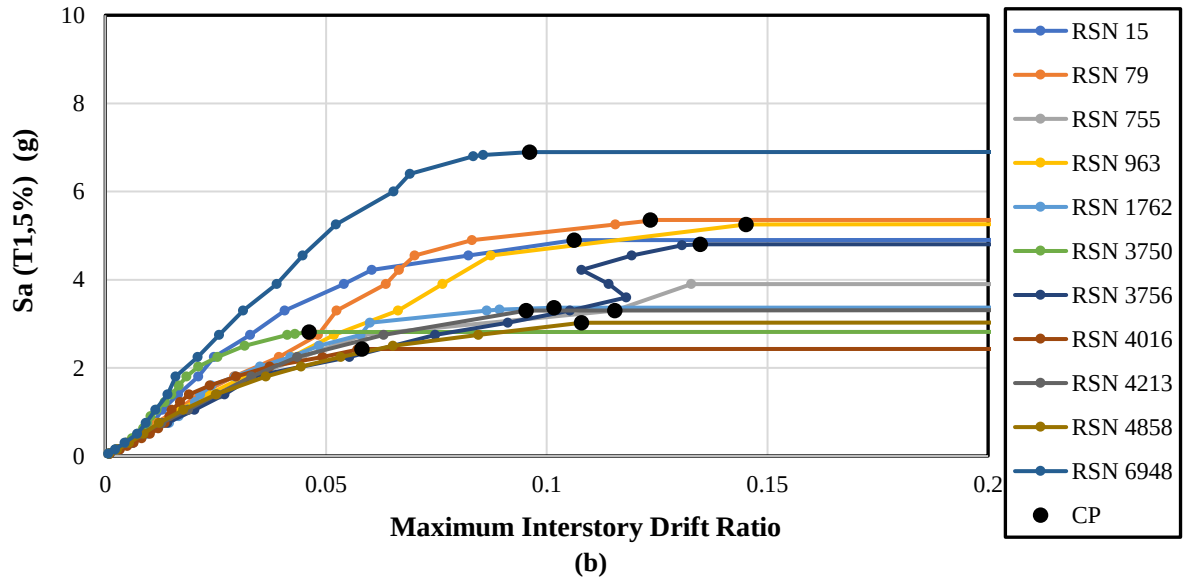

(b)

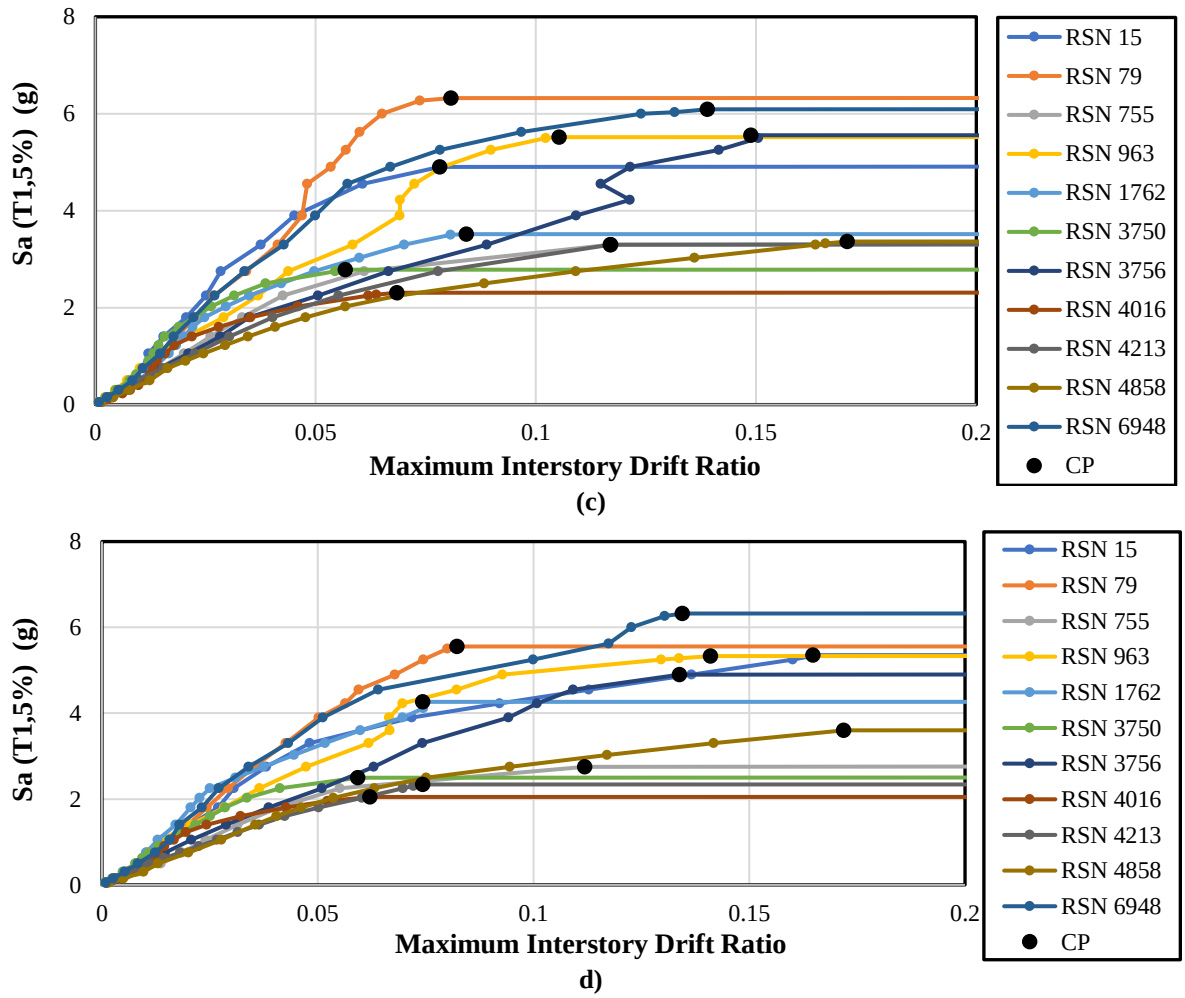

Fig. 11. The IDA curves of the 4-story building on the soil type C for the eccentricity ratios of: a) 0%; b) 5%; c) 10%; and d) 15%

Each of the four parts of Figure 10 gives 11 values of collapse spectral acceleration. If a Log-Normal distribution is assumed for these 11 values, it will be possible to depict the fragility curve that represents the probability of collapse against the increasing spectral accelerations. The resulting curves are shown for various eccentricities in the case of the 4-story building on the soil types C and D in Figure 11.

Similarly, fragility curves of the other buildings on both soil types are shown in Figures 13 and 14.

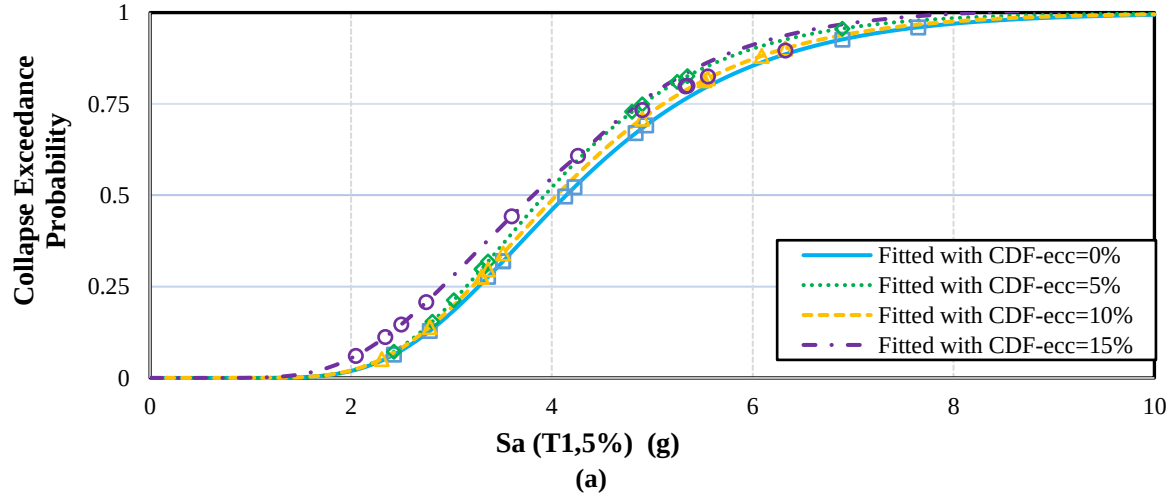

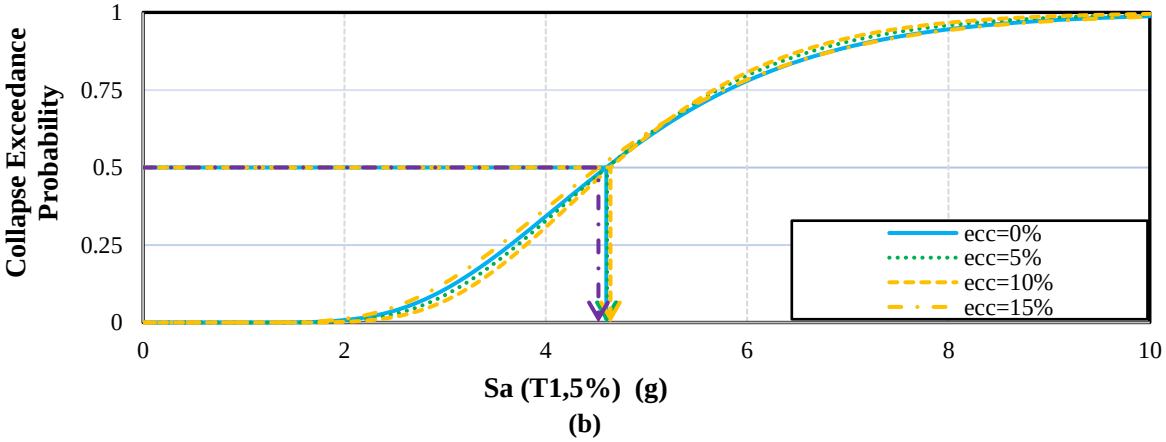

(b)

Fig. 12. Fragility curves of the 4-story building under various eccentricities on the soil types: a) C; and b) D

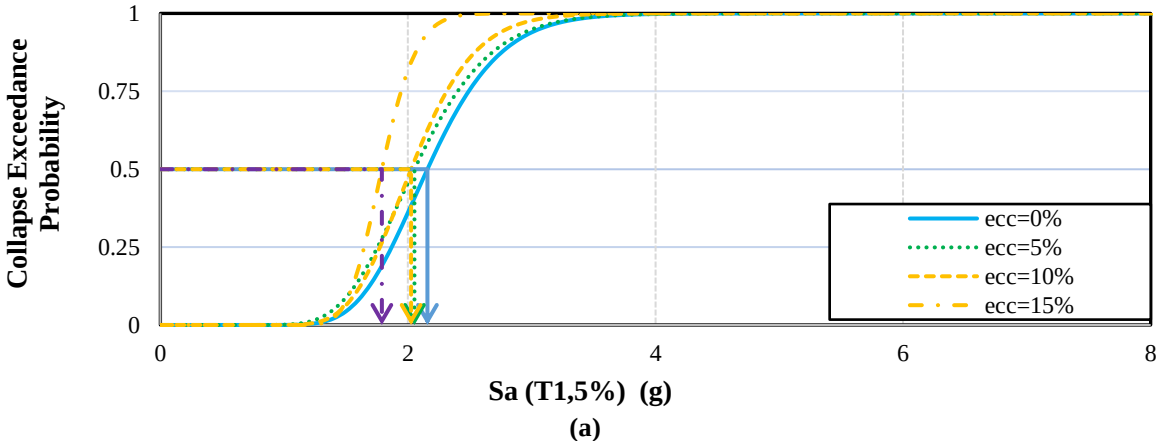

(a)

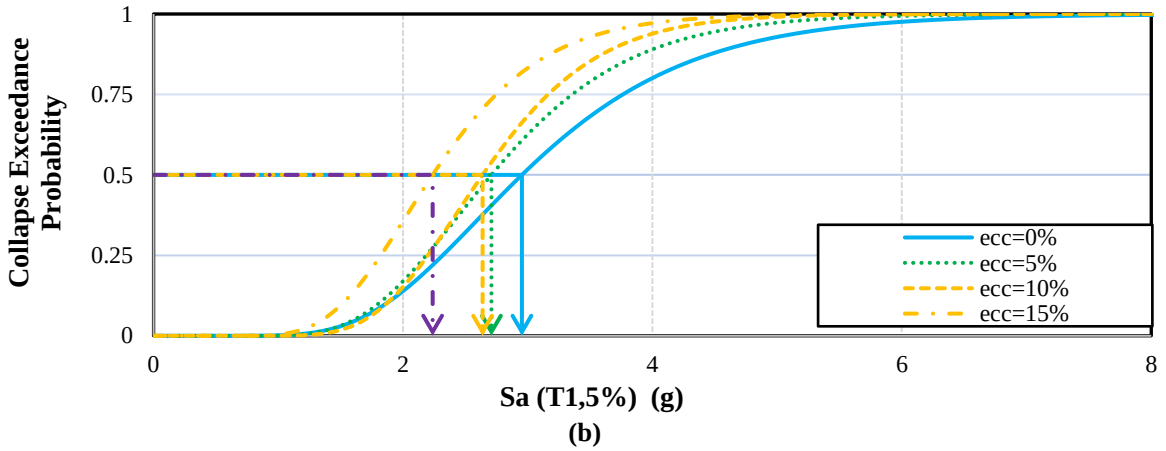

(b)

Fig. 13. Fragility curves of the 7-story building on the soil types: a) C; and b) D

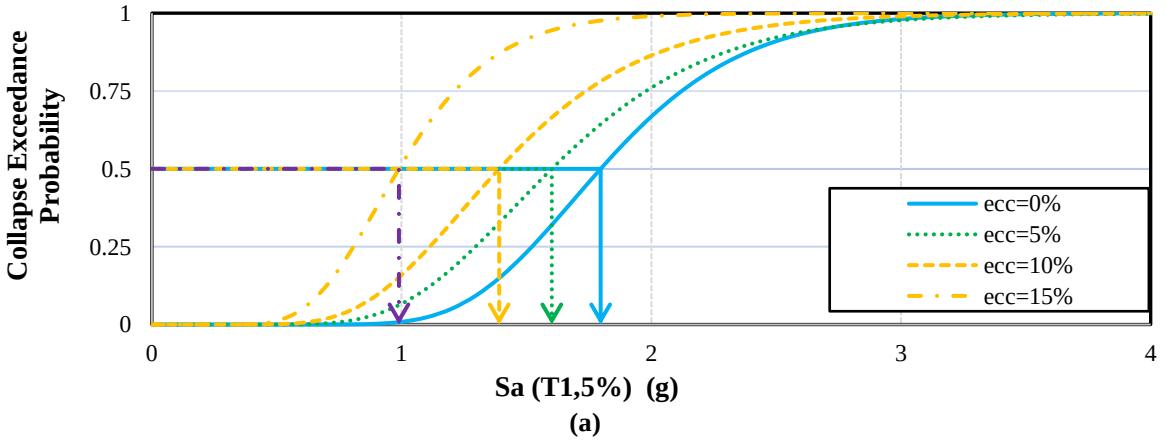

(a)

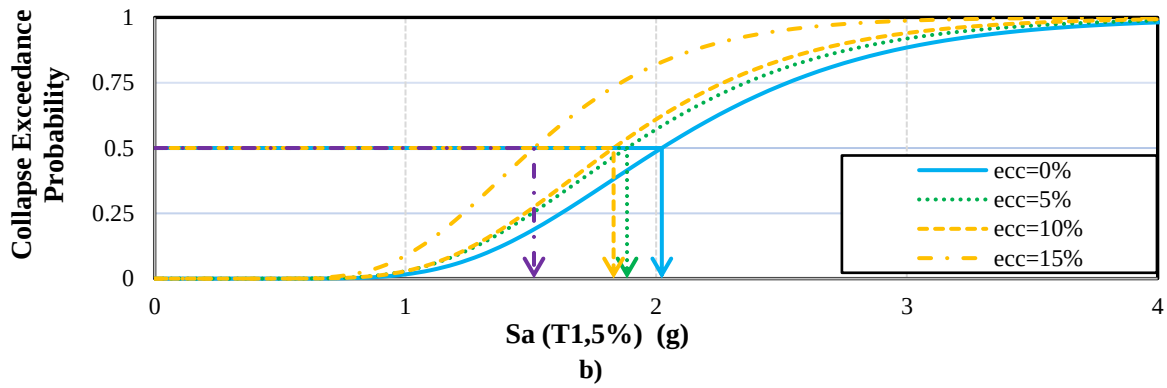

b)

Fig. 14. Fragility curves of the 10-story building on the soil types: a) C; and b) D

As demonstrated in the above figures, in general, increase of torsional eccentricity results in decrease of the collapse spectral acceleration for a certain probability, or in increase of the collapse probability for a certain spectral acceleration.

To have some numerical criteria for comparison, the spectral acceleration at the mean (50%) collapse probability is selected. Furthermore, the Collapse Margin Ratio (CMR) is calculated for each case. It is defined as follows:

$$CMR = \frac{S_{CT}}{S_{MT}} \times C_{3D} \quad (4)$$

where S_{CT} and S_{MT}: are the median collapse and the maximum considered earthquake (MCE) spectral accelerations at the fundamental period of the building, respectively, and C_{3D}: is a correction coefficient equal to 1.0 for 2D and 1.2 for 3D analysis to account for the effect of simultaneous ground motion pairs in the latter analysis. Values of the above parameters are summarized in Table 5 for the soil type C and in Table 6 for the soil type D.

Moreover, Tables 7 and 8 exhibit the reduction percentages of CMR relative to the no-torsion (i.e. zero eccentricity) cases.

Table 5. Collapse margin ratio for the buildings on the soil type C: a) 4-story; b) 7-story; and c) 10-story building

No. of stories	S_a (g)	S_{MT} (g)	S_{CT} (g)				CMR			
			e=0%	e=5%	e=10%	e=15%	e=0%	e=5%	e=10%	e=15%
4	0.77	1.15	4.16	3.95	4.05	3.80	4.34	4.23	4.12	3.97
7	0.49	0.74	2.16	2.05	2.02	1.78	3.53	3.35	3.30	2.91
10	0.37	0.56	1.80	1.60	1.39	0.98	3.89	3.46	3.01	2.12

Table 6. Collapse margin ratio for the buildings on the soil type D: a) 4-story; b) 7-story; and c) 10-story building

No. of stories	S_a (g)	S_{MT} (g)	S_{CT} (g)				CMR			
			e=0%	e=5%	e=10%	e=15%	e=0%	e=5%	e=10%	e=15%
4	0.92	1.38	4.58	4.57	4.64	4.52	3.99	3.98	4.04	3.94
7	0.78	1.17	2.95	2.71	2.63	2.25	3.02	2.78	2.69	2.30
10	0.59	0.88	2.03	1.90	1.82	1.52	2.77	2.59	2.48	2.07

Table 7. Reduction percentages of CMR relative to the no-torsion cases, soil type C.

No. of stories	ecc=5%	ecc=10%	ecc=15%
4	2.6%	5.1%	8.7%
7	5.1%	6.5%	17.6%
10	11.1%	22.8%	45.6%

Table 8. Reduction percentages of CMR relative to the no-torsion cases, soil type D

No. of stories	ecc=5%	ecc=10%	ecc=15%
4	0.2%	1.3%	1.3%
7	8.1%	10.9%	23.7%
10	6.4%	10.3%	25.1%

The above tables clearly show how increase of the torsional eccentricity reduces the collapse margin ratio hence the safety of the buildings. Notably, the decrease of CMR is much more extensive when the eccentricity ratio increases from 10 to 15%. Note that the more significant effect of torsion seen for taller structures is somewhat exaggerated because possibility of existence of a uniform simultaneous eccentricity at all stories, assumed in this study, is low.

Moreover, the reduction percentages are different for the buildings on the two soil types. The design spectral ordinates are larger for the softer soil. The buildings designed under the design spectrum belonging to this soil type are more or less, stronger than their counterparts on the soil type C. Of course, the input motion is correspondingly larger too. Since the ground motions are different for the two soil type cases, finding a ready reason is not possible for the observed difference between the CMR values for similar cases on the two soil types.

For the taller buildings of this study, the CMR reduction surpasses a desirable 10% threshold sooner, i.e. under smaller eccentricities. Therefore, the design regulations of buildings should be modified in such a way that results in more or less identical CMRs for different buildings at similar eccentricities.

In the following, results of the present study are compared with two similar studies.

In the study of Manie et al (2015), described in the Introduction, the collapse behavior of asymmetric RC-SMF structures was evaluated. The studied buildings were in three and six stories with one-way mass eccentricity and were subjected to two-component earthquakes. According to the IDA curves in terms of SRSS drift of the 6-story structures, reduction percentage of the safety margin compared to structures without torsion were respectively 0%, 37% and 42% for structures with eccentricity ratios of 10%, 20% and 30%. Thus, for structures with eccentricity ratios of more than 10%, reduction of the safety margin was considerable. Therefore, it can be said that the results of the mentioned study are in good agreement with those of the seven- and ten-story structures of the present study, where the case of 15% eccentricity ratio significantly affects the safety margin.

Badri et al. (2016) investigated effects of variability of deterioration parameters on the response of RC-SMF buildings. The studied five-story buildings assumed to be either symmetrical or having 10% or 20% mass eccentricity under unidirectional earthquakes. Comparison of the IDA curves of the studied structures showed that increasing the eccentricity of the structures had a slight decreasing effect on the collapse spectral acceleration. Therefore, the results of their study are consistent with the results of the four-story structure of the present study.

Finally, by reviewing the previous studies, it can be said that only a small number of studies include explicit results related to the effect of torsion on the structure collapse behavior. Also, the range of their studied structures are limited. The results of these few studies are not completely consistent with each other, which may be due to their different assumptions. One of the advantages of the present study is the wider range of structures studied here than the previous studies, which can lead to more comprehensive and reliable conclusions.

7. Conclusions

Fragility curves of 4, 7 and 10-story special steel moment frames were calculated each one under 11 consistent pairs of earthquake motions on two types of soils in this study. The torsional irregularity of the buildings was the result of bi-directional simultaneous stiffness and mass eccentricities. It was observed that:

- Based on a discussion conducted in the form of examples with exaggerated eccentricity conditions, after the final

design process of moment frame systems, the stiffness center was shifted and the torsional eccentricity was reduced considerably. Therefore, it seems that assuming large eccentricity values for moment frame structures in previous studies has not been realistic.

- With regard to the previous item, it can be said that taking eccentricity ratios more than about 15% is not realistic for moment frame buildings. The current building design regulations tend to decrease the eccentricity in final design of the members.
- The median collapse probabilities of the studied buildings were increased by torsional eccentricity. Value of the increase was not considerable up to an eccentricity ratio equal to about 10%. Eccentricity ratios larger than 10% had a significant effect on the collapse behavior of 7 and 10-story buildings.
- For the eccentricity ratio of 15%, the amount by which the collapse margin ratio decreased was extensive, especially for the taller buildings. Such eccentricities should be prevented in real design tasks. Accordingly, seismic building code should be more developed and specific to eccentricity ratios larger than 10%.
- Effect of torsion on the collapse margin ratio of the studied buildings designed for stiffer soil conditions was generally more extensive, even though their base was assumed to be fixed. Further studies on the structural torsion on different soils should account for base flexibility.

As a final point of consideration, it should be mentioned that the main limitations of this study are the facts that it includes short and midrise buildings (up to 10 stories) consisting of special steel moment frames on two types of soils (stiff and firm).

Though the results are specifically applicable to the cases within the same limitations, conclusions that can be named to be the generally applicable findings of this study are as follows.

Regarding the realistic limit of the eccentricity ratio, the fact that torsional eccentricity increases the collapse probability especially for taller buildings and the effect of soil flexibility on the collapse probability due to torsional eccentricity requires more research.

8. References

AISC360-16. (2016). *Specification for structural steel buildings*, American Institute of Steel Construction (AISC), Chicago.

Altoontash, A. (2004). "Simulation and damage models for performance assessment of reinforced concrete beam-column joints", Ph.D. Thesis, Stanford University Stanford, California.

Anvarsamarin, A., Rahimzadeh Rofooei, F. and Nekooei, M. (2020). “Torsion effect on the RC structures using fragility curves considering with soil-Structure interaction”, *Journal of Rehabilitation in Civil Engineering*, 8(1), 1-21. https://doi.org/10.22075/jrce.2019.16080.1302.

ASCE/SEI 7-16. (2016). *Minimum design loads and associated criteria for buildings and other structures*, ASCE Standard ASCE/SEI 7-16, American Society of Civil Engineers (ASCE).

ASCE41-17. (2017). *Seismic rehabilitation of existing buildings*, ASCE Standard ASCE/SEI 41-17, American Society of Civil Engineers (ASCE).

Ashwini, P. and Stephen, S. (2022). “Seismic fragility analysis of structures containing supplemental damping system”, *International Journal of Scientific and Research Publications*, 12(1), 417-425, https://doi.org/10.29322/IJSRP.12.01.2022.p12156.

Aziminejad, A. and Moghadam, A. (2010). "Fragility-based performance evaluation of asymmetric single-story buildings in near field and far field earthquakes", *Journal of Earthquake Engineering*, 14(6), 789-816, https://doi.org/10.1080/13632460902837728.

Badri, R.K., Moghadam, A. and Nekooei, M. (2016). "The influence of deterioration parameters on the response of low-rise symmetric and asymmetric RC buildings", *International Journal of Civil Engineering*, 14(8), 547-560, https://doi.org/10.1007/s40999-016-0038-x.

Bensalah, M.D., Bensaibi, M. and Modaressi, A. (2013). "Assessment of the torsion effect in asymmetric buildings under seismic loading", *Applied Mechanics and Materials*, 256, 2222-2228, https://doi.org/10.4028/www.scientific.net/AMM.256-259.2222.

Chen, P. and Collins, K.R. (2001). "Some observations on performance-based and

reliability-based seismic design of asymmetric building structures", *Engineering Structures*, 23(8), 1005-1010, https://doi.org/10.1016/S0141-0296(00)00108-5.

Chiou, B., Darragh, R., Gregor, N. and Silva, W. (2008). "NGA project strong-motion database", *Earthquake Spectra*, 24(1), 23-44, https://doi.org/10.1193/1.2894831.

Collins, K., Wen, Y.K. and Foutch, D. (1996). "Dual-level seismic design: a reliability-based methodology", *Earthquake Engineering & Structural Dynamics*, 25(12), 1433-1467, https://doi.org/10.1002/(SICI)1096-9845(199612)25:12<1433::AID-EQE629>3.0.CO;2-M.

Das, P.K., Dutta, S.C. and Datta, T.K. (2021). "Seismic behavior of plan and vertically irregular structures: State of art and future challenges", *Natural Hazards Review*, 22(2), 04020062, https://doi.org/10.1061/(ASCE)NH.1527-6996.0000440.

DeBock, D.J., Liel, A.B., Haselton, C.B., Hooper, J.D. and Henige, R.A. Jr. (2014). "Importance of seismic design accidental torsion requirements for building collapse capacity", *Earthquake Engineering & Structural Dynamics*, 43(6), 831-850, https://doi.org/10.1002/eqe.2375.

Dehghani, E. and Soltanimohajer, M. (2022). "Development of the fragility curves for conventional reinforced concrete moment resistant frame structures in Qods Town, Qom City, Iran", *Civil Engineering Infrastructures Journal*, 55(1), 31-41, https://doi.org/10.22059/CEIJ.2021.306156.1690.

De Stefano, M. and Pintucchi, B. (2008). "A review of research on seismic behaviour of irregular building structures since 2002", *Bulletin of Earthquake Engineering*, 6(2), 285-308, https://doi.org/10.1007/s10518-007-9052-3.

De Stefano, M. and Mariani, V. (2014). "Pushover analysis for plan irregular building structures", *Perspectives on European Earthquake Engineering and Seismology*, 34, 429-448, https://doi.org/10.1007/978-3-319-07118-3_13.

Eivani, H., Moghadam, A.S., Aziminejad, A. and Nekooei, M. (2018). "Seismic response of plan-asymmetric structures with diaphragm flexibility", *Shock and Vibration*, 2018, 1-18, https://doi.org/10.1155/2018/4149212

Elghazouli, Y. (2010). "Assessment of European seismic design procedures for steel framed structures", *Bulletin of Earthquake Engineering*, 8, 65-89, http://doi.org/10.1007/s10518-009-9125-6.

Farahani, D., Behnamfar, F., Sayyadpour, H. and Ghandil, M. (2019). "Seismic impact between adjacent torsionally coupled buildings", *Soil Dynamics and Earthquake Engineering*, 117, 81-95, https://doi.org/10.1016/j.soildyn.2018.11.015.

Fujii, K. (2014). "Prediction of the largest peak nonlinear seismic response of asymmetric buildings under bi-directional excitation using pushover analyses", *Bulletin of Earthquake Engineering*, 12(2), 909-938, http://doi.org/10.1007/s10518-013-9557-x.

Ferraioli, M., Lavino, A., Mandara, A. (2014). "Behaviour factor of code-designed steel moment-resisting frames", *International Journal of Steel Structures*, 14(2), 243-254, http://doi.org/10.1007/s13296-014-2005-1.

Ferraioli, M. (2015). "Case study of seismic performance assessment of irregular RC buildings: hospital structure of Avezzano (L'Aquila, Italy)", *Earthquake Engineering and Engineering Vibration*, 14(1), 141-156, http://doi.org/10.1007/s11803-015-0012-7.

Gioncu, V. and Mazzolani, F. (2010). *Seismic design of steel structures*, Taylor & Francis Ltd., https://doi.org/10.1201/b16053.

Habiby, Y.M. (2020). "Collapse analysis of torsional moment frame structures against earthquake", M.Sc. Thesis, Isfahan University of Technology.
Han, S.W., O Kim, T., Kim, D.H. and Baek, S.J. (2017). "Seismic collapse performance of special moment steel frames with torsional irregularities", *Engineering Structures*, 141, 482-494, https://doi.org/10.1016/j.engstruct.2017.03.045.

Hentri, M., Hemsas, M. and Nedjar, D. (2018). "Vulnerability of asymmetric multi-storey buildings in the context of performance-based seismic design", *European Journal of Environmental and Civil Engineering*, 25, 1-22, http://doi.org/10.1080/19648189.2018.1548380.

Hwang, S.-H., Mangalathu, S., Shin, J., and Jeon, J.-S. (2021). "Machine learning-based approaches for seismic demand and collapse of ductile reinforced concrete building frames", *Journal of Building Engineering*, 34, 101905, https://doi.org/10.1016/j.jobe.2020.101905.

Kazemi, F. and Jankowski, R. (2023). "Machine learning-based prediction of seismic limit-state capacity of steel moment-resisting frames considering soil-structure interaction", *Computers & Structures*, 274, 106886, https://doi.org/10.1016/j.compstruc.2022.106886.

Landolfo, R. (2018). "Seismic design of steel structures: New trends of research and updates of Eurocode 8", *Geotechnical, Geological and Earthquake Engineering*, 46, 413-438, http://doi.org/10.1007/978-3-319-75741-4_18.

Lignos, D.G. and Krawinkler, H. (2011). "Deterioration modeling of steel components in support of collapse prediction of steel moment frames under earthquake loading", *Journal of Structural Engineering*, 137(11), 1291-1302,

http://doi.org/10.1061/(ASCE)ST.1943-541X.0000376.

Manie, S., Moghadam, A.S. and Ghafory-Ashtiany, M. (2015). "Collapse behavior evaluation of asymmetric buildings subjected to bi-directional ground motion", *The Structural Design of Tall and Special Buildings*, 24(8), 607-628, https://doi.org/10.1002/tal.1202.

Marušić, D. and Fajfar, P. (2005). "On the inelastic seismic response of asymmetric buildings under bi-axial excitation", *Earthquake Engineering & Structural Dynamics*, 34(8), 943-963, https://doi.org/10.1002/eqe.463.

Mazzolani F.M. and Piluso V. (1996). *Theory and design of seismic resistant steel frames*, E & FN SPON, an imprint of Chapman & Hall, London, https://doi.org/10.1201/9781482271348.

McKenna, F. (2011). "OpenSees: A framework for earthquake engineering simulation", *Computing in Science & Engineering*, 13(4), 58-66, https://doi.org/10.1109/MCSE.2011.66.

Moon, D.S., Lee, Y.J. and Lee, S. (2018). "Fragility analysis of space reinforced concrete frame structures with structural irregularity in plan", *Journal of Structural Engineering*, ASCE, 144(8), 04018096, https://doi.org/10.1061/(ASCE)ST.1943-541X.0002092.

Moradi, M., Tavakoli, H. and Abdollahzadeh, G.R. (2022). "Collapse probability assessment of a 4-Story RC frame under post-earthquake fire scenario", *Civil Engineering Infrastructures Journal*, 55(1), 121-137, https://doi.org/10.22059/ceij.2021.313241.1718.

Patel, S.A., Darji, A.R., Parikh, K.B. and Patel, B.R. (2016). "Fragility analysis of high-rise building structure", *Journal of Emerging Technologies and Innovative Research (JETIR)*, 3(7), 127-133.

Puppio, M.L., Pellegrino, M., Giresini, L. and Sassu, M. (2017). "Effect of material variability and mechanical eccentricity on the seismic vulnerability assessment of reinforced concrete buildings", *Buildings*, 7(3), 66, https://doi.org/10.3390/buildings7030066.

Rahnama, M. and Krawinkler, H. (1993). "Effect of soft soils and hysteresis models on seismic design spectra", Report 108(TB), The John A. Blume Earthquake Engineering Center, Stanford University, Stanford, CA.

Razmkhah, M.H., Kouhestanian, H., Shafaei, J., Pahlavan, H. and Shamekhi Amiri, M. (2021). "Probabilistic seismic assessment of moment resisting steel buildings considering soft-story and torsional irregularities", 34(11), 2476-2493, http://doi.org/10.5829/IJE.2021.34.11B.11.

Seo, J. (2018). "Seismic fragility characteristics of structural populations with irregularities", *International Journal of Computational Methods and Experimental Measurements*, 6(5), 944-954, https://doi.org/10.2495/CMEM-V6-N5-944-954.

Sharifi, N.P. and Sakulich, A.R. (2014). "Effects of eccentricity and order of vibration modes on the inelastic seismic response of 3D steel structures", In: *Active and Passive Smart Structures and Integrated Systems*, (Vol. 9057, pp. 897-903), SPIE, http://doi.org/10.1117/12.2044345.

Tavakoli, H., Moradi, M., Goodarzi, M. and Najafi, H. (2022). "Outrigger braced system placement effect on seismic collapse probability of tall buildings", *Civil Engineering Infrastructures Journal*, 20, 736-749, https://doi.org/10.1016/j.jobe.2018.09.019.

Xu, C., Deng, J., Peng, S. and Li, C. (2018). "Seismic fragility analysis of steel reinforced concrete frame structures based on different engineering demand parameters", *Journal of Building Engineering*, 20, 736-749, https://doi.org/10.1016/j.jobe.2018.09.019.

Zeng, F., Huang, Y., Zhou, J. and Bu, G. (2022). "Seismic fragility analysis and index evaluation of concrete-filled steel tube column frame-core tube structures", *Journal of Asian Architecture and Building Engineering*, 21(6), 2371-2387, https://doi.org/10.1080/13467581.2021.1972001.

Reviewers

The Editorial Board of the Civil Engineering Infrastructures Journal (CEIJ) would like to express sincere thanks to all reviewers of papers submitted to CEIJ during years 2022 and 2023 for their time and efforts in evaluating papers for this journal.

Abdoli, M.
University of Tehran
Aghabayk, K.
University of Tehran
Ahmadi, B.
Building and Housing Research Center
Ahmadi, M.
Malayer University
Akbari, Z.
University of Tehran
Alavi, S.M.Z.
University of Tehran
Alielahi, H.
Islamic Azad University
Arvin, M.R.
Fasa University
Asadi, P.
Isfahan University of Technology
Asakereh, A.
Semnan University
Asghari, A.
University of Tehran
Askari, F.
International Institute of Earthquake Engineering and Seismology
Aslani, F.
University of Western Australia
Azarhomayun, F.
University of Tehran
Babazadeh, A.
University of Tehran
Bagherih, A.
Malayer University
Bahmanpour, A.
Islamic Azad University
Baraldi, D.
Iuav University of Venice
Bayat, M.
IA University, Najafabad Branch
Behnam Far, F.
Isfahan University of Technology
Bitaraf, M.
University of Tehran
Burak Bozdogan, K.
Anakkale Onsekiz Mart University
Castaldo, P.
Politecnico di Torino
Chen, J.T.
National Taiwan University
Chen, Z.W.
Shenzhen University
Chenaghlou, M.R.
Sahand University of Technology
Chini, M.
Road, Housing & Urban Development Research Center (BHRC)
Dabiri, R.
Islamic Azad University
Daneshvar, D.
Vienna University of Technology
Davoodi, M.
International Institute of Earthquake Engineering and Seismology
Dousti, A.
Road, Housing & Urban development Research Center (BHRC)
Eftekhar, M.H.
University of Tehran
Eskandari-Ghadi, M.
University of Tehran
Faghihi, S.V.
University of Tehran
Farzane, O.
University of Tehran
Ferraioli, M.
University of Campania
Ganjian, N.
IA University, Science and Research Branch
Ghafarpour Jahormi, S.
Shahid Rajaee Teacher Training University
Ghaffari, J.
University of Tabriz
Ghanbari, A.
Kharazmi University
Ghandi, E.
University of Mohaghegh Ardabili
Ghasemzadeh, S.H.
Gilan University
Habibi, A.R.
Shahed University
Huang, Y.
Delft University of Technology
Jahed Armaghani, D.
University of Technology Sydney
Jalili, J.
International Institute of Earthquake Engineering and Seismology

Abhishek, J.
Central University of Haryana
Johari, A.
Shiraz University of Technology
Kabir, M.Z.
Amirkabir University of Technology
Kalantary, F.
K.N. Toosi University of Technology
Karami, M.
University of Nevada
Karami Mohammadi, R.
K.N. Toosi University of Technology
Kerachian, R.
University of Tehran
Khanmohmmadi, M.
University of Tehran
Kolahdoozan, M.
Amirkabir University of Technology
Kumar, V.
Universidade Federal de Sao Carlos
Kumar, M.
SRM Institute of Science and Technology
Kumar, A.
National Institute of Technology Delhi
Lantsoght, E.
Delft University of Technology
Lei, Y.
Xiamen University
Li, S.Q.
Heilongjiang University
Madani, S.H.
Graduate University of Advanced Technology
Mahdikhani, M.M.
Imam Khomeini International University
Mahmoudzadeh Kani, I.
University of Tehran
Mandal, S.
Indian Institute of Technology (BHU) Varanasi
Marchione, F.
Marche Polytechnic University
Marefat, M.S.
University of Tehran
Mariani, S.
Politecnico di Milano
Masoudi, M.
K.N. Toosi University of Technology
Massah, S.R.
Iran University of Science and Technology
Moghadas Nejad, F.
Amirkabir University of Technology
Mohammadi, M.A.
Urmia University Faculty of Engineering
Moodi, F.
Amirkabir University of Technology
Naderpour, H.
Semnan University
Naghipour, M.
Babol Noshirvani University of Technology
Nazif, S.
University of Tehran
Noroozinejad Farsangi, E.
Graduate University of Advanced Technology
Ozturk, B.
Hacettepe University
Revathi, P.
Puducherry Technological University
Panji, M.
Islamic Azad University
Patel, N.K.
Navrachana University Vadodara Gujrat India
Rafiee, R.
University of Tehran
Rahdar, H.A.
University of Zabol
Rahnavard, R.
University of Coimbra
Ranjbar Karkanaki, A.
Islamic Azad University
Rezaeian, A.
Shahid Chamran University of Ahvaz
Rezaie, F.
Bu-Ali Sina University
Rutkowska, G.
Warsaw University of Life Sciences
Sharma, V.
GEC Rajkot
She, G.L.
Harbin Institute of Technology, China
Shekarchi Zadeh, M.
University of Tehran
Shidmoosavi, S.
University of Central Florida
Sobhani, J.
Road, Housing & Urban development Research Center (BHRC)
Soroushian, A.
International Institute of Earthquake Engineering and Seismology
Tabesh, M.
University of Tehran
Taghaddos, H.
University of Tehran
Tajmir Riahi, H.
University of Isfahan
Toloukian, A.R.
Iran University of Science and Technology
Touran, A.
Northeastern University College of Engineering
Valizadeh, H.
Özyeğin University
Vaseghi Amiri, J.
Babol Noshirvani University of Technology

AIMS AND SCOPE

Since the College of Engineering (Former Faculty of Engineering, FOE) of the University of Tehran has renewed its policy toward scientific publication, the Civil Engineering transaction of the well- built 45 years old Persian journal of *"Nashrieh Daneshkadeh Fanni"* is to be published in English and as separate independent journal with the name of ***Civil Engineering Infrastructures Journal***.

Civil Engineering Infrastructures Journal is an international journal which publishes high quality scientific papers in all areas of engineering and management of civil infrastructures. The civil infrastructures include, but are not limited to: buildings, bridges, dams, transportation systems, geotechnical structures, underground constructions, water distribution systems, offshore platforms, pipelines, ocean structures, airports and power plants.

The scope of this journal encompasses, but is not restricted to the following aspects of engineering and management of infrastructures:

- Mathematical modeling
- Computational and experimental methods
- Environmental Impact assessment
- Passive defense and security issues
- Monitoring and assessment
- Construction and design for durability
- Deterioration modeling and aging
- Failure analysis
- Field testing
- Financial planning
- Inspection and diagnostics
- Life-cycle analysis and prediction

- Maintenance, rehabilitation, repair and replacement strategies
- Non-destructive testing
- Optimization of maintenance and management
- Specifications and codes
- Reliability and risk management
- Supervisory Control and Data Assimilation (SCADA)
- Automation and Robotics in Construction
- Smart civil infrastructure Systems
- Sustainable civil infrastructure systems
- Case studies

Audiences of ***Civil Engineering Infrastructures Journal*** are researchers and practitioners as well as people working in infrastructure design, construction, maintenance and operation. Papers considered for publication must contain a clear and well-defined engineering component and make a significant contribution to the engineering and management of civil infrastructures. All articles submitted to this journal will undergo a rigorous peer review by anonymous independent experts.

Additional information can be obtained from:

Civil Engineering Infrastructures Journal
College of Engineering,
University of Tehran
P.O. Box: 11155- 4563
Tehran, Iran
Tel/ Fax: +98-21-88956097
Web Site: www.ceij.ir
Email: ceij@ut.ac.ir

University of Tehran
College of Engineering

Copyright Transfer Agreement

In order to protect the author(s), from the consequences of unauthorized use, the publisher requests that all author(s) sign the appropriate statement below:
The author(s) undersigned hereby approves submission of this work and all subsequent revisions for publication and transfers, assigns, or otherwise conveys copyright ownership to the Civil Engineering Infrastructures Journal (CEIJ). I (we) acknowledge that i) the submitted material represents original material, ii) does not infringe upon the copyright of any third party, and iii) that no part of the work has been published or under consideration for publication elsewhere unless and until it is rejected by Civil Engineering Infrastructures Journal (CEIJ). I (we) agree to indemnify the publisher against any loss or damages arising out of a breach of this agreement. In the event that my (our) submission is not published, copyright ownership shall revert to the author (s).

Manuscript Title:

Corresponding Author

Author:
Date: Signature;

Author:
Date: Signature:

Author:
Date: Signature:

Author:
Date: Signature:

Please submit the signed agreement with the final manuscript to:
Civil Engineering Infrastructures Journal (CEIJ)
School of Civil Engineering,
College of Engineering, University of Tehran
Enghelab Ave., P.O. Box: 11155-4563, Tehran, Iran.
Tel: 88956097
Fax: 66498981
E-mail: ceij@ut.ac.ir
Website: www.ceij.ir

CIVIL ENGINEERING INFRASTRUCTURES JOURNAL (CEIJ)

is indexed and abstracted in the bibliographical databases including:

Web of Science (ESCI)
http://science.thomsonreuters.com

Scopus
https://www.scopus.com

Islamic World Science Citation Center;
http://www.isc.gov.ir

Directory of Open Access Journals (DOAJ)
https://doaj.org

Google Scholar
https://scholar.google.com

General Impact Factor (GIF)
http://generalimpactfactor.com

Scientific Indexing Services (SIS)
http://www.sindexs.org

International Institute of Organized Research (I2OR)
http://www.i2or.com

Information Matrix for the Analysis of Journals (MAIR)
http://miar.ub.edu

ROAD: the Directory of Open Access scholarly Resources
http://road.issn.org

Scientific World Index
http://www.sciwindex.com

International Innovative Journal Impact Factor (IIJIF)
http://www.iijif.com

Science library index
http://scinli.com

Journal Factor
http://www.journalfactor.org

Open Academic Journals Index (OAJI)
http://oaji.net

Electronic Journals Library (EZB)
https://rzblx1.uni-regensburg.de

Systematic Impact Factor (SIF)
http://www.sifactor.org

COSMOS IMPACT FACTOR
http://www.cosmosimpactfactor.com

Polish Ministry of Science and Higher Education (MSHE)
https://journals.indexcopernicus.com

Magiran
http://www.magiran.com

Scientific Information Database (SID); Iran;
http://www.Sid.ir

Ministry of Science, Research and Technology of Iran has granted the Science and Research (Elmi-Pajouheshi) credit to CEIJ according to the letter No. 3/252445 at 25 Feb. 2012.

College of Engineering

Civil Engineering Infrastructures Journal

Volume 56, Number 2, December 2023

CONTENTS:

Research Papers

Rehabilitation Prospects of Concrete Pavements with Self-Compacting Concrete 221
Containing Wollastonite Micro-Fiber
Jindal, A., G.D. Ransinchung, R.N., Kumar, P., Kumar, V. and Rana, D.

A Simplified Continuum Damage Model for Nonlinear Seismic Analysis of Concrete 235
Arch Dams Using Different Damping Algorithms
Hashempour, S.A.R., Akbari, R. and Lotfi, V.

Performance Improved Multi-Objective Optimization in Applying Low-Impact 257
Development Strategies to Control Urban Runoff
Naghibzadeh, H., Saadat, M., Basirat, S. and Iranpour Mobarakeh, M.

Performance Evaluation of Terrazyme as Soil Stabilizer 277
Aswar, D.S., Bajad, M.N. and Ambadkar, S.D.

The Comparison of Tunnel Convergence from Numerical Analysis with Monitoring 301
Data Based on Different Constitutive Models in Rock Medium
Chalajour, S. and Hataf, N.

Behavioral Study of Raft Reinforced with Geogrid and Geocell Through 321
Experiments and Neural Models
Kumar, V., Priyadarshee, A., Chandra, S., Jindal, A. and Rana, D.

Ageing Resistance of Bituminous Binder Modified with Propitious Antioxidant 333
Chakravarty,H., Sinha, S. and Gupta, S.

Performance of Grape Extract Addition as an Admixture in Concrete Construction 347
Mahmood, H.F., Dabbagh, H. and Mohammed, A.A.

Experimental Study of Properties of Green Concrete Based on Geopolymer Materials 365
under High Temperature
Mansourghanaei, M.H., Biklaryan, M. and Mardookhpour, A.

Use of Reclaimed Asphalt Pavement (RAP) in Concrete in Perspective of Rigid Pavements 381
Jadoon, N., Ullah, I., Sarir, M., Noman, M. and Shah, A.A.

Evaluating UHP-SFRCs Performance under Flexural and Tensile Loadings and Aggressive 393
Environment by Assessing the Applicability of Different Constituent Materials in UHPC Production
Pourjahanshahi, A., Madani, H. and Khaghani Boroujeni, A.

Seismic Fragility Analysis of Torsionally-Coupled Steel Moment Frames Against Collapse 415
Mesr Habiby, Y. and Behnamfar, F.

Civil Engineering Infrastructures Journal (CEIJ)

Volume 56, Number 2, December 2023